

## **Aeroacoustics of Jet-Surface Interaction and Passive Solutions for Mitigating Jet-Installation Noise**

Rego, Leandro

**DOI**

[10.4233/uuid:a50e3a9c-af3a-4e4f-836c-80f70c75847c](https://doi.org/10.4233/uuid:a50e3a9c-af3a-4e4f-836c-80f70c75847c)

**Publication date**

2022

**Document Version**

Final published version

**Citation (APA)**

Rego, L. (2022). *Aeroacoustics of Jet-Surface Interaction and Passive Solutions for Mitigating Jet-Installation Noise*. [Dissertation (TU Delft), Delft University of Technology].  
<https://doi.org/10.4233/uuid:a50e3a9c-af3a-4e4f-836c-80f70c75847c>

**Important note**

To cite this publication, please use the final published version (if applicable).  
Please check the document version above.

**Copyright**

Other than for strictly personal use, it is not permitted to download, forward or distribute the text or part of it, without the consent of the author(s) and/or copyright holder(s), unless the work is under an open content license such as Creative Commons.

**Takedown policy**

Please contact us and provide details if you believe this document breaches copyrights.  
We will remove access to the work immediately and investigate your claim.

**AEROACOUSTICS OF JET-SURFACE INTERACTION  
AND PASSIVE SOLUTIONS FOR MITIGATING  
JET-INSTALLATION NOISE**



# **AEROACOUSTICS OF JET-SURFACE INTERACTION AND PASSIVE SOLUTIONS FOR MITIGATING JET-INSTALLATION NOISE**

## **Proefschrift**

ter verkrijging van de graad van doctor  
aan de Technische Universiteit Delft,  
op gezag van de Rector Magnificus prof. dr. ir. T. H. J. J. van der Hagen,  
voorzitter van het College voor Promoties,  
in het openbaar te verdedigen op dinsdag 13 september 2022 om 15:00 uur

door

**Leandro FALCÃO LOUREIRO REGO**

Master of Science in Mechanical Engineering,  
Universidade de São Paulo, Brazilië  
geboren te São Luis, MA, Brazilië.

Dit proefschrift is goedgekeurd door de

promotor: Prof. dr. D. Casalino

promotor: Dr. D. Ragni

copromotor: Dr. F. Avallone

Samenstelling promotiecommissie:

Rector Magnificus,  
Prof. dr. D. Casalino,  
Dr. D. Ragni,  
Dr. F. Avallone,

voorzitter  
Technische Universiteit Delft, promotor  
Technische Universiteit Delft, promotor  
Technische Universiteit Delft, copromotor

*Onafhankelijke leden:*

Prof. dr. ir. M. Snellen,  
Prof. dr. F. M. Catalano,  
Prof. dr. R. Camussi,  
Dr. C. A. Brown,  
Prof. dr. ir. S. van der Zwaag,

Technische Universiteit Delft  
Universidade de São Paulo, Brazilië  
Università Roma Tre, Italië  
NASA Glenn Research Center, Verenigde Staten  
Technische Universiteit Delft, reservelid



*Keywords:* Aeroacoustics, Jet-Installation Noise, Permeable Materials, Acoustic Liners

*Printed by:* Ridderprint

*Front & Back:* Illustration of the jet-installation noise source on an aircraft.

Copyright © 2022 by L. Rego

ISBN 000-00-0000-000-0

An electronic version of this dissertation is available at

<http://repository.tudelft.nl/>.

*Success flourishes only in perseverance - ceaseless, restless perseverance.*

Baron Manfred von Richthofen (a.k.a. The Red Baron)



# CONTENTS

<b>Summary</b>	<b>xi</b>
<b>Samenvatting</b>	<b>xv</b>
<b>1 Introduction</b>	<b>1</b>
1.1 Aircraft Noise Challenges and Trends . . . . .	2
1.2 Jet-Flap Interaction and Jet-Installation Noise . . . . .	4
1.3 Passive Solutions for JIN Mitigation . . . . .	6
1.4 Research Objectives and Thesis Outline . . . . .	9
References . . . . .	10
<b>2 Fundamentals of Jet Aerodynamics and Jet-Installation Noise</b>	<b>13</b>
2.1 Jet Aerodynamics . . . . .	14
2.2 Turbulence-Mixing Noise . . . . .	17
2.3 Noise due to Surface Pressure Fluctuations and Edge Scattering . . . . .	21
2.4 Jet-Installation Noise . . . . .	24
References . . . . .	26
<b>3 Permeable Materials and Acoustic Liners as NRS</b>	<b>31</b>
3.1 Properties of Permeable Materials . . . . .	32
3.2 Applications for Aerodynamic Noise Reduction . . . . .	33
3.3 Acoustic Liners . . . . .	36
References . . . . .	39
<b>4 Numerical and Experimental Methodology</b>	<b>43</b>
4.1 Numerical Approach . . . . .	44
4.1.1 Lattice-Boltzmann Method . . . . .	44
4.1.2 VLES Turbulence Model . . . . .	46
4.1.3 Acoustic Predictions . . . . .	49
4.2 Experimental Approach . . . . .	52
4.2.1 Flow Field Measurements . . . . .	52
4.2.2 Acoustic Measurements . . . . .	55
References . . . . .	59
<b>5 JIN and Near-Field Characteristics of Jet-Surface Interaction</b>	<b>63</b>
5.1 Objectives . . . . .	64
5.2 Computational Set-up . . . . .	64
5.3 Jet Flow Field and Grid Convergence . . . . .	67
5.4 Installation Effects and Trailing-Edge Scattering . . . . .	70
5.5 Source Characteristics and Far-field Noise . . . . .	75

5.6	Far-field Noise Scaling based on Near-field Properties . . . . .	80
5.6.1	Radial direction scaling law . . . . .	81
5.6.2	Axial direction scaling law . . . . .	84
5.7	Concluding Remarks . . . . .	92
	References . . . . .	94
<b>6</b>	<b>JIN Reduction with Flow-Permeable Trailing-Edges</b>	<b>97</b>
6.1	Objectives. . . . .	98
6.2	Experimental Set-up . . . . .	98
6.2.1	Flow-permeable Materials . . . . .	101
6.2.2	Instrumentation and Measurement Techniques . . . . .	101
6.3	Jet Flow Field . . . . .	104
6.4	Far-field Acoustic Results . . . . .	107
6.5	Concluding remarks . . . . .	118
	References . . . . .	119
<b>7</b>	<b>Mechanisms of JIN Reduction with Flow-Permeable Trailing Edges</b>	<b>123</b>
7.1	Objectives. . . . .	124
7.2	Computational Set-up . . . . .	124
7.2.1	Installed jet configuration and flow conditions. . . . .	124
7.2.2	Flow-permeable materials . . . . .	125
7.2.3	Set-up components and simulation parameters . . . . .	127
7.3	Jet Flow Field and Set-up Validation. . . . .	130
7.4	Far-field Noise . . . . .	134
7.4.1	Far-field Spectra . . . . .	134
7.4.2	Far-field Noise Breakdown . . . . .	135
7.5	Volumetric Flow Rate and Surface Pressure Fluctuations . . . . .	138
7.6	Noise from Pressure Wave Impingement and Trailing Edge Scattering . . . . .	141
7.7	Concluding Remarks . . . . .	147
	References . . . . .	149
<b>8</b>	<b>Acoustic Liners for JIN Reduction</b>	<b>151</b>
8.1	Objectives. . . . .	152
8.2	Installed Jet Case . . . . .	152
8.2.1	Computational Set-Up. . . . .	152
8.2.2	Acoustic Input Parameters . . . . .	154
8.3	Resonator Design and Validation . . . . .	156
8.4	Resonator Impedance Characteristics. . . . .	161
8.5	Jet-Installation Noise with Lined Plate . . . . .	164
8.5.1	Far-field Spectra . . . . .	164
8.5.2	Surface Pressure Fluctuations . . . . .	167
8.6	Lined Plate with Perforated Trailing Edge . . . . .	170
8.7	Concluding Remarks . . . . .	172
	References . . . . .	174

<b>9</b>	<b>Permeable Flaps for IJN Reduction at In-Flight Conditions</b>	<b>177</b>
9.1	Objectives . . . . .	178
9.2	Experimental Set-up . . . . .	178
9.2.1	Wind Tunnel Facility and Models . . . . .	178
9.2.2	Permeable Flaps . . . . .	180
9.2.3	Instrumentation and Measurement Techniques . . . . .	182
9.3	Results and Discussions . . . . .	184
9.3.1	Aerodynamic Forces . . . . .	184
9.3.2	Flow Field . . . . .	185
9.3.3	Beamforming Maps and Noise Spectra . . . . .	188
9.4	Concluding Remarks . . . . .	191
	References . . . . .	193
<b>10</b>	<b>Conclusions and Recommendations</b>	<b>195</b>
10.1	Summary and Conclusions . . . . .	196
10.2	Recommendations for Future Work . . . . .	199
<b>A</b>	<b>Signal Processing Techniques and Acoustic Parameters</b>	<b>201</b>
A.1	Time-domain statistics . . . . .	201
A.1.1	Mean value . . . . .	201
A.1.2	Variance and standard deviation . . . . .	202
A.1.3	Root-mean-square . . . . .	202
A.1.4	Auto-correlation and Cross-correlation . . . . .	202
A.2	Frequency-domain statistics . . . . .	203
A.2.1	Fourier transform . . . . .	203
A.2.2	Power spectral density . . . . .	203
A.2.3	Cross-Power spectral density . . . . .	204
A.2.4	Coherence . . . . .	204
A.2.5	Welch's method . . . . .	205
A.3	Sound pressure level and Overall sound pressure level . . . . .	205
	References . . . . .	206
<b>B</b>	<b>Design and Characterization of the A-Tunnel Jet Test Section</b>	<b>207</b>
B.1	Wind tunnel facility . . . . .	207
B.2	Nozzle design . . . . .	207
B.3	Instrumentation . . . . .	209
B.4	Jet flow characteristics . . . . .	210
B.5	Acoustic characteristics . . . . .	212
	References . . . . .	213
	<b>List of Publications</b>	<b>215</b>



# SUMMARY

Aircraft noise levels have been significantly reduced with the introduction of high-bypass ratio turbofan engines, particularly jet noise due to turbulence mixing. This, however, has led to engines with larger diameters and a closer coupling between them and the airframe. As a result, interactions between the exhaust jet flow and the wing give rise to an acoustic source known as jet-installation noise. In more detail, this source is generated by the impingement of unsteady pressure waves from the jet mixing-layer on the airframe surfaces and their scattering as noise at the wing trailing edge. Jet-installation noise becomes relevant particularly during take-off and approach conditions since the deployed flaps are located closer to the turbulent jet flow. Therefore, this thesis aims to elucidate the physical mechanisms behind jet-installation noise, followed by the development of passive mitigation solutions based on porous material technology and acoustic liners. A study on their effects and working mechanisms is performed, as well as on their feasibility from the aerodynamic perspective.

Initially, the link between jet-installation noise and the near-field flow features of the corresponding isolated jet is studied by means of lattice-Boltzmann numerical simulations. The computational set-up consists of a flat plate placed in proximity of a turbulent jet. It is shown that the Helmholtz number, based on the wavelength of eddies in the mixing layer and their distance to the plate trailing edge, predicts the frequency range where installation noise occurs. Based on the isolated jet near-field, scaling laws are also found for the far-field noise produced by different plate geometries. By moving the plate away from the jet in the radial direction, an exponential decay in noise levels is obtained, which is characteristic of the linear hydrodynamic field of the jet, where the plate is located. In the axial direction, spectral proper orthogonal decomposition is applied to filter out jet acoustic waves, which contaminate the pressure signals. The resultant hydrodynamic pressure fluctuations display a wavepacket behaviour, which can be fitted with a Gaussian envelope. It is found that installation noise for different plate lengths is proportional to the amplitude of the Gaussian curve at the position of the plate trailing edge. These analyses show that trends of jet-installation noise can be predicted by analysing the near-field of the isolated case.

Subsequently, the application of flow-permeable materials as a solution for reducing jet-installation noise is studied. Experiments are carried out with a flat plate placed in the near field of a single-stream subsonic jet. The plate trailing edge can be replaced with different flow-permeable inserts, such as a metal foam and a perforated plate structure. The former provides noise abatement of up to 9 dB at the spectral peak for  $M_a = 0.3$  and a polar angle  $\theta = 40^\circ$ , with an overall reduction in the entire frequency range where jet-installation noise is dominant. The perforated plate provides lower noise reduction than the metal foam (7 dB at the spectral peak for  $M_a = 0.3$  and  $\theta = 40^\circ$ ), and it is less effective at low frequencies. This is related to the values of permeability and form coefficient of the materials, which are the major parameters controlling the pressure balance across

the trailing edge and, consequently, the noise generated by the plate. However, despite having a high permeability, the plate with the metal-foam trailing edge still has a distinct noise production at mid frequencies ( $St \approx 0.43$  for  $M_a = 0.3$ ).

It is conjectured that the solid-permeable junction in the plate acts as a new scattering region, and thus its position also affects the far-field noise. This is confirmed by numerical simulations and the application of the beamforming technique, which shows that the dominant acoustic source is located at the solid-permeable junction for highly permeable materials, such as the metal foam. On the other hand, the perforated case has the source positioned near the trailing edge, similarly to the solid case. From the simulations, a breakdown of the far-field noise generated by the plate is also performed, where the contributions from the solid and permeable sections are computed separately. The former has distinct regions in the noise spectrum, which are dominated either by surface pressure fluctuations or trailing-edge scattering. However, for the permeable region, the results point to a significant mitigation of the noise due to scattering, which is no longer the dominant mechanism in any frequency range. This is confirmed by lower values of spanwise coherence, computed from the surface pressure. Therefore, the clear dominant mechanism in the permeable region of the plate is the unsteady loading to pressure wave impingement. This is verified for all investigated configurations so that even with a low permeability structure, significant noise reduction can still be achieved.

A different passive solution for jet-installation noise studied in this work is the application of Helmholtz resonators with a curved cavity. The face-sheet and cavity are designed with the Guess method and the impedance is verified through an experiment and a simulation of an impedance tube. Numerical simulations of the installed jet are performed with an array of resonators placed inside a flat plate with the face-sheet on the lower side, targeting noise reduction at a ground observer. Far-field spectra show that noise reduction in the order of 7 dB is obtained with respect to the baseline solid plate, at the resonance frequency. Moreover, there is a broad frequency range around the resonance in which the sound pressure levels of the lined plate are lower. The results also show that a slight noise reduction (2 - 3 dB) occurs for an observer on the shielded side of the plate, but in a significantly narrower band around the resonance frequency. This is attributed to the absorption of acoustic waves from the jet itself prior to their scattering at the trailing edge, coupled with a less abrupt impedance discontinuity at the trailing edge. Consequently, the resonators also act by reducing the strength of the acoustic source at the designed resonance frequency.

Finally, an experimental investigation on jet-installation noise reduction with permeable flaps on an aircraft half-model is performed, focusing on the effects on the noise levels as well as the aerodynamic properties of the model (lift and drag forces). Two perforated flaps with different hole patterns are investigated. The first one has a uniform hole distribution with equal hole spacing in both streamwise and spanwise directions, whereas the second one has a gradient permeability, with the hole spacing progressively decreasing towards the trailing edge. Aerodynamic force measurements carried out with a balance show that the permeable flaps are responsible for a lift reduction in the order of 7%, and a slight drag increase, in the order of 0.5%, with the gradient permeability flap outperforming the uniform one. Acoustic results obtained from phased array measurements show that the source at the flap trailing edge, generated due to the interaction with

the jet, has a reduction of 3 dB in amplitude with both permeable flaps, which perform similarly in terms of noise mitigation. Therefore, the permeable flaps are able to significantly reduce jet-installation noise for an aircraft configuration under flight conditions, with the potential of having a minor impact on the aerodynamic characteristics.



# SAMENVATTING

Het geluid van vliegtuigen is in de afgelopen jaren aanzienlijk verminderd door de ontwikkeling van turbofanmotoren met een hoge bypass-ratio, waardoor met name het geluid van de luchtstraal als gevolg van turbulente menging afgenomen is. Deze trend heeft geleid tot motoren met grotere diameters en daarmee tot kleinere afstanden tussen de motor en het eigenlijke vliegtuig. De resulterende interacties tussen de uitlaatstraalstroom en de vleugel leiden tot een nieuwe akoestische bron: straal-installatiegeluid. Deze geluidsbron wordt gegenereerd door de interactie van onstabiele drukfluctuaties in de menglaag van de straal met de diverse oppervlakken van het vliegtuig, resulterend in de emissie van geluid aan de achterrand van de vleugel. Deze vorm van geluid wordt vooral relevant tijdens het opstijgen en het landen van een vliegtuig, aangezien de vleugelkleppen zich dan nog dichterbij de turbulente straalstroom bevinden. Gezien de maatschappelijke relevantie van het probleem heeft dit proefschrift tot doel enerzijds de fysieke mechanismen achter straal-installatiegeluid te achterhalen, en anderzijds hiervoor passende oplossingen te vinden door gebruik te maken van permeabele materialen en akoestische deklagen. Het betreft een uitgebreide studie naar de effecten en werkingsmechanismen, met een speciale focus op de uiteindelijke technische haalbaarheid, bekeken vanuit een aerodynamisch perspectief.

Allereerst wordt het verband tussen straal-installatiegeluid en de eigenschappen van de luchtstromingen op kleine schaal in een geïsoleerde jet bestudeerd door middel van numerieke Lattice-Boltzmann-simulaties. De in het model gesimuleerde situatie bestaat uit een vlakke plaat die in de buurt van een turbulente straal is geplaatst. Het onderzoek laat zien dat het Helmholtz-getal, dat berekend wordt uit de golfengte van de wervelingen in de menglaag en hun afstand tot de plaat, het frequentiegebied van dit type geluid bepaalt. Op basis van de resultaten voor straalstromingen berekend voor effecten optredend op een kleinere lengteschaal zijn ook schaalwetten gevonden voor het voorspellen van het geluidsniveau op grotere afstand in het geval van andere dan vlakke-plaat geometrieën. Wanneer de plaat in radiale richting van de straal af bewogen wordt, wordt een exponentieel verval van het geluidsniveau verkregen, hetgeen een karakteristieke eigenschap is van het lineaire hydrodynamische veld waarin de plaat zich bevindt. In de axiale richting wordt vervolgens 'spectral proper orthogonal decomposition' toegepast om de effecten van de akoestische golven van de straalstroming, die de druksignalen vervuilen, uit te filteren. De resulterende hydrodynamische drukfluctuaties vertonen een wavepacket-gedrag, dat met een Gaussian envelope gefit kan worden. Het blijkt dat het installatiegeluid voor verschillende plaatlengtes proportioneel is aan de amplitude van de Gauss-curve ter plaatse van de achterrand van de installatie. Deze analyses laten tevens zien dat macroscopische trends in straal-installatiegeluid voorspeld kunnen worden door het near-field van een geïsoleerde jet te analyseren.

Vervolgens wordt de toepassing van permeabele materialen ter vermindering van het straal-installatiegeluid bestudeerd. Er wordt geëxperimenteerd met een vlakke plaat die

in de nabijheid van een enkelvoudige subsonische straal wordt geplaatst. De achterrand van de massieve plaat kan worden vervangen door verschillende doorlatende inzetmaterialen, zoals een open-cel metaalschuim en een geperforeerde plaat. De eerste zorgt voor een ruisonderdrukking tot 9 dB bij de spectrale piek voor  $M_a = 0,3$  en een polaire hoek  $\theta = 40^\circ$ , gekoppeld aan een algehele reductie in geluidsterkte voor het gehele relevante frequentiegebied. De geperforeerde plaat zorgt voor een kleinere geluidsreductie dan het metaalschuim (7 dB bij de spectrale piek voor  $M_a = 0,3$  en  $\theta = 40^\circ$ ), en is tevens minder effectief bij lage frequenties. De verschillen zijn gerelateerd aan de doorlaatbaarheid en vormcoëfficiënt van beide permeabele materialen, die samen de belangrijkste parameters zijn om de drukbalans over de achterrand te regelen en die bijgevolg de karakteristieken van het gegenereerde geluid bepalen. Ondanks zijn hoge permeabiliteit, heeft de plaat met een achterrand uit metaalschuim nog steeds een duidelijke geluidsproductie bij midden-frequenties ( $St \approx 0,43$  voor  $M_a = 0,3$ ). Aangenomen wordt dat de abrupte overgang tussen de volledig dichte plaat en het permeabele eindstuk zich als een nieuw verstrooiingsgebied ontwikkelt, wat dan vervolgens het geluid op grotere afstand beïnvloedt.

Deze hypothese wordt bevestigd door numerieke simulaties en de toepassing van de 'beamforming'-techniek op de data, die beide aantonen dat de dominante akoestische bron zich nu bevindt op de overgang tussen het massieve materiaal en het poreuze metaalschuim. In het geval van een geperforeerd einddeel blijft de belangrijkste geluidsbron net als bij een volledig dichte achterrand dichtbij de achterrand gelegen. Op basis van de simulaties wordt ook berekend welke bijdrages de massieve en de permeabele componenten aan het geluid op afstand leveren. De bijdrage van de eerste kent verschillende gebieden in het geluidsspectrum, die vooral bepaald worden door ofwel fluctuaties in de oppervlaktedruk danwel verstrooiing aan de randen. Voor de permeabele component wijzen de resultaten echter op een significante vermindering van het geluid afkomstig van verstrooiingsverschijnselen, zodat dat niet langer het dominante mechanisme is. Deze conclusie wordt bevestigd door lagere waarden voor de spanwijdtecoherentie berekend uit de oppervlaktedruk. Daarom is het duidelijk dat het dominante geluidsproductie mechanisme in het permeabele gebied van de plaat het gevolg is van onstabiele belastingen door de inwerking van drukgolven. Deze hypothese wordt geverifieerd voor alle onderzochte configuraties, leidend tot configuraties waarbij zelfs met een minimaal doorlatende structuur een significante geluidsreductie bereikt kan worden.

Een andere passieve oplossing ter reductie van jet-installatiegeluid, welke in dit werk wordt bestudeerd, is de toepassing van Helmholtz-resonatoren met een gekromde holle ruimte. De topologie van het buitenste oppervlak en die van de holle ruimte zijn ontworpen met de Guess-methode. De impedantie van de resonatoren wordt experimenteel bepaald en berekend middels simulatie van een impedantiebus. Numerieke simulaties van de luchtstroom worden uitgevoerd waarbij het voorste buitenblad van de resonatoren zich bevindt aan de onderkant van de plaat waarin ze gemonteerd zijn. Door deze configuratie wordt de geluidsreductie waarneembaar voor een waarnemer op de grond gesimuleerd. Far-field spectra laten zien dat bij de resonantiefrequentie een geluidsreductie van ongeveer 7 dB wordt verkregen ten opzichte van de massieve basisplaat. Bovendien is er een breed frequentiebereik rond de resonantiepiek waarbij het geluids-

niveau voor de met resonatoren beklede plaat lager is. De resultaten laten ook zien dat er een lichte geluidsreductie (2 - 3 dB) is als de waarnemer aan de afgeschermd zijde van de plaat gestationeerd is. In dat geval treedt de reductie alleen op een aanzienlijk smallere band rond de resonantiefrequentie. De reductie wordt toegeschreven aan de absorptie van akoestische golven van de straal zelf voordat ze verstrooien aan de achterrand, in combinatie met een minder abrupte impedantiediscontinuïteit ter plaatse. De resonatoren verlagen zodoende de sterkte van de akoestische bron bij de gewenste resonantiefrequentie.

Aan het einde van dit promotieonderzoek is experimenteel onderzoek gedaan naar de reductie van straal-installatiegeluid middels permeabele vleugelkleppen gemonteerd op een half schaalmodel van een vliegtuig, waarbij de nadruk ligt op het bepalen van de simultane effecten op het geluidsniveau en de aerodynamische eigenschappen van het model (lift- en wrijvings-krachten). Twee geperforeerde vleugelkleppen met verschillende gatenpatronen worden onderzocht. De eerste heeft een uniforme gatverdeling met gelijke gatafstand zowel in de breedte en de lengte van de vleugelklep. De tweede heeft een gradient in de doorlaatbaarheid gradiëntpermeabiliteit, waarbij de gatafstand afneemt dichterbij de achterrand. Aerodynamische krachtmetingen uitgevoerd met een balans tonen aan dat de permeabele vleugelkleppen verantwoordelijk zijn voor een vermindering in de hefkracht in de orde van 7%, en een lichte toename van de stromingsweerstand ter grootte van 0,5%. De vleugelklep met de gradiënt in het gatpatroon presteert iets beter dan de klep met het uniforme gatpatroon. Akoestische resultaten, verkregen via phased array-metingen, tonen aan dat voor beide vleugelkleppen de ontwikkelde geluidsbron gelegen is aan de achterrand van de vleugelklep. Beide configuratie leverden een geluidsreductie van 3 dB en presteren dus gelijkwaardig qua geluiddemping.

De eindconclusie van het onderzoek is derhalve dat permeabele vleugelkleppen in staat zijn om het geluid opgewekt door de interactie tussen de lucht en de vliegtuigconstructie onder gesimuleerde vluchtomstandigheden aanzienlijk te verminderen, zonder dat dit grote negatieve consequenties heeft voor de aerodynamische prestaties van de vleugel.



# 1

## INTRODUCTION

*Every new beginning comes from some other beginning's end.*

Seneca

*Aircraft noise, particularly that due to turbulent mixing between the exhaust jet flow from the engine and the ambient air, has been considerably reduced with the introduction of high-bypass ratio turbofans. This, however, has led to larger engines which are located closer to airframe lifting surfaces, resulting in the generation of a system-level acoustic source known as jet-installation noise (JIN). This source is important during take-off and approach conditions, which are critical for aircraft certification. In this chapter, the main characteristics of JIN are described along with the motivations behind the research in this thesis. Moreover, noise reduction solutions based on permeable materials are introduced and proposed for this application. The research goals are also included in this chapter, along with an outline of the thesis structure.*

## 1.1. AIRCRAFT NOISE CHALLENGES AND TRENDS

AIRCRAFT emissions have been a topic of intense debate for the past decades. Either concerning the release of greenhouse gasses ( $\text{CO}_2$  and  $\text{NO}_x$ ) in the atmosphere or noise pollution, particularly near airport areas, aircraft have a significant environmental impact. Focusing on the latter, reports have shown that tens of millions of people are affected by aircraft noise, and this figure is expected to increase significantly in the future with the expansion of air traffic [1].

Aircraft manufacturers and aviation organizations have defined different strategies to reduce the impact caused by noise emissions. The International Civil Aviation Organization (ICAO) defines a 4-pronged approach to aircraft noise management in order to achieve maximum environmental benefit in a cost-effective manner. This consists of: reduction of noise at source, land-use planning and management, noise abatement operational procedures and operating restrictions [2]. This thesis focuses on the first aspect, targeting the mitigation of the noise produced by the aircraft itself.

Aircraft noise levels are controlled via standards defined by ICAO and adopted by regulating authorities in each country. The goal of these standards is to ensure technological development and incorporation of noise reduction solutions into future generations of aircraft. The standards are included in the Chapters of a document known as Annex 16, which is progressively updated with the introduction of more stringent maximum emission noise levels. The latest amendment to Annex 16 has been adopted in 2014, into the so-called Chapter 14, defining the current regulations for jet and propeller-driven aircraft undergoing certification.

The maximum emission levels are a function of the aircraft Maximum Take-Off Mass (MTOM), as shown in Fig. 1.1 in terms of Effective Perceived Noise in Decibels (EPNdB) [3]. The chart also includes previous standards as reference. Future goals are even more ambitious than Chapter 14 levels, as reported in Table 1.1 for different types of aircraft, and for a given Entry Into Service (EIS) year [4].

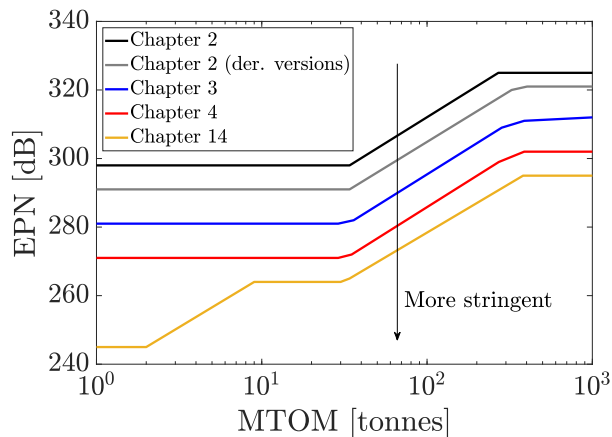


Figure 1.1: Noise standards for jet and propeller-driven aircraft, as a function of the maximum take-off mass, based on each Chapter of ICAO's Annex 16. Adapted from [3].

EIS Date	Business Jets	Regional Jets	Single-Aisle	Twin-Aisle
2027	10.0	14.5	15.5	19.5
2037	15.0	17.0	24.0	26.5

Table 1.1: Noise goals for future entry into service aircraft, expressed as EPNdB with respect to Chapter 14 levels. Adapted from [4].

The development of the next generation of noise reduction technologies is conditioned to a deep analysis of the acoustic sources in a modern aircraft, as shown in Fig. 1.2 for a twin-aisle category. These sources can be classified either as generated by the airframe or by the engine. The former includes the landing gear, flap side-edge, slat/flap cove and wing trailing edge, whereas the latter comprises the fan, turbine, combustion and the exhaust jet. Engine noise sources are usually dominant during take-off due to the high loading of the fan and high velocity of the jet, considering an average of the acoustic measurements in the sideline and flyover certification positions. On the other hand, during approach, airframe sources become more relevant, since the high-lift systems and landing gear are deployed for a significant amount of time [4].

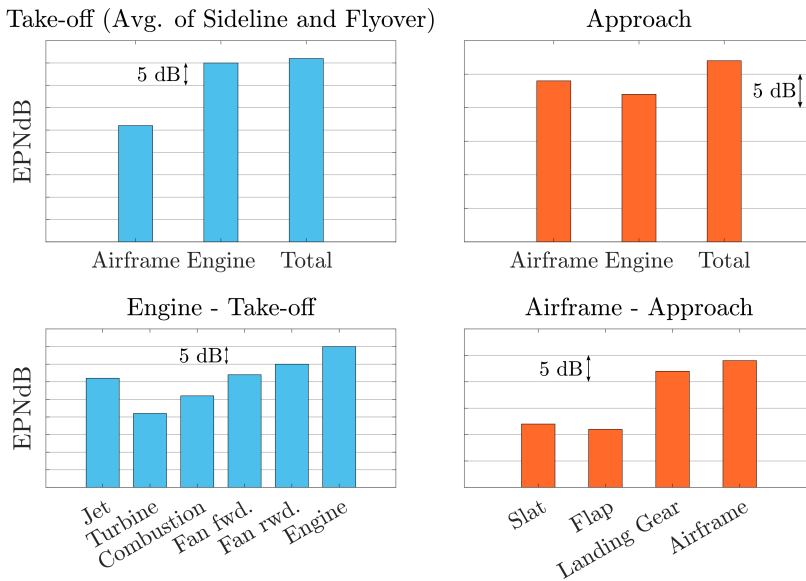


Figure 1.2: Breakdown of main acoustic sources in a twin-aisle commercial aircraft. Adapted from [4].

Even during take-off condition, the figure shows that the jet is no longer the dominant source, as it was for aircraft decades ago [4]. Since the advent of the turbofan engine, steps to augment propulsive efficiency by increasing the bypass ratio have also resulted in significant noise reduction. With an increased bypass, the same amount of thrust can be generated with a relatively lower exhaust velocity, corresponding to lower noise emission [4]. The current trend for turbofan engines is to increase the bypass ra-

tio even further (ultra-high bypass concepts) in order to reduce the overall emissions [5]. While it is expected that the jet noise component will also be reduced, it cannot be stated with certainty that the same will happen for the overall aircraft noise [4].

A higher bypass ratio results in a larger engine diameter; there is, however, a minimum necessary clearance with the ground that needs to be respected, and thus the engines have to be mounted closer to the airframe. Therefore, engine-airframe integration starts playing a major role and interaction between these components needs to be considered, such as the generation of a system-level acoustic source known as Jet-Installation Noise (JIN). With the introduction of ultra-high bypass turbofans, it is expected that this source will become ever more relevant [5] and thus its mechanisms need to be completely understood and mitigated.

## 1.2. JET-FLAP INTERACTION AND JET-INSTALLATION NOISE

Jet-installation noise results from the interaction between the exhaust flow from a turbofan engine and a nearby airframe surface such as the wing or the flap. The main mechanism by which this source is generated is visualized in Fig. 1.3.

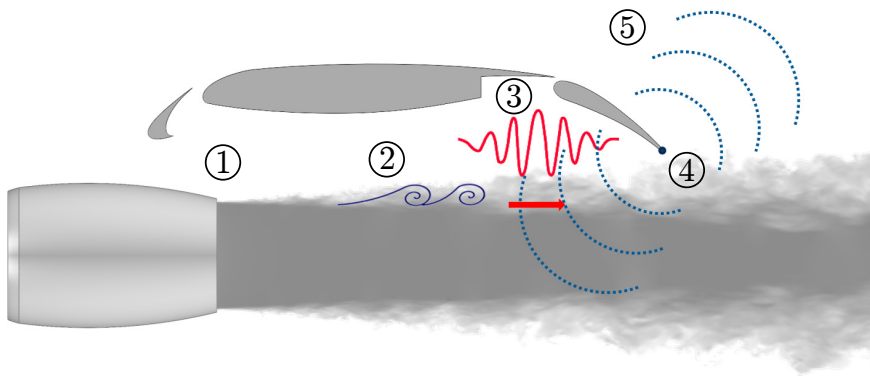


Figure 1.3: Jet-installation noise generation mechanism. (1) Engine jet flow. (2) Turbulent structures in the mixing layer. (3) Hydrodynamic pressure fluctuations convecting with the jet and impinging on the airframe. (4) Geometric discontinuity - flap trailing edge. (5) Scattering of acoustic waves.

First, a turbulent jet flow exhausted from a turbofan engine is considered (1). Due to shear stresses between the flow and the ambient, turbulent structures are generated in a region known as the mixing layer (2). This region is characterized by intense unsteadiness and large velocity and pressure fluctuations; some of those have a convective characteristic, i.e. they are displaced with a certain convection velocity, usually lower than the speed of the jet itself (3). These disturbances impinge on the airframe, generating surface pressure fluctuations and, consequently, noise. Moreover, when they reach a geometric discontinuity such as the flap trailing edge (4), they scatter as acoustic waves (5). Aside from this diffraction mechanism, the airframe also reflects acoustic waves from the jet itself towards an observer on the ground, thus leading to an effectively higher noise level than that of the jet and airframe as isolated and uncorrelated sources. It should be

noted that this phenomenon occurs even when there is not direct grazing of the jet on the airframe; the pressure fluctuations that impinge on the wing and are scattered at the trailing edge are usually of evanescent nature. This characteristic is described in more detail in Chapter 2.

This phenomenon has been demonstrated, for example, through phased array measurements coupled with the beamforming technique for source localization. Mengle *et al.* [6] have studied a scaled model configuration comprised by an engine and a swept wing with deployed flaps. The results are compared with the respective isolated nozzle. Beamforming results show that the dominant source for the installed case is located at the flap trailing edge, in a region close to the jet plume, whereas for the isolated jet, the source is located at the nozzle. For this case, JIN is responsible for a noise increase of approximately 12 dB at the investigated frequency [6].

The trailing-edge scattering mechanism results in a low-frequency broadband noise increase with respect to the isolated jet levels, whereas at relatively higher frequencies, acoustic waves from turbulence-mixing noise in the jet are reflected on the lower side of the wing, augmenting the noise for an observer on the ground [7, 8]. The low-frequency noise increase is also more pronounced in the upstream direction of the jet axis, whereas turbulence-mixing noise is still dominant towards downstream of the axis [9, 10]. A more detailed description of the noise generation mechanisms in an installed jet is reported in Chapter 2.

At the full aircraft level, computations of acoustic footprint have shown that installation effects increase the overall produced noise and are the dominant source for a significant amount of time during the aircraft flyover [11]. It is shown in Fig. 1.4 that they are responsible for an increase of approximately 4 dB in the full aircraft perceived noise levels [11]. The EPNL maps in Fig. 1.5 show a change in shape of the acoustic footprint due to the installation effects, and a larger area of increased noise levels [11]. The large role played by JIN in the overall aircraft emission imposes the need for understanding the physical mechanisms behind sound production and its potential reduction.

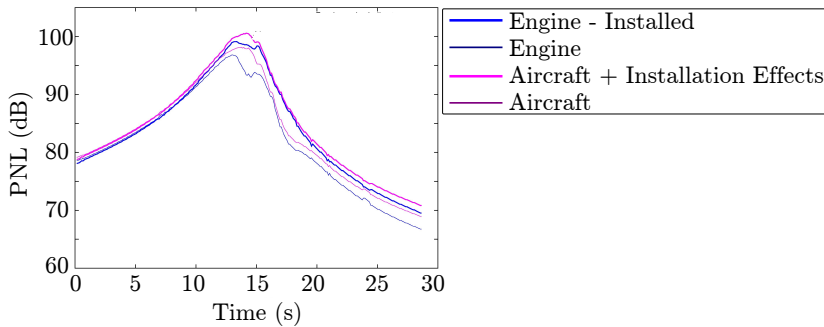


Figure 1.4: Perceived noise levels for an aircraft during flyover in approach condition, focusing on the contribution of engine installation effects. Adapted from [11].

JIN reduction has been investigated through the use of chevron nozzles in a jet-flap configuration [6]. Wind tunnel tests have been carried out by Mengle *et al.* [6] and the results show that the chevrons reduce noise up to 2.6 dB at the spectral peak. However,

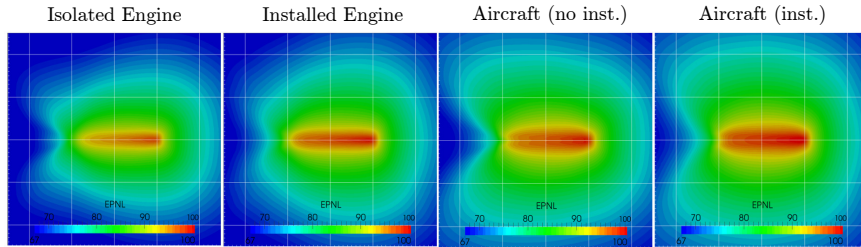


Figure 1.5: EPNL maps over a 5 km square area for an approach condition, considering engine installation effects. Adapted from [11].

although the chevrons provide some benefits, they are still not sufficient to bring the noise back to the isolated jet levels, and thus the trailing-edge source is still present and dominant. Therefore, a different strategy has to be adopted to tackle the JIN problem. In this thesis, the application of permeable materials and acoustic liners in the scattering surface is studied as a potential solution, as described in the next section.

### 1.3. PASSIVE SOLUTIONS FOR JIN MITIGATION

The noise mitigation trend in the past few years has been progressively reduced and it is possible that further decrease will only be achieved with disruptive concepts that may affect the aircraft operating cost [12]. One concept that has recently become the subject of intensive research is the application of permeable materials for mitigating aeroacoustic sound sources.

One objective for the application of permeable materials for JIN reduction is to modify the surface impedance close to the edge, in order to reduce the discontinuity at that region, providing a smoother transition from the surface to the flow [12, 13]. Moreover, open-cell permeable materials such as the insert shown in Fig. 1.6 [14], allow for flow communication. Therefore, by applying them on airframe surfaces, it is possible to mitigate the pressure imbalance and damp fluctuations [13] caused by the impingement of turbulent structures from the jet on the lower side of the wing/flap.



Figure 1.6: Metal foam trailing-edge insert for airfoil noise reduction [14].

Despite not yet applied to JIN reduction, permeable materials have been verified to mitigate other aeroacoustic sources with similar physical mechanisms. For flap side-edge noise, Revell *et al.* [15] have obtained 8 dB reduction with a permeable flap surface.

It has been conjectured that the reduction in surface pressure fluctuations and far-field sound are due to dissipation of acoustic waves, flow communication between upper and lower side (reducing the pressure imbalance between them), and lower impedance of the surface interacting with the vortex [15].

For turbulence-impingement noise, wherein sound is generated by the impact of vortical structures on a surface, Roger and Moreau [16] have studied the acoustic behaviour of a NACA 0012 airfoil with a porous leading edge and a turbulence grid installed upstream. The results show a 6 dB noise reduction with respect to the solid configuration, which is linked to viscous effects in the permeable material progressively slowing down the incident turbulent field, thus reducing temporal variations and mitigating noise generation [16, 17].

For turbulent boundary-layer trailing-edge noise, which is similar to JIN in terms of sound generation due to scattering, Herr *et al.* [18] have studied the application of permeable materials at the last 10% of the chord of a DLR F16 airfoil. Results have shown significant noise reduction at low frequencies with respect to the solid case, indicating that the scattering mechanism has been weakened. It has been also concluded that communication between the pressure and suction sides of the airfoil is necessary to obtain noise reduction, indicating that an improvement of the pressure balance is essential [18].

From the conclusions of the aforementioned studies, it is hypothesized that JIN can be mitigated with permeable materials at the surface near the jet. Flow communication and viscous dissipation are expected to reduce noise due to the impinging turbulent field [16, 17]. Moreover, a smoother impedance change and weakening of the scattering mechanism are likely to reduce the trailing-edge noise component [12, 18]. Therefore, these materials have a strong potential for being effective JIN reduction solutions. It is necessary, however, to study the magnitude of noise abatement that can be achieved, as well as determine how the permeable materials affect the noise generation mechanisms of an installed jet.

A different concept of noise reduction solution is the acoustic liner. This concept is based on an array of Helmholtz resonators, comprising a porous face-sheet, a cavity and a solid backplate, as shown in Fig. 1.7, which is also known as a Single Degree-of-Freedom (SDOF) liner. The working principle of a liner is to dampen noise by dissipating acoustic energy and converting it into vorticity within the orifices in the face-sheet [12, 19]. A different concept can be created by adding a perforated septum inside the cavity, the so-called Double Degree-of-Freedom (DDOF) liner, in order to expand the frequency range of sound absorption.

Acoustic liners are commonly applied at the inlet and exhaust of aircraft turbofan engines in order to reduce fan noise, transmitted through the nacelle [12]. Liners are usually effective acoustic treatments in a narrow frequency band, but, under certain conditions, they can provide noise mitigation in a sufficiently broad range. This happens, for example, with high-amplitude incident sound waves, for which the liner presents a non-linear behaviour. Under these conditions, vortex shedding occurs at the openings of the face-sheet and the frequency range of reduction is a function of the Reynolds number at the orifice [12, 21].

Despite the usual application for tonal noise reduction, acoustic liner technology has been studied for mitigation of aircraft broadband sources. Casalino and Barbarino [22]

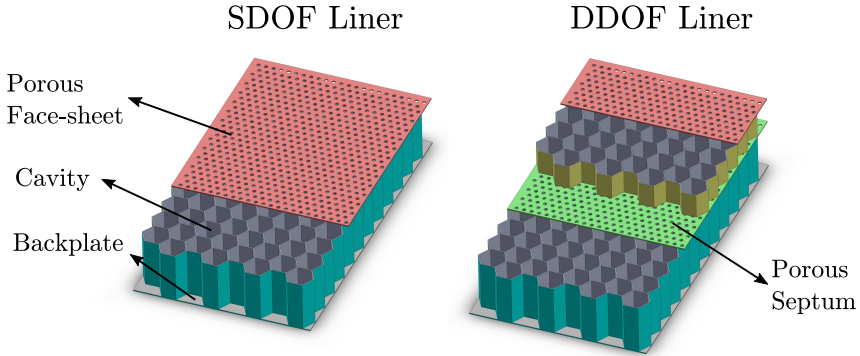


Figure 1.7: Single and Double Degree-of-Freedom liners and their main components. Adapted from [20].

have developed a lined flap concept, for which the whole flap is conceived as a liner composite structure. The goal of this treatment is to attenuate noise from TBL-TE scattering and side-edge, which are inherently broadband sources [22]. Both SDOF and DDOF configurations with the porous face-sheet on the lower side of the flap have been analyzed through a combination of a numerical CFD solution and a finite-element method for the acoustic propagation. The lined flap provides noise reduction in the order of 6.4 dB with respect to the baseline case, as shown in Fig. 1.8, thus confirming that a lined airframe structure is effective in reducing noise of broadband characteristic [22].

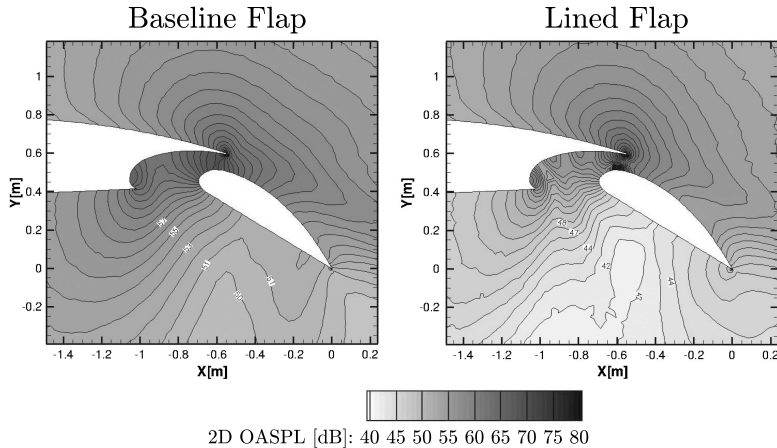


Figure 1.8: OASPL contours plots for the baseline (left) and lined (right) flaps, showing noise reduction, particularly in the direction normal to the flap. Adapted from [22].

Therefore, aside from open-cell permeable materials, the application of acoustic liners on a surface located in the vicinity of a jet is also studied in order to determine if they are effective JIN reduction solutions, as well as identify the relevant physical phenomena behind the noise mitigation.

### 1.4. RESEARCH OBJECTIVES AND THESIS OUTLINE

Based on the reported studies, permeable materials and acoustic liners are effective noise mitigation solutions for a wide range of aeroacoustic sources. Therefore, this thesis studies their application for jet-installation noise abatement and the main phenomena by which reduction is achieved. As a first step, it is necessary to understand the mechanisms behind jet-installation noise, and their link to the jet near-field characteristics, as well as trends that occur for different configurations and flow conditions. Therefore, the goals of the research reported in this thesis can be described as:

1. Perform an analysis on jet-installation noise in order to explain how the far-field noise is affected by the near-field characteristics of the isolated jet, such as the amplitude of pressure fluctuations and their frequency content.
2. Evaluate the noise reduction capabilities of permeable materials and acoustic liners mounted at the trailing edge of a surface in the vicinity of a jet.
3. Study the main mechanisms behind the achieved noise reduction, linking the results to the properties of the permeable materials and the near-field properties of the isolated jet.
4. Develop a permeable flap concept to be applied on a realistic aircraft geometry and investigate the effect of porous material under flight conditions, and their effect on the aircraft aerodynamic characteristics.

Focusing on the aforementioned goals, this thesis is structured as follows:

- Chapter 2 reports a literature review on the fundamentals of jet aerodynamics and the noise generation mechanisms in an installed jet configuration. It includes a review on turbulence-mixing noise, as well as the near-pressure field of a turbulent jet and characteristics of edge scattering, which need to be understood in order to achieve the first goal mentioned above.
- Chapter 3 reports a literature review and description of the main parameters of permeable materials and acoustic liners and their connection to noise reduction capabilities and mechanisms, which are necessary to achieve the subsequent goals of this thesis.
- Chapter 4 reports the methodology applied to achieve the goals of this thesis. It focuses on the applied numerical formulation, based on the Lattice-Boltzmann Method (LBM) for computational simulations, as well as the techniques applied in the experimental campaigns.
- Chapter 5 reports the analysis of the jet near field and its effect on the far-field noise. Through numerical simulations, it is shown that the frequency range where installation noise occurs can be predicted from the wavelength of the eddies in the mixing layer and their distance to the plate trailing edge. Moreover, it is shown that the far-field noise spectrum can be scaled based on properties of the near-pressure field, such as an exponential decay in the radial direction and a Gaussian wavepacket behaviour in the axial direction.

- Chapter 6 reports the analyses of JIN reduction with open-cell permeable materials mounted at the surface trailing edge. Experimental results show significant noise abatement, with an overall reduction in the entire frequency range where JIN is dominant. The achieved reduction is shown to be linked to the material properties, such as resistivity.
- Chapter 7 reports a further investigation on the noise generation mechanisms of an installed jet with a surface equipped with a permeable trailing edge. Beam-forming results show that the dominant acoustic source is located at the solid-permeable junction for highly permeable structures. Finally, for the permeable region, the results point to a significant mitigation of the noise due to scattering, which is no longer the dominant mechanism in the frequency range where installation effects are relevant.
- Chapter 8 reports the design and study of a Helmholtz resonator concept for JIN reduction. Impedance analyses are used to verify that the liners can provide noise reduction at the desired conditions, matching the characteristics of the installed jet configuration. There is a broad frequency range around the resonance in which the sound pressure levels of the lined plate are lower, thus showing a significant mitigation of the installation noise.
- Chapter 9 reports the study of permeable flaps in a realistic aircraft configuration, based on experimental results. A semi-span aircraft model is set at in-flight conditions. Noise reduction is achieved with the permeable flaps in a broad frequency range. A reduction in the lift force is also verified and connected to tridimensional flow features around the flap, whereas only a minor impact on drag is obtained.
- The conclusions drawn from the previous chapters in the thesis are reported, as well as recommendation for future work on the topic.

## REFERENCES

- [1] International Civil Aviation Organization (ICAO), *ICAO Environmental Report*, (2016).
- [2] International Civil Aviation Organization (ICAO), *Resolution A39-1 Appendix C*, (2016).
- [3] N. Dickson, *ICAO Noise Standards*, in *ICAO Symposium on Aviation and Climate Change, "Destination Green"* (Montréal, Canada, 2013) pp. 1–17.
- [4] N. Cumpsty, D. Mavris, and M. Kirby, *ICAO Environmental Report*, Tech. Rep. (2019).
- [5] C. Hughes, *The Promise and Challenges of Ultra High Bypass Ratio Engine Technology and Integration*, in *AIAA Aerospace Sciences Meeting* (Orlando, FL, USA, 2011).
- [6] V. G. Mingle, L. Brusniak, R. Elkoby, and R. H. Thomas, *Reducing Propulsion Airframe Aeroacoustic Interactions with Uniquely Tailored Chevrons: 3. Jet-Flap Interaction*, in *12th AIAA/CEAS Aeroacoustics Conference* (Cambridge, MA, USA, 2006).

- [7] C. J. Mead and P. J. R. Strange, *Under-Wing Installation effects on Jet Noise at Sideline*, in *4th AIAA/CEAS Aeroacoustics Conference* (Toulouse, France, 1998).
- [8] C. Brown, *Jet-Surface Interaction Test: Far-Field Noise Results*, in *Proceedings of the ASME Turbo Expo 2012: Power for Land, Sea and Air* (Copenhagen, Denmark, 2012) pp. 1–13.
- [9] R. W. Head and M. J. Fisher, *Jet/Surface Interaction Noise: - Analysis of Farfield Low Frequency Augmentations of Jet Noise due to the Presence of a Solid Shield*, in *3rd AIAA Aeroacoustics Conference* (Palo Alto, CA, USA, 1976).
- [10] J. L. T. Lawrence, M. Azarpeyvand, and R. H. Self, *Interaction between a Flat Plate and a Circular Subsonic Jet*, in *17th AIAA/CEAS Aeroacoustics Conference* (Portland, OR, USA, 2011).
- [11] D. Casalino and A. Hazir, *Lattice Boltzmann Based Aeroacoustic Simulation of Turbofan Noise Installation Effects*, in *23rd International Congress on Sound & Vibration* (Athens, Greece, 2014) pp. 1–8.
- [12] D. Casalino, F. Diozzi, R. Sannino, and A. Paonessa, *Aircraft noise reduction technologies: A bibliographic review*, *Aerospace Science and Technology* **12**, 1 (2008).
- [13] M. Herr, *Design Criteria for Low-Noise Trailing-Edges*, in *13th AIAA/CEAS Aeroacoustics Conference* (Rome, Italy, 2007).
- [14] A. Rubio Carpio, R. Merino Martínez, F. Avallone, D. Ragni, M. Snellen, and S. Van Der Zwaag, *Experimental characterization of the turbulent boundary layer over a porous trailing edge for noise abatement*, *Journal of Sound and Vibration* **443**, 537 (2019).
- [15] J. D. Revell, H. L. Kuntz, F. J. Balena, B. L. Storms, and R. P. Dougherty, *Trailing-Edge Flap Noise Reduction by Porous Acoustic Treatment*, in *3rd AIAA/CEAS Aeroacoustics Conference* (Atlanta, GA, USA, 1997).
- [16] M. Roger and S. Moreau, *Airfoil Turbulence-Impingement Noise Reduction by Porosity or Wavy Leading-Edge Cut: Experimental Investigations*, in *Inter-Noise* (Hamburg, Germany, 2016).
- [17] M. Roger, C. Schram, and L. de Santana, *Reduction of airfoil turbulence-impingement noise by means of leading-edge serrations and/or porous materials*, in *19th AIAA/CEAS Aeroacoustics Conference* (2013) p. 105.
- [18] M. Herr, K. Rossignol, J. Delfs, N. Lippitz, and M. Mößner, *Specification of Porous Materials for Low-Noise Trailing-Edge Applications*, in *20th AIAA/CEAS Aeroacoustics Conference* (Atlanta, GA, USA, 2014).
- [19] J. D. Eldredge and A. P. Dowling, *The absorption of axial acoustic waves by a perforated liner with bias flow*, *Journal of Fluid Mechanics*, **307** (2003).

- [20] M. G. Jones, D. M. Nark, A. Baca, and C. R. Smith, *Applications of Parallel-Element, Embedded Mesh-Cap Acoustic Liner Concepts*, in *2018 AIAA/CEAS Aeroacoustics Conference* (Atlanta, GA, USA, 2018).
- [21] C. K. Tam and K. A. Kurbatskii, *Microfluid dynamics and acoustics of resonant liners*, *AIAA journal* **38**, 1331 (2000).
- [22] D. Casalino and M. Barbarino, *Optimization of a Single-Slotted Lined Flap for Wing Trailing-Edge Noise Reduction*, *Journal of Aircraft* **49** (2012), 10.2514/1.C031561.

# 2

## FUNDAMENTALS OF JET AERODYNAMICS AND JET-INSTALLATION NOISE

*The more that you read, the more things you will know.  
The more that you learn, the more places you will go.*

Theodor Seuss Geisel (Dr. Seuss)

*This chapter contains a literature review on the aerodynamics of a turbulent jet flow and the fundamental noise generation mechanisms present in an installed jet, i.e. turbulence mixing and edge scattering. Finally, previous studies on jet-installation noise are reported in order to guide the research performed in this work. Focus is given to the spectral characteristics and radiation pattern, as well as the links between the far-field and near-field properties of the installed jet.*

## 2.1. JET AERODYNAMICS

AT the exhaust of an aircraft turbofan engine, fluid is discharged into the ambient, generating a turbulent free shear flow or jet, which is characterized by a higher nominal velocity than the ambient. For modern turbofan engines, a dual jet stream is present at the core, which is usually of high velocity and temperature since it undergoes combustion, and at the bypass, which comes straight from the fan, and it is of considerably lower velocity and temperature than the core. The ratio between mass flows at the bypass and core is also known as bypass ratio, which, as described in Chapter 1, has been progressively increasing over the years.

A more simplified version of a turbulent jet consists of a single stream flow generated by a nozzle. For a circular nozzle with exit diameter  $D_j$ , the flow has a uniform or flat-topped velocity profile at the nozzle exit, with velocity  $U_j$  (nominal jet velocity). For an axisymmetric jet, a mixing layer starts to form at the nozzle exit due to strong shear stresses between the jet flow and the ambient. In that region, flow instabilities (usually of Kelvin-Helmholtz type [1]) cause turbulent fluid motion, resulting in the formation of eddies. Due to those shear stresses, the jet velocity decreases moving downstream from the nozzle exit in the axial direction, changing to a Gaussian shaped profile, and resulting in an expansion of the mixing layer in the radial direction with a certain spreading angle  $\delta_j$ . The region where the flow maintains the nominal jet velocity is known as the potential core due to the laminar characteristic of the flow in that region. A sketch showing the different regions in a circular jet is shown in Fig. 2.1, along with a representation of the local velocity profiles near the nozzle exit and at end of the potential core.

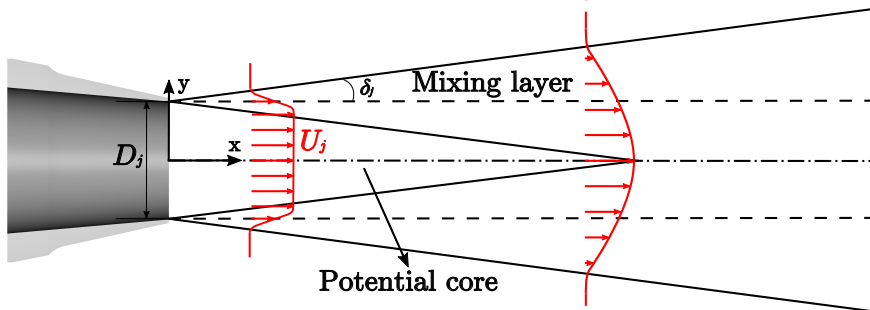


Figure 2.1: Sketch of a single-stream jet flow from a circular nozzle with exit diameter  $D_j$  and nominal velocity  $U_j$ . In the potential core, the flow is nominally laminar with parallel streamlines, whereas in the mixing layer, strong shear stresses lead to a highly turbulent flow.

The velocity profiles at different axial stations of a typical turbulent jet are shown in Fig. 2.2, in terms of time-averaged and standard deviation of the axial velocity,  $\bar{u}$  and  $u'$ , respectively. Near the nozzle exit, at  $x = 1D_j$ , the velocity profile has a top-hat shape, with the nominal jet velocity at the center, characterizing the flow in the potential core. At the lipline ( $y = 0.5D_j$ ), there is a sharp decay down to ambient conditions. Moving downstream in the jet, the flat region of the profile becomes narrower and the centerline velocity ( $y = 0$ ) eventually becomes lower than  $U_j$ , defining the end of the potential core. For the velocity fluctuations (measured in terms of  $u'$ ) near the nozzle, there are distinct

peaks at the lipline, where the mixing is the strongest. On the other hand, at the centerline there is no significant fluctuation in velocity. At further downstream stations, there is a consistent increase in the fluctuations near the centerline, indicating the end of the potential core and the merging of the mixing layers from the two sides.

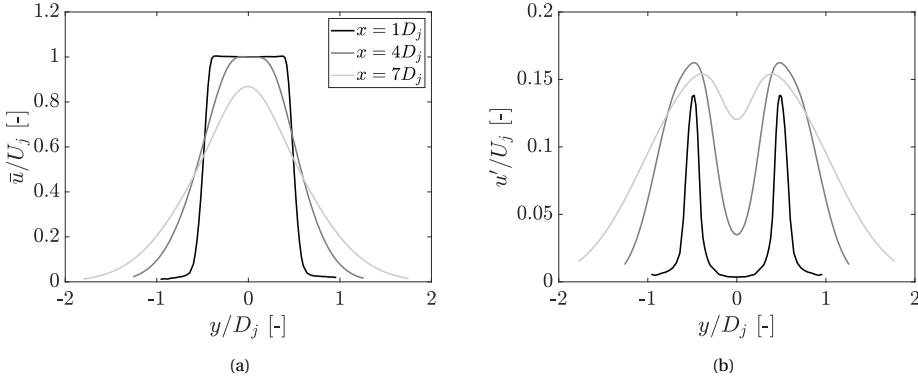


Figure 2.2: Radial profiles of (a) Time-averaged axial velocity (b) Standard deviation of the axial velocity at different axial stations.

As shown by the profiles of velocity fluctuations, the jet mixing layer is a region of intense unsteadiness. An important parameter to quantify the unsteadiness in a jet flow is the Reynolds stress tensor. Reynolds stresses are the covariances of the flow velocities at a single point, at a specific instant, usually denoted by  $u_i u_j$ . This term arises from the Reynolds decomposition, for which a flow variable is represented by a sum of a time-averaged value and temporal fluctuations, and represents the transfer of momentum by a fluctuating velocity field [1]. The Reynolds stress tensor is comprised by diagonal elements (e.g.  $u_1 u_1$ ), which are known as normal stresses and off-diagonal elements (e.g.  $u_1 u_2$ ), known as shear stresses [1]. The turbulent kinetic energy (energy of the fluctuating velocity field) is then defined as the trace of the tensor. As described in section 2.2, the Reynolds stresses are also important parameters for the noise production of a jet flow.

Due to the many temporal scales present in a turbulent jet at relatively high Reynolds number, the turbulent kinetic energy spectrum for this type of flow is usually broadband in shape. Moreover, the flow is characterized by rapidly decaying two-point correlations and significant dissipation of mean kinetic energy [2]. In terms of pressure fluctuations in the frequency domain  $P^2(f)$ , the unsteady region of a turbulent jet flow has a distinct spectrum, usually comprised by four ranges with different behaviours, as shown in Fig. 2.3 in terms of Power Spectral Density (PSD) as function of frequency.

The low-wavenumber region of the spectrum consists of very large scale structures that are still developing at the measurement point. The energy-containing region comprises the most energetic scales of eddies at that point, and it is characterized by relatively flat levels of pressure fluctuations with frequency. A further increase in frequency leads to a sharp decay in amplitude, defining a region known as the inertial subrange. Here, the turbulent kinetic energy spectrum follows Kolmogorov's law, decaying with

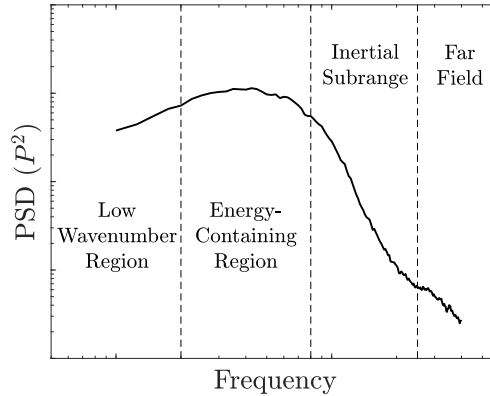


Figure 2.3: Spectrum of pressure fluctuations in the near field of a turbulent jet, outside the rotational flow region. Four regions can be distinguished: a low-wavenumber region, an energy-containing region, the inertial subrange and the far-field. Adapted from [3].

$k^{-5/3}$ , where  $k$  is the wavenumber [1]. Finally, at sufficiently high frequencies, the pressure fluctuations propagate at the speed of sound, thus characterizing the acoustic far-field [3].

In the energy-containing region, for a constant wavenumber, the pressure fluctuations have a spatial decay as a function of  $kr^{-6}$ , with  $r$  being the distance from the source, whereas in the inertial subrange, the decay is a function of  $kr^{-6.67}$  due to the energy dependence on the wavenumber. Finally, in the far-field, the pressure fluctuations decay with  $kr^{-2}$ , which is characteristic of acoustic wave propagation [3, 4]. The dividing line between near and far field is frequency-dependent and thus, at sufficiently high frequencies, far-field behaviour can be observed even at positions near the jet. Moreover, the relative amplitude and frequency range of each region is dependent on both axial and radial positions of the measurement point in the jet.

Despite the apparent chaotic characteristic of a turbulent jet, it has been shown that coherent structures are present in the mixing layer, convecting with the flow. Mollo-Christensen [5] was among the first who observed the existence of coherent large-scale structures and hydrodynamic instability waves in turbulent flows. For a jet flow, it was later found that disturbances produced by those coherent structures grow downstream of the nozzle in the axial direction, and subsequently saturate and decay in a Gaussian manner [6, 7].

The pressure field caused by instability waves has an evanescent characteristic, with exponentially decaying amplitude moving away from the jet in the radial direction [8]. Therefore, near the boundary between the mixing layer and the ambient, known as the entrainment region, there is unsteady irrotational flow with zero-mean velocity. In this region, linear approximations can be performed for the flow disturbances due to the much lower amplitude of fluctuations with respect to the rotational region of the jet. It is interesting, therefore, to plot the radial evolution of the pressure fluctuations in a jet flow, for a constant wavenumber, as shown in Fig. 2.4.

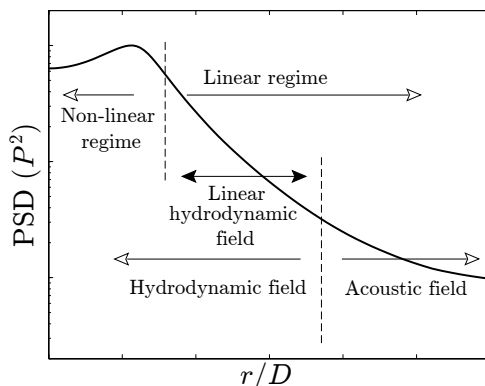


Figure 2.4: Pressure decay in the radial direction of a turbulent jet. Linear and non-linear regimes can be distinguished, as well as fields with either hydrodynamic or acoustic characteristics. Adapted from [8].

In the jet flow region with non-zero mean velocity, the pressure field is dominated by non-linear disturbances associated with vorticity in the mixing layer [4, 8]. Moving further away from the jet, there is a region characterized by linear hydrodynamic fluctuations (also known as non-radiating pseudosound), where there is no steady flow (zero mean velocity) and pressure levels decay exponentially with radius [4, 8]. These two regions are collectively referred to as the hydrodynamic field, due to the dominant convective character of the pressure fluctuations [9], produced by flow structures with a convective velocity lower than the nominal speed of the flow [4]. Finally, at distances far enough from the mixing layer, the pressure field is dominated by acoustic waves propagating at the ambient speed of sound and with an algebraic decay with radius [8].

There are, therefore, two crossover regions: the first from the non-linear to the linear hydrodynamic regions and the other from the linear hydrodynamic fluctuations to acoustic ones [10]. The existence of those different types of disturbances also affects the pressure field in the axial direction. In the entrainment region, a growth-saturation-decay [6] behaviour is expected, considering only the instability wave characteristic of the flow. However, in the expected decay region of the Gaussian, it was shown by Suzuki and Colonius [8] that acoustic waves become dominant and alter the overall shape of the curve, which becomes a plateau. This occurs because acoustic fluctuations have a much slower decay with respect to linear hydrodynamic ones. There is, therefore, an intricate relationship between the turbulence characteristics of a jet and the noise produced by the flow structures present in the mixing layer, which is known as turbulence-mixing noise.

## 2.2. TURBULENCE-MIXING NOISE

In an unsteady flow, such as a turbulent jet, low-amplitude pressure fluctuations are generated and propagate outwards from the flow at the speed of sound and persist at large distances, into what is known as the acoustic field, where the homogeneous wave equation is valid [11]. This phenomenon is known as aerodynamic sound.

Aerodynamic sources of sound have been originally studied by Lighthill [12], who proposed a pioneering theory linking fluctuations in a flow to the production of noise. This theory, also known as Lighthill's acoustic analogy, addresses sound generation by a turbulent flow, coupling the fluctuations that occur inside of it with acoustic wave propagation to the far-field [13]. The mathematical formulation of Lighthill's analogy is derived by combining the wave propagation equation along with the flow equations of motion (Navier-Stokes), and it is written as:

$$\frac{\partial^2 \rho'}{\partial t^2} - c_0^2 \nabla^2 \rho' = \frac{\partial^2 T_{ij}}{\partial x_i \partial x_j}, \quad (2.1)$$

$$T_{ij} = \rho u_i u_j + (p - c_0^2 \rho) \delta_{ij} - \tau_{ij}, \quad (2.2)$$

where  $\rho'$  is the fluctuation in density,  $c_0$  is the speed of sound and the  $T_{ij}$  term is known as the Lighthill stress tensor [11, 12]. The left side of Eq. (2.1) represents the acoustic wave propagation in a uniform medium, whereas the right side is referred to as the source term. Lighthill's acoustic analogy represents the unsteady flow by a volume distribution of equivalent acoustic sources embedded in a uniform medium at rest, assuming no solid boundaries are present [14]. In the formulation of Lighthill's stress tensor, the term  $\rho u_i u_j$  is known as the Reynolds stresses, with the subscripts representing Cartesian directions [12]. The  $(p - c_0^2 \rho) \delta_{ij}$  term is the compressive stress tensor, and  $\delta_{ij}$  is the Kronecker delta function. For a homentropic flow, which has constant and uniform entropy among all fluid particles, this term is equal to zero [13]. This assumption can be made for an unheated turbulent flow, for example. The viscous stress term  $\tau_{ij}$  can also be disregarded by assuming the velocity fluctuations are dominated by turbulence, rather than viscosity, which is applicable for high-Reynolds number flows [13].

Therefore, the source term in an incompressible turbulent flow is dominated by the Reynolds stresses, which correspond to variable rates of momentum flux across fixed surfaces in the flow [12]. The mechanism of converting kinetic energy from a turbulent flow into acoustic energy is, therefore, linked to the variation of these momentum flux rates [12]. This type of motion can be represented by a distribution of quadrupole sources throughout the turbulent flow, whose strength per unit volume is proportional to the local stress field [12].

Lighthill shows that the density field generated by quadrupole sources can be approximated by an integral over the source volume  $dV(\mathbf{y})$  [12]:

$$\rho' \sim \frac{1}{4\pi c_0^2} \frac{x_i x_j}{x^3} \int_V \frac{1}{c_0^2} \frac{\partial^2}{\partial t^2} T_{ij} \left( \mathbf{y}, t - \frac{|\mathbf{x} - \mathbf{y}|}{c_0} \right) dV(\mathbf{y}), \quad (2.3)$$

where  $\mathbf{x}$  and  $\mathbf{y}$  are the tridimensional coordinates of the observer and the center of the source, respectively, given in vectorial notation. Eq. (2.3) is evaluated in the retarded time  $t_r = t - |\mathbf{x} - \mathbf{y}|/c_0$ , and assuming points in the far field and disregarding the contribution from viscous stresses [12]. This formulation is used to estimate the intensity field generated by quadrupole sources, for a given turbulence length scale  $D$  and a distance  $r$  between source and observer. Through dimensional analysis, it is shown that the total acoustic power [12]:

$$I \propto \frac{\rho D^2 U^8}{r^2 c_0^5} \quad (2.4)$$

is approximately proportional to the eighth power of the flow velocity ( $U^8$ ) [12].

For a turbulent jet, the dominant sources are located around the central region of the mixing layer between the jet and the ambient, convecting downstream parallel to the jet axis [14]. Therefore, the integral in Eq. (2.3) can be evaluated in a frame of reference moving with the convection velocity of the turbulence  $U_c$  [14]. This is performed with a moving coordinates system defined by:

$$\boldsymbol{\eta} = \mathbf{y} + M_c |\mathbf{x} - \mathbf{y}|, \quad (2.5)$$

where  $M_c$  is the convection Mach number ( $U_c/c_0$ ). The resulting density field, similarly as Eq. (2.3), becomes [12]:

$$\rho' \sim \frac{1}{4\pi c_0^2} \int_V \frac{(x_i - y_i)(x_j - y_j)}{[|\mathbf{x} - \mathbf{y}| - M_c \cdot (\mathbf{x} - \mathbf{y})]^3} \frac{1}{c_0^2} \frac{\partial^2}{\partial t^2} T_{ij} \left( \boldsymbol{\eta}, t - \frac{|\mathbf{x} - \mathbf{y}|}{c_0} \right) dV(\boldsymbol{\eta}). \quad (2.6)$$

The total acoustic intensity calculated with this formulation is found to be [15]:

$$I \propto \frac{\rho D^2 U^8}{r^2 c_0^5} (1 - M_c \cos \theta)^{-6}, \quad (2.7)$$

where  $\theta$  is the angle of the observer with respect to the jet centerline and the term  $(1 - M_c \cos \theta)^{-6}$  is an amplification factor to the acoustic intensity obtained from the original static frame formulation. This term shows that there is a preferential direction of radiation in the downstream direction, particularly for high Mach number flows [15]. Ffowcs-Williams [16] has shown, however, that this amplification factor needs to be modified to  $(1 - M_c \cos \theta)^{-5}$  to account for a limited source volume. Moreover, acoustic frequencies also undergo a Doppler shift by a factor of  $(1 - M_c \cos \theta)$ .

The interaction between the mean flow and the sound field, including not only convective effects, but also refraction due to propagation throughout the non-uniform jet flow is accounted by modifying the source term [11]. However, this is not feasible without prior knowledge of the sound field, which can only be obtained by solving Lighthill's equation. Therefore, another approach was proposed by Lilley [14], wherein this interaction is incorporated into the wave propagation operator, and thus was obtained as part of the solution of the equation [17].

For the specific case of turbulent, subsonic, cold jet flows, Lighthill summarizes the characteristics of the produced sound [15]:

- The average acoustic power output is approximately proportional to the eighth power of the jet velocity;
- The sound spectrum has a clear broadband characteristic due to the stochastic characteristics of the turbulent flow;
- High-frequency sound is believed to be emitted near the nozzle exit;

- Most of the sound is radiated towards the downstream direction of the jet axis, particularly at low frequencies;
- At shallow downstream angles, the sound intensity is proportional to a higher power of the jet velocity, in comparison to the average acoustic power.

These statements were made during a time when the notion of turbulence was no more than a chaotic assortment of small eddies with stochastic motion [17, 18]. The discovery of coherent structures and hydrodynamic instability waves in a jet flow eventually led to a correlation between them and the sound production by a subsonic, turbulent jet [5]. The wavepacket behaviour, with the characteristic growth-saturation-decay [6, 7], was analyzed in terms of Lighthill's analogy by replacing the source term on the right-hand side of Eq. (2.1) with a one-dimensional, convected wavy disturbance with Gaussian spatial modulation, resulting in a sound field described by [18, 19]:

$$p'(\mathbf{x}, t) = -\frac{\rho U \bar{u} M_c^2 (kD)^2 L \sqrt{\pi} \cos^2 \theta}{8|\mathbf{x}|} e^{-\frac{L^2 k^2 (1-M_c \cos \theta)^2}{4}} e^{i\omega \left(t - \frac{|\mathbf{x}|}{c_0}\right)}, \quad (2.8)$$

An important parameter for sound production in the wavepacket formulation is the axial compactness  $kL$ , where  $L$  is defined as the characteristic length of the Gaussian envelope fitting the wavepacket. It was shown that the less compact the source (lower frequencies, for example), the more sound is produced towards shallow axial angles, with an exponential directivity pattern (superdirective), given by the  $e^{(1-M_c \cos \theta)^2}$  term [10, 18], which is linked to the fourth statement by Lighthill as listed above [15]. Moreover, the same statement includes that this downstream radiation is particularly significant at low frequencies. Armstrong *et al.* [20] showed from near-field/far-field coherence measurements that different frequency components are generated at different axial segments of the jet, and that most of the noise at low frequencies is generated far downstream of the nozzle. In terms of locating sound sources in a turbulent jet, Bogey *et al.* [21] showed that most of the low-frequency noise is generated at the region where the shear layers merge, at the end of the potential core. The intermittent breakdown of the shear layers with sudden periodic accelerations of vortical structures in that region was claimed to be responsible for the clear peak in the sound spectra measured in the downstream direction [21].

One of the most important characteristics of sound production by wavepackets is the spatial modulation, given by growth, saturation and decay, which occurs when the convection velocity is subsonic [22, 23]. For this case, a portion of the energy is acoustically matched to a wave propagating at an angle  $\theta = \arccos\left(\frac{k_x c_0}{\omega}\right)$ , as a function of the axial wavenumber  $k_x$  [18, 23]. The amount of energy leaked from advecting turbulence into the far-field is dependent on the wavepacket characteristics, which can lead to the superdirective radiation [10, 23]. Cavalieri *et al.* [24, 25] showed that this feature occurs for the axisymmetric azimuthal mode of the wavepacket, which is dominant in terms of sound production towards shallow downstream radiation, even for low Mach number jets. A temporal intermittency, or jitter, was also found to be linked to the unsteadiness in a wavepacket and responsible for a significant portion of the sound emitted in the downstream direction [18, 24]. It was thus concluded that the high level of space-time

coherence in a wavepacket makes it considerably more acoustically efficient than the more disorganized, although more energetic, compact eddies. [23, 26, 27].

While there is a general agreement that jet noise production at shallow angles is related to large scale coherent structures, with a clear peak in the spectrum, there is still a debate on the sources responsible for the broader sound spectrum found in the sideline (nozzle exit plane) and upstream directions [4]. Tam *et al.* [28], for example, suggests that this behaviour is the result of noise produced by fine-scale incoherent turbulent structures, which are present in the jet mixing layer, particularly near the nozzle exit. However, Papamoschou [29] shows that the broadening of the sound spectrum moving towards the upstream direction of the jet can be also achieved with a wavepacket source, and thus it is associated with coherent structures, similarly as the downstream noise production. For this case, however, it is necessary to include higher order azimuthal modes (first and second helical modes) to account for the noise emission at mid and high frequencies that dominate in this direction [30]. Nevertheless, Papamoschou [29] shows that additional sources, possibly associated with reflections on the nozzle, are still necessary for the model to match the noise amplitude at high frequencies, thus representing the contribution from incoherent sources [29].

The noise mechanisms and characteristics described in this section apply to an isolated jet, in the absence of solid boundaries which would interfere either with the flow or the sound field. When a surface is placed in the vicinity of a turbulent flow, which is the case of an installed jet, other phenomena must be taken into account, as described in the next section.

## 2.3. NOISE DUE TO SURFACE PRESSURE FLUCTUATIONS AND EDGE SCATTERING

Lighthill's analogy allows for the calculation of propagated sound, which is produced by an unbounded volume distribution of quadrupole sources, whose amplitude is connected to the properties of the turbulent flow [12]. Curle [31] expanded this theory to account for the influence of a solid boundary on the sound field. This influence is defined as twofold: the solid boundaries both reflect and diffract the acoustic waves generated by quadrupole sources. As a consequence, a distribution of dipole sources occurs at the solid boundaries, related to external fluctuating forces applied by the fluid on them and vice-versa [31]. The mathematical formulation of Curle's analogy is given by [31]:

$$\rho' = \frac{1}{4\pi c_0^2} \frac{\partial^2}{\partial x_i \partial x_j} \int_V \frac{T_{ij} \left( \mathbf{y}, t - \frac{|\mathbf{x}-\mathbf{y}|}{c_0} \right)}{|\mathbf{x}-\mathbf{y}|} dV(\mathbf{y}) + \frac{1}{4\pi c_0^2} \frac{\partial}{\partial x_i} \int_S \frac{P_i \left( \mathbf{y}, t - \frac{|\mathbf{x}-\mathbf{y}|}{c_0} \right)}{|\mathbf{x}-\mathbf{y}|} dS(\mathbf{y}), \quad (2.9)$$

where the first term on the right-hand side is the same obtained from Lighthill's theory [12], and the second term (surface integral) is the additional contribution by a distribution of dipoles of strength  $P_i$  per unit area. Therefore, the resultant sound field is that produced by a volume distribution of quadrupoles (fluctuating stresses) and a surface distribution of dipoles due to fluctuating forces on the boundaries [31].

By assuming an observer at large enough distance with respect to the acoustic wavelength and the characteristic length of the body, a dimensional analysis of the total acoustic intensity for the dipole sources provides [31]:

$$I \propto \frac{\rho D^2 U^6}{r^2 c_0^3}, \quad (2.10)$$

a dependence to the sixth power of the flow velocity ( $U^6$ ). Therefore, at sufficiently low Mach numbers, the contribution from dipole sources to the overall sound field is expected to be dominant over that from the quadrupoles [31].

It was shown by Powell [32], however, that if the solid boundary was infinite, it caused no augmentation of the sound field, except for reflection effects. This was due to the equivalent image sources caused by the boundary with equal and opposite strength to the incident quadrupoles [11, 32]. If the surface has a finite length or a discontinuity, such as a sharp edge, it was shown by Ffowcs-Williams and Hall [33] that the sound field was then governed by diffraction effects. An example of this phenomenon is the interaction between turbulence and an edge, where some of the energy present in near-field hydrodynamic fluctuations is converted into acoustic waves at the edge [34]. Ffowcs-Williams and Hall [33] considered this effect by studying the potential field generated by a quadrupole distribution in the vicinity of a thin half plane with a sharp edge. A schematic of the problem is shown in Fig. 2.5 for a single point source, also considering the equivalent image source.

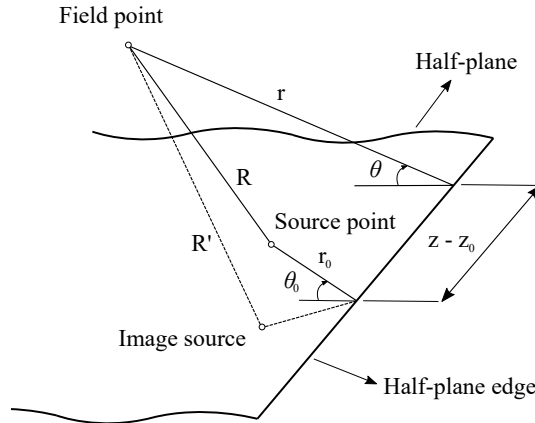


Figure 2.5: Source point in the vicinity of a half-plane edge, with a respective image source on the opposite side of the boundary, for studies on sound scattering by an edge. Adapted from [33].

A solution for Lighthill's equation with a no-penetration boundary condition on the surface was achieved in terms of an exact Green's function, for which the sound field is expressed in terms of pressure fluctuations in the frequency domain as [33]:

$$\bar{p}(\mathbf{x}, \omega) = \frac{1}{4\pi} \int_V (\rho u_i u_j) \frac{\partial^2 G}{\partial x_i \partial x_j} dV(\mathbf{y}), \quad (2.11)$$

where the Lighthill stress tensor is approximated to the Reynolds stresses, for a high Reynolds and low Mach number flow [13]. To account for correct approximations, the solution was made dependent on the compactness of the turbulent fluctuations with respect to their distance to the edge [33]. For eddies within a wavelength from the edge,

which satisfy the inequality  $2kr_0 \ll 1$ , the pressure field generated by Reynolds stresses at certain directions, particularly quadrupoles with axes in a plane normal to the edge, was amplified by a factor of  $(2kr_0)^{-3/2}$ , thus resulting in significant additional noise with respect to free turbulence [33]. Isolated quadrupoles are usually inefficient sound sources due to phase cancellations between its component monopoles. However, a nearby edge has the effect of reducing this cancellation, thus increasing the efficiency of the source [11]. An important conclusion from this analysis was that the edge converts formerly non-propagating near-field flow fluctuations into a sound field [11]. For this case, the acoustic intensity was found to be [14, 33, 35]:

$$I \approx \rho^2 U^5 \frac{L\delta}{r^2} \sin(\phi) \cos^2(\theta/2), \quad (2.12)$$

thus proportional to the fifth power of the flow velocity ( $U^5$ ). Therefore, it was shown that the sound generated by edge scattering at sufficiently low Mach numbers was dominant over that of free turbulence ( $U^8$ ) and turbulence in the vicinity of an infinite plane ( $U^6$ ) [33]. Moreover, an important characteristic from Eq. (2.12) is the term  $\cos^2(\theta/2)$ , which shows that the noise produced by edge scattering has a cardioid directivity, with maximum levels in the upstream direction and minimum propagation downstream [13].

For eddies far from the edge, where the inequality  $(kr_0)^{1/2} \gg 1$  is valid, it was found that the resultant sound field is dependent on the location of the eddy with respect to the observer. If the eddy is on the same side of the surface as the observer and upstream of the edge, the boundary can be regarded as infinite and the amplification factor to the sound field is negligible, but reflection effects must be taken into account [11, 33]. If the source is downstream of the edge, the produced sound field was found to be the same as that of free turbulence [33]. Finally, if the source is in the geometrical shadow of the observer (upstream of the edge and on the opposite side of the half-plane), the sound levels are lowered due to shielding effects [33].

Amiet [36] developed a different approach for the study of trailing-edge noise, which is based on the surface pressure spectrum upstream of the edge, caused by a convecting turbulent flow with stationary statistical properties, plus its mirrored image [36]. Therefore, it was assumed that the noise is generated completely by surface dipoles near the trailing edge, with equal and anticorrelated propagation at the upper and lower sides [36]. The resultant formulation for the far-field sound spectrum is given by:

$$S_{pp}(x, 0, z, \omega) = \left( \frac{\omega bz}{2\pi c_0 \sigma^2} \right)^2 l_y(\omega) d|\mathcal{L}|^2 S_{qq}(\omega, 0), \quad (2.13)$$

which is a function of the surface pressure auto-spectrum  $S_{qq}(\omega, 0)$ , the spanwise correlation length  $l_y(\omega)$ , and the chordwise integral of the surface loading  $\mathcal{L}$ , related to the transfer function between the airfoil surface pressure fluctuations and the far-field sound [36, 37]. Approximations to the far-field spectrum term showed that Amiet's formulation also provides a cardioid directivity pattern with a dependence with  $U^5$ , in agreement with the observations from Ffowcs-Williams and Hall [13]. An important addition to Amiet's model was performed by Roger and Moreau [38, 39], by adding a leading-edge back-scattering correction and a 3D extension to the original formulation. This correction was shown to be of high importance, particularly for low frequencies, for which the

airfoil chord is acoustically compact with respect to the wavelength of pressure fluctuations [38, 39].

The theory of edge scattering is usually applied for turbulent boundary-layer trailing-edge noise, but it is also applicable to the interaction between a turbulent jet flow and a nearby finite surface, such as a wing or a flap, as pointed out by Roger *et al.* [40]. As stated in Chapter 1, this interaction is known as jet-installation noise, which is approached in more detail in the next section.

## 2.4. JET-INSTALLATION NOISE

This section contains a review on the characteristics of jet-installation noise, focusing on the mechanisms described in the previous sections along with its connection to the near-field properties of the jet flow.

Head and Fisher [41] were among the first who studied JIN through experiments with a solid flat surface placed close to a subsonic, round jet. Far-field results showed a low frequency noise increase in the spectra with respect to isolated jet levels, measured without the surface [41]. Moreover, maximum noise levels were obtained in the direction normal to the surface, with similar amplitude at both reflected and shielded sides, but with a phase difference of  $180^\circ$  between them [41]. Towards the downstream jet axis direction, the installation effects were shown to be reduced and the obtained noise levels were more similar to those of the isolated jet [41]. This directivity pattern, along with a dependence of the peak noise levels with the sixth power of the jet velocity for the installed case, led to the conclusion that dipole sources were present at the surface trailing edge, generated by the interaction between the unsteady flow and the half plane [41].

A benchmark study on jet-surface interaction was carried out at NASA Glenn with the aim to generate a database of experimental results for a flat plate positioned in the vicinity of a subsonic jet [42, 43]. A single-stream nozzle (SMC-000) was used in the measurements, similarly as performed in the isolated jet study by Brown and Bridges [44], and the geometric characteristics of the surface were assessed in terms of length and radial position, relative to the jet, as shown in Fig. 2.6a.

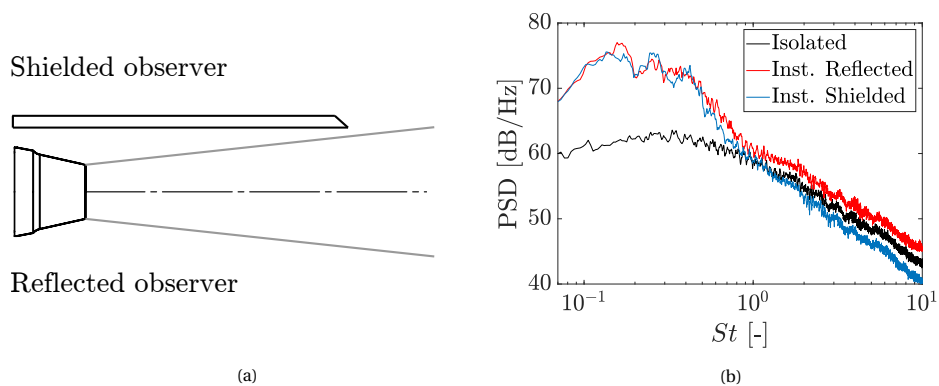


Figure 2.6: (a) SMC-000 nozzle with a nearby flat plate. (b) Far-field spectra for isolated and installed jets at a polar angle of  $\pm 90^\circ$  (reflected and shielded observers). Adapted from [42].

The far-field noise measurements produced spectra such as the one shown in Fig. 2.6b, at a polar angle of  $90^\circ$ , relative to the jet axis. Installation effects caused a low-frequency noise augmentation with respect to the isolated jet, with similar levels for observers on the reflected and shielded sides, indicating that the dominant source was located at the plate trailing edge [42]. This was later confirmed through the application of beamforming for source localization [43]. At high frequencies, two different behaviours were observed: at the lower side (reflected), there was noise increase due to reflection of acoustic waves generated by turbulent mixing on the surface, whereas at the upper side, shielding effects resulted in noise reduction [42].

The surface length and radial position relative to the jet centerline have a significant impact on the surface pressure fluctuations and the far-field noise [45, 46]. Lawrence *et al.* [45] showed that, by increasing the plate length, the peak in noise levels increased in amplitude and moved to lower frequencies due to the presence of larger and more energetic eddies further downstream from the nozzle exit plane, which were diffracted at plate trailing edge [45]. By moving the surface closer to the jet in the radial direction, the interaction peak increased in amplitude and shifted to higher frequencies, which was related to additional contributions from the jet hydrodynamic field and grazing flow [45]. It was also found that the dependence between the Overall Sound Pressure Level (OASPL) and the jet velocity increased from  $U_j^5$  to  $U_j^6$  as the plate length was increased, implying that the dominant noise generation mechanisms are different and configuration-dependent [45].

The trends in the far-field spectra for different plate geometries imply that there is a strong correlation between the near-field properties of the jet, particularly the pressure field near the trailing edge, and the produced noise. This has been also suggested by Head and Fisher [41]. Cavalieri *et al.* [47] investigated this relationship by modelling the jet as wavepacket sources and computing the scattered noise using both a tailored Green's function and a Boundary Element Method (BEM) to solve the Helmholtz equation. Aside from the typical low-frequency noise amplification, some connections between the near-field characteristics of the flow and the far-field noise were verified. By changing the radial position of the plate with respect to the jet, an exponential variation of the noise levels was detected, which is connected to the hydrodynamic field of the jet that also has an exponential radial decay [8, 47]. However, this was found to happen only for non-compact sources with respect to their distance to the trailing edge, thus showing another effect from the near-field on the produced noise. Similar results were obtained by Piantanida *et al.* [48] for an installed jet with a swept plate.

Lyu *et al.* [49] proposed a semi-analytical model capable of predicting turbulence-mixing noise and edge scattering in an installed jet. The former is modelled through Lighthill's analogy [12], whereas the latter is computed via Amiet's approach [36]. The results show that the low-frequency noise amplification is caused by the scattering of near-field evanescent instability waves, when there is no grazing flow on the surface, thus indicating the relationship between JIN and the jet coherent structures [49]. Moreover, with the plate placed sufficiently far away from the jet, there was no visible low-frequency noise increase and the only noticeable installation effects were reflection and shielding by the surface [49].

Therefore, three different mechanisms can occur based on the radial position of the plate with respect to the jet:

- The surface is placed inside the steady flow region of the jet, thus disrupting its development and leading to the formation of a boundary layer on the surface, and leading to significant noise increase [45, 46];
- The surface is placed inside the linear hydrodynamic region of the jet, with an exponential pressure decay in the radial direction. The evanescent waves, characteristic of this region, are scattered as sound to the far-field at the surface trailing edge [47, 49];
- The surface is placed sufficiently far from the jet, in the acoustic field with algebraic pressure decay along the radial direction. No significant change in the overall acoustic intensity occurs, except for reflection and shielding effects [47, 49];

The second type of interaction is the main objective of study of this work since direct grazing is usually prevented due to the high velocity and temperature of exhaust flows in turbofan engines. It is not yet fully understood, however, how the coherent flow structures in the mixing layer, particularly those near the surface trailing edge, affect the far-field characteristics of the system. This is studied and reported in Chapter 5.

## REFERENCES

- [1] S. B. Pope, *Turbulent Flows* (Cambridge University Press, 2000).
- [2] J. B. Freund, *Noise sources in a low-Reynolds-number turbulent jet at Mach 0.9*, *Journal of Fluid Mechanics* **438**, 277 (2001).
- [3] R. E. A. Arndt, D. F. Long, and M. N. Glauser, *The proper orthogonal decomposition of pressure fluctuations surrounding a turbulent jet*, *Journal of Fluid Mechanics* **340**, 1 (1997).
- [4] C. E. Tinney and P. Jordan, *The near pressure field of co-axial subsonic jets*, *Journal of Fluid Mechanics* **611**, 175 (2008).
- [5] E. Mollo-Christensen, *Jet Noise and Shear Flow Instability Seen From an Experimenter's Viewpoint*, *Journal of Applied Mechanics* **34**, 1 (1967).
- [6] S. C. Crow and F. H. Champagne, *Orderly structure in jet turbulence*, *Journal of Fluid Mechanics* **48**, 547 (1971).
- [7] S. C. Crow, *Acoustic gain of a turbulent jet*, in *Phys. Soc. Meeting, paper IE, vol. 6* (Boulder, CO, USA, 1972).
- [8] T. Suzuki and T. Colonius, *Instability waves in a subsonic round jet detected using a near-field phased microphone array*, *Journal of Fluid Mechanics* **565**, 197 (2006).
- [9] K. Gudmundsson and T. Colonius, *Instability wave models for the near-field fluctuations of turbulent jets*, *Journal of Fluid Mechanics* **689**, 97 (2011).

## REFERENCES

---

- [10] D. G. Crighton and P. Huerre, *Shear-layer pressure fluctuations and superdirective acoustic sources*, [Journal of Fluid Mechanics](#) **220**, 355 (1990).
- [11] M. E. Goldstein, *Aeroacoustics* (McGraw-Hill International Book Company, 1976).
- [12] M. J. Lighthill, *On Sound Generated Aerodynamically I. General Theory*, [Proceedings of the Royal Society of London. Series A. Mathematical and Physical Sciences](#) **211**, 564 (1952).
- [13] S. Glegg and W. Devenport, *Aeroacoustics of Low Mach Number Flows*, 1st ed. (Academic Press, 2017).
- [14] H. H. Hubbard, *Aeroacoustics of Flight Vehicles: Theory and Practice Vol. 1: Noise Sources*, Tech. Rep. (NASA Reference Publication 1258, 1991).
- [15] M. J. Lighthill, *On Sound Generated Aerodynamically II. Turbulence as a Source of Sound*, [Proceedings of the Royal Society of London. Series A. Mathematical and Physical Sciences](#) **222**, 1 (1954).
- [16] J. E. Ffowcs-Williams, *The noise from turbulence convected at high speed*, [Philosophical Transactions of the Royal Society of London. Series A. Mathematical and Physical Sciences](#) **255**, 469 (1963).
- [17] C. K. W. Tam, *Jet Noise: Since 1952*, [Theoretical and Computational Fluid Dynamics](#) **10**, 393 (1998).
- [18] P. Jordan, *Coherent structures and jet aeroacoustics*, Tech. Rep. (VKI Lecture Series - Advanced post-processing of experimental and numerical data, 2014).
- [19] A. Michalke, *A Wave Model for Sound Generation in Circular Jets*, Tech. Rep. (1970).
- [20] R. R. Armstrong, A. Michalke, and H. V. Fuchs, *Coherent Structures in Jet Turbulence and Noise*, [AIAA Journal](#) **15**, 1011 (1977).
- [21] C. Bogey, C. Bailly, and D. Juvé, *Noise investigation of a high subsonic, moderate Reynolds number jet using a compressible Large Eddy Simulation*, [Theoretical and Computational Fluid Dynamics](#) **16**, 273 (2003).
- [22] J. Laufer and T. Yen, *Noise generation by a low-Mach-number jet*, [Journal of Fluid Mechanics](#) **134**, 1 (1983).
- [23] P. Jordan and T. Colonius, *Wave Packets and Turbulent Jet Noise*, [Annual Review of Fluid Mechanics](#) **45**, 173 (2013).
- [24] A. V. G. Cavalieri, P. Jordan, A. Agarwal, and Y. Gervais, *Jittering wave-packet models for subsonic jet noise*, [Journal of Sound and Vibration](#) **330**, 4474 (2011).
- [25] A. V. G. Cavalieri, P. Jordan, T. Colonius, and Y. Gervais, *Axisymmetric superdirectivity in subsonic jets*, [Journal of Fluid Mechanics](#) **704**, 388 (2012).

- [26] J. E. Ffowcs-Williams and A. J. Kempton, *The noise from the large-scale structure of a jet*, *Journal of Fluid Mechanics* **84**, 673 (1978).
- [27] A. V. G. Cavalieri, D. Rodríguez, P. Jordan, T. Colonius, and Y. Gervais, *Wavepackets in the velocity field of turbulent jets*, *Journal of Fluid Mechanics* **730**, 559 (2013).
- [28] C. K. Tam, K. Viswanathan, K. K. Ahuja, and J. Panda, *The sources of jet noise: Experimental evidence*, *Journal of Fluid Mechanics* **615**, 253 (2008).
- [29] D. Papamoschou, *Wavepacket Modeling of the Jet Noise Source*, *International Journal of Aeroacoustics* **17** (2018), <https://doi.org/10.1177/1475472X17743653>.
- [30] D. Papamoschou, *Prediction of Jet Noise Shielding*, in *48th AIAA Aerospace Sciences Meeting Including the New Horizons Forum and Aerospace Exposition* (Orlando, FL, USA, 2010).
- [31] N. Curle, *The influence of solid boundaries upon aerodynamic sound*, in *Proceedings of the Royal Society A* **231** (1955) pp. 505–514.
- [32] A. Powell, *Aerodynamic noise and the plane boundary*, *Journal of the Acoustical Society of America* **32**, 982 (1960).
- [33] J. E. Ffowcs-Williams and L. H. Hall, *Aerodynamic sound generation by turbulent flow in the vicinity of a scattering half plane*, *Journal of Fluid Mechanics* **40**, 657 (1970).
- [34] D. G. Crighton and F. G. Leppington, *Scattering of aerodynamic noise by a semi-infinite compliant plate*, *Journal of Fluid Mechanics* **43**, 721 (1970).
- [35] M. S. Howe, *A review of the theory of trailing edge noise*, *Journal of Sound and Vibration* **61**, 437 (1978).
- [36] R. K. Amiet, *Noise due to turbulent flow past a trailing edge*, *Journal of Sound and Vibration* **47**, 387 (1976).
- [37] R. K. Amiet, *Acoustic radiation from an airfoil in a turbulent stream*, *Journal of Sound and Vibration* **41**, 407 (1975).
- [38] M. Roger and S. Moreau, *Back-scattering correction and further extensions of Amiet's trailing-edge noise model. Part I: Theory*, *Journal of Sound and Vibration* **286**, 477 (2005).
- [39] S. Moreau and M. Roger, *Back-scattering correction and further extensions of Amiet's trailing-edge noise model. Part II: Application*, *Journal of Sound and Vibration* **323**, 397 (2009).
- [40] M. Roger, S. Moreau, and K. Kucukcoskun, *On sound scattering by rigid edges and wedges in a flow, with applications to high-lift device aeroacoustics*, *Journal of Sound and Vibration* **362**, 252 (2016).

- [41] R. W. Head and M. J. Fisher, *Jet/Surface Interaction Noise: - Analysis of Farfield Low Frequency Augmentations of Jet Noise due to the Presence of a Solid Shield*, in *3rd AIAA Aeroacoustics Conference* (Palo Alto, CA, USA, 1976).
- [42] C. Brown, *Jet-Surface Interaction Test: Far-Field Noise Results*, in *Proceedings of the ASME Turbo Expo 2012: Power for Land, Sea and Air* (Copenhagen, Denmark, 2012) pp. 1–13.
- [43] G. G. Podboy, *Jet-Surface Interaction Test: Phased Array Noise Source Localization Results*, [NASA/TM—2013-218085](#) (2013), [10.1115/GT2012-69801](#).
- [44] C. Brown and J. Bridges, *Small Hot Jet Acoustic Rig Validation*, Tech. Rep. (NASA/TM-2001-214234, Cleveland, OH, USA, 2006).
- [45] J. L. T. Lawrence, M. Azarpeyvand, and R. H. Self, *Interaction between a Flat Plate and a Circular Subsonic Jet*, in *17th AIAA/CEAS Aeroacoustics Conference* (Portland, OR, USA, 2011).
- [46] S. Meloni, A. Di Marco, M. Mancinelli, and R. Camussi, *Experimental investigation of jet-induced wall pressure fluctuations over a tangential flat plate at two Reynolds numbers*, [Nature Scientific Reports](#) **10** (2020), [10.1038/s41598-020-66037-2](#).
- [47] A. V. G. Cavalieri, P. Jordan, W. R. Wolf, and Y. Gervais, *Scattering of wavepackets by a flat plate in the vicinity of a turbulent jet*, [Journal of Sound and Vibration](#) **333**, 6516 (2014).
- [48] S. Piantanida, V. Jaunet, J. Huber, W. Wolf, P. Jordan, and A. V. G. Cavalieri, *Scattering of turbulent-jet wavepackets by a swept trailing edge*, [The Journal of the Acoustical Society of America](#) **140**, 4350 (2016).
- [49] B. Lyu, A. P. Dowling, and I. Naqavi, *Prediction of installed jet noise*, [Journal of Fluid Mechanics](#) **811**, 234 (2017).



# 3

## PERMEABLE MATERIALS AND ACOUSTIC LINERS AS NOISE REDUCTION SOLUTIONS

*A pessimist sees the difficulty in every opportunity;  
An optimist sees the opportunity in every difficulty.*

Winston Churchill

*This chapter contains a literature review on the properties of permeable materials (porosity and resistivity), as well as a report of their applications for mitigation of different aeroacoustic sources. This chapter also contains a description of acoustic liners, based on the concept of impedance, modelling and noise attenuation. Focus is given to the relationship between the material and geometrical properties of each noise reduction solution, the flow characteristics and the far-field noise behaviour, particularly the mechanisms and results which are relevant for their application for jet-installation noise mitigation.*

### 3.1. PROPERTIES OF PERMEABLE MATERIALS

PERMEABLE materials are categorized as metamaterials, which have properties not directly found in nature, but instead they are engineered for specific applications [1]. These materials are characterized by a number of properties such as porosity, tortuosity and resistivity. The porosity  $\sigma$  is defined as the ratio between the volumetric densities of the permeable material  $\rho_p$  and the original solid structure  $\rho_s$ , as shown in Eq. (3.1):

$$\sigma = 1 - \frac{\rho_p}{\rho_s}. \quad (3.1)$$

The tortuosity is defined as the ratio between the average pore length  $l_p$  and the thickness of the permeable medium,  $t_p$  ( $\tau_p = l_p/t_p$ ) [2]. This parameter is related to the geometry of the structure: for straight channels the tortuosity is 1 in its axial direction; for random porous media, this value is higher than 1.

Finally, the resistivity  $\mathbf{R}$  is related to the flow pressure gradient  $\nabla p$  (spatial derivative of pressure in each direction) through the permeable material, which is also a function of the Darcian velocity  $\mathbf{u}_f$  (volumetric flow rate divided by the cross-sectional area), as given by Hazen-Dupuit-Darcy equation, considering all directions of motion [3]:

$$\nabla p = -\rho \mathbf{R} \cdot \mathbf{u}_f, \quad (3.2)$$

where  $\rho$  is the fluid density,  $\mathbf{R}$  is the overall material resistivity in three dimensions, which is comprised of the inertial ( $\mathbf{R}_I$ ) and viscous ( $\mathbf{R}_V$ ) resistivity components [4], given by:

$$\mathbf{R} = \mathbf{R}_V + \mathbf{R}_I \mathbf{u}_f, \quad (3.3)$$

$$\mathbf{R}_V = \frac{\mu}{\rho \mathbf{K}}, \quad \mathbf{R}_I = \mathbf{C}, \quad (3.4)$$

where  $\mu$  is the fluid dynamic viscosity,  $\mathbf{K}$  is the permeability and  $\mathbf{C}$  is the form coefficient of the permeable structure. Substituting Eq. (3.3) in Eq. (3.2), it is shown that the pressure gradient has a term of linear dependency with velocity and another of quadratic. The former is related to viscous effects on the fluid motion, whereas the latter is the form force imposed to the fluid by any solid surface obstructing the flow path [4]. The permeability  $\mathbf{K}$ , as linked to viscous drag, relates to the effective length of the porous matrix. The form coefficient  $\mathbf{C}$ , on the other hand, does not depend on the length of the body, but on the structure of the matrix [4].

In order to determine the material resistivity, the permeability and form coefficient need to be obtained either from experimental [5] or numerical methods [6]. Rubio Carpio *et al.* [5], for example, calculated the parameters of a metal foam using an experimental rig that allowed the measurement of the pressure drop across the material. Using this value as input, as well as the fluid properties, the curves shown in Fig. 3.1 can be obtained for a sweep of flow velocities and material samples with different thickness [5]. Through a curve fitting with a quadratic polynomial, both unknown terms in Eq. (3.4) are calculated.

From the curves, it is visible that, for a higher thickness, the quadratic term is dominant over the linear one in the resistivity [5]. Moreover, when the curves are scaled with

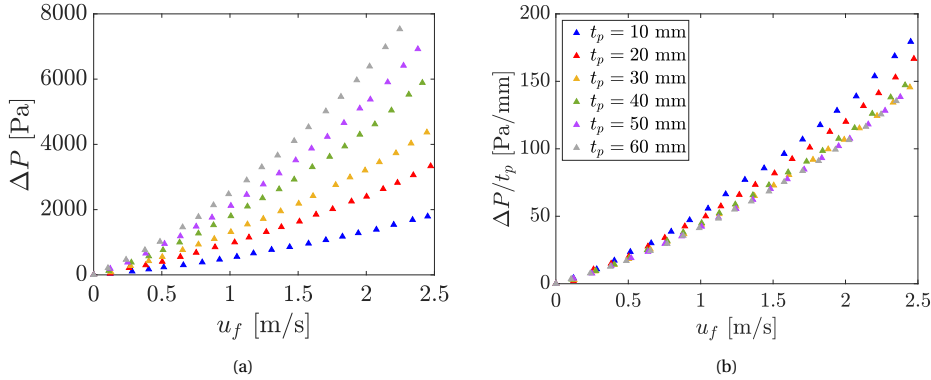


Figure 3.1: Pressure drop across metal foam samples of 450  $\mu\text{m}$  cell diameter for different flow velocities. (a) Measured pressure drop. (b) Measured pressure drop normalized by the sample thickness. Adapted from [5].

the material thickness, they approximately collapse after this parameter reaches a minimum value, in this case  $t_p = 30$  mm. At this point (critical thickness), the resistivity properties of the porous material become independent of the sample thickness [7]. For relatively thin samples, entrance/exit effects that are affected by variations of local permeability and flow regime play a major role in the pressure drop instead [8].

The described parameters are important when permeable materials are applied as noise reduction solutions, as they affect the flow behaviour at the source and, consequently, the emitted noise. In the next section, studies on the mitigation of aeroacoustic sources with permeable materials are reported, focusing on the link between noise reduction, the material properties and flow characteristics.

### 3.2. APPLICATIONS FOR AERODYNAMIC NOISE REDUCTION

As described in Chapter 1, the application of a permeable material at a sound source such as the flap side edge results in significant noise reduction [9]. The flow communication has been especially regarded as an important condition since the noise attenuation provided by the permeable material occurs in a wide frequency range, thus connected to an overall reduction in the strength of the side-edge vortex [9]. This has been confirmed by England *et al.* [10], who show that the magnitude of vorticity in the shear layer of the porous flap is reduced with respect to the solid one, and that the vortex is displaced further away from the flap, thus resulting in a weaker acoustic source. In terms of performance, a slight increase in drag, but no measurable effects on lift are identified [10].

The noise reduction and the effects on performance due to a permeable flap side edge can be linked to the properties of the applied material. With a high resistivity, little flow travels through the permeable area and thus a behaviour similar of a hard surface is obtained [9]. By lowering the surface resistivity, there is more flow through the permeable flap, equalizing the pressure differential in that region, thus weakening the vortex and reducing the produced noise. However, with a significantly lower resistivity, most

of the flow travels through the permeable section and little energy is dissipated, while a strong vortex is formed at the junction between the solid and permeable regions [9]. Therefore, for this case, no significant noise reduction is achieved but the performance is highly affected by lift loss and drag increase [9, 10].

Given the benefits obtained for the flap side edge, Sarradj and Geyer [11] have studied the use of permeable materials for mitigating airfoil turbulent boundary-layer trailing-edge (TBL-TE) noise. The results show that a fully porous airfoil reduces the sound pressure level up to 10 dB with respect to the solid case. The properties of the material, such as porosity and resistivity, have been found to affect the frequency range and amplitude of noise reduction [11]. However, the acoustic results are coupled with a significant loss in performance (lift decrease and drag increase), particularly for the materials with low resistivity. For those materials, excessive flow communication leads to an increase of the boundary-layer thickness and turbulence intensity near the trailing edge, which is responsible for the undesired aerodynamic results [12]. In order to mitigate these negative effects, the authors have restricted the porous section of the airfoil to the trailing-edge region [12, 13]. The shortest porous length (last 5% of the airfoil chord) provides 8 dB noise reduction with minor effects on the aerodynamic characteristics. It is concluded that not only the properties of the permeable material have a significant impact on noise and performance, but also that the extent of the permeable surface affects the latter more than the former [12, 13]. Therefore, there is potential on reducing the extension of the permeable region in order to minimize performance degradation, while still providing considerable noise reduction.

Rubio-Carpio *et al.* [5, 14] have studied TBL-TE noise reduction by replacing sections of the trailing edge (last 20% of the chord) of a NACA 0018 airfoil with porous inserts manufactured out of metallic foams. Acoustic beamforming results show noise reduction at low and mid frequencies, on the order of 10 dB with respect to the solid airfoil, and an increase at high frequencies, which is attributed to the surface roughness of the porous material, as shown in the spectra in Fig. 3.2. Furthermore, in the frequency range where noise reduction is achieved, the dominant source location in the beamforming maps has shifted from the original trailing-edge position to the solid-permeable junction, which becomes the dominant acoustic scattering region [5, 14].

Kisil and Ayton [15] have studied the effect of a finite porous extension to a semi-infinite impermeable flat plate, modelling the sound generated by scattering of a convecting gust at both the trailing edge and the solid-permeable junction. The results show that the acoustic directivity for the permeable trailing-edge case changes with respect to the baseline solid one, with considerable noise reduction at shallow upstream angles and an overall shift from a cardioid shape to a dipole-like one [15, 16]. Moreover, increasing porosity (in the model, this is equivalent to decreasing the material resistivity) reduces the magnitude of the trailing-edge source term, while the junction one is increased. Therefore, considering the overall configuration, the produced sound does not monotonically decrease with higher porosity [15].

Further analyses by Rubio Carpio *et al.* [17] have shown that the relative noise reduction provided by the permeable materials has a maximum limit and further decrease of resistivity does not lead to lower noise. This threshold is dependent on the topology of the materials (e.g. metal foam or perforated plate) and the flow conditions, and can

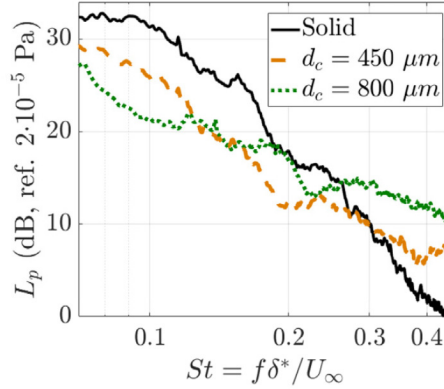


Figure 3.2: Sound pressure level spectra of an airfoil with permeable trailing edges with different cell diameters, compared to the reference solid case. Adapted from [14].

be used as a design guideline to minimize aerodynamic penalties, while still providing effective noise reduction [17]. Moreover, this is also valid for the extension of the permeable region, which can be restricted to a short section near the trailing edge for relatively high noise reduction and low performance degradation [17]. These results are, however, applicable for an airfoil case, wherein there are pressure fluctuations on both upper and lower sides. For the case of an installed jet, with impingement only on the lower surface, it is not yet clear if there is a similar noise reduction threshold with permeability or the size of the permeable region.

Numerical investigations of a partially porous airfoil have been performed by Teruna *et al.* [18]. The permeable section is modelled using an equivalent fluid region approach based on Darcy's law, wherein the porosity and flow resistivity of a metal foam are applied. Aside from the baseline solid and the porous trailing edges, a third configuration with a thin solid core at the symmetry plane of the porous trailing edge has been studied. Noise reduction of up to 9 dB is obtained with the porous edge, whereas the blocked one does not provide any benefit [18, 19]. In order to explain this behaviour, the spatial variation of flow impedance in the porous medium is analyzed through the ratio between pressure and normal velocity fluctuations, as shown in Fig. 3.3 [18].

The results show that the impedance of the porous case gradually decreases towards the trailing edge, resulting in a less severe discontinuity at that region [18]. However, this does not occur for the blocked case, for which large surface pressure fluctuations persist at the trailing edge. Consequently, the scattering mechanism is similar to the baseline solid case [18, 19]. Therefore, it is concluded that not only flow communication is an important condition for noise reduction, but also a progressive impedance decrease from the solid section until the trailing edge is essential.

Further evidence on the effect of permeable materials on trailing-edge scattering is reported in an analytical study by Jaworski and Peake [20]. The interaction of a turbulent eddy with a semi-infinite poroelastic edge is studied, focusing on the effect of both permeability and elasticity on the produced noise, particularly the dependence on the

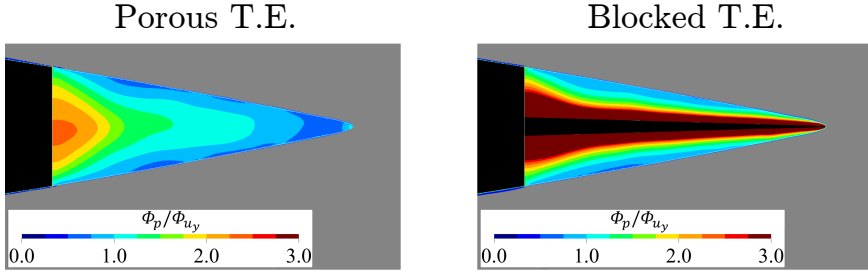


Figure 3.3: Contours of the ratio between pressure and normal velocity fluctuations inside the porous medium. Adapted from [18].

characteristic flow velocity. The scattering problem is solved using the Wiener–Hopf technique and the results show that the dependence of the noise levels with flow velocity changes from  $U^5$  for the solid case to  $U^6$  for the permeable one [20]. This result indicates that the scattering mechanism becomes weaker with a permeable surface and other sources tend to become dominant in a partially permeable surface.

The aforementioned studies describe the most important effects of permeable materials, particularly for trailing-edge noise applications. The change in directivity shape and dependence on flow velocity are strong indicators of less dominant scattering effects, which would be essential for JIN reduction. However, it is not yet clear the magnitude of noise reduction that can be achieved for this application, also considering properties such as the material resistivity or possible junction effects. Moreover, not only the noise due to scattering needs to be considered, but also that due to impingement of turbulent fluctuations. These questions are addressed in this thesis and the study is reported in Chapters 6 and 7.

### 3.3. ACOUSTIC LINERS

Acoustic liners are also commonly used solutions for aeroacoustic applications. As described in Chapter 1, a SDOF liner is comprised by a perforated face-sheet, a cavity and a solid backplate. Its main working principle is to convert acoustic energy into flow kinetic energy through shear stresses and the generation and shedding of vorticity at the face-sheet orifices [21]. This mechanism is modelled through the concept of acoustic impedance, defined in the frequency domain as the ratio between the Fourier components of the acoustic pressure  $p$  and of acoustic velocity normal to the liner  $u_n$ , and given by Eq. (3.5) [22]:

$$z = \frac{p}{\rho c_0 u_n} = \theta + i\chi, \quad (3.5)$$

where  $\theta$  is the resistance and  $\chi$  is the reactance. The former is the main driver of acoustic energy dissipation, whereas the latter is associated with the inertia of the medium. The impedance terms are governed by the geometry of the resonator and the characteristics of the incident acoustic waves.

The resistance is responsible for the energy dissipation mechanisms, comprising the

pressure loss inside the orifice due to pipe-flow friction, as well as entrance/exit effects related to vortex shedding [22]. Moreover, the amplitude of the incident sound wave can also affect the impedance, triggering a non-linear response from the liner, which is dependent on the geometry of the orifice, the discharge coefficient and the acoustic particle velocity [23]. Therefore, a model for the resistance taking into account all the relevant parameters can be written as [24]:

$$\theta = \frac{\sqrt{8\nu\omega}}{\sigma c_0} \left(1 + \frac{t}{d}\right) + \frac{\pi^2}{2\sigma} \left(\frac{d}{\lambda}\right)^2 + \frac{(1-\sigma^2)}{\sigma} \left[ \frac{|\mathbf{u}_0|}{c_0} + k_l M \right], \quad (3.6)$$

where  $\nu$  is the fluid kinematic viscosity,  $\omega$  is the angular frequency ( $\omega = 2\pi f$ ),  $\sigma$  is the fractional open area with respect to the total area of the porous face-sheet,  $t$  and  $d$  are the thickness of the face-sheet and the hole diameter, respectively, and  $\lambda$  is the acoustic wavelength ( $c_0/f$ ).  $|\mathbf{u}_0|$  represents the acoustic particle velocity through the orifices,  $M$  is the steady flow Mach number around the face-sheet, and  $k_l$  is an empirical constant related to the boundary layer properties of the grazing flow [25, 26].

The first term on the right-hand side in Eq. (3.6) refers to the Helmholtz resistance value for a perforated plate, which is related to viscous dissipation effects [23, 27]. The second term represents the resistance due to radiation effects [23]. The last term refers to non-linear effects, due to a high amplitude of pressure fluctuations (represented in the acoustic particle velocity) or due to steady flow tangential to the holes in the face-sheet (represented by the free-stream Mach number) [28]. The acoustic particle velocity through the orifice is given by Eq. (3.7) [24]:

$$|\mathbf{u}_0| = \frac{2|p_i|}{\sigma\rho c_0[(\theta + 1/\cos\phi)^2 + \chi^2]^{1/2}}, \quad (3.7)$$

where  $p_i$  and  $\phi$  are the pressure amplitude and incidence angle of the acoustic wave on the face-sheet, respectively. According to Guess [24], this formulation is valid for certain conditions, which have to be considered during the design phase:

$$\frac{d}{2} \left(\frac{\omega}{\nu}\right)^{1/2} > 10, \quad \frac{\omega d}{c_0} < 0.5.$$

The expression for the reactance is given by Eq. (3.8) [24]:

$$\chi = \frac{\sqrt{8\nu\omega}}{\sigma c_0} \left(1 + \frac{t}{d}\right) + \frac{\omega(t+\delta)}{\sigma c_0} - \cot\left(\frac{\omega L_c}{c_0}\right), \quad (3.8)$$

where  $\delta$  is the orifice end correction term and  $L_c$  is the cavity depth (distance between the face-sheet and backplate). The first and second terms on the right-hand side refer to the viscous reactance and mass inertance terms, whereas the third term is related to the impedance of the cavity [23]. The mass inertance is dependent on the parameter  $\delta$ , given by Eq. (3.9) [24].

$$\delta = \frac{8}{3\pi} \frac{d(1-0.7\sqrt{\sigma})}{1+305M^3} \left( \frac{1+5 \times 10^3 M_0^2}{1+10^4 M_0^2} \right), \quad (3.9)$$

where  $M_0$  is the acoustic particle Mach number through the orifice ( $|\mathbf{u}_0|/c_0$ ). The orifice end correction term takes into account interior and exterior orifice interactions, steady flow effects and high amplitude of pressure fluctuations [23].

The values of resistance and reactance can be used to calculate the resonator absorption coefficient  $\alpha$ , given by Eq. (3.10) [24]:

$$\alpha = \frac{4\theta \cos \phi}{(\theta \cos \phi + 1)^2 + \chi^2 \cos^2 \phi}, \quad (3.10)$$

The goal of the design procedure is, therefore, to select parameters which result in maximum absorption at a specified frequency value. For this condition, it is thus necessary that  $\alpha = 1$  and  $d\alpha/d\omega = 0$ , which result in  $\theta = 1/\cos \phi$  and  $\chi = 0$ .

In order to increase the frequency range of high sound absorption by the resonator, a DDOF liner concept can be designed, as described in Chapter 1. The presence of the septum inside the cavity results in a second peak in the absorption coefficient curve, thus resulting in higher noise reduction in the frequency range near this additional peak [22]. The overall impedance of a DDOF resonator is given by Eq. (3.11) [22]:

$$z = z_1 + \frac{z_2 \frac{\cos(kL_{c1}) \sin(kL_{c2})}{\sin(kL_c)} - i \cot(kL_c)}{1 + iz_2 \frac{\sin(kL_{c1}) \sin(kL_{c2})}{\sin(kL_c)}}, \quad (3.11)$$

where  $z_1$  and  $z_2$  represent the impedance of the face-sheet and septum, respectively. The parameters  $L_{c1}$  and  $L_{c2}$  are the distances between the face-sheet and septum, and between the septum and the backplate, respectively. Their sum is equivalent to the total cavity depth  $L_c$ . The face-sheet and septum impedance values consider all the resistance and reactance terms in Eqs. (3.6) and (3.8), with the exception of the cavity reactance, which is now included in Eq. (3.11) [22].

Acoustic liners are usually designed for noise reduction at discrete frequencies, i.e. to mitigate noise of tonal characteristic. They have been successfully applied in aircraft to attenuate the fan noise transmitted along the nacelle ducts [29, 30]. However, as mentioned in Chapter 1, under high-amplitude incident sound waves, the liner presents a non-linear response. This changes the dominant attenuation mechanism from viscous dissipation in the shear layer to a strong vortex shedding at the orifice, occurring at certain acoustic frequency bands, whose width is a function of the Reynolds number at the orifice [29, 31]. This broadband noise attenuation characteristic can be further enhanced through the use DDOF liners [32], or resonators with variable-depth cavities, which are tuned to different frequencies [33].

Therefore, a potential JIN reduction solution with minimum effect on performance is the application of acoustic liners on the surface close to the jet. Since the resonators only have open channels on the face-sheet, but the backplate is fully solid, there is no flow communication between the two sides of the airframe surface thus reducing the impact on its aerodynamic characteristics. Moreover, acoustic liners have been used for fan noise attenuation and are already present in currently operating aircraft [30, 34]. Therefore, their full-scale application for other aeroacoustic sources is also more practical and straightforward than open-cell permeable materials. As described in Chapter 1,

they are effective for airfoil trailing-edge noise reduction, while mounted in an aircraft flap [35], and thus also likely to mitigate JIN.

A study on JIN reduction with Helmholtz resonators mounted in a surface located in the vicinity of a jet is reported in Chapter 8.

## REFERENCES

- [1] R. Kshetrimayum, *A brief intro to metamaterials*, *IEEE Potentials* **23** (2005), [10.1109/MP2005.1368916](https://doi.org/10.1109/MP2005.1368916).
- [2] N. Epstein, *On tortuosity and the tortuosity factor in flow and diffusion through porous media*, *Chemical Engineering Science* **44** (1989), [10.1016/0009-2509\(89\)85053-5](https://doi.org/10.1016/0009-2509(89)85053-5).
- [3] S. P. Neuman, *Theoretical Derivation of Darcy's Law*, *Acta Mechanica* **25**, 153 (1977).
- [4] D. B. Ingham and I. Pop, *Transport Phenomena in Porous Media*, 1st ed. (Pergamon, Kidlington, Oxford, UK, 1998).
- [5] A. Rubio Carpio, R. Merino Martínez, F. Avallone, D. Ragni, M. Snellen, and S. Van Der Zwaag, *Broadband Trailing Edge Noise Reduction Using Permeable Metal Foams*, in *InterNoise Conference* (Hong Kong, 2017).
- [6] C. Teruna, L. Rego, F. Avallone, D. Ragni, and D. Casalino, *Applications of the Multi-layer Porous Medium Modeling Approach for Noise Mitigation*, *Journal of Aerospace Engineering* **34**, 04021074 (2021).
- [7] N. Dukhan and C. A. Minjaur, *Minimum thickness for open-cell metal foam to behave as a porous medium*, in *40th AIAA Fluid Dynamics Conference*, Vol. 1 (American Institute of Aeronautics and Astronautics Inc., 2010).
- [8] E. Baril, A. Mostafid, L. P. Lefebvre, and M. Medraj, *Experimental demonstration of entrance/exit effects on the permeability measurements of porous materials*, *Advanced Engineering Materials* **10**, 889 (2008).
- [9] J. D. Revell, H. L. Kuntz, F. J. Balena, B. L. Storms, and R. P. Dougherty, *Trailing-Edge Flap Noise Reduction by Porous Acoustic Treatment*, in *3rd AIAA/CEAS Aeroacoustics Conference* (Atlanta, GA, USA, 1997).
- [10] D. Angland, X. Zhang, and N. Molin, *Measurements of Flow Around a Flap Side Edge with Porous Edge Treatment*, *AIAA Journal* (2009), [10.2514/1.39311](https://doi.org/10.2514/1.39311).
- [11] E. Sarradj and T. Geyer, *Noise Generation by Porous Airfoils*, in *13th AIAA/CEAS Aeroacoustics Conference* (Rome, Italy, 2007).
- [12] T. Geyer and E. Sarradj, *Trailing edge noise of partially porous airfoils*, in *20th AIAA/CEAS Aeroacoustics Conference* (Atlanta, GA, USA, 2014).
- [13] T. F. Geyer, A. Lucius, M. Schrödter, M. Schneider, and E. Sarradj, *Reduction of Turbulence Interaction Noise Through Airfoils With Perforated Leading Edges*, *Acta Acustica united with Acustica* **105** (2019), [10.3813/AAA.919292](https://doi.org/10.3813/AAA.919292).

- 
- [14] A. Rubio Carpio, R. Merino Martínez, F. Avallone, D. Ragni, M. Snellen, and S. Van Der Zwaag, *Experimental characterization of the turbulent boundary layer over a porous trailing edge for noise abatement*, *Journal of Sound and Vibration* **443**, 537 (2019).
- [15] A. Kisil and L. J. Ayton, *Aerodynamic noise from rigid trailing edges with finite porous extensions*, *Journal of Fluid Mechanics* **836**, 117 (2018).
- [16] L. J. Ayton, *Acoustic scattering by a finite rigid plate with a poroelastic extension*, *Journal of Fluid Mechanics* **791**, 414 (2016).
- [17] A. Rubio Carpio, F. Avallone, D. Ragni, M. Snellen, and S. van der Zwaag, *Quantitative criteria to design optimal permeable trailing edges for noise abatement*, *Journal of Sound and Vibration* **485** (2020), 10.1016/j.jsv.2020.115596.
- [18] C. Teruna, F. Manegar, F. Avallone, D. Ragni, D. Casalino, and T. Carolus, *Noise reduction mechanisms of an open-cell metal-foam trailing edge*, *Journal of Fluid Mechanics* **898** (2020), 10.1017/jfm.2020.363.
- [19] C. Teruna, F. Avallone, D. Ragni, A. Rubio-Carpio, and D. Casalino, *Numerical analysis of a 3-D printed porous trailing edge for broadband noise reduction*, *Journal of Fluid Mechanics* **926**, A17 (2021).
- [20] J. W. Jaworski and N. Peake, *Aerodynamic noise from a poroelastic edge with implications for the silent flight of owls*, *Journal of Fluid Mechanics* **723**, 456 (2013).
- [21] J. D. Eldredge and A. P. Dowling, *The absorption of axial acoustic waves by a perforated liner with bias flow*, *Journal of Fluid Mechanics* , 307 (2003).
- [22] H. H. Hubbard, *Aeroacoustics of Flight Vehicles: Theory and Practice Vol. 2: Noise Control*, Vol. 2 (NASA Reference Publication 1258, 1991) pp. 165–206.
- [23] U. Ingard, *On the theory and design of acoustic resonators*, *Journal of the Acoustical Society of America* **25**, 1037 (1953).
- [24] A. W. Guess, *Calculation of perforated plate liner parameters from specified acoustic resistance and reactance*, *Journal of Sound and Vibration* **40**, 119 (1975).
- [25] E. Feder and L. W. Dean, *Analytical and experimental studies for predicting noise attenuation in acoustically treated ducts for turbofan engines*, Tech. Rep. (NASA CR-1373, 1969).
- [26] E. Rice, *A model for the pressure excitation spectrum and acoustic impedance of sound absorbers in the presence of grazing flow*, (American Institute of Aeronautics and Astronautics (AIAA), 1973).
- [27] T. H. Melling, *The Acoustic Impedance of Perforates at Medium and High Sound Pressure Levels*, *Journal of Sound and Vibration* **29**, 1 (1973).
- [28] U. Ingard and H. Ising, *Acoustic nonlinearity of an orifice*, *The Journal of the Acoustical Society of America* **42**, 6 (1967).

- [29] D. Casalino, F. Diozzi, R. Sannino, and A. Paonessa, *Aircraft noise reduction technologies: A bibliographic review*, *Aerospace Science and Technology* **12**, 1 (2008).
- [30] D. L. Sutliff and M. G. Jones, *Low-speed fan noise attenuation from a foam-metal liner*, *Journal of Aircraft* **46**, 1381 (2009).
- [31] C. K. Tam and K. A. Kurbatskii, *Microfluid dynamics and acoustics of resonant liners*, *AIAA journal* **38**, 1331 (2000).
- [32] D. M. Nark, M. G. Jones, D. L. Sutliff, E. Ayle, and F. Ichihashi, *Improved broadband liner optimization applied to the advanced noise control fan*, in *20th AIAA/CEAS Aeroacoustics Conference* (2014).
- [33] M. G. Jones, W. R. Watson, D. M. Nark, and B. M. Howerton, *Evaluation of variable-depth liner configurations for increased broadband noise reduction*, in *21st AIAA/CEAS Aeroacoustics Conference* (2015).
- [34] D. L. Huff, *Noise Reduction Technologies for Turbofan Engines*, NASA/TM—2007-214495, 1 (2007).
- [35] D. Casalino and M. Barbarino, *Optimization of a Single-Slotted Lined Flap for Wing Trailing-Edge Noise Reduction*, *Journal of Aircraft* **49** (2012), 10.2514/1.C031561.



# 4

## NUMERICAL AND EXPERIMENTAL METHODOLOGY

*Science is more than a body of knowledge. It is a way of thinking;  
A way of skeptically interrogating the universe  
with a fine understanding of human fallibility.*

Carl Sagan

*This chapter reports the methodologies applied in this thesis. In section 4.1, the numerical approach is described, focusing on the characteristics of the chosen flow solver and the noise prediction formulation. Section 4.2 contains the experimental techniques for the measurement of flow field and acoustic properties. Complementary information on signal processing techniques is included in Appendix A.*

## 4.1. NUMERICAL APPROACH

### 4.1.1. LATTICE-BOLTZMANN METHOD

THE numerical approach adopted throughout this thesis is the Lattice-Boltzmann Method (LBM), which is implemented in the commercial software Simulia PowerFLOW 6-2019. The LBM solves the discrete form of the Boltzmann equation, which describes the advection of fluid particles in microscopic scale and momentum exchange due to collisions between them. The particle motion is statistically described at a position  $\mathbf{x}$  with a discrete velocity  $\mathbf{V}_q$ , at the time  $t$  by making use of a probability density function  $F(\mathbf{x}, t, \mathbf{V}_q)$ . In the LBM, the solution of the Boltzmann equation is performed on a Cartesian mesh (lattice), given by:

$$F_q(\mathbf{x} + \mathbf{V}_q \Delta t, t + \Delta t) - F_q(\mathbf{x}, t) = \kappa_q(\mathbf{x}, t), \quad (4.1)$$

where the  $q$  subscript designates a specific direction of the lattice, which is equal to the number of discrete velocity vectors. The left-hand side of Eq. (4.1) represents a time-explicit advection with space and time increments represented by  $\mathbf{V}_q \Delta t$  and  $\Delta t$ , respectively. The right-hand side is the collision operator  $\kappa_q(\mathbf{x}, t)$ , which represents variations in the particle velocity distribution due to momentum exchange between particles.

The macroscopic flow properties such as density  $\rho$ , velocity  $\mathbf{u}$  and internal energy  $E$  are obtained from computing the moments of the particle distribution functions [1]:

$$\rho(\mathbf{x}, t) = \sum_q F_q(\mathbf{x}, t), \quad (4.2)$$

$$\rho \mathbf{u}(\mathbf{x}, t) = \sum_q \mathbf{V}_q F_q(\mathbf{x}, t), \quad (4.3)$$

$$\rho E(\mathbf{x}, t) = \sum_q \frac{1}{2} \mathbf{V}_q^2 F_q(\mathbf{x}, t). \quad (4.4)$$

Not only the flow properties, but also the system of Navier-Stokes equations can be recovered from LBM through the Chapman-Enskog expansion [2], for which the particle distribution function is described as a series in terms of Knudsen number.

In the LBM, every time step of the solution is comprised by two processes: advection and collision. For the former, the particle distribution function in each lattice is shifted to the adjacent ones, following the discrete velocity directions. This is performed using Eq. (4.1), but considering the collision term equal to zero. For the latter, macroscopic flow quantities are firstly computed at each node using the previously advected distribution functions. These quantities are also used for computing the local equilibrium distribution function and the collision term. Finally, the the local distribution functions are updated ( $F_q^*$ ) by incorporating the outcome of the collision process:

$$F_q^*(\mathbf{x} + \mathbf{V}_q \Delta t, t + \Delta t) = F_q(\mathbf{x} + \mathbf{V}_q \Delta t, t + \Delta t) + \kappa_q(\mathbf{x}, t). \quad (4.5)$$

The employed collision operator in the LBM is the Bhatnagar-Gross-Krook (BGK) model [3], expressed as:

$$\kappa_q = -\frac{1}{\tau} [F_q(\mathbf{x}, t) - F_q^{\text{eq}}(\mathbf{x}, t)], \quad (4.6)$$

which states that the local distribution function returns to the equilibrium one ( $F_q^{\text{eq}}$ ) within a time scale  $\tau$  [1] and it assumes that all the scales of relaxation processes happen at the same rate since the deviations from the equilibrium state are small. The equilibrium distribution  $F_q^{\text{eq}}$  of Maxwell-Boltzmann is adopted, given by [4]:

$$F_q^{\text{eq}} = \frac{\rho}{(2\pi RT)^{D/2}} e^{-\frac{|\mathbf{V}_q - \mathbf{u}|^2}{2RT}}, \quad (4.7)$$

where  $R$  is the ideal gas constant,  $T$  is the gas temperature, and  $D$  is the number of spatial dimensions. The discretization of the Boltzmann equation in the velocity space employs a Gauss-Hermite quadrature, wherein the distribution function is expanded as a Hermite polynomial. This is performed because the expansion coefficients are exactly the velocity moments of the distribution function, including the macroscopic flow variables such as density and velocity [5]. For that purpose, Eq. (4.1) is rewritten into [5, 6]:

$$\frac{\partial F_q}{\partial t} + \mathbf{V}_q \cdot \nabla F_q = \frac{F_q^{\text{eq}} - F_q}{\tau}. \quad (4.8)$$

Then  $F_q^{\text{eq}}$  is expressed as a Hermite expansion for a set of discrete velocities  $\mathbf{V}_q$  [5]:

$$F_q^{\text{eq}} = w_q \sum_{n=0}^{\infty} \frac{1}{n!} a^{(n)} \mathcal{H}^{(n)}(\mathbf{V}_q), \quad (4.9)$$

where  $w_q$  is a weight function and  $\mathcal{H}^{(n)}(\mathbf{V}_q)$  is the  $n^{\text{th}}$  order Hermite polynomial. The Hermite expansion coefficients are given by [5]:

$$a^{(n)} = \sum_{q=1}^Q F_q^{\text{eq}} \mathcal{H}^{(n)}(\mathbf{V}_q), \quad (4.10)$$

where the selected number of discrete velocities  $Q$  depends on the truncation order of the Hermite expansion  $n$ , which in turn determines the accuracy of the approximation. Due to orthogonality, the series can be truncated without altering the low order coefficients and flow quantities. With a third-order truncation ( $n = 3$ ), the pressure tensor and momentum dynamics are accurate at the Navier-Stokes level (second order moments), whereas with  $n = 4$ , the modelling of internal energy and heat flux is included [5].

The simulations in this work are performed with imposed ambient fluid temperature and no significant thermal effects are expected that require a highly accurate solution for the energy equation. Therefore, a third-order expansion is employed to approximate the equilibrium distribution function  $F_q^{\text{eq}}$ , given by [4, 7]:

$$F_q^{\text{eq}} \approx \rho w_q \left[ 1 + \frac{\mathbf{V}_q \cdot \mathbf{u}}{\Theta} + \frac{(\mathbf{V}_q \cdot \mathbf{u})^2}{2\Theta^2} - \frac{\mathbf{u}^2}{2\Theta} + \frac{(\mathbf{V}_q \cdot \mathbf{u})^3}{6\Theta^3} - \frac{(\mathbf{V}_q \cdot \mathbf{u})\mathbf{u}^2}{2\Theta^2} \right]. \quad (4.11)$$

This formulation is used for a 3-dimensional lattice with 19 discrete velocity vectors, which are the abscissae of Gaussian-Hermite quadratures, also known as the D3Q19

model [5]. For this model, the non-dimensional lattice temperature is  $\Theta = 1/3$ , while  $w_q = 1/3$  for the rest velocity ( $q = 0$ ),  $1/18$  for the main axes, and  $1/36$  for the diagonals [7].

Finally, the relaxation time  $\tau$  in the BGK model (Eq. (4.6)) acts as a kinematic viscosity. Using the Chapman-Enskog expansion and considering a lattice with grid spacing  $\Delta x$  and time-step  $\Delta t$ , the relationship between the two terms is given by [8]:

$$\nu = \frac{1}{3} \left( \frac{\Delta x}{\Delta t} \right)^2 \left( \tau - \frac{\Delta t}{2} \right). \quad (4.12)$$

With a single relaxation time, the BGK model cannot distinguish between momentum exchanges through viscosity and energy exchanges through thermal conduction. Consequently, the model assumes a unitary Prandtl number, which does not necessarily match the empirical value for different types of fluid [9]. Alternatively, Chen *et al.* [9] proposed a two-relaxation-time approach, wherein relaxation times are assigned separately for dynamic viscosity and thermal conductivity. Moreover, since the BGK model is always Galilean invariant, it has been demonstrated that this property can be recovered by defining the collision operator in a relative reference frame, such that the discrete velocity vectors are expressed with respect to the flow macroscopic velocity [9].

The LBM scheme is carried out on lattices corresponding to volumetric cell elements known as voxels [10]. The different levels of grid refinement are defined by virtual volumes known as variable resolution (VR) regions. The voxel resolution (number of voxels in a characteristic length) changes by a factor of 2 at each adjacent VR [11]. For the finest resolution region, the distribution function in each voxel is computed and updated at every time step. At coarser VRs, this process occurs at every  $2^M$  time steps, where  $M$  is the difference between the finest VR level and the respective one. To ensure conservation of mass, momentum, and energy, across regions with different resolution levels, a voxel-centered lattice scheme is employed [11]. Solid walls are represented by planar surfaces known as surfels, which are tangential to the wall curvature.

Wall boundary conditions are implemented in two different manners, depending on the desired surface characteristic. A no-slip wall is modelled with a bounce-back mapping of the particle velocities, wherein both normal and tangential components are inverted after collision with the surface and thus the particles are reflected back to their original direction [12]. On the other hand, a free-slip wall is modelled with a specular reflection process, wherein the tangential velocity component is kept while the normal one is inverted [12].

#### 4.1.2. VLES TURBULENCE MODEL

The described LBM is coupled with a Very Large Eddy Simulation (VLES) approach for turbulence modelling. Similarly to the ones usually applied for Navier-Stokes formulations, this approach is based on the eddy viscosity model, derived from the Boussinesq hypothesis. This hypothesis states that the turbulent shear stress is linearly proportional to the mean rate of strain via the eddy viscosity, due to the apparent viscosity increase of the flow field caused by turbulent eddies. Considering an analogy between eddy transport phenomena and Maxwell's kinetic theory of gas, Chen *et al.* [13] demonstrated that

turbulence can be described using the Boltzmann equation with a distribution function  $F_{\text{turb}}$ , given by:

$$\frac{\partial F_{\text{turb}}}{\partial t} + \mathbf{V}_{\text{turb}} \cdot \frac{\partial F_{\text{turb}}}{\partial \mathbf{x}} = \kappa_{\text{turb}}, \quad (4.13)$$

$$\kappa_{\text{turb}} = -\frac{1}{\tau_{\text{turb}}} (F_{\text{turb}} - F_{\text{turb}}^{\text{eq}}), \quad (4.14)$$

where, in this case,  $\mathbf{V}_{\text{turb}}$  is not the particle velocity, but rather the turbulent velocity of a fluid parcel. The collision term  $\kappa_{\text{turb}}$  follows the BGK model [3], with a turbulent relaxation time  $\tau_{\text{turb}}$ . The equilibrium distribution function of Maxwell-Boltzmann is also adopted for  $F_{\text{turb}}^{\text{eq}}$ , centered around a mean velocity  $\mathbf{U}$  and a half-width of  $\frac{2}{3}k$ , where  $k$  is the turbulent kinetic energy [13]. Subsequently, the density  $\rho$ , mean velocity  $\mathbf{U}$ , and turbulent kinetic energy  $k$  are defined as:

$$\rho = \int F_{\text{turb}} d\mathbf{V}_{\text{turb}}, \quad (4.15)$$

$$\mathbf{U} = \langle \mathbf{V}_{\text{turb}} \rangle = \int \frac{1}{\rho} F_{\text{turb}} \mathbf{V}_{\text{turb}} d\mathbf{V}_{\text{turb}}, \quad (4.16)$$

$$k = \frac{1}{2} \langle (\mathbf{u}')^2 \rangle = \frac{1}{2} \langle (\mathbf{V}_{\text{turb}} - \mathbf{U})^2 \rangle, \quad (4.17)$$

where the operator  $\langle A \rangle = \int \frac{1}{\rho} F_{\text{turb}} A d\mathbf{V}_{\text{turb}}$ .

Similarly as previously described, the particle distribution function  $F_{\text{turb}}$  is expanded into a series in terms of Knudsen number, defined as the ratio between the characteristic time scale of turbulence and that of the mean flow field ( $\tau_{\text{turb}}/t_{\text{mean}}$ ). From this expansion, the Reynolds stress tensor is given by:

$$\sigma_{ij}^{(n)} = -\int \frac{1}{\rho} F_{\text{turb}}^{(n)} (\mathbf{V}_{\text{turb}} - \mathbf{U})_i (\mathbf{V}_{\text{turb}} - \mathbf{U})_j d\mathbf{V}_{\text{turb}}. \quad (4.18)$$

The Reynolds stress tensor at different orders is thus given by:

$$\begin{aligned} \sigma_{ij}^{(0)} &= -\frac{2}{3} k \delta_{ij} \\ \sigma_{ij}^{(1)} &= -2\nu_{\text{turb}} S_{ij}, \quad \nu_{\text{turb}} = \frac{2}{3} k \tau_{\text{turb}} \\ \sigma_{ij}^{(2)} &= -2\nu_{\text{turb}} \frac{D}{Dt} [\tau_{\text{turb}} S_{ij}] - 6 \frac{\nu_{\text{turb}}^2}{k} \left[ S_{ik} S_{kj} - \frac{1}{3} \delta_{ij} S_{kl} S_{kl} \right] \\ &\quad + 3 \frac{\nu_{\text{turb}}^2}{k} [S_{ik} \Omega_{kj} + S_{jk} \Omega_{ki}] \end{aligned} \quad (4.19)$$

where  $\frac{D}{Dt}$  is a material derivative operator,  $S_{ij} = \frac{1}{2} \left( \frac{\partial U_i}{\partial x_j} + \frac{\partial U_j}{\partial x_i} \right)$ , and  $\Omega_{ij} = \frac{1}{2} \left( \frac{\partial U_i}{\partial x_j} - \frac{\partial U_j}{\partial x_i} \right)$ .

The material derivative of the strain rate tensor indicates that the local instantaneous Reynolds stress is linked to the changes in the strain rate with respect to an earlier time

and location, depending on  $\tau_{\text{turb}}$ . Moreover, higher-order terms in Eq. (4.19), which are caused by the non-linearity of Reynolds stress, also resemble the expression for the turbulence closure in non-linear turbulence models [14].

In the applied LBM-VLES approach, the  $k-\epsilon$  Renormalisation Group (RNG) [15] formulation has been employed, which takes into account the contribution of all scales of turbulence on diffusion, unlike the regular  $k-\epsilon$  model. The output from the  $k-\epsilon$  RNG model is then used to locally replace the original relaxation time  $\tau$  with  $\tau_{\text{turb}}$ :

$$\tau_{\text{turb}} = \tau + C_{\mu} \frac{k^2/\epsilon}{(1 + \eta^2)^{1/2}}, \quad (4.20)$$

where the term  $\eta$  is a constant based on the local strain parameter ( $k|S_{ij}/\epsilon|$ ), the local vorticity parameter ( $k|\Omega_{ij}/\epsilon|$ ), and local helicity parameters [16]; it allows for the mitigation of the sub-grid scale viscosity, so that the resolved large-scale structures are not numerically damped.

The relaxation time is then used to adapt the Boltzmann model to the characteristic time scales of a turbulent flow motion. Hence, the Reynolds stresses are not explicitly added to the governing equations, but they are an implicit consequence of the chaotic exchange of momentum driven by the turbulent flow, with characteristic times smaller than the slowly-varying turbulent flow. The Reynolds stresses have then a non-linear structure and are better suited to represent turbulence in a state far from equilibrium, as in the presence of distortion, shear, and rotation [13].

Therefore, in the LBM-VLES, the Reynolds stresses are not solved simultaneously with the flow governing equations, as they are in Navier-Stokes based formulations. For the latter, the turbulence model is used as a closure of the flow governing equations, given that the Reynolds stresses are unknown, whereas for the former, they are part of the solution [13]. Similarly as the macroscopic flow properties, such as velocity and pressure, the Reynolds stresses can be recovered through the computation of the moment around the particle distribution function [17].

Finally, a wall function is applied on the first voxel adjacent to a no-slip surface. This treatment is performed in order to avoid extensive mesh refinement near the wall to resolve the inner part of the boundary layer (e.g., viscous sublayer), whose thickness decreases with increasing Reynolds number. The wall function is based on the generalized law-of-the-wall model [18], extended to consider the effects of pressure gradient and surface roughness, expressed as:

$$u^+ = \frac{1}{K} \ln \left( \frac{y^+}{A} \right) + B, \quad (4.21)$$

$$A = 1 + g \left( \frac{dp}{ds} \right), \quad B = 5.0, \quad K = 0.41, \quad y^+ = \frac{u_{\tau} y}{\nu} \quad (4.21a-d)$$

where  $A$  is a function of the pressure gradient  $\frac{dp}{ds}$ .

The main advantage of using the LBM-VLES in this study, with respect to a Navier-Stokes formulation, is its inherent low dissipative and dispersive characteristic, which is necessary for the accurate prediction of acoustic perturbations that are usually orders of

magnitude lower than the characteristic pressure of a flow [19, 20]. An accurate prediction of acoustic wave propagation from source to the far field usually requires high order numerical schemes, but this can be achieved effectively with LBM, which is a third order scheme and less dissipative [20]. Moreover, the particle collision step in the solution process occurs locally at each node and it is independent of the others. This allows for an easy parallelisation of the computation, thus reducing the computational time and cost [19].

### 4.1.3. ACOUSTIC PREDICTIONS

From a compressible and time-dependent flow simulation, the acoustic field can be extracted directly by sampling the time history of radiated acoustic pressure. This is, however, computationally expensive since the spatial resolution in the domain must be sufficiently high to accurately resolve the acoustic waveform from the source until the observer location [21, 22]. Therefore, a hybrid method is applied for acoustic prediction, wherein the noise sources are computed in a relatively small region of the domain using the LBM-VLES, whereas beyond the source region (in the far field), the noise propagation is obtained from linear acoustic theory [23].

A hybrid method of sound prediction is the adoption of the acoustic analogy, such as that of Lighthill [24] and Curle [25], described in Chapter 2. As already mentioned, these formulations are mathematically exact and can be used to obtain the acoustic pressure in the far field, given the source characteristics. However, their application is limited to turbulent flows either free or bounded by an infinite surface [24, 25]. A more generic approach has been developed by Ffowcs-Williams and Hawkings (FW-H) [26]. Considering a source region, encompassed by a control surface  $S$ , whose points have a local normal direction  $\hat{n}$  and move with a velocity  $\mathbf{v}$ , while the fluid moves with velocity  $\mathbf{u}$ . The source region is also contained within a control volume  $V$ . The FW-H analogy is derived considering that the portion of the flow field inside the control surface can be replaced by a quiescent fluid and a distribution of sources on the surface. The FW-H equation is given by [26, 27]:

$$\square^2 [c_0^2(\rho - \rho_0)H(S)] = \frac{\partial}{\partial t} [Q\delta(S)] - \frac{\partial}{\partial x_i} [L_i\delta(S)] + \frac{\partial^2}{\partial x_i x_j} [T_{ij}H(S)], \quad (4.22)$$

with

$$Q = Q_i \hat{n}_i = [\rho_0 v_i + \rho(u_i - v_i)] \hat{n}_i, \quad (4.23)$$

$$L_i = L_{ij} \hat{n}_j = [P_{ij} + \rho u_i(u_j - v_j)] \hat{n}_j, \quad (4.24)$$

where  $\square^2 = \frac{1}{c_0^2} \frac{\partial^2}{\partial t^2} - \frac{\partial^2}{\partial x_i^2}$  is the d'Alembert operator, with  $c_0$  as the ambient speed of sound,  $\hat{n}$  is the versor at a given direction and  $\delta$  is the Kronecker delta function. Similarly to Lighthill's analogy, the left-hand side of Eq. (4.22) describes the acoustic wave propagation, whereas the right-hand side contains the noise sources. The first term is the thickness source term, which accounts for fluid displacement by the control surface, whereas the second one represents the unsteady forces exerted by the control surface onto the

surrounding fluid, also known as the loading source term [26]. Finally, the last term represents the contribution of the Lighthill stress tensor throughout the control volume. These sources are equivalent to acoustic monopoles, dipoles and quadrupoles, respectively. The Heaviside function  $H(S)$  restricts the validity of the equation to the surface boundary and the exterior.

The solution of the FW-H equation in the acoustic far-field can be obtained using the free-space Green's function, resulting in [26]:

$$\begin{aligned}
4\pi p' = & \frac{\partial}{\partial t} \int_{S=0} \left[ \frac{Q}{\mathbf{r}(1-M_r)} \right]_{t_r} dS \\
& - \frac{\partial}{\partial x_i} \int_{S=0} \left[ \frac{L_i}{\mathbf{r}(1-M_r)} \right]_{t_r} dS \\
& + \frac{\partial^2}{\partial x_i x_j} \int_{S>0} \left[ \frac{T_{ij}}{\mathbf{r}(1-M_r)} \right]_{t_r} dV,
\end{aligned} \tag{4.25}$$

where the sources are evaluated at the retarded time  $t_r$ .  $M_r$  is the projected source Mach number vector in the direction of the observer. Finally, the denominator in each source term accounts for the Doppler shift due to the relative motion between source and observer [26].

Approximations can be made to simplify the solution of Eq. (4.25). For example, at low Mach numbers, the quadrupole source term can be neglected with respect to the other two, since they are less efficient at radiating noise at this condition, as reported in Chapter 2. Moreover, if the control surface is considered to be solid, rigid and non-vibrating, the monopole source term can also be disregarded. As a result, only the dipoles on the solid surface are considered to be relevant sources in this case.

For turbulent jet flows, wherein the quadrupole terms are not negligible, the computation of the FW-H analogy can prove expensive due to the volumetric integral term [28]. A different approach has been proposed by di Francescantonio [29], wherein the FW-H analogy is computed using a permeable control surface. As a result, the quadrupole term in Eq. (4.25) is neglected by assuming that Lighthill's stress tensor is zero outside of the permeable surface [30]. The overall contribution from quadrupole sources is instead taken into account by equivalent monopoles and dipoles distributed along the permeable surface [29].

However, an inherent problem for this application is that the turbulent region of a jet extends considerably far from the nozzle exit, and thus in order to keep the feasibility of the computation, the surface integral is truncated at a distance of typically 25-30 diameters from the nozzle [31]. Moreover, in the region where the surface is closed, there is an unavoidable crossing of turbulence across it, which generates spurious noise that would be theoretically compensated by the volume term in the FW-H formulation [32]. Therefore, this violates the necessary assumptions for using a permeable FW-H surface.

A possible solution for this problem is to keep the downstream end of the permeable FW-H surface open. However, this leads to additional problems such as missing data necessary for noise computation at shallow downstream angles or even artificial spurious noise at low frequencies due to the truncation of the surface [31]. A more accepted solution is the definition of several, equally-spaced outflow disks (or end-caps)

at the downstream end of the FW-H surface and then averaging the information of all disks [31]. The basis of this procedure is the assumption of frozen turbulence convecting across the end-caps, generating a spurious signal in each of them, but with a specific time delay. Therefore, this time delay can be controlled in order to provide maximum destructive interference between the signals by defining a proper spacing and number of end-caps [32]. These parameters are also a function of the frequency range of the spurious noise (in terms of Strouhal number  $St_{\text{caps}}$ ), given by [32]:

$$\frac{U_c D_j}{2U_j L_{\text{caps}}} < St_{\text{caps}} < \frac{U_c D_j}{2U_j \Delta_{\text{caps}}}, \quad (4.26)$$

where  $U_c$  is the convective velocity of the eddies crossing the end-caps,  $D_j$  is the nozzle exit diameter,  $U_j$  is the nominal jet velocity,  $\Delta_{\text{caps}}$  is the distance between consecutive caps and  $L_{\text{caps}}$  is the distance between the first and last ones. The left and right inequalities in Eq. (4.26) define the minimum and maximum frequency for which the caps are effective, respectively [32]. Moreover, the acoustic signals of the sources of interest are not affected by this approach.

The numerical implementation of the FW-H analogy follows the formulation 1A derived by Farassat [33], wherein the spatial derivatives in Eq. (4.25) are converted into time derivatives, which are subsequently moved inside the integrals using the retarded time formulation [34]. Therefore, the temporal variation of the sources properties is used to estimate the thickness and loading noise components, also considering the possibility of a moving observer, which simplifies the computation to a large extent [33, 34].

This formulation is implemented in the time domain using a source-time dominant algorithm, wherein the current status of a source is projected at the observer time domain where the received signal is progressively built [35]. At each time-step and for each source element, the instant at which a disturbance from the source will reach the observer is calculated and referred to as advanced time. The signal is finally built up at the observer time domain through a summation over all the computed contributions. The advanced time solution is given by [35]:

$$t_{\text{adv}} = t + \frac{|\mathbf{r}(t)|}{c_0} \left[ \frac{M_{o,r}(t) + \sqrt{M_{o,r}^2(t) + (1 - M_o^2)}}{1 - M_o^2} \right], \quad (4.27)$$

where  $M_o$  is the observer Mach number and  $M_{o,r}$  is its projection towards the source direction. In this formulation, the Doppler effect may cause a mismatch between the discrete time-step at the source and observer time domains. To overcome this issue, a linear interpolation procedure is used to ensure the correspondence between both time domains. The main advantage of this formulation is that no iterative retarded time equations must be solved, and the noise acoustic prediction step can be processed in parallel to the flow field computation [35].

In addition, a frequency-domain formulation of the FW-H analogy is applied. This method is based on the one proposed by Lockard [36], extended to a three-dimensional flow field. It is theoretically consistent with the time-domain approach previously described, but Fourier transforms are realized on the FW-H source terms before propaga-

tion to the far-field [37]. This frequency-domain approach is applied for the computation of a cross-spectral matrix of microphones mounted in a phased array. This matrix is subsequently used in beamforming calculations for acoustic source localization. A more detailed description of the beamforming procedure is included in Section 4.2.2.

The described methodologies for both flow-field and acoustic computations are implemented in the commercial software Simulia PowerFLOW 6-2019. This software has been also used and validated for aero-engine aeroacoustic applications to predict fan broadband noise in subsonic [38, 39] and transonic conditions [40]. A validation study for the isolated SMC000 jet has been accomplished by van der Velden *et al.* [37], showing a very good agreement with experimental results. For an installed jet, computations have been performed by da Silva *et al.* [41]. The results, in terms of far-field noise spectra, also showed a good agreement with experimental data, indicating the capability of the solver to accurately predict JIN.

## 4.2. EXPERIMENTAL APPROACH

### 4.2.1. FLOW FIELD MEASUREMENTS

The flow-field measurement techniques utilized in this thesis are reported in this section. The first one consists in velocity measurements with a multihole probe. These probes usually comprise a central tube to measure the stagnation or total pressure and several downstream holes symmetrically placed to measure the static pressure, such as depicted in Fig. 4.1 [42]. For an incompressible flow, a differential measurement between the stagnation and static pressures (the latter considered as reference) yields the dynamic pressure, which can be used to calculate the flow velocity. It is also possible to apply this technique for compressible flows under the assumption that isentropic relations are valid. An appropriate transducer, usually a diaphragm, is selected based on the order of magnitude of the measurement [42].

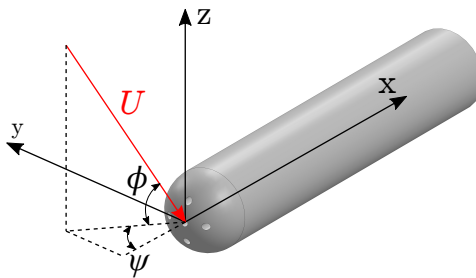


Figure 4.1: Multi-hole pressure probe, capable of determining the velocity magnitude and direction at a single point. Adapted from [42].

A multihole probe is sensitive to the three velocity components, in terms of the angles  $\phi$  and  $\psi$ , and thus the flow direction can be obtained. This is achieved via a calibration of pressure ratios between individual holes, which is a function of the local flow angle. However, this method becomes prohibitive when excessive angles are involved, in the order of  $30^\circ$  for five-hole probes [42]. While it is a simple and inexpensive technique,

multihole pressure probes are rather intrusive in the flow since they are commonly attached to bulky traverse systems and they usually only allow for steady measurements [42].

The second flow field measurement technique is hot-wire anemometry. This method is based on changes in heat transferred from a small sensor exposed to a flow. The sensor is usually a thin wire (diameter in the order of micrometers) made of a material whose electric resistivity depends on the temperature. The sensor is then heated through the application of an electrical current  $I$ , and cooled due to forced convection caused by the flow, as shown in the sketch in Fig. 4.2 [43].

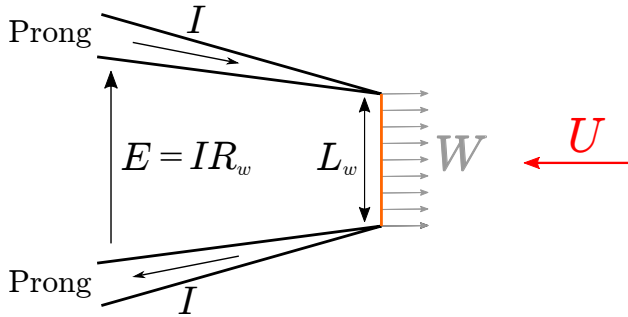


Figure 4.2: Sketch of a hot-wire anemometer (wire depicted in orange), mounted with prongs to measure the oncoming flow velocity  $U$ . Adapted from [43].

The constant temperature anemometry (CTA) method is used, wherein the temperature, and consequently the resistance of the sensor  $R_w$ , is maintained constant throughout the measurement. The sensor is placed in one arm of a Wheatstone bridge; when there is a change in the flow speed  $U$ , and consequently in the amount of heat lost due to convection  $W$ , the voltage difference across the bridge is a measure of the change in wire resistance. This voltage difference is fed to an operational amplifier, which has a current output as feedback to the top of the bridge in order to restore the probe resistance. The amplified voltage constitutes the measurable signal, which can be used to obtain the flow velocity by means of a calibration curve [43].

Hot-wire anemometry is particularly useful for investigations on turbulent flows, since it allows for the measurement of velocity fluctuations in the time domain with considerable temporal resolution and in a wide range of temporal scales. Due to the small size of the wire, the method has a good spatial resolution and it is capable of detecting turbulent fluctuations with a large dynamic response at relatively high frequency. However, similarly as with the multihole probe, large traversing devices are usually necessary to map the flow field and thus the instrumentation can become intrusive in the flow [42].

The last applied flow field measurement technique is Particle Image Velocimetry (PIV). PIV is a method for measuring the velocity of a flow field through the displacement of tracer particles that are carried by the fluid during a short time interval [42]. The tracer particles are sufficiently small so that they accurately follow the fluid motion and do not alter the fluid properties or flow characteristics [42]. They are then illuminated by means of a thin light sheet generated from a pulsed light source (usually a double-head

pulsed laser system), and the light scattered by them is recorded onto two subsequent image frames by a digital imaging device such as a camera [42]. The flow velocity field is then obtained from consecutive image pairs by knowing the magnification, the particle displacement and the time delay [43].

A typical PIV set-up, such as the one shown in Fig. 4.3, is comprised by the light source, lenses, one or more cameras, an acquisition hardware and an imaging processing software.

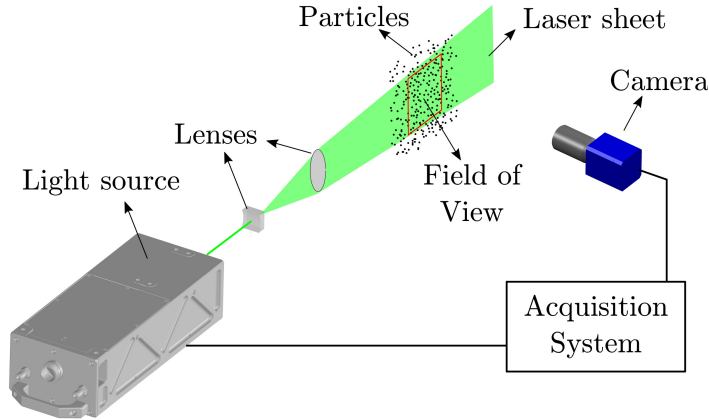


Figure 4.3: Sketch of a typical PIV set-up. Adapted from [42].

A Quantel Evergreen Nd:YAG (15 Hz, 200 mJ/pulse, 532 nm wavelength) laser is used as light source in the PIV experiments. The images are recorded with Complementary Metal–Oxide–Semiconductor (CMOS) cameras with 4 MP resolution. A lens is also attached to the camera, characterized by its focal length  $f$ , aperture number  $f\#$  (focal length divided by the aperture diameter), and the image magnification  $M_0$ , defined as the ratio of the distance between lens and image ( $Z_0$ ) and the distance between lens and object ( $z_0$ ) [42]. Before performing the flow measurements, it is necessary to acquire images that can be used to determine the physical location and size of the camera field of view as calibration. This is performed with a calibration plate, which contains a grid with evenly spaced points, and a pinhole model [43].

A cross-correlation analysis of the particle-image patterns in the interrogation windows is performed between each pair of images in order to determine the particle displacement, given by the location of the largest peak in the correlation plane [43]. Once this has been found, the displacement value is divided by the image magnification and the time delay between the images to yield the local flow velocity. This process is then repeated for the entire image domain, which provides the instantaneous velocity in a planar cross section of the observed flow [42]. A subpixel level estimation is performed using a three-point Gaussian fit, wherein the peak location is obtained by interpolation of the correlation values around the maximum [42].

It is only possible to identify the correct displacement peak when its amplitude is much larger than the highest random one. The ratio between these two peaks can be considered as the lower limit of the signal-to-noise ratio [42]. The probability of identi-

finding the correct peak in the cross-correlation procedure can be defined as the product of several parameters, namely the image density  $N_I$ , the loss of correlation due to in-plane and out-of-plane particle motion ( $F_I$  and  $F_O$ , respectively) and loss of correlation in dimensions smaller than the interrogation window  $F_\Delta$  [42, 43].

The accuracy of the cross-correlation step can be augmented by making use of iterative schemes. One of them is known as window deformation, implemented as a two-step analysis, in a predictor-corrector loop, where the interrogation is repeated a second time with a shifted window obtained from the first pass [44]. A second iterative scheme is the multigrid approach, wherein the correlation process is repeated several times with the interrogation window size progressively decreased [42, 45]. This approach is particularly useful to reduce losses due to in-plane motion.

After the cross-correlation step, incorrect vectors are filtered out using the Universal Outlier Detection method [46]. The filtering of these incorrect vectors is performed based on the principle that the measured displacements at each location should be statistically similar to the adjacent vectors [46]. The discarded vectors are then replaced by interpolation based on adjacent data. Additionally, sources of uncertainty in the measurements include errors in the calibration of the camera-lens system, timing errors in the recording of the images or the laser pulse sequences, and errors in the determination of displacement and velocity fields from particle fields [43]. The uncertainty levels are estimated through the correlation statistics method, which provides the uncertainty of a PIV displacement field by projecting the particles from one point to another with the obtained vectors and checking the resultant disparity [47].

In this thesis, the illumination and image acquisition are triggered synchronously by the LaVision DaVis 8.4 software, which is also used for the post-processing of the images.

### 4.2.2. ACOUSTIC MEASUREMENTS

Acoustic measurements are carried out using condenser microphones, which contain a metallic diaphragm connected to a capacitor, forming one plate of the electrical condenser [43]. The diaphragm deforms due to pressure fluctuations (sound waves), thereby changing the electrical capacitance, which is recorded as a voltage signal [48]. The measurements are performed in a differential manner with respect to the current ambient pressure due to a capillary aperture connecting the internal side of the membrane to the exterior [43]. The calibration of a condenser microphone is performed with a pistonphone, wherein a sinusoidal signal at a prescribed amplitude and frequency is generated and measured by the microphone, providing the sensitivity (usually in the order of mV/Pa).

In terms of facilities, the experiments are performed in both open and closed test section wind tunnels. The former is comprised by an open jet built in an anechoic room, which contains sound absorbing material on the walls in order to avoid reflections that can contaminate the measurements and provide inaccurate results. In an anechoic chamber, acoustic measurements are performed directly with microphones positioned at the desired observer location. In order to measure sound directivity, for example, several microphones are mounted in a circular arc, centered at the source of interest.

On the other hand, for a closed-section wind tunnel, the microphones have to be mounted in the walls. In order to avoid that the membrane is exposed to the flow, which

leads to significant spurious noise due to the boundary layer, the microphones are recessed within the wall [48]. However, the cavity formed between the wall and the microphone can still act as a wave guide or generate additional noise. Therefore, a porous membrane made of Kevlar is applied over the cavity in order to keep out the flow, but still allow for acoustic waves to reach the microphone, as shown in the sketch in Fig. 4.4. Moreover, by applying signal processing techniques, such as a cross-correlation between the measured signals of several microphones, the wall boundary-layer noise can be attenuated since it is not well correlated over the entire surface of the array [48].

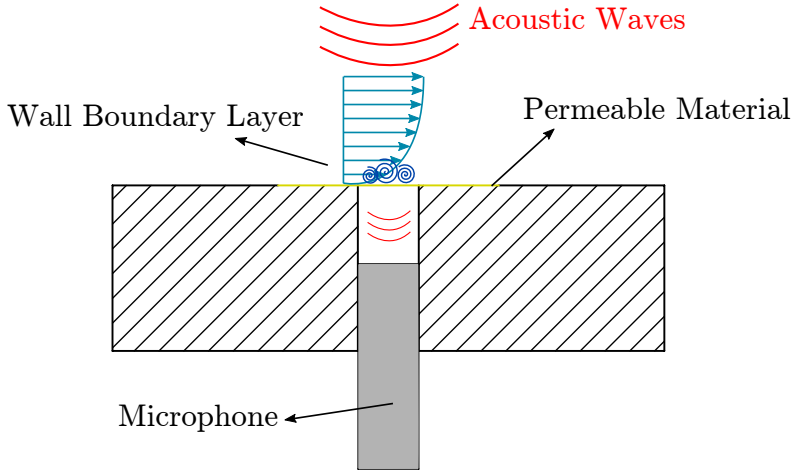


Figure 4.4: Sketch representing the concept behind acoustic measurements with a recessed microphone with a permeable material covering the cavity. The fluctuations in the wall boundary layer are not able to reach the microphone, unlike the acoustic waves from the source of interest.

Finally, phased array measurements can be performed in conjunction with processing algorithms for acoustic source localization, such as beamforming. The main principle of this technique is to apply time delays to the signals recorded by each individual microphone (or phase shifts in the frequency domain) to focus the array at a specific point in space, assuming spherical wave propagation, thereby measuring the apparent source strength distribution [48]. This is particularly useful for measurements in closed-section, reverberant wind tunnels in order to restrict the analysis to the desired (or expected) source region and mitigate external ones, including image sources reflected on the walls, as well as increase the dynamic range of the measurement [48].

The beamforming process is performed using the microphone recorded data, under the assumption of a specific source model, and usually in the frequency domain [49]. Considering an array with  $N$  microphones, each one located at  $\mathbf{x}_n$ , a Cross-Spectral Matrix (CSM)  $\mathbf{C}$  of order  $N \times N$  is created by computing the cross-spectrum of the pressure amplitudes of each microphone with the remaining ones, for each frequency [49]. Details of cross-spectral analysis are given in Appendix A. The main diagonal of this matrix represents the pressure auto-spectra of each microphone. For measurements performed in a closed-section wind tunnel, the wall boundary-layer noise is incoherent between

microphones and thus it appears only in the auto-spectra. Therefore, by discarding the main diagonal of the CSM prior to the beamforming, the undesired boundary-layer noise can be mitigated [49].

The source description is included in the steering vector  $\mathbf{g}$ , wherein each component is the pressure amplitude of an assumed source formulation, with a unit strength, at the microphone locations [49, 50]. A typical assumption is a monopole point source with uniform directivity and located at the position  $\boldsymbol{\xi}$  in a specified scan plane. For this case, the steering vector formulation is given by [49]:

$$\mathbf{g}_n = \frac{e^{-i2\pi f \Delta t_n}}{4\pi r_n}, \quad (4.28)$$

where  $i = \sqrt{-1}$ ,  $f$  is the frequency,  $\Delta t_n$  is the emission time delay, which is computed for an acoustic wave traveling from the evaluated scan grid point up to each microphone, and  $r_n$  is the distance between these two points. For a wind tunnel test with uniform flow at Mach number  $M$ , the distance between the scan point and microphone needs to be corrected for convective effects, given by [49]:

$$r_n = \sqrt{(M \cdot (\mathbf{x}_n - \boldsymbol{\xi}))^2 + \beta^2 \|\mathbf{x}_n - \boldsymbol{\xi}\|^2}, \quad (4.29)$$

where  $\beta$  is the Prandtl–Glauert factor ( $\beta = \sqrt{1 - \|M\|^2}$ ), and the operator  $\|\cdot\|$  is the Euclidean norm [49]. Therefore, the time delay  $\Delta t_n$  is given by [49]:

$$\Delta t_n = \frac{1}{c_0 \beta^2} (-M \cdot (\mathbf{x}_n - \boldsymbol{\xi}) + r_n). \quad (4.30)$$

The source auto-power at each scan point is computed by minimizing the difference between the measured pressure amplitude and the steering vector at that point, given by [49]:

$$B = \mathbf{w}^* \mathbf{C} \mathbf{w}, \quad (4.31)$$

where  $\mathbf{w}$  is the weighted steering vector [49]:

$$\mathbf{w} = \frac{\mathbf{g}}{\|\mathbf{g}\|^2}, \quad (4.32)$$

and the operator  $(\cdot)^*$  denotes the complex conjugate transpose. Eq. (4.31) is known as Conventional Beamforming [49]. By calculating the auto-power at each scan point, a source map is obtained, such as the one shown in Fig. 4.5 [51], for each computed frequency.

In a beamforming map, even though a point monopole model is assumed, the resulting source has always a certain width. The beamwidth is usually defined considering the space between the peak source level and a point where it decreases by 3 dB. This parameter also corresponds to the array resolution since it determines the ability of the array to locate and resolve closely spaced sources [48]. The array resolution can be estimated through the Rayleigh limit, which provides the minimum distance that two distinct sources can be solved, given by [52]:

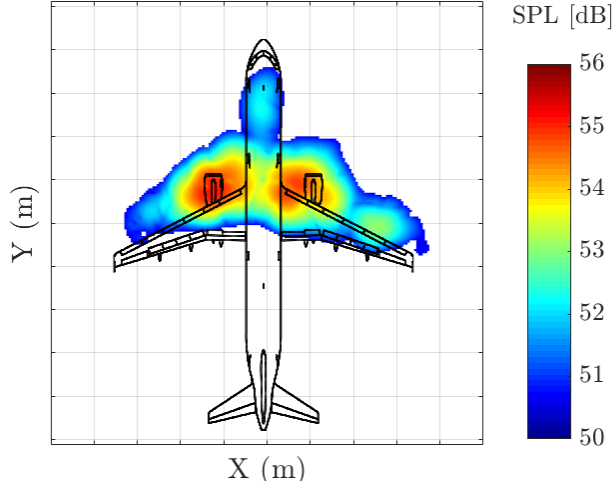


Figure 4.5: Beamforming source map on an aircraft model. Adapted from [51].

$$R_a = h_a \tan\left(1.22 \frac{c_0}{f D_a}\right), \quad (4.33)$$

where  $h_a$  is the distance between the array and scan plane,  $f$  is the frequency and  $D_a$  is the array diameter (aperture). Therefore, Eq. (4.33) shows that the array resolution is higher when the microphones are placed closer to the source, or if the array diameter is larger.

Another important feature in a beamforming map is the presence of sidelobes, which represent energy from sources in directions other than the one where the array is being focused [48]. These secondary sources are usually much weaker than the main lobe, and their relative strength is a measure of the array effective dynamic range [48]. The existence and strength of sidelobes is also dependent on the array characteristics; they can usually be mitigated by decreasing the space between microphones, which reduces spatial aliasing, and removing periodicities in their locations [48]. From this requirement, multi-arm spiral arrays are used in this thesis; they provide efficient sidelobe suppression over a wide range of frequencies, while maintaining a relatively large aperture for higher resolution [52, 53].

Aside from the source location, absolute sound pressure levels are obtained by applying the Source Power Integration technique, wherein the source auto-powers, obtained from beamforming in all points of the scan grid, are summed [54]. In order to increase the stability and accuracy of the method, only positive source powers higher than a certain threshold, defined with respect to the peak levels, are considered [49]. This reduces the contribution of sidelobes in the overall sound levels. It should be noted, however, that a simple sum of the auto powers provides an incorrect value due to the beamwidth. Therefore, it is necessary to normalize the integral with the array Point Spread Function (PSF), which corresponds to the array response to a point source at a given frequency, and it is given by [48]:

$$\text{PSF} = |\mathbf{w}^*(\boldsymbol{\xi})\mathbf{w}(\boldsymbol{\xi}_s)|^2, \quad (4.34)$$

where  $\mathbf{w}^*(\boldsymbol{\xi})$  is the complex conjugate weighted steering vector at the specified grid point  $\boldsymbol{\xi}$ , whereas  $\mathbf{w}(\boldsymbol{\xi}_s)$  is the weighted steering vector, considering a virtual unitary point source at the center of the integration region ( $\boldsymbol{\xi}_s$ ). By dividing the integrated sound powers with the PSF at each frequency, the beamwidth effects are removed and the correct noise amplitude is obtained [48].

## REFERENCES

- [1] S. Succi, *The lattice Boltzmann equation for fluid dynamics and beyond* (Oxford University Press, New York, NY, USA, 2001).
- [2] S. Chapman and T. G. Cowling, *The Mathematical Theory of Non-uniform Gases*, 1st ed. (Cambridge Mathematical Library, 1991).
- [3] P. L. Bhatnagar, E. P. Gross, and M. Krook, *A Model for Collision Processes in Gases. I. Small Amplitude Processes in Charged and Neutral One-Component Systems*, [Physical Review](#) **94**, 511 (1954).
- [4] H. Chen, S. Chen, and W. H. Matthaeus, *Recovery of the Navier-Stokes equations using a lattice-gas Boltzmann method*, [Physical Review A](#) **45** (1992).
- [5] X. Shan, X. Yuan, and H. Chen, *Kinetic theory representation of hydrodynamics: A way beyond the Navier-Stokes equation*, [Journal of Fluid Mechanics](#) **550**, 413 (2006).
- [6] H. Grad, *Note on N-dimensional hermite polynomials*, [Communications on Pure and Applied Mathematics](#) **2** (1949), [10.1002/cpa.3160020402](https://doi.org/10.1002/cpa.3160020402).
- [7] H. Chen, I. Goldhirsch, and S. A. Orszag, *Discrete Rotational Symmetry, Moment Isotropy, and Higher Order Lattice Boltzmann Models*, [Journal of Scientific Computing](#) **34** (2008), [10.1007/s10915-007-9159-3](https://doi.org/10.1007/s10915-007-9159-3).
- [8] X. He and L.-S. Luo, *Theory of the lattice Boltzmann method: From the Boltzmann equation to the lattice Boltzmann equation*, [Physical Review E](#) **56** (1997), [10.1103/PhysRevE.56.6811](https://doi.org/10.1103/PhysRevE.56.6811).
- [9] H. Chen, P. Gopalakrishnan, and R. Zhang, *Recovery of Galilean Invariance in Thermal Lattice Boltzmann Models for Arbitrary Prandtl Number*, [International Journal of Modern Physics C](#) **25** (2014), [10.1142/S0129183114500466](https://doi.org/10.1142/S0129183114500466).
- [10] H. Chen, C. Teixeira, and K. Molvig, *Realization of Fluid Boundary Conditions via Discrete Boltzmann Dynamics*, [International Journal of Modern Physics C](#) **09** (1998), [10.1142/S0129183198001151](https://doi.org/10.1142/S0129183198001151).
- [11] H. Chen, O. Filippova, J. Hoch, K. Molvig, R. Shock, C. Teixeira, and R. Zhang, *Grid refinement in lattice Boltzmann methods based on volumetric formulation*, [Physica A: Statistical Mechanics and its Applications](#) **362** (2006), [10.1016/j.physa.2005.09.036](https://doi.org/10.1016/j.physa.2005.09.036).

- 
- [12] H. Chen, *Volumetric formulation of the lattice Boltzmann method for fluid dynamics: Basic concept*, *Phys. Rev. E* **58** (1998).
- [13] H. Chen, S. A. Orszag, I. Staroselsky, and S. Succi, *Expanded analogy between Boltzmann kinetic theory of fluids and turbulence*, *Journal of Fluid Mechanics* **519**, 301 (2004).
- [14] R. Rubinstein and J. M. Barton, *Nonlinear Reynolds stress models and the renormalization group*, *Physics of Fluids A: Fluid Dynamics* **2** (1990), 10.1063/1.857595.
- [15] V. Yakhot and S. A. Orszag, *Renormalization group analysis of turbulence. I. Basic theory*, *Journal of Scientific Computing* **1**, 3 (1986).
- [16] V. Yakhot, S. A. Orszag, S. Thangam, T. B. Gatski, and C. G. Speziale, *Development of turbulence models for shear flows by a double expansion technique*, *Physics of Fluids A: Fluid Dynamics* (1992), 10.1063/1.858424.
- [17] P. Lew, L. Mongeau, and A. Lyrintzis, *Noise prediction of a subsonic turbulent round jet using the lattice-Boltzmann method*, *The Journal of the Acoustical Society of America* **128**, 1118 (2010).
- [18] B. E. Launder and D. B. Spalding, *The Numerical Computation of Turbulent Flows*, *Computer Methods in Applied Mechanics and Engineering* **3**, 269 (1974).
- [19] G. Brès, F. Pérot, and D. Freed, *Properties of the Lattice Boltzmann Method for Acoustics*, in *15th AIAA/CEAS Aeroacoustics Conference* (Miami, FL, USA, 2009).
- [20] S. Marié, D. Ricot, and P. Sagaut, *Comparison between lattice Boltzmann method and Navier-Stokes high order schemes for computational aeroacoustics*, *Journal of Computational Physics* **228**, 1056 (2009).
- [21] C. K. W. Tam, *Computational aeroacoustics - Issues and methods*, *AIAA Journal* **33** (1995), 10.2514/3.12728.
- [22] C. K. Tam, *Computational Aeroacoustics: An Overview of Computational Challenges and Applications*, *International Journal of Computational Fluid Dynamics* **18** (2004), 10.1080/10618560410001673551.
- [23] S. Glegg and W. Devenport, *Aeroacoustics of Low Mach Number Flows*, 1st ed. (Academic Press, 2017).
- [24] M. J. Lighthill, *On Sound Generated Aerodynamically I. General Theory*, *Proceedings of the Royal Society of London. Series A. Mathematical and Physical Sciences* **211**, 564 (1952).
- [25] N. Curle, *The influence of solid boundaries upon aerodynamic sound*, in *Proceedings of the Royal Society A* **231** (1955) pp. 505–514.
- [26] J. E. Ffowcs-Williams and D. L. Hawkings, *Sound Generation by Turbulence and Surfaces in Arbitrary Motion*, *Philosophical Transactions of the Royal Society A: Mathematical, Physical and Engineering Sciences* **264**, 321 (1969).

- [27] G. Brès, F. Pérot, and D. Freed, *A Ffowcs Williams - Hawkings Solver for Lattice-Boltzmann Based Computational Aeroacoustics*, in *16th AIAA/CEAS Aeroacoustics Conference* (Stockholm, Sweden, 2010).
- [28] P. R. Spalart and M. L. Shur, *Variants of the Ffowcs Williams-Hawkings equation and their coupling with simulations of hot jets*, *International Journal of Aeroacoustics* **8**, 477 (2009).
- [29] P. di Francescantonio, *A New Boundary Integral Formulation for the Prediction of Sound Radiation*, *Journal of Sound and Vibration* **202**, 491 (1997).
- [30] K. S. Brentner and F. Farassat, *Analytical Comparison of the Acoustic Analogy and Kirchhoff Formulation for Moving Surfaces*, *AIAA Journal* **36** (1998), 10.2514/2.558.
- [31] M. L. Shur, P. R. Spalart, and M. K. Strelets, *Noise prediction for increasingly complex jets. Part I: Methods and tests*, *International Journal of Aeroacoustics* **4**, 213 (2005).
- [32] S. Mendez, M. Shoebybi, S. K. Lele, and P. Moin, *On the use of the Ffowcs Williams-Hawkings equation to predict far-field jet noise from large-eddy simulations*, *International Journal of Aeroacoustics* **12**, 1 (2013).
- [33] F. Farassat, *Derivation of Formulations 1 and 1A of Farassat*, Tech. Rep. (NASA/TM-2007-214853, 2007).
- [34] F. Farassat and G. P. Succi, *A review of propeller discrete frequency noise prediction technology with emphasis on two current methods for time domain calculations*, *Journal of Sound and Vibration* **71**, 399 (1980).
- [35] D. Casalino, *An advanced time approach for acoustic analogy predictions*, *Journal of Sound and Vibration* **261**, 583–612 (2003).
- [36] D. P. Lockard, *An efficient, two-dimensional implementation of the Ffowcs Williams and Hawkings equation*, *Journal of Sound and Vibration* **229**, 897 (2000).
- [37] W. C. P. van der Velden, D. Casalino, P. Gopalakrishnan, A. Jammalamadaka, Y. Li, R. Zhang, and H. Chen, *Jet Noise Prediction : Validation and Physical Insight*, in *24th AIAA/CEAS Aeroacoustics Conference* (Atlanta, GA, USA, 2018) pp. 1–16.
- [38] D. Casalino, A. Hazir, and A. Mann, *Turbofan Broadband Noise Prediction Using the Lattice Boltzmann Method*, *AIAA Journal* **56**, 609 (2017).
- [39] D. Casalino, F. Avallone, I. Gonzalez-Martino, and D. Ragni, *Aeroacoustic study of a wavy stator leading edge in a realistic fan/OGV stage*, *Journal of Sound and Vibration* **442**, 138 (2019).
- [40] I. Gonzalez-Martino and D. Casalino, *Fan Tonal and Broadband Noise Simulations at Transonic Operating Conditions Using Lattice-Boltzmann Methods*, in *2018 AIAA/CEAS Aeroacoustics Conference* (Atlanta, GA, USA, 2018).

- 
- [41] F. D. da Silva, C. J. Deschamps, A. R. da Silva, and L. G. C. Simões, *Assessment of Jet-Plate Interaction Noise Using the Lattice Boltzmann Method*, in *21st AIAA/CEAS Aeroacoustics Conference* (Dallas, TX, USA, 2015).
- [42] C. Tropea, J. F. Foss, and A. Yarin, *Handbook of Experimental Fluid Mechanics*, 1st ed. (Springer, 2007).
- [43] S. Discetti and A. Ianiro, *Experimental Aerodynamics*, 1st ed. (Taylor & Francis Group, 2017).
- [44] F. Scarano, *Iterative image deformation methods in PIV*, *Measurement Science and Technology* **13** (2001).
- [45] F. Scarano and M. L. Riethmuller, *Advances in iterative multigrid PIV image processing*, *Experiments in Fluids* **29**, S051 (2000).
- [46] J. Westerweel and F. Scarano, *Universal outlier detection for PIV data*, *Experiments in Fluids* **39**, 1096 (2005).
- [47] B. Wieneke, *PIV uncertainty quantification from correlation statistics*, *Measurement Science and Technology* **26** (2015), 10.1088/0957-0233/26/7/074002.
- [48] T. J. Mueller, *Aeroacoustic Measurements*, 1st ed. (Springer-Verlag, Berlin, Germany, 2002).
- [49] P. Sijtsma, *Phased array beamforming applied to wind tunnel and fly-over tests*, Tech. Rep. (National Aerospace Laboratory (NLR), Amsterdam, The Netherlands, 2010).
- [50] E. Sarradj, *Three-Dimensional Acoustic Source Mapping with Different Beamforming Steering Vector Formulations*, *Advances in Acoustics and Vibration* **2012** (2012), 10.1155/2012/292695.
- [51] M. Snellen, R. Merino-Martínez, and D. G. Simons, *Assessment of Noise Variability of Landing Aircraft Using Phased Microphone Array*, *Journal of Aircraft* **54** (2017), 10.2514/1.C033950.
- [52] S. Luesutthiviboon, A. Malgoezar, M. Snellen, P. Sijtsma, and D. Simons, *Improving source discrimination performance by using an optimized acoustic array and adaptive high-resolution CLEAN-SC beamforming*, in *7th Berlin Beamforming Conference* (Berlin, Germany, 2018).
- [53] J. R. Underbrink and R. P. Dougherty, *Array design for non-intrusive measurement of noise sources*, in *Noise-Con 96* (1996) pp. 757–762.
- [54] T. F. Brooks and W. M. Humphreys, *Effect of directional array size on the measurement of airframe noise components*, in *5th AIAA/CEAS Aeroacoustics Conference and Exhibit* (American Institute of Aeronautics and Astronautics Inc, AIAA, Bellevue, WA, USA, 1999).

# 5

## JET-INSTALLATION NOISE AND NEAR-FIELD CHARACTERISTICS OF JET-SURFACE INTERACTION

*Research is what I am doing when I do not know what I am doing.*

Wernher von Braun

*In this chapter, the link between jet-installation noise and the near-field flow features of the isolated jet is studied. The configuration is comprised by a subsonic jet and a nearby flat plate placed outside the rotational flow region. It is shown that the Helmholtz number, based on the wavelength of eddies in the mixing layer and their distance to the plate trailing edge, predicts the frequency range where installation noise occurs. Additionally, the linear hydrodynamic field of the isolated jet shows an exponential decay of pressure fluctuations in the radial direction; it is shown that far-field spectra follows the same trend when moving the plate in this direction. In the axial direction, spectral proper orthogonal decomposition is applied to filter out jet acoustic waves. The resultant hydrodynamic pressure fluctuations display a wavepacket behaviour, which is fitted with a Gaussian envelope. It is found that installation noise for different plate lengths is proportional to the amplitude of the Gaussian curve at the position of the plate trailing edge.*

---

Parts of this chapter have been included in Reference [1].

## 5.1. OBJECTIVES

THE goal of the analyses in this chapter is to link the near-field properties of an isolated jet, focusing on the pressure fluctuations in the mixing layer, and the far-field noise of a jet installed with a flat plate. Initially, the frequency range where noise amplification due to edge scattering occurs is determined by applying the compactness inequalities defined by Ffowcs-Williams and Hall [2] in terms of the Helmholtz number  $kr_0$ , where  $k$  is the wavenumber and  $r_0$  is the distance between the center of the source and the trailing edge. For that purpose, the turbulent jet flow is represented by an appropriate equivalent source, which is determined following the approach reported by Arndt *et al.* [3]. This approach uses the amplitude decay of the near-pressure field to determine an approximate location for a single equivalent source responsible for that particular decay, at a given wavenumber. This methodology is described in more detail in Section 5.5.

For the amplitude of the installed jet spectra, the characteristics of the irrotational hydrodynamic field are used to link the convection and development of pressure waves from the jet to the installed far-field noise for different surface heights and lengths. For the former, the far-field spectra are scaled according to the exponential decay of evanescent pressure fluctuations in the radial direction of the jet. For the latter, the initial hypothesis is that the far-field noise amplification trends in the axial direction are dependent on the growth-saturation-decay, characteristic of instability waves in the jet mixing layer [4]. Therefore, by modelling this wavepacket behaviour with a Gaussian envelope, it should be possible to scale JIN for different surface lengths.

However, as reported in Chapter 2, the decay region of the Gaussian curve can be contaminated by acoustic waves and a proper scaling cannot be performed. In order to characterize the development of coherent turbulent structures in the mixing layer, and filter out the contribution from the jet acoustic waves, the Spectral Proper Orthogonal Decomposition (SPOD) technique is applied [3, 5, 6]. The SPOD decomposes a time series of an unsteady flow property into a sequence of frequency-dependent modes [7, 8]. When applied to a pressure time series from the jet flow, the resulting streamwise eigenfunctions show a characteristic growth, saturation and decay of pressure fluctuations, which agrees with the behaviour of instability waves or wavepackets [4, 9].

In this chapter, the characteristics of the jet hydrodynamic pressure fluctuations are thus investigated in both radial and axial directions, and the trends are used as scaling parameters for the spectra obtained for different surface positions and lengths, as reported in Section 5.6.

## 5.2. COMPUTATIONAL SET-UP

This study is carried out numerically with LBM-VLES. The installed jet model replicates the one of the NASA Glenn benchmark experiments [10, 11], where a flat plate is placed in the vicinity of a single-stream jet nozzle (SMC000). The SMC000 is a round, convergent nozzle with an exit diameter  $D_j = 50.8$  mm, used for studies on subsonic jets [12]. The primary convergent nozzle has a 152 mm diameter inlet, followed by a contraction with a  $5^\circ$  taper angle up to the exit plane.

Different geometric configurations are investigated, for which the length and height

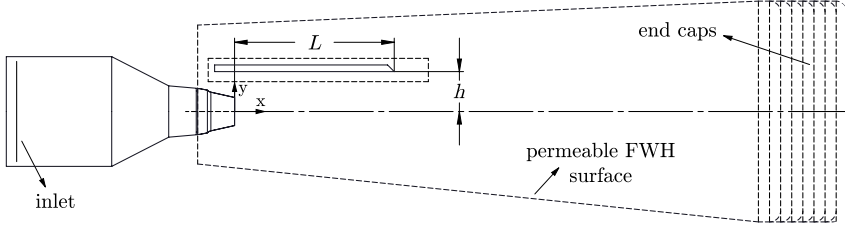


Figure 5.1: Schematic of the computational set-up, with the flat plate length  $L$  and height  $h$ . A permeable FW-H surface encompasses the jet and the flat plate. Caps are placed at the downstream end of the surface, and cut-outs are placed in the regions of the plate and nozzle.

of the plate are varied. As shown in Fig. 5.1, the length  $L$  is defined as the distance between the plate trailing edge and the nozzle exit plane, and the height  $h$  as the radial position of the plate with respect to the jet centerline. The simulated cases are listed in Table 5.1, marked with an X. For a given flat plate length, the minimum radial position is determined based on a jet spreading angle of  $7^\circ$  [12] to avoid grazing flow on the surface. The plate is 12.7 mm thick and it has a chamfer angle of  $40^\circ$  at the trailing edge. It extends  $0.75D_j$  upstream of the nozzle exit plane to avoid scattering effects at the leading edge. In the spanwise direction, the plate has a width of  $36D_j$  to avoid side-edge scattering.

	$h = 1.0D_j$	$h = 1.25D_j$	$h = 1.5D_j$
$L = 4D_j$	X	X	X
$L = 5D_j$	-	X	X
$L = 6D_j$	-	X	X

Table 5.1: Investigated geometric cases, based on the flat plate length  $L$  and height  $h$ .

The simulated flow conditions are based on setpoints 01, 03 and 06 from the NASA wind tunnel experiments [12]. All setpoints are characterized by subsonic jets with different acoustic Mach numbers ( $M_a = U_j/c_\infty$ ). The jet flow characteristics are included in Table 5.2, such as the Nozzle Pressure Ratio (NPR), the temperature ratio  $T_R$  (ratio between the jet and ambient static temperatures) and the Reynolds number  $Re$ , based on the nozzle exit diameter. Static flow parameters, such as ambient pressure and temperature, are taken from the work of Brown and Bridges [12].

The jet and the flat plate are placed in an almost quiescent domain, i.e. with a speed equal to 1% of the jet exit velocity, at ambient pressure. This free-stream condition is added to avoid that eddies escaping the jet shear layer are trapped in the domain and do not dissipate, allowing the solver to operate and converge faster. This free-stream speed is considered negligible compared to the jet velocity, thus it does not alter the far-field noise. To generate the jet flow, an additional inlet boundary condition is placed  $8D_j$  upstream of the nozzle exit plane (Fig. 5.1), with the physical parameters taken from experimental data (Table 5.2). A zig-zag trip, with a thickness of  $1\text{ mm}$  ( $0.02D_j$ )

Setpoint	NPR [-]	$T_R$ [-]	$M_a$ [-]	$Re$ [ $10^5$ ]
01	1.090	0.98	0.35	4.14
03	1.196	0.95	0.50	5.92
06	1.617	0.87	0.80	9.47

Table 5.2: Jet flow conditions for setpoints 01, 03 and 06 based on Nozzle Pressure Ratio (NPR), acoustic Mach number  $M_a$  and Reynolds number  $Re$ .

and spacing of  $1.62 \text{ mm}$  ( $0.03D_j$ ), is added inside the nozzle,  $1.5D_j$  upstream of the exit plane, to force a fully turbulent boundary layer. This nozzle set-up was validated for the isolated jet case by van der Velden *et al.* [13]. The same strategy is adopted in this work for the installed case.

The main components of the set-up are shown in Fig. 5.1. A permeable Ffowcs Williams-Hawkings (FW-H) surface, represented by dashed lines, is used for the far-field noise computations. Its shape and dimensions are chosen such that the same surface can be used for all studied configurations. A length of  $22D_j$  downstream of the nozzle exit plane and a width of  $10D_j$  are used for the permeable surface to include all the sources of noise relevant for the current investigation.

Spurious effects due to hydrodynamic pressure fluctuations occurring on the FW-H are avoided by placing cutouts at the nozzle and flat plate regions. Additional sources caused by the jet crossing the downstream end of the FW-H are mitigated by placing 7 outflow surfaces (or end-caps) at that region (Fig 5.1). The far-field pressure signals obtained from each cap (located at different streamwise positions) are averaged, so that the spurious noise produced by the eddies crossing the permeable surface can be removed from the final far-field spectra [14].

Acoustic sponges, which consist of regions of increased viscosity, are added to the set-up in order to prevent wave reflection at solid boundaries and at the walls of the computational domain [15]. Inside the nozzle, the sponge extends from the inlet plane up to  $3.8D_j$  upstream of the exit plane. A spherical sponge with a diameter  $130D_j$ , centered at the nozzle exit plane and encompassing the entire geometry, is also added. A progressive coarsening of the grid towards the boundaries also contributes to the dampening of reflected acoustic waves.

The physical time of the simulations is divided into an initial transient, consisting of 10 flow passes through the FW-H surface, and an acquisition time of 13 flow passes (total simulation time of 23 flow passes). The latter is defined based on the minimum output frequency to be analyzed (defined as  $St = 0.04$ ), and the number of spectral averages (defined as 20), for an overlap coefficient of 0.5 in the Fast Fourier Transform (FFT) computation. For the finest grid resolution investigated, the physical time step is  $1.5 \times 10^{-7}$  s for all setpoints, and the unsteady pressure on the FW-H surface is sampled with a frequency of 120 kHz. The resultant physical simulation time and acquisition parameters are shown in Table 5.3. The frequency resolution refers to the frequency band obtained from the Fast Fourier Transform of the computed acoustic signals, based on the acquisition time and the selected number of averages.

Setpoint	Physical Simulation	FW-H Acquisition	Frequency Resolution
	Time [s]	Time [s]	[Hz]
01	0.221	0.16	63
03	0.198	0.11	91
06	0.081	0.07	143

Table 5.3: Simulation physical time and acquisition parameters for each setpoint.

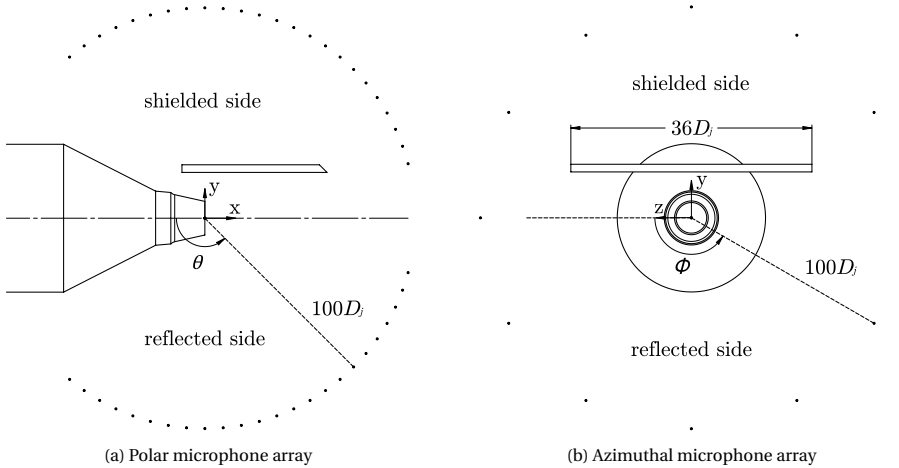


Figure 5.2: Far-field microphone positions. (a) 48 microphones in the polar array, divided for the reflected and shielded sides. (b) 12 microphones in the azimuthal array, normal to the jet axis. Microphone distance not to scale.

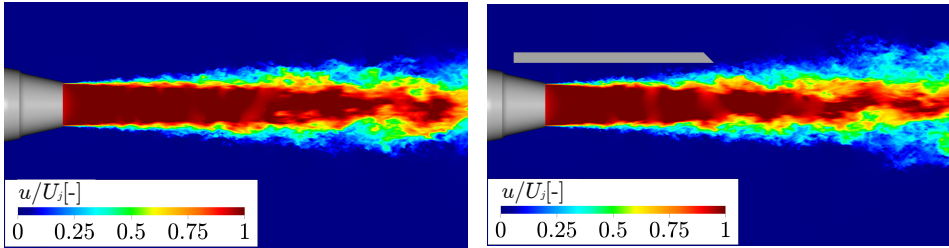
Similarly as performed in the NASA benchmark experiments [10], the far-field noise levels are computed with a microphone arc array. The array is centered at the nozzle exit plane, with a radius of  $100D_j$ . Microphones are placed at an interval of  $5^\circ$ , ranging from  $\theta = 50^\circ$  to  $\theta = 165^\circ$  ( $\theta = 180^\circ$  corresponds to the jet axis). The noise levels are evaluated at both shielded and reflected sides of the plate, as shown in Fig. 5.2a. An additional azimuthal array is located around the nozzle exit plane, normal to the jet axis, with 12 microphones spaced of  $30^\circ$ , as shown in Fig. 5.2b.

### 5.3. JET FLOW FIELD AND GRID CONVERGENCE

A mesh convergence study is performed to assess the sensitivity of the numerical results to the discretization of the computational domain. The mesh resolution is defined as the number of *voxels* at the nozzle exit diameter. The obtained element size is used throughout the jet plume. Three grids are investigated: coarse (resolution = 32 voxels/ $D_j$ ), medium (resolution = 45 voxels/ $D_j$ ), and fine (resolution = 64 voxels/ $D_j$ ). The features of each grid are summarized in table 5.4.

Grid	Resolution	Voxel Size at Nozzle Exit and Jet Plume [mm]	Finest Voxel Size [mm]	Number of Voxels [ $10^6$ ]	kCPUh
Coarse	32	1.588	0.1985	153.2	5.5
Medium	45	1.129	0.1411	371.2	23
Fine	64	0.794	0.0992	942.4	48

Table 5.4: Grid characteristics for convergence analysis.

Figure 5.3: Snapshots of the instantaneous flow field for isolated and installed jet configurations ( $L = 4D_j$  and  $h = 1D_j$ ). No visible change to the jet development caused by the plate.

The isolated and installed ( $L = 4D_j$  and  $h = 1D_j$ ) configurations, in the conditions of setpoint 03 ( $Ma = 0.5$ ), are used for the flow-field convergence study. The chosen installed case represents the configuration for which the surface is closest to the plume. Results are also compared with experimental data from reference [16] for validation. Flow-field measurements from particle image velocimetry are available for the isolated jet case [16]. The absence of hydrodynamic interaction between the jet flow and the solid surface allows the use of these results for validation of all configurations. As can be appreciated from both the instantaneous flow realizations for the isolated and installed jet cases in Fig. 5.3, and the time-averaged velocity profiles and r.m.s. of velocity fluctuations in Fig. 5.4, no significant difference between isolated and installed configurations is found in either the jet-flow field, or in the centerline velocity profiles.

From Fig. 5.4, it is shown that the potential core is well captured, compared to the experimental results, extending up to  $6.5D_j$  from the exit plane. A small over-prediction of the velocity decay at the centerline, in the order of  $0.04U_j$ , is also found. Minor deviations in velocity amplitude are also seen between the medium and fine isolated cases around  $12 < x/D_j < 15$ , likely due to the strong unsteadiness of the flow in that region. Similarly, both the amplitude and the spatial development of the turbulent velocity fluctuations are well captured with minor differences between the three grids and the experimental results. It is conjectured that these small deviations in the velocity r.m.s. occur due to the turbulence properties set at the nozzle inlet, which do not match perfectly the experimental conditions.

A key element for assessing the quality of the simulation is that turbulence in the

### 5.3. JET FLOW FIELD AND GRID CONVERGENCE

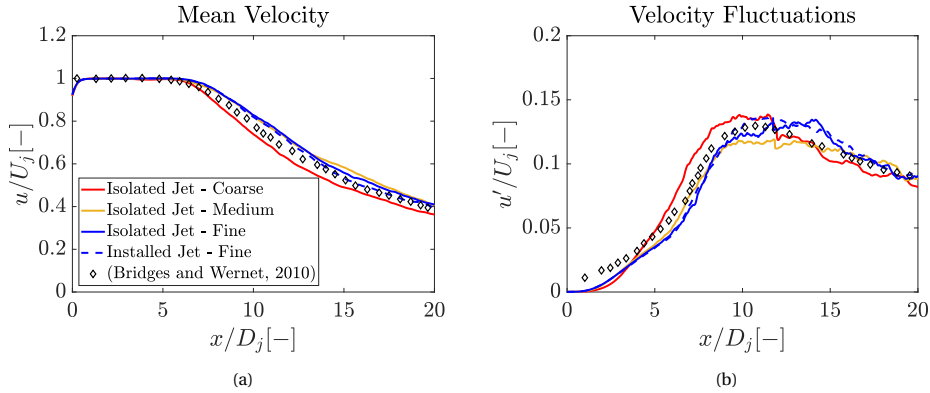


Figure 5.4: Profiles of the time-averaged and r.m.s. of fluctuations of the axial velocity component at the nozzle centerline for different grid resolutions, and compared to experimental data for setpoint 03.

mixing layer is accurately resolved in the frequency range of interest. The spectrum of turbulent kinetic energy  $E$  versus Strouhal number ( $St = f \times D_j/U_j$ ), obtained for setpoint 03, is shown in Fig. 5.5 for two probes placed at the nozzle lipline ( $y = 0.5D_j$ ) of the isolated jet, at positions  $x = 5D_j$  and  $x = 10D_j$ . The spectra are shown to follow Kolmogorov's 5/3 decay law up to high frequencies, in the order of  $St = 2$  (6.7 kHz). These results indicate that the turbulence characteristics are correctly modeled and the resultant spectral analyses, including the far-field noise resultant from turbulent mixing, are reliable.

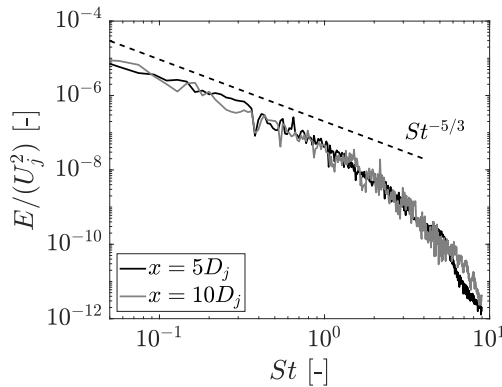


Figure 5.5: Spectra of turbulent kinetic energy for two probes at the nozzle lipline ( $y = 0.5D_j$ ) of the isolated jet (setpoint 03).

The far-field spectra for the installed configuration are compared to the experimental results from Brown [10]. For the comparisons, an intermediary case ( $L = 4D_j$  and  $h = 1.25D_j$  at setpoint 03) is chosen. The narrowband Sound Pressure Levels (SPL), obtained for a constant frequency band of 100 Hz, are plotted against the Strouhal number in Fig.

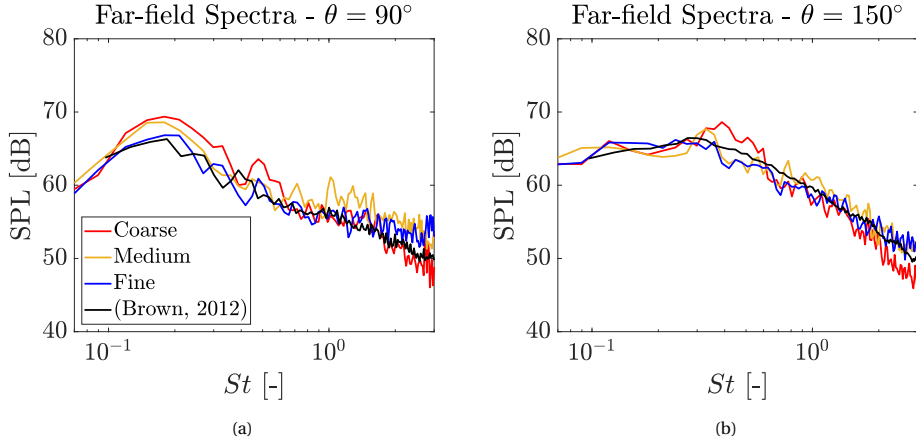


Figure 5.6: Grid convergence and validation of aeroacoustic results for the installed jet ( $L = 4D_j$  and  $h = 1.25D_j$ ). Spectra obtained for the reflected side of the plate ( $\theta = 90^\circ$  and  $\theta = 150^\circ$ ) and setpoint 03.

5.6. Results are displayed for the reflected side of the plate (refer to Fig. 5.2a), at two polar angles:  $\theta = 90^\circ$ , i.e. the sideline direction, and  $\theta = 150^\circ$ , i.e. near the direction of the jet axis. A reference pressure of  $2 \times 10^{-5}$  Pa is used for the conversion to dB. The frequency band of the experimental data has been also changed from 12.2 Hz to 100 Hz, so that it is comparable with the simulation results.

The spectral shape is correctly predicted by the simulations from all grids, at both polar angles. At low and mid frequencies, the curves for the medium and fine grids display similar amplitudes and convergence is achieved. For high frequencies, the effect of grid resolution is more evident and it is related to the cut-off frequency. For the coarse mesh, the cut-off frequency occurs at  $St \approx 1.8$  whereas, for the fine case, it occurs at  $St \approx 3$ , based on the chosen element sizes. At frequencies higher than  $St = 3$ , there is less agreement between the numerical (fine case) and experimental results, likely due to grid resolution effects. Up to this frequency, which is the range of interest, the maximum deviation between the results of the fine mesh and the experiments is approximately 4 dB. This shows the capability of the model to correctly predict JIN with sufficient accuracy. The results shown in the next sections of this manuscript are therefore obtained from the fine resolution grid so that analyses can be performed up to high frequencies ( $St < 3$ ).

## 5.4. INSTALLATION EFFECTS AND TRAILING-EDGE SCATTERING

The far-field SPL for the isolated and installed jets ( $L = 4D_j$  and  $h = 1D_j$ ) at setpoint 03 are plotted versus the Strouhal number in Fig. 5.7. The spectra are obtained for a constant frequency band of 100 Hz, and at polar angles  $\theta = \pm 90^\circ$  and  $\theta = \pm 150^\circ$ .

In the sideline direction ( $\theta = \pm 90^\circ$ ), installation effects result in low-frequency noise amplification, up to  $St = 0.7$ . The maximum increase, relative to the isolated case, is

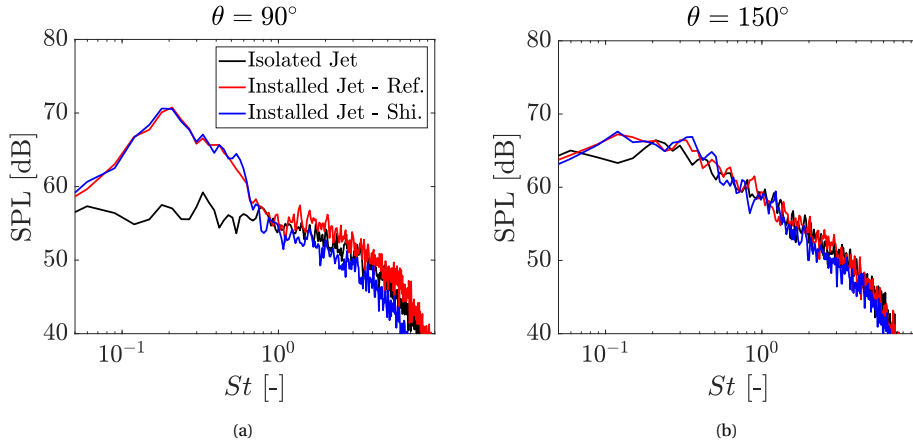


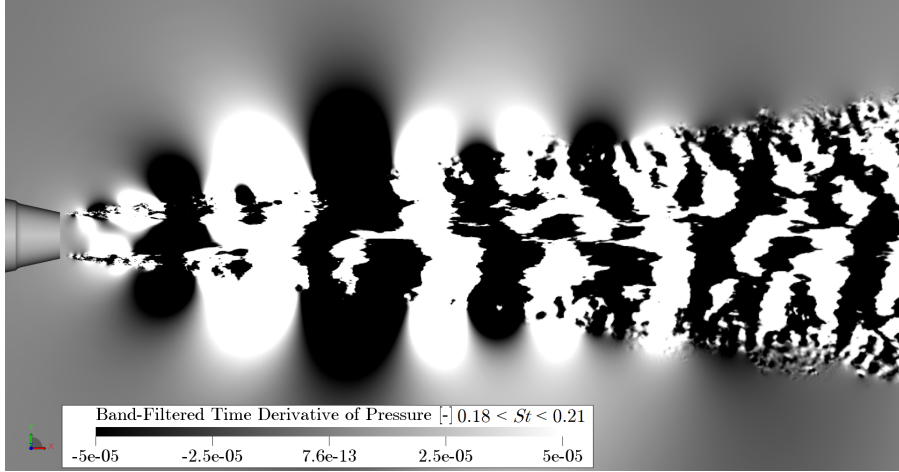
Figure 5.7: Far-field spectra of the installed jet ( $L = 4D_j$  and  $h = 1D_j$ ), at the reflected and shielded sides of the plate, compared to the isolated configuration (setpoint 03).

14 dB at  $St = 0.19$ . In the frequency range  $0.05 < St < 0.7$ , the spectra at the reflected and shielded sides display similar shape and amplitude, in agreement with the results of Head and Fisher [17]. This confirms that, for this frequency range, the dominant noise generation mechanism is the scattering of the near-field hydrodynamic waves at the trailing edge of the flat plate. For  $St > 0.7$ , the spectra for the installed cases are dominated by quadrupole noise sources. At the reflected side, noise levels are approximately 3 dB higher than those of the isolated case, as expected from the reflection on a half plane [18]. For  $\theta = \pm 150^\circ$ , i.e. towards the jet axis, installation effects are no longer significant and the spectra are similar to that of the isolated jet.

To determine the dominant noise sources for each configuration, instantaneous dilatation field contours for the jet at setpoint 03 are shown in Figs. 5.8a and 5.8b. They are obtained for a frequency band of  $0.18 < St < 0.21$ , corresponding to the region of maximum noise increase due to installation effects. Contours are saturated so that pressure waves outside of the jet plume can be identified.

For the isolated case, the dilatation field shows pressure waves convecting with the jet. Given the low Mach number investigated ( $Ma = 0.5$ ), it is expected that a large portion of those waves convects at subsonic speeds. A distinct change of their amplitude, characterized by growth, saturation (peak region) and decay, can be observed. Therefore, due to this spatial modulation, a small portion of the energy of the waves in the evanescent near-pressure field propagates to the far-field as noise [19]. For the installed jet, additional acoustic waves are generated due to scattering at the plate trailing edge. Waves on the shielded and reflected sides of the plate have opposite sign, indicating a phase-shift of  $180^\circ$ , as described by Head and Fisher [17] and Cavalieri *et al.* [18]. These scattered waves then propagate in the upstream direction of the jet.

The previous observations are confirmed by the directivity plots of Overall Sound Pressure Level (OASPL), integrated in the range  $0.05 < St < 3$ , shown in Fig. 5.9. In the polar direction (Fig. 5.9a), the maximum noise increase occurs at  $\theta \approx \pm 50^\circ$ . Smaller an-



(a) Isolated jet

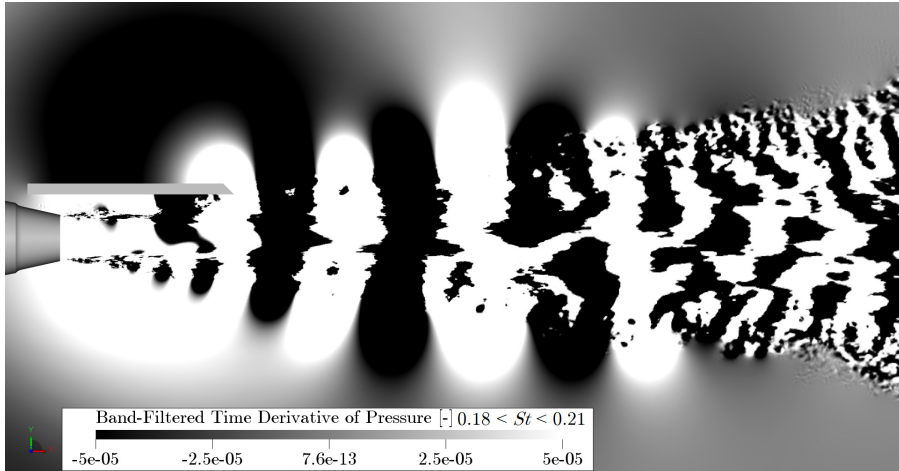
(b) Installed jet ( $L = 4D_j$  and  $h = 1D_j$ )

Figure 5.8: Contours of the time-derivative of the pressure field of isolated and installed jets, band-pass-filtered over a frequency range  $0.18 < St < 0.21$ . Contours are saturated so that pressure waves outside of the jet plume can be identified.

gles could not be computed due to the presence of the nozzle, which acts as a shielding body. However, the trend is consistent with the cardioid directivity, proposed by Ffowcs-Williams and Hall [2]. Approaching the jet axis, the curves for the isolated and installed cases collapse, confirming that the quadrupole sources dominate. In the azimuthal direction, the OASPL values are plotted normal to the jet axis, for a fixed polar angle of  $\theta = 90^\circ$ . The isolated jet displays an axisymmetric behavior, with similar noise levels at all azimuthal angles. For the installed jet, a maximum noise increase of 5 dB is obtained in the direction normal to the flat plate ( $\phi = \pm 90^\circ$ ), whereas no difference is present for

$\phi = 0^\circ$  and  $\phi = 180^\circ$ . For intermediate angles, a small difference is visible between the upper and lower sides, due to shielding and reflection effects. This directivity pattern is consistent with the presence of acoustic dipoles, with axes perpendicular to the surface, in agreement with Head and Fisher [17].

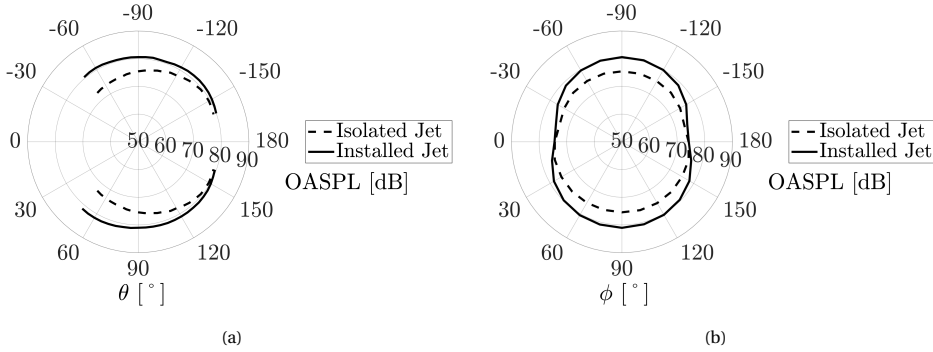


Figure 5.9: Polar and azimuthal directivities of the isolated and installed jets ( $L = 4D_j$  and  $h = 1D_j$ ) for setpoint 03.

The SPL of the installed jet ( $L = 4D_j$  and  $h = 1D_j$ ) for the other setpoints are plotted with the respective isolated configuration spectra in Fig. 5.10, for polar angles  $\theta = \pm 90^\circ$ . For the low Mach number jet ( $M_a = 0.35$ ), shown in Fig. 5.10a, a strong amplification occurs at low frequencies, similarly as the previous results for setpoint 03. At the spectral peak ( $St = 0.26$ ), there is a difference of 19 dB between installed and isolated noise levels. The spectra for shielded and reflected sides show similar values up to  $St = 0.77$ , which marks the maximum frequency for which the scattering at the trailing edge is the dominant source. For the high Mach number case ( $M_a = 0.8$ ), installation effects result in a lower amplification with respect to the isolated case at the spectral peak (5 dB at  $St = 0.4$ ). This is due to the dependence of the sound intensity with the jet velocity ( $U_j^5$  for the scattering [2] and  $U_j^8$  for turbulence-mixing noise [20]). Therefore, with a high velocity jet, the spectrum is dominated by the isolated jet noise due to turbulent mixing.

The influence of the solid plate geometry on the installed far-field noise is also assessed. Results pertaining to the change of the plate radial position relative to the jet centerline are shown in Fig. 5.11, for the three investigated plate lengths and  $M_a = 0.5$ . The spectra, plotted for  $\theta = 90^\circ$  (reflected side of the plate), show that moving the surface away from the plume results in lower noise levels, especially at mid frequencies. For the case with  $L = 4D_j$ , there is a decrease of 4 dB between  $h = 1D_j$  and  $h = 1.25D_j$ , and 6 dB between  $h = 1D_j$  and  $h = 1.5D_j$  at the spectral peak ( $St = 0.2$ ). Similar trends occur for other plate lengths and jet setpoints. The cross-over point with respect to the isolated jet curve also moves to higher frequencies for surfaces closer to the jet. For  $L = 4D_j$ , the cross-over shifts from  $St = 0.33$  ( $h = 1.5D_j$ ) to  $St = 0.70$  ( $h = 1D_j$ ). This is likely due to the increased proximity of the surface to smaller scale eddies that generate higher frequency noise when scattered.

The effect of changing the plate length is shown in Fig. 5.12. Spectra are obtained for three surface lengths, at fixed radial positions  $h = 1.25D_j$  and  $h = 1.5D_j$ , for  $\theta = -90^\circ$  and

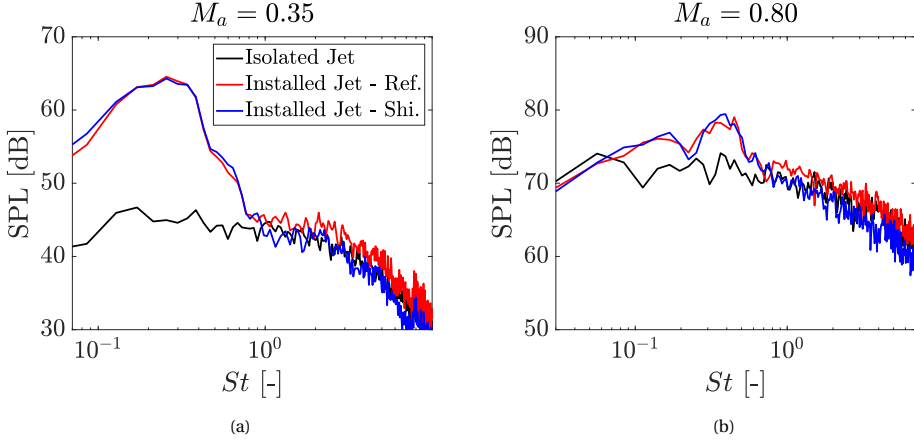


Figure 5.10: Far-field spectra of the installed jet ( $L = 4D_j$  and  $h = 1D_j$ ), at the reflected and shielded sides of the plate, compared to the isolated configuration for setpoints 01 ( $Ma = 0.35$ ) and 06 ( $Ma = 0.80$ ), for polar angles  $\theta = \pm 90^\circ$ .

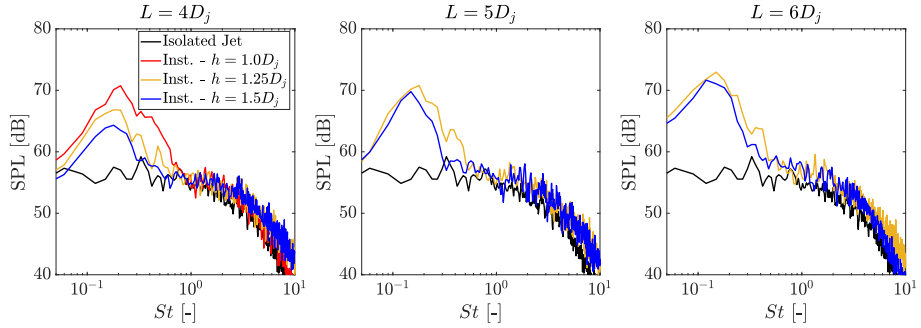


Figure 5.11: Effect of changing the plate radial position on the far-field noise levels. Spectra are plotted for different plate lengths ( $L = 4D_j$ ,  $L = 5D_j$  and  $L = 6D_j$ ), at a polar angle  $\theta = 90^\circ$  (reflected side) and for  $Ma = 0.5$ .

$Ma = 0.5$ . It is shown that, for longer surfaces, noise increase is higher at low frequencies with a difference of 7 dB between the curves for  $L = 6D_j$  and  $L = 4D_j$ , for  $h = 1.25D_j$  and  $St = 0.15$ . For longer plates, the spectral peak also moves towards lower frequencies: for  $h = 1.25D_j$  the spectral peak is at  $St = 0.18$  to  $St = 0.15$  for the shortest and longest plates, respectively. This is due to the increase of energy content of large-scale structures in the mixing layer in the downstream direction of the jet [21]. Since these structures generate low-frequency hydrodynamic pressure waves, the scattering effects are also amplified in that frequency range. At frequencies higher than  $St = 0.2$ , the difference between the curves is small and the cross-over frequency with the isolated curve is not significantly changed for different plate lengths. At high frequencies, the scattering is not strongly affected by changing the surface length since small-scale structures show similar characteristics and amplitude in the streamwise direction [3].

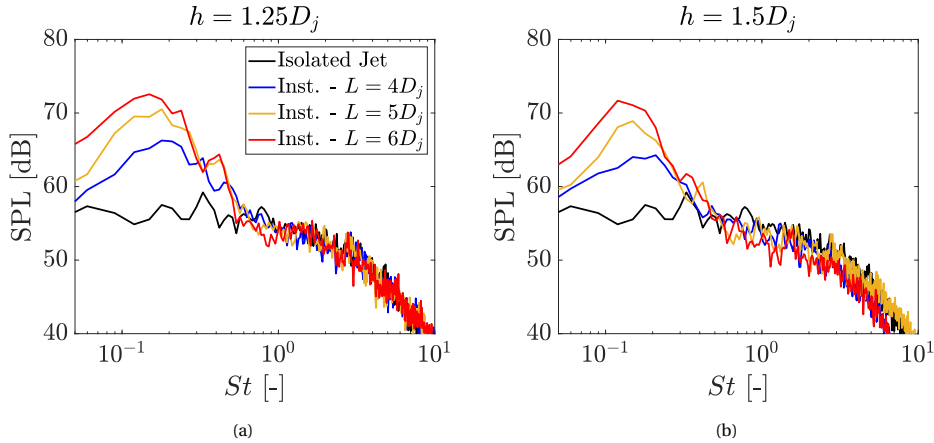


Figure 5.12: Effect of changing the plate length on the far-field noise levels. Spectra are plotted for different plate heights: (a)  $h = 1.25D_j$  and (b)  $h = 1.5D_j$ , at a polar angle  $\theta = -90^\circ$  (shielded side) and for  $Ma = 0.5$ .

The results show that the far-field noise of the installed case is dependent on the characteristics of the near-field of the jet and the position of the trailing edge. The phenomena behind JIN are therefore investigated in the next sections, linking the edge scattering phenomenon with jet near-field properties at the trailing-edge region.

## 5.5. SOURCE CHARACTERISTICS AND FAR-FIELD NOISE

The goal of this section is to identify the frequency range in which JIN is the dominant noise source, for a given plate length and radial position, starting from near-field data of the isolated jet.

This is performed by making use of the inequalities proposed by Ffowcs-Williams and Hall [2]. They have shown that, for a half plane, noise amplification is caused by the scattering of eddies within a wavelength from the edge; this satisfies the inequality  $2kr_0 \ll 1$ , where  $k$  is the wavenumber, and  $r_0$  the distance from the center of the eddy to the edge of the half plane. On the other hand, for eddies far from the edge, which satisfy the inequality  $(kr_0)^{1/2} \gg 1$ , there is no noise increase due to scattering. These parameters can then be regarded as a measure of source compactness, expressed as the Helmholtz number  $kr_0$ , based on the distance between the source and the edge. As a consequence, once this distance is known, a wavenumber envelope of flow structures that are effectively scattered at the trailing edge can be found.

To compute the envelope, an equivalent hydrodynamic source distant  $r_0$  from the plate trailing edge is used, for a given wavenumber, as shown in Fig. 5.13. It is assumed that this equivalent source is located within the jet mixing layer, positioned at  $(x_{\text{source}}, y_{\text{source}})$ . The radial position of the source is assumed to be at the nozzle lipline ( $y_{\text{source}} \approx 0.5D_j$ ), which corresponds to the center of the mixing region in the jet shear layer, i.e. the region of maximum amplitude of hydrodynamic fluctuations [3]. More in detail, the hypothesis assumes that small changes in the radial position of the equivalent source (around the lipline) are negligible with respect to the distance from the edge. The

remaining variable,  $x_{\text{source}}$ , is determined by using the near-field pressure spectra of the isolated jet [3].

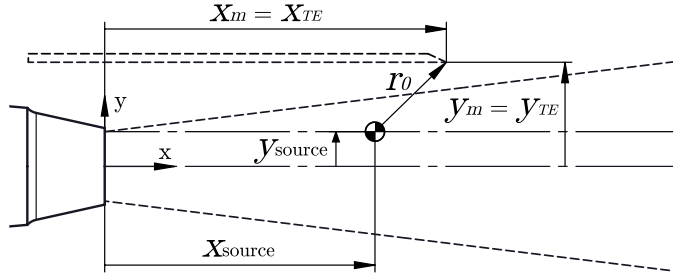


Figure 5.13: Sketch representation of an equivalent source located in the center of the jet mixing layer (assumed to be the nozzle lipline), at a certain distance  $r_0$  from a defined measurement point (plate trailing edge), for a given wavenumber.

Following Arndt *et al.* [3], the pressure spectrum in the near-field of an isolated jet can be divided into four regions (Fig. 2.3). There is an energy-containing region, characterized by amplitude slowly increasing with frequency. This region extends up to the spectral peak, and then it is followed by the inertial subrange, where there is a steep amplitude decay. Finally there is the acoustic region, where pressure fluctuations travelling at the speed of sound are dominant. The intensity of the pressure fluctuations scales as:

$$I \propto \rho_0 a_0 U_0^2 (kr_0)^n, \quad (5.1)$$

where  $\rho_0$  is the fluid density,  $a_0$  is the speed of sound and  $U_0$  is the source velocity. For the energy-containing region, where the sources display hydrodynamic behaviour,  $n = -6$ . For the inertial subrange,  $n = -6.67$  to take into account the spectral decay with frequency. Finally when  $n = -2$  the sources display an acoustic behaviour [3].

Since the goal is to correlate JIN to hydrodynamic pressure fluctuations [4],  $x_{\text{source}}$  can be found by fitting the amplitude of pressure fluctuations from a set of near-field spectra of the isolated jet, for a given wavenumber. For a given plate length with the trailing edge located at  $x_m$ , the procedure for the fitting is the following:

1. Spectra in the near-field of the isolated jet data set are extracted at different radial positions ( $y_m$ );
2. A source position ( $x_{\text{source}}$ ) is assumed upstream of  $x_m$ ;
3. The Helmholtz number ( $kr_0$ ) is computed at the radial locations defined in (i), using the source position from (ii);
4. For a given  $St$  chosen as input, the exponent of  $\hat{P} \propto (kr_0)^n$ , i.e. along the  $r_0$  direction, as described in equation 6.1, is computed;
5. If  $n \neq -6$ ,  $x_{\text{source}}$  is shifted and the exponent is recomputed. When  $n = -6$ , the source position is converged.

An example of the method is shown in Fig. 5.14a, where a set of near-field spectra extracted at  $x_m = 4D_j$  and at different radial stations, for setpoint 03 ( $M_a = 0.5$ ), is shown. After a source position is converged for a chosen frequency value, spectra are represented as a function of  $kr_0$ , as shown in Fig. 5.14b. The black dotted line represents the slope of  $kr_0^{-6}$ , crossing the points of constant frequency  $St = 0.2$  for each radial position  $y$ . For this specific frequency and measurement point, the axial position of the source is found at  $x_{\text{source}} = 0.9x_m$ , or  $x_{\text{source}} = 3.6D_j$ . This analysis is then carried out similarly at other frequencies, and for the two other axial measurement positions ( $x_m = 5D_j$  and  $x_m = 6D_j$ ), as shown in Fig. 5.15. Similar trends are obtained for the other setpoints ( $M_a = 0.35$  and  $M_a = 0.8$ ).

It is shown that, for increasing frequency, the equivalent source position moves towards  $x_m$  for all analyzed cases. These results show that small scale equivalent sources need to be positioned axially closer to the trailing-edge location in order to generate hydrodynamic pressure fluctuations able to scatter as noise at that point.

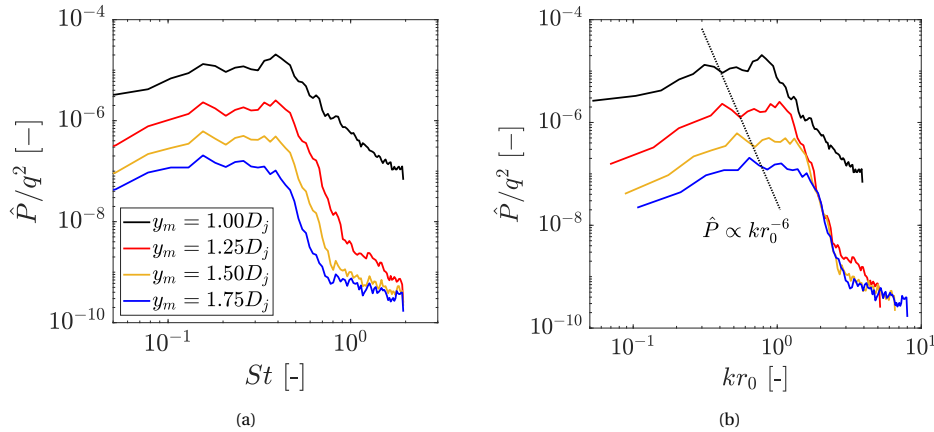


Figure 5.14: Near-field pressure spectra at different radial positions for the calculation of source-edge distance, obtained at  $x = 4D_j$  and  $M_a = 0.5$ . (a) Spectra as a function of Strouhal number. (b) Spectra as a function of the Helmholtz number  $kr_0$ , based on a converged equivalent source position. The dotted line represents a  $r_0^{-6}$  (hydrodynamic characteristic) slope on the pressure data for a constant frequency  $St = 0.2$ .

The determination of the equivalent source position allows for the computation of an equivalent distance between source and measurement points, which can be used in the compactness analogy defined by Ffowcs-Williams and Hall [2]. The plots in Figs. 5.16a and 5.16b show the dependence with frequency of the parameters  $2kr_0$  (eddies near the edge) and  $kr_0^{1/2}$  (eddies far from the edge), respectively. Results are included for the three jet setpoints and four geometrical cases. A dotted line is also included to mark the points where the curves are equal to 1. It can be seen that the values of both parameters increase with frequency, for all conditions. For  $M_a = 0.5$  and a case with  $L = 4D_j$  and  $h = 1D_j$ , the condition  $2kr_0$  reaches 1 for a frequency  $St = 0.21$ . For the other cases, this occurs at lower frequencies ( $St \approx 0.17$ ). For the same case, the other condition  $kr_0^{1/2}$  reaches 1 for a frequency  $St = 0.65$  with a similar trend for the other cases. Therefore, it is concluded that there is a frequency range in each case where neither condition de-

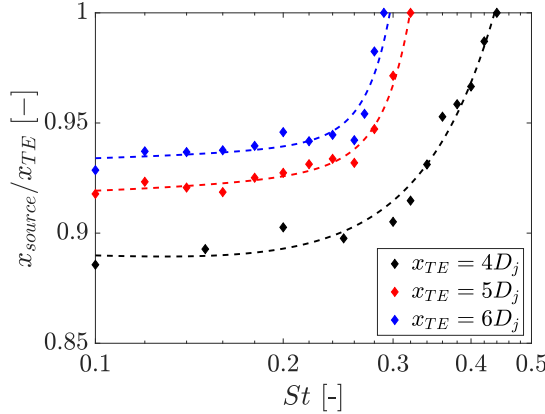


Figure 5.15: Equivalent source position, obtained for different frequencies and axial measurement positions  $x_m$ , for setpoint 03. For increasing frequency, the equivalent source moves toward  $x_m$ .

finied by Ffowcs-Williams and Hall [2] is satisfied. In this transition region, a less efficient scattering at the edge (lower sound amplification) is expected due to the structures becoming increasingly compact.

For a better understanding of the physical meaning of these two compactness conditions, and how they relate to the produced noise, isolated and installed far-field spectra are plotted in Fig. 5.17, highlighting the frequencies where the compactness parameters are equal to 1 with dotted lines. The spectra are obtained for  $M_a = 0.5$  at the shielded side of the plate ( $\theta = -90^\circ$ ), for a better visualization of the cross-over frequency between the installed and isolated curves.

The compactness parameters relate to the far-field spectra in two different manners. The frequency limit for eddies very near the edge ( $2kr_0 = 1$ ) occurs approximately at the location of the peak noise levels for the installed configuration. This is valid for all investigated configurations, and it indicates that the maximum amplification occurs at the limit Helmholtz number where the structures are regarded as non-compact with respect to the edge distance. On the other hand, the frequency limit for eddies far from the edge ( $(kr_0)^{1/2} = 1$ ) occurs approximately at the location where the far-field noise levels for the installed configuration cross the curve of the isolated jet. This is consistent with the analytical formulation of Ffowcs-Williams and Hall [2], which states that eddies far from the edge produce noise levels equivalent to that of free turbulence, when effects of shielding and reflection by the surface are disregarded. Finally, the transition region, where neither inequality is satisfied, is characterized by a decay in noise levels with increasing frequency.

Spectra for two geometric cases, obtained for the other jet setpoints and  $\theta = -90^\circ$ , are plotted in Fig. 5.18. Similar trends are obtained for other configurations. The results for  $M_a = 0.35$  are in agreement with those obtained previously for  $M_a = 0.5$ , where the condition  $2kr_0 = 1$  occurs at a frequency near the spectral peak, and  $kr_0^{1/2} = 1$  occurs near the cross-over between isolated and installed curves. For  $M_a = 0.8$ , however, this approach does not provide the same conclusions. While the cross-over frequency is still

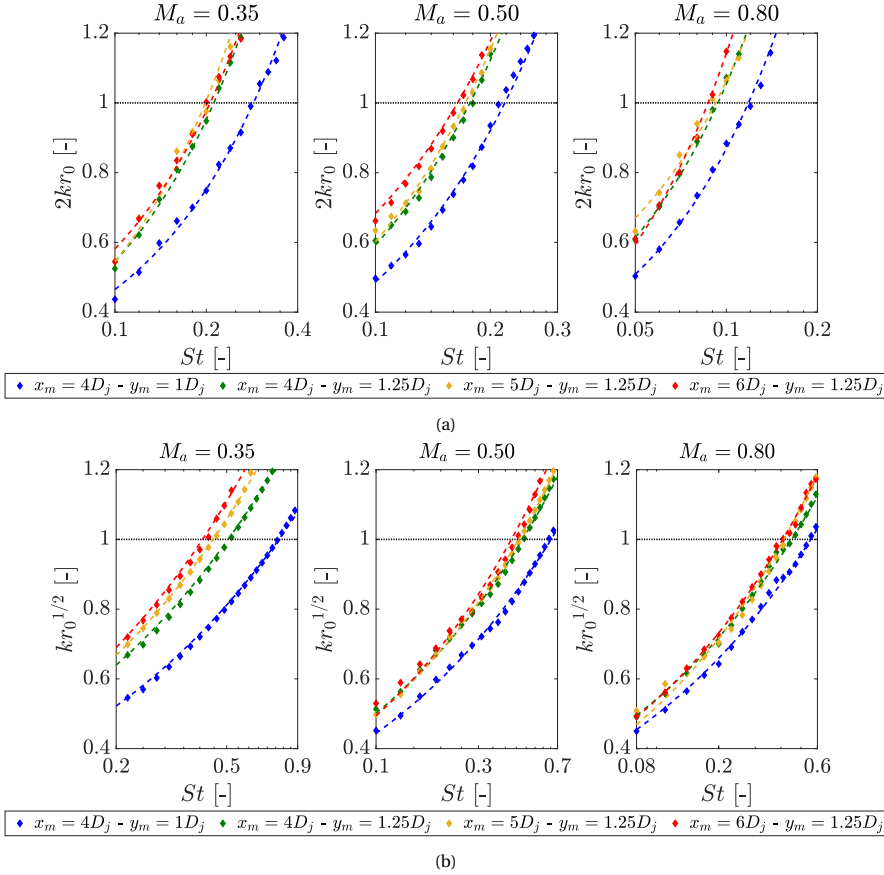


Figure 5.16: Compactness parameters ( $2kr_0$  and  $kr_0^{1/2}$ ) as a function of frequency, obtained for different measurement points at three jet acoustic Mach numbers. A dotted line is included to determine the frequency where these parameters are equal to 1.

predicted fairly accurately, the first condition does not predict the spectral peak ( $St = 0.4$ , for  $L = 4D_j - h = 1D_j$ ), but rather a much lower frequency ( $St = 0.12$ ).

To better understand the reasons behind the discrepancy, Fig. 5.19 shows the spectra for the isolated and installed configurations, at  $\theta = -90^\circ$ , along with those obtained by integrating only the surface pressure fluctuations on the plate using the FW-H solid formulation [22]. The latter only accounts for dipole sources on the plate, and thus noise from quadrupoles in the jet is disregarded. The spectra are computed on the upper and lower sides of the plate, separately, as well as considering the entire surface. On the upper side of the plate, two peaks are visible at  $St = 0.12$  and  $St = 0.4$ , with similar amplitudes. The former occurs approximately at the frequency predicted by the method proposed in this section. The second spectral peak, which is dominant on the lower side of the plate, suggests that other sources of sound in addition to trailing-edge scattering might be present.

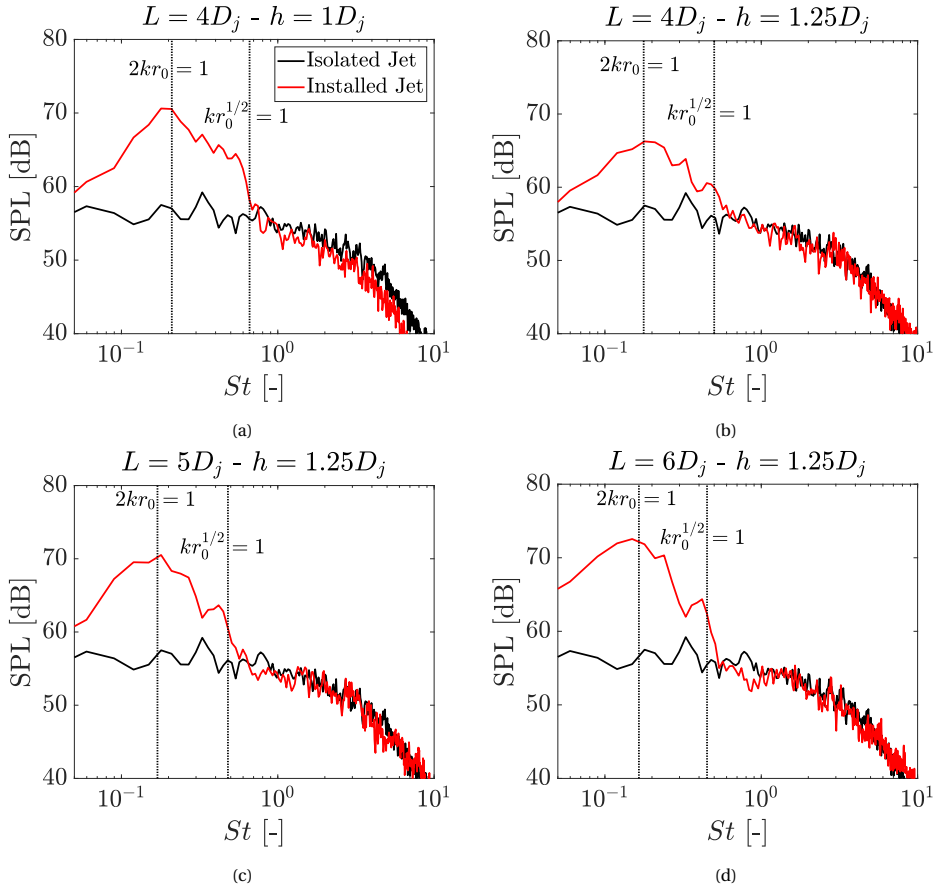


Figure 5.17: Far-field spectra with the frequency values where the compactness parameters  $2kr_0$  and  $kr_0^{1/2}$  are equal to 1, for different plate geometries. The former approaches the peak frequency, whereas the latter approaches the cross-over between installed and isolated curves. Spectra obtained for  $\theta = -90^\circ$  and  $M_a = 0.5$ .

It is concluded that the main characteristics of the frequencies related to JIN are related to the degree of compactness of the sources with respect to their distance to the scattering point.

## 5.6. FAR-FIELD NOISE SCALING BASED ON NEAR-FIELD PROPERTIES

In this section, the effect of near-field properties on the spectral amplitude of an installed jet is addressed. This is performed by finding scaling laws for the far-field spectra for different geometric cases, using only information from the isolated jet. Those scaling laws are deemed to predict the far-field noise independently of the geometric configuration adopted for the plate, reducing the need for testing or computing several cases. First,

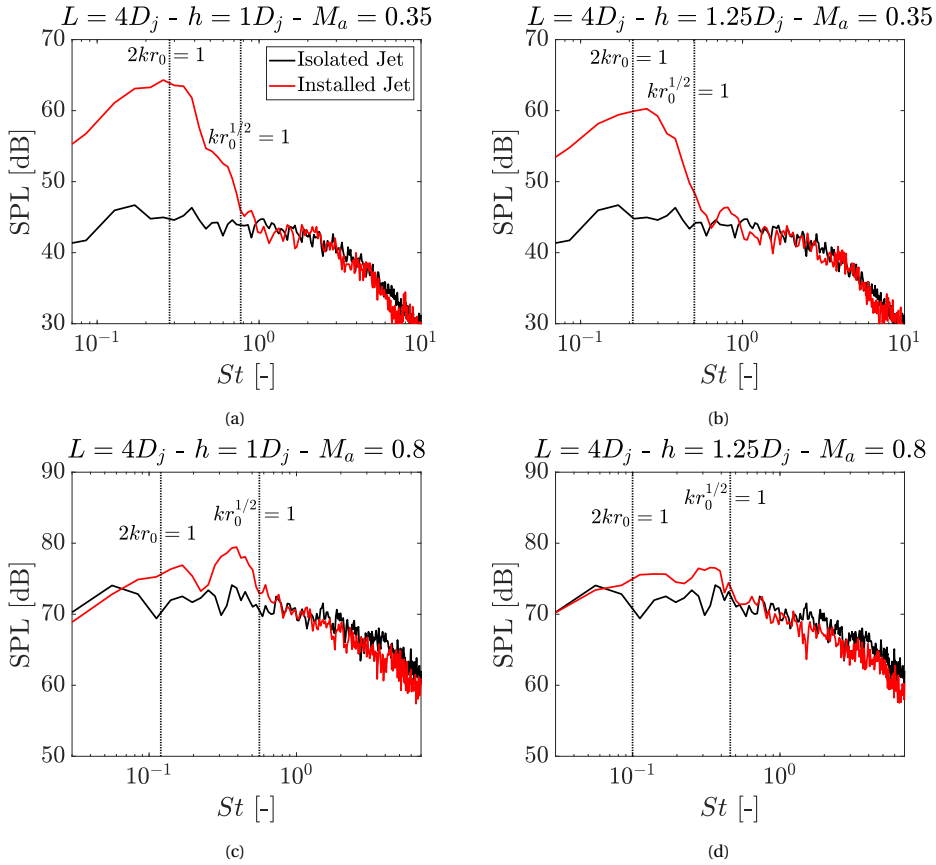


Figure 5.18: Far-field spectra with the frequency values where the compactness parameters  $2kr_0$  and  $kr_0^{1/2}$  are equal to 1, for  $Ma = 0.35$  (a and b) and  $Ma = 0.80$  (c and d). Spectra obtained for  $\theta = -90^\circ$ .

a scaling law is found for moving the plate in the radial direction, and afterwards for changing the plate length.

### 5.6.1. RADIAL DIRECTION SCALING LAW

Far-field noise data in Fig. 5.11 show higher noise levels and a broader frequency range of amplification when the surface is closer to the jet in the radial direction. To relate this behaviour to the near-field characteristics of the isolated jet, spectra of pressure fluctuations from the latter are computed at several locations outside of the plume, similarly as shown in Fig. 5.14a. To determine how the pressure fluctuations for an isolated jet vary in the radial direction, they are plotted against  $y$  in Fig. 5.20 for  $Ma = 0.5$ . The curves display the decay at the axial position of  $x = 4D_j$  and frequencies equal to  $St = 0.2$  and  $St = 0.4$  (selected in the noise amplification region for the installed configuration with  $h = 1D_j$ ).

Strong fluctuations occur at  $y = 0.5D_j$ , which corresponds to the nozzle lipline. This

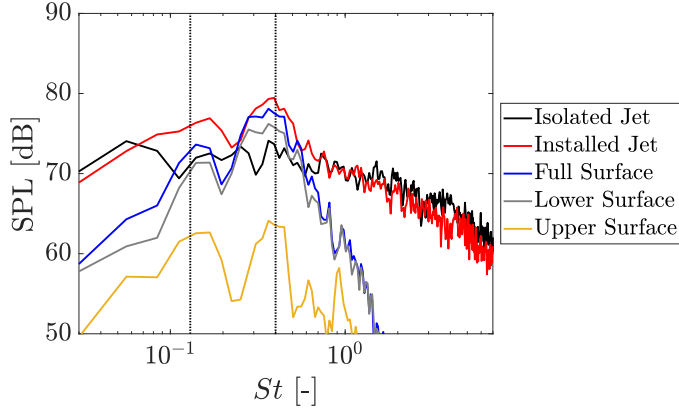


Figure 5.19: Far-field spectra of the isolated and installed jets, with the noise from pressure fluctuations computed on the overall surface, and on the upper and lower sides separately. Spectra obtained for  $\theta = -90^\circ$  and  $Ma = 0.8$ .

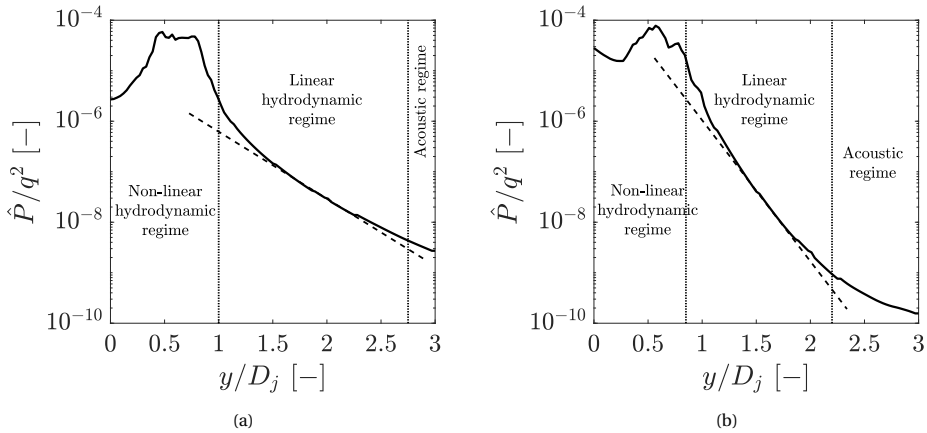


Figure 5.20: Near-field decay of pressure fluctuations in the radial direction for an isolated jet, at  $St = 0.2$  and  $St = 0.4$ , at an axial position  $x = 4D_j$  and for  $Ma = 0.5$ .

is in agreement with the assumption made in the previous section that the lipline can be considered the center of the structures in the mixing layer. Moving away from the jet axis, the near-pressure field in the radial direction can be divided into three regions: a non-linear hydrodynamic field, a linear hydrodynamic field and an acoustic field, similarly as reported in Chapter 2 [3]. The first one is characterized by the flow inside the plume and nearby regions. Further away from the jet, the hydrodynamic pressure fluctuations display an exponential decay in the  $y$  direction. For  $St = 0.2$ , the linear hydrodynamic region is placed between  $1 < y/D_j < 2.7$ , whereas for  $St = 0.4$  it occurs closer to the plume, between  $0.8 < y/D_j < 2.2$ . Finally, even farther from the jet, pressure fluctuations display acoustic wave characteristics and an algebraic decay [3]. These results are in agreement

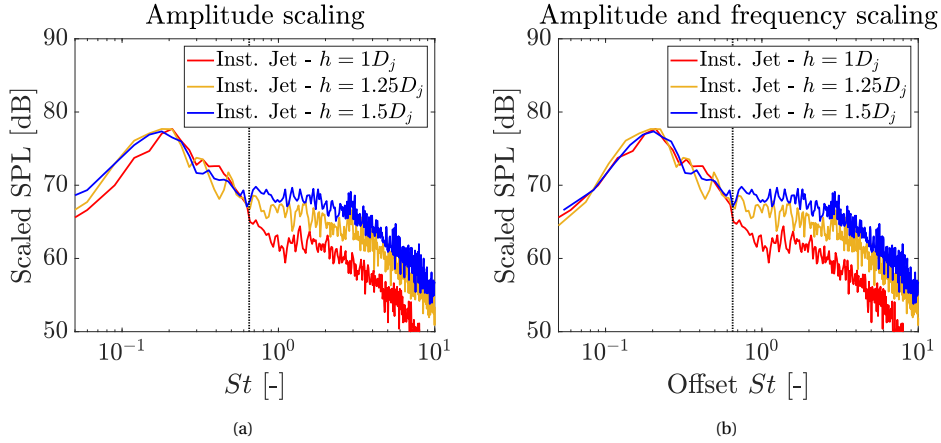


Figure 5.21: Far-field spectra of installed jets, scaled by the exponential of the plate radial position ( $L = 4D_j$  and  $\theta = 90^\circ$ ), for  $M_a = 0.5$ . (a) Only the amplitude of the curves is scaled. (b) The amplitude is scaled and the curves are offset to match the spectral peak.

with measurements performed in the near-field of a jet [3, 5, 6]. The position and extension of the linear hydrodynamic field, which is the most relevant for this work, are shown to be frequency-dependent. At higher frequencies, the linear decay is steeper and the far-field begins closer to the jet. This is consistent with the results from the previous section, where it was shown that small-scale structures become quickly compact when moving away from the lipline. Similar trends are obtained for the other setpoints.

In the linear hydrodynamic region, the pressure fluctuations show an exponential pressure decay. Therefore, the installed far-field noise levels can be scaled with  $e^h$ , based on the respective plate height for each case. This is shown in Fig. 5.21a, where there is a fairly good agreement between the curves for  $0.18 < St < 0.65$ . For  $St > 0.65$ , the curves diverge since this region of the spectra is dominated by noise from quadrupole sources reflected on the surface. In the previous sections, it was shown that the spectral peak changes for plates at different radial positions. Therefore, if the scaled spectra are offset in frequency, a better agreement between the curves is found, as shown in Fig. 5.21b. In these plots, the scaled SPL spectra ( $SPL \times e^h$ ) for  $h = 1.25D_j$  and  $h = 1.5D_j$  are offset in frequency (Offset  $St$ ) so that their peak matches that of  $h = 1D_j$ .

It is then concluded that a combination of amplitude and frequency scaling is necessary to match the noise levels of different radial configurations. While the amplitude can be easily scaled as an exponential function of the plate height ( $e^h$ ), knowledge of the spectral peak frequency is necessary beforehand. The method described in the previous section can provide a fairly good prediction of the spectral peak for low/mid Mach number jets, and thus it can be used together with the amplitude scaling in order to obtain the far-field spectra of different geometric configurations. This scaling is also applied for plates with different lengths ( $L = 5D_j$  and  $L = 6D_j$ ) as shown in Fig. 5.22, with a good agreement between the curves. Scaled spectra for the other jet setpoints are shown in Fig. 5.23. For these other conditions there is also a good agreement between the curves.

For  $M_a = 0.8$ , however, there is a slight difference in amplitude, particularly at low frequencies ( $St < 0.1$ ), possibly due to effects discussed in the previous section.

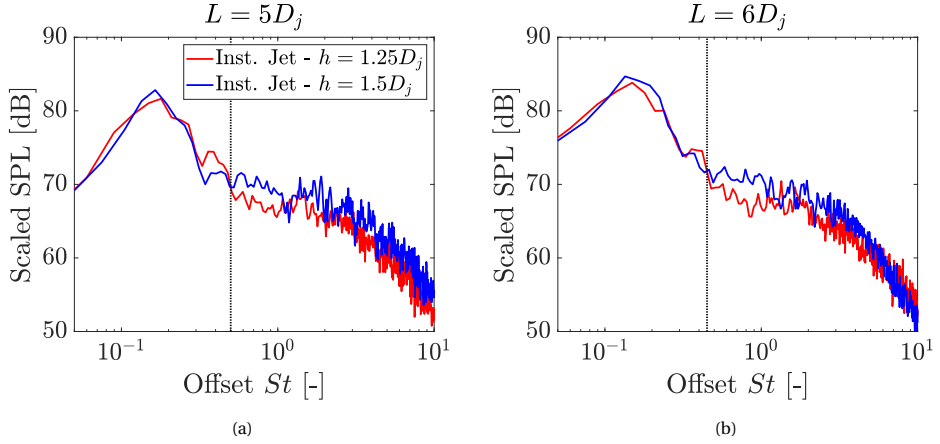


Figure 5.22: Far-field spectra of installed jets, scaled by the exponential of the plate radial position, for  $\theta = 90^\circ$  and  $M_a = 0.5$ . (a)  $L = 5D_j$  (b)  $L = 6D_j$ .

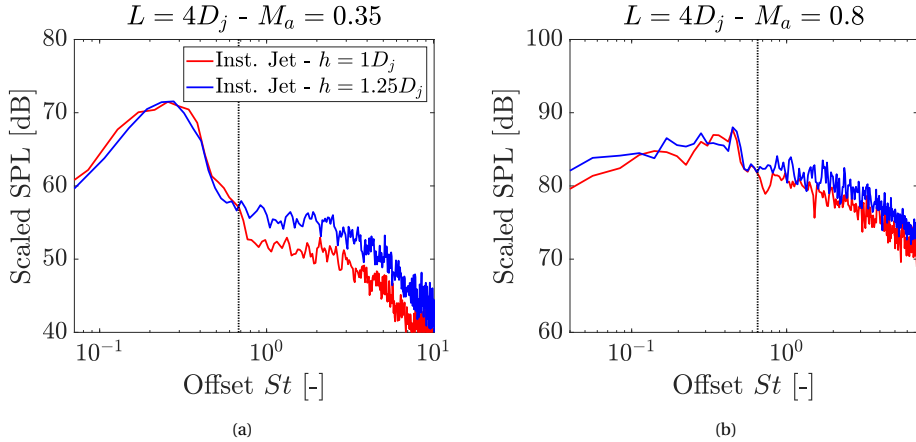


Figure 5.23: Far-field spectra of installed jets ( $L = 4D_j$ ), scaled by the exponential of the plate radial position, for  $\theta = 90^\circ$ . (a)  $M_a = 0.35$  (b)  $M_a = 0.8$ .

### 5.6.2. AXIAL DIRECTION SCALING LAW

A similar procedure is carried out to find a scaling law for the noise generated by plates with different lengths. Spectra of near-field pressure fluctuations computed at different axial locations, for  $y = 1.5D_j$  and  $M_a = 0.5$ , are shown in Fig. 5.24a. The results show an increase of low-frequency fluctuations at positions farther from the nozzle exit plane due to the presence of highly-energetic large-scale structures. It can be noticed that, aside for

$x = 3D_j$ , the curves tend to collapse at  $St \approx 0.45$  suggesting that, at high frequencies, the amplitude of the pressure fluctuations remains constant in the axial direction.

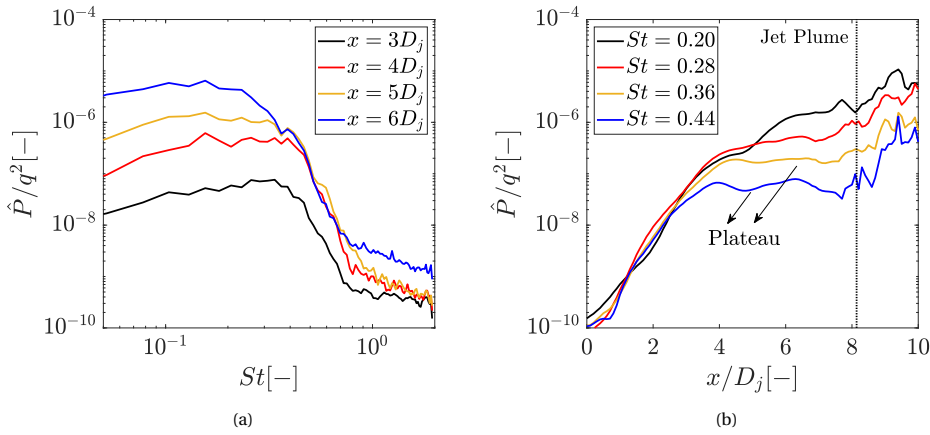


Figure 5.24: (a) Near-field pressure spectra. (b) Progression of near-field pressure in the axial direction. Data obtained for  $\gamma = 1.5D_j$  and  $Ma = 0.5$ .

This behaviour can be better visualized by plotting the amplitude of the pressure fluctuations in the axial direction for specific frequencies (Fig. 5.24b). At relatively low frequencies ( $St = 0.20$  and  $St = 0.28$ ), the amplitude of pressure fluctuations increases in the axial direction. Due to the large wavelength associated with these structures, they grow and saturate at positions farther from the nozzle exit plane when compared to small-scale eddies. A non-linear behaviour is also found downstream of  $x = 8D_j$  due to the presence of the rotational flow inside of the jet plume. At higher frequencies, the amplitude of the pressure fluctuations raises up to a constant value in the axial direction. This plateau is due to the contamination of the signal by the jet acoustic waves [5]. If only the coherent, hydrodynamic fluctuations were present, a decay was expected to follow the saturation point due to the wavepacket nature of the jet [23]. Therefore, after the saturation point, acoustic fluctuations, which have a slower decay rate, become dominant with respect to hydrodynamic ones.

To remove the contribution of non-coherent fluctuations in the near field, a frequency domain form of POD, known as SPOD, is applied [7, 8], similarly as done in other studies on jet noise [3, 6, 24]. SPOD is preferred to space-only POD because it can properly describe spatio-temporal coherent structures, due to its spectral-based kernel. In this way, the flow is decomposed at different time scales and, consequently, the characteristics of the structures can be analyzed for each frequency band [7], which is necessary for a posterior scaling of the far-field noise. Moreover, due to the segmentation of the signals based on a specified block length, few eigenvectors are obtained and, therefore, few modes are required to reconstruct the wavepacket. On the other hand, to achieve similar results using space-only POD, several modes need to be selected since each of them contains information in the entire frequency range of the analysis.

The SPOD is based on the decomposition of the cross-spectral density tensor, lead-

ing to energy-ranked modes, in the form of coherent structures, that each oscillates at a single frequency. These modes are orthogonal to each other at any frequency and, as a set, optimally represent the space-time flow statistics [8].

For the decomposition of a given flow-field property  $\mathbf{q}(\mathbf{x}, t)$  into orthogonal modes in the frequency domain, the cross-spectral density tensor is necessary. The tensor can be obtained, for example, using the method of snapshots, which is commonly used for space-only POD [25]. The Welch's method [26] is applied to average the spectra over multiple realizations of the flow in order to ensure convergence for analyses with a large number of snapshots. The data is split into blocks, for which the Fourier coefficients are computed, allowing the cross-spectral density tensor to be determined for each frequency [7]. In order to obtain the SPOD modes the following spectral eigenvalue problem must be solved:

$$\int_{\Omega} \mathbf{S}(\mathbf{x}, \mathbf{x}', f') \mathbf{W}(\mathbf{x}') \psi(\mathbf{x}', f') d\mathbf{x}' = \lambda(f') \psi(\mathbf{x}, f'), \quad (5.2)$$

where  $\mathbf{S}$  is the cross-spectral density tensor, the weight  $\mathbf{W}$  is a positive-definite Hermitian tensor and the superscript  $'$  indicates the position or frequency used in the calculation of the two-point correlation. The eigenvectors  $\psi$ , with their respective eigenvalue  $\lambda$  are computed for a given frequency  $f'$  [7]. Thus, the Fourier modes of the flow-field  $\hat{\mathbf{q}}(\mathbf{x}, f)$  can be expanded as:

$$\hat{\mathbf{q}}(\mathbf{x}, f) = \sum_{j=1}^{\infty} a_j(f) \psi_j(\mathbf{x}, f), \quad (5.3)$$

where  $a_j(f) = \langle \hat{\mathbf{q}}(\mathbf{x}, f), \psi_j(\mathbf{x}, f) \rangle_x$ . According to Towne *et al.* [7], for the space-only POD, a stochastic flow ensemble is obtained from snapshots of the flow field at different time instances, representing a realization of the stochastic process. The time evolution of the flow has no effect on those modes, and a temporal correlation of the data is not possible. Therefore, the space-only POD modes are composed of structures at many frequencies, which do not necessarily evolve coherently in time. In the spectral POD, on the other hand, the stochastic ensemble is based on realizations of the time-dependent flow. Each SPOD mode is perfectly correlated with itself at all times, and thus they provide spatiotemporal coherent structures.

The SPOD is applied to the near-pressure field of the isolated jet. Data are extracted on a vertical plane crossing the center of the nozzle. The plane extends  $15D_j$  in the axial direction, relative to the nozzle exit plane, in order to capture low frequency fluctuations. In the radial direction, the plane extends up to  $2.5D_j$  from the jet centerline. Thus, only the upper half of the jet is considered, enforcing an axisymmetry condition. Based on the available flow-field data of 621 snapshots, 8 blocks of 128 snapshots are created, with an overlap of 50%. A standard Hann window is applied. This allows for the decomposition of the pressure field onto 8 independent modes, orthogonal to each other at each computed frequency. The energy content of each mode is plotted in Fig. 5.25 for the isolated jet at  $M_a = 0.5$ .

The spectral energy content shown in Fig. 5.25 is obtained from the eigenvalues  $\lambda_j(f)$  extracted from the SPOD analysis. The results show a progressive decrease of  $\lambda_j(f)$  for higher mode numbers. The large separation between modes 1 and 2 indicates that

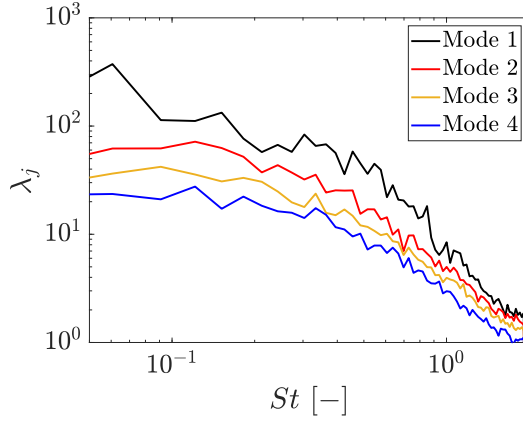


Figure 5.25: Energy content of each SPOD mode as function of frequency, obtained for  $M_a = 0.5$ .

the former is dominant and the flow exhibits a low-rank behaviour [8]. The eigenvectors  $\psi_j(\mathbf{x}, f)$  represent the modal shape. Contour plots in Fig. 5.26 represent the shapes of the two most energetic modes at  $St = 0.18$ . The eigenvalues shown above each contour plot represent the fraction of the total energy content for that frequency; the first two modes collect 60% of the total energy, and mode 1 alone has 36%. This mode is shown to resemble structures that evolve coherently in space and time. For the remainder of the analysis, only the first SPOD mode is used. Based on the block length selected for the FFT of the near-field pressure data, the wavepacket structures are concentrated in the most energetic mode. Higher order modes show a behaviour different from wavepacket-like structures and are disregarded. This is in agreement with analyses by Breakey *et al.* [24] and Unnikrishnan *et al.* [27], where the results from the first SPOD mode compare well with analytical methods and experimental data. Therefore, proceeding in the investigation on the behaviour of the structures, the amplitude of mode 1 is then extracted in the axial direction for a fixed height, as shown in Fig. 5.27.

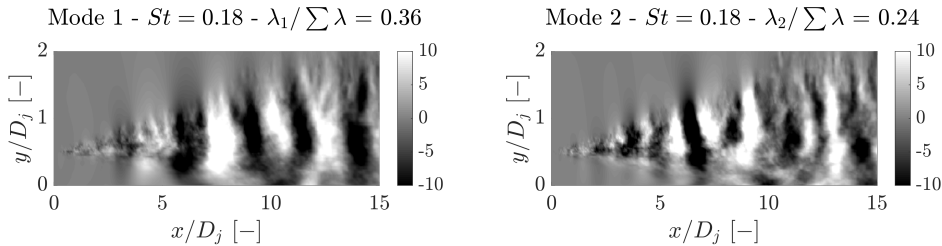


Figure 5.26: First and second SPOD eigenvectors, for a frequency of  $St = 0.18$ , obtained for  $M_a = 0.5$ .

The curves in Fig. 5.27 display a sinusoidal shape as expected for instability waves or wavepackets. This indicates that SPOD extracts only the coherent part of the pressure field while the acoustic waves, which cause the plateau in the axial distribution of

the pressure fluctuations, are filtered out. It can also be seen that the instability waves start growing at  $x = 2D_j$  in agreement with the results of Suzuki and Colonius [5]. The frequency dependence of mode 1 is shown in Fig. 5.27a. For  $St = 0.18$ , the amplitude of the wave increases in the axial direction, but no saturation or decay is found. At approximately  $x = 8D_j$ , non-linearities due to the rotational component of the jet flow become significant, as remarked by the modification of the sinusoidal behaviour in the plot. At higher frequencies ( $St = 0.49$ ), growth, saturation and decay occur upstream of the non-linear region. The spatial dependence in the radial direction, for  $St = 0.18$  (Fig. 5.27b), shows a similar trend as the previous figure, with an increase in amplitude for locations closer to the jet axis. For a single axial position ( $x = 6D_j$ ), the radial decay is plotted in Fig. 5.28, similarly as done in Section 5.6.1. The results are consistent with the ones shown in Fig. 5.20, where the hydrodynamic pressure field is divided into linear and non-linear regions. Therefore, the SPOD analysis confirms the results concerning the exponential pressure decay in the radial direction, described in the previous section.

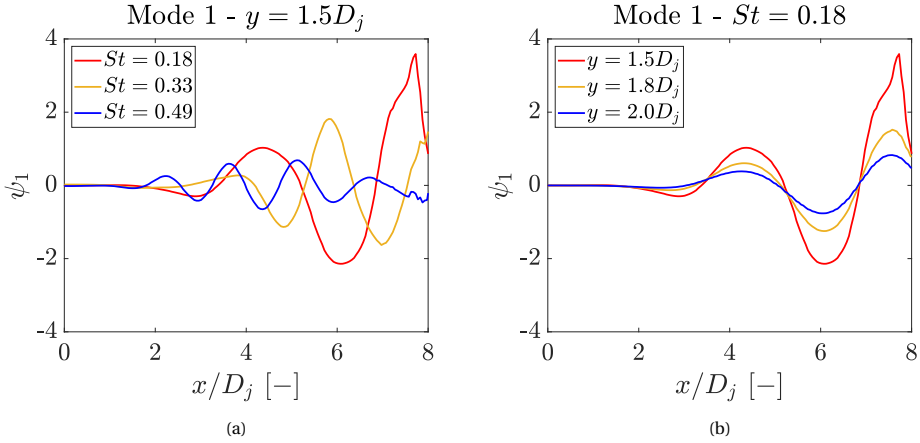


Figure 5.27: Characteristics of SPOD mode 1 in the axial direction, as a function of (a) frequency and (b) radial position. Data obtained for  $Ma = 0.5$ .

The spatial modulation of the instability waves, as plotted in Fig. 5.27, can be fitted with a Gaussian function [23]. In Fig. 5.29, this fitting procedure is applied to SPOD mode 1 at  $y = 2.0D_j$  for  $St = 0.18$  and  $St = 0.33$ . This height is chosen to avoid contamination of the data by non-linearities in the jet plume. The Gaussian curves, aside from accurately describing the shape of the instability waves, offer the possibility to approximate the axial behaviour of the pressure fluctuations  $\hat{P}(x, f)$  caused by coherent structures. The width of the Gaussian curve is related to the hydrodynamic wavelength  $\lambda_H(f)$  of the structures, as given by Eq. 5.4 [28, 29], for a given frequency:

$$\hat{P}(x, f) = \hat{P}_{\max}(f) e^{-\left(\frac{x - x_{\max}(f)}{\lambda_H(f)}\right)^2}, \quad (5.4)$$

where  $\hat{P}_{\max}(f)$  and  $x_{\max}(f)$  represent the maximum amplitude of the Gaussian envelope and its axial position, respectively. Therefore, by using Eq. 5.4, the hydrodynamic wave-

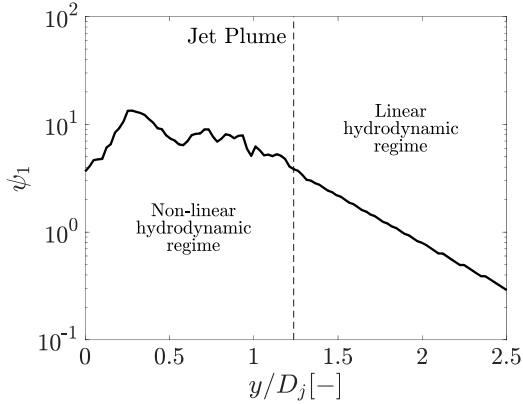


Figure 5.28: Radial decay of SPOD mode 1 for  $x = 6D_j$  and  $St = 0.18$ . Data obtained for  $Ma = 0.5$ .

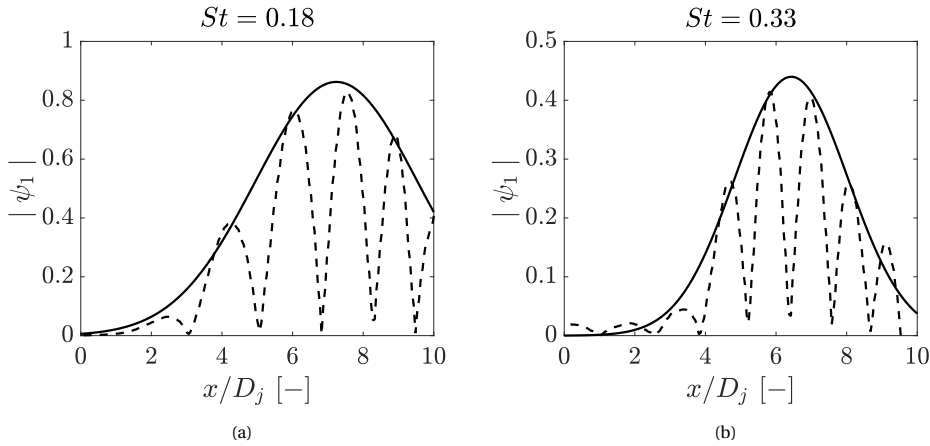


Figure 5.29: Gaussian envelopes around SPOD mode 1, at  $y = 2.0D_j$  for frequencies  $St = 0.18$  and  $St = 0.33$ . Data obtained for  $Ma = 0.5$ .

length can be determined for every frequency and, consequently, the convective velocity  $U_c$  of the structures ( $U_c = \lambda_H f$ ). Fig. 5.30 shows the convective velocity for a wide range of frequencies, calculated from the fitted Gaussian curves of SPOD mode 1 at  $y = 2D_j$ . At low frequencies ( $St < 0.15$ ), no results are present due to the non-linear effects from the plume affecting the data fitting. Similarly, at high frequencies ( $St > 0.7$ ), the quality of the fitting does not allow for conclusions on the hydrodynamic wavelength. In the mid-frequency range, a consistent value of  $U_c \approx 0.6U_j$  is obtained up to  $St = 0.52$ . This is in agreement with the values usually applied in linear stability theory and wavepacket modelling of jets [4, 9]. The results also agree with those obtained by Arndt *et al.* [3], who used POD eigenfunctions for the estimation of the convective velocity. For  $St > 0.52$ , a sudden jump is observed, and the convective velocity approximates the nominal jet speed. It is hypothesized that, at the height where this velocity is computed, the pressure

fluctuations generated at those mid/high frequencies already display acoustic characteristics (refer to Fig. 2.3), and therefore no coherent behaviour can be obtained.

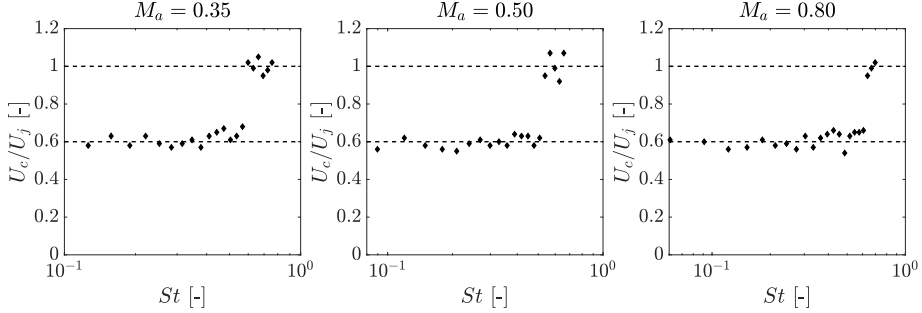


Figure 5.30: Convective velocity ( $U_c$ ) of the structures present in the jet mixing-layer, as a function of frequency, obtained from the axial evolution of SPOD Mode 1 for three setpoints.

Based on the results of the convective velocity, the SPOD mode 1 represents the coherent hydrodynamic structures in the jet. Given the good agreement of the Gaussian fitting with the axial distribution of pressure fluctuations, Eq. 5.5 is used for the far-field noise scaling from axial position 1 to axial position 2 (Scaled SPL):

$$\text{SPL}_{x_1}(f) = \text{SPL}_{x_2}(f) e^{\left[ -\left( \frac{x_1 - x_{\max}(f)}{\lambda_H(f)} \right)^2 + \left( \frac{x_2 - x_{\max}(f)}{\lambda_H(f)} \right)^2 \right]}. \quad (5.5)$$

The maximum pressure at each frequency  $\hat{P}_{\max}$  is canceled out when dividing the amplitudes at the two axial positions. Therefore the only necessary inputs are the hydrodynamic wavelength, which has been calculated along with the convective velocity, and the axial position of the Gaussian peak, which depends on frequency as shown in Fig. 5.31 for the three jet setpoints. The positions  $x_1$  and  $x_2$  are considered to be the flat plate lengths ( $L = 4D_j$ ,  $L = 5D_j$  and  $L = 6D_j$ ), which is consistent with the trailing-edge location for each case.

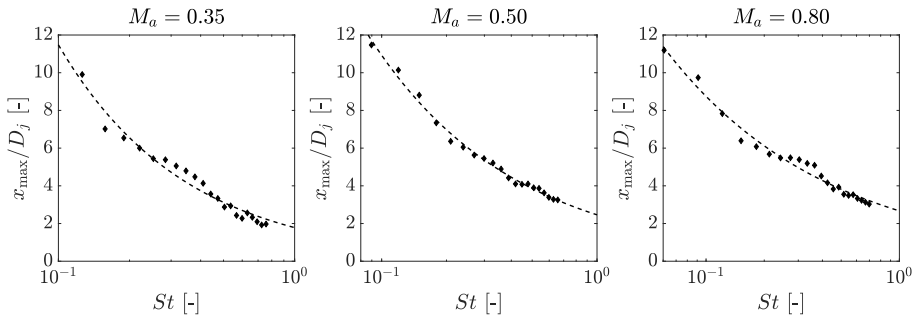


Figure 5.31: Axial position of the Gaussian envelope peak ( $x_{\max}$ ), as a function of frequency for three setpoints.

With all the inputs available, the far-field noise levels of the cases with  $L = 4D_j$  and  $L = 5D_j$  are scaled to a position  $x = 6D_j$  (Scaled SPL) through Eq. 5.5 and plotted against the spectra for the actual case with  $L = 6D_j$ . This is equivalent to divide the far-field SPL of each installed configuration by the amplitude of the Gaussian at the respective trailing edge position, for every frequency. These spectra are shown in Fig. 5.32, for constant plate heights  $h = 1.25D_j$  and  $h = 1.5D_j$ , and  $Ma = 0.5$ . At low frequencies  $St < 0.06$ , results are omitted since an appropriate Gaussian fitting was not possible due to the limited amount of available datapoints. The scaling in the axial direction is performed only in the frequency range where the convective velocity is equal to  $0.6U_j$  (up to  $St = 0.50$ , as shown by the dotted line).

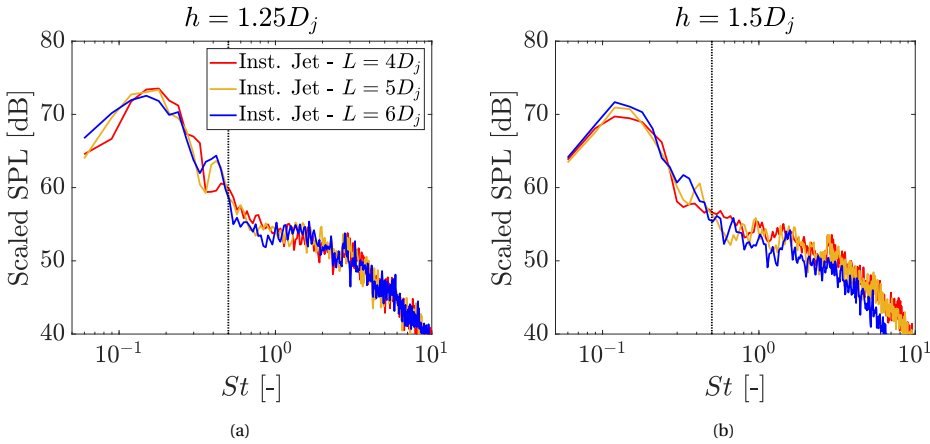


Figure 5.32: Far-field spectra of installed jets for a fixed radial position, scaled from positions  $L = 4D_j$  and  $L = 5D_j$  to  $L = 6D_j$  through the amplitude of the Gaussian fitting of SPOD Mode 1. Spectra obtained for  $\theta = -90^\circ$  and  $Ma = 0.5$ .

A good agreement is found for the scaled spectra for both plate heights, with minor deviations for very low frequencies ( $St < 0.1$ ) and when approaching the maximum frequency where  $U_c = 0.6U_j$  ( $St = 0.5$ ). Since the scaling factor is frequency dependent, the spectral shape for the scaled curves changes, as well as the frequency of the spectral peak. Spectra for the other jet setpoints are shown in Fig. 5.33, with a good agreement between the curves as well, indicating that the procedure works for all investigated flow conditions.

The results show that the Gaussian fitting is an adequate parameter for scaling the pressure fluctuations that are scattered by flat plates with different lengths. To obtain this fitting, it is either necessary to have a predicted distribution of coherent structures, or to obtain it *a priori* from a narrow-band analysis of similar coherent structures in the isolated jet flow with a dedicated technique such as Spectral POD. The results also show that jet-installation noise is essentially related to coherent hydrodynamic structures present in the jet mixing layer. The characteristics of these structures determine the far-field noise signature of the installation effects for a given trailing edge position (scattering region). The acoustic waves produced by quadrupole sources in the jet do

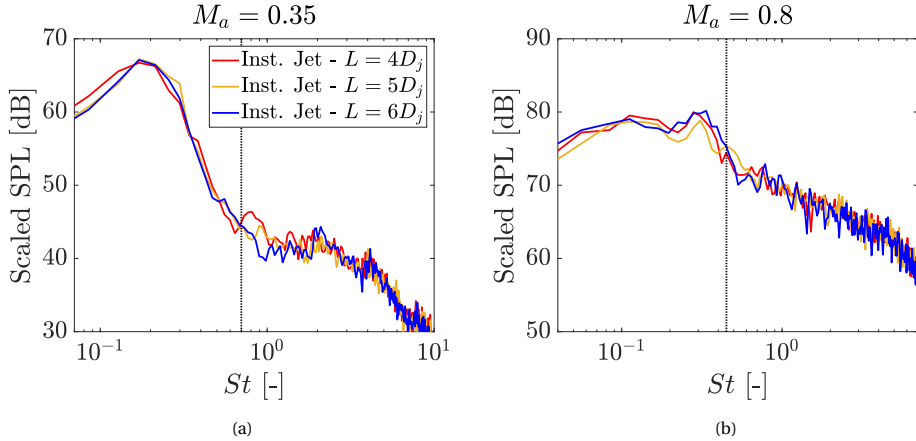


Figure 5.33: Far-field spectra of installed jets for a fixed radial position ( $h = 1.25D_j$ ), scaled from positions  $L = 4D_j$  and  $L = 5D_j$  to  $L = 6D_j$  through the amplitude of the Gaussian fitting of SPOD Mode 1. Spectra obtained for  $\theta = -90^\circ$ .

not contribute to installation noise and can be considered uncorrelated to the acoustic dipoles on the surface. With scaling laws found for both radial and axial directions, fast predictions of jet-installation noise can be performed without the need of investigating several geometric configurations. With results from the isolated jet and one installed configuration, the far-field spectra for other plate geometries can be found with relatively good accuracy, thus reducing the need for extensive parametric analyses.

## 5.7. CONCLUDING REMARKS

A high-fidelity numerical investigation of an installed jet is performed using LBM-VLES. A configuration comprised by a single-stream nozzle and a nearby flat plate is chosen for the analyses. The simulation results are validated through comparison with experimental data, obtained from tests at NASA Glenn. The far-field spectral results, obtained from the Ffowcs-Williams Hawkins analogy, indicate a large noise increase at low and mid frequencies, followed by reflection or shielding of the quadrupole sources, associated to jet noise, at high frequencies. Through dilatation field plots, this amplification is shown to be caused by the hydrodynamic waves generated by the jet that are bounded by the plate and, as they reach a geometric discontinuity (surface trailing edge), they are scattered to the far-field as noise. This new source displays a dipolar characteristic in the azimuthal direction, and a cardioid directivity pattern in the polar direction. Maximum noise levels are obtained in the upstream direction of the jet axis, whereas in the downstream direction there is no amplification.

The geometry of the plate also affects the far-field noise. Moving the plate closer to the jet results in higher noise levels, particularly at mid frequencies, whereas increasing the plate length results in low-frequency noise increase. The different trends in frequency noticed in both radial and axial analyses are then related to the compactness characteristics of the sources. In order to determine the compactness level of a source

with respect to a trailing edge position, two inequalities based on the wavenumber and the relative distance between source and edge are used. For that purpose, the position of the sources must be known beforehand. An equivalent source localization method is proposed by fitting a set of near-field spectra into a decay law, for each frequency of interest. Thereafter, envelopes based on the compactness parameters are determined, which are related to features in the installed far-field spectra. The limit for non-compact eddies agrees with the frequency of the spectral peak, whereas the envelope for compact eddies coincides with the frequency limit of the installation effects. The analysis also yields the existence of a transition region, where neither inequality is satisfied, which is characterized by a progressive decay in amplitude. This method and conclusions are shown to be valid for low and mid Mach number jets. For  $M_a = 0.8$ , it is possible that the far-field spectra is dominated by sources other than trailing-edge scattering, and thus the method fails to provide correct information on the spectral peak. Further research into this hypothesis is necessary.

The amplitude of the far-field spectra of the installed cases is also related to the near-field properties through scaling laws. For the radial direction, the plate is placed in the linear hydrodynamic region, where the pressure decays exponentially with increasing radial distance. This characteristic is also visible in the far-field results for the installed case. However, in order to obtain a better agreement, a frequency scaling is also necessary to match the spectral peak of different configurations. This can be performed using the compactness analysis with an equivalent source. Moreover, this exponential scaling is found to be valid only in the frequency range where the trailing edge is the dominant source.

In order to characterize the hydrodynamic pressure fluctuations along the axial direction, SPOD is applied in the near-pressure field to remove the contribution of acoustic fluctuations that contaminate the signal. The first SPOD eigenvector, which has the highest energy content, is shown to display the characteristics of instability waves, with a clear trend of growth, saturation and decay. This trend can be modelled with a Gaussian envelope, which is related to the hydrodynamic wavelength, thus being frequency-dependent. The amplitude of the Gaussian at different axial positions, for each frequency, is found to be an appropriate scaling parameter for the installed far-field noise. The scaled spectra from configurations with different plate lengths collapse in the entire frequency range of the installation effects. Therefore, in order to correctly assess the effects of the near-field characteristics on the far-field noise, it is necessary that the coherent part of the flow-field is deduced beforehand.

The methodologies developed in this chapter are shown to be valid when the plate trailing-edge is positioned in the linear hydrodynamic field of the jet. Therefore, the constraints for the validity of the approach are: no grazing flow on the plate and thus  $h/L > \tan(\delta)$ , where  $\delta$  is the spreading angle of the jet; the trailing edge must not be placed in the jet acoustic field, where there will be no sound amplification due to installation. Based on the results in this chapter, a conservative upper bound for the linear hydrodynamic field, in the frequency range of interest for the investigated plate lengths ( $St \approx 0.2$ ), would be  $h/D_j < 2.5$ . Additionally, for very short and very long plates (e.g.  $L/D_j < 3$  or  $L/D_j > 10$ ), a proper Gaussian fitting of the wavepacket in the isolated jet would not be possible.

It is concluded that the characteristics of the jet pressure field have a strong influence on the noise produced by the scattering at the plate trailing edge. The scaling analysis can be used, for example, to save on costs of simulating or testing several geometric configurations. If the flow-field information is available for the isolated case, the data can be used to predict the far-field characteristics of the installation effects. The compactness analysis provides an interesting method for equivalent source localization, which outputs the frequency envelope of the noise amplification for the installed case. Therefore, by making use of the near-field properties of the jet, the surface can be dimensioned to restrict the frequencies where the amplification occurs or, for example, shift the far-field peak to frequencies where the scattering is no longer the dominant source, resulting in significant noise reductions.

## REFERENCES

- [1] L. Rego, F. Avallone, D. Ragni, and D. Casalino, *Jet-installation noise and near-field characteristics of jet-surface interaction*, *Journal of Fluid Mechanics* **895** (2020), [10.1017/jfm.2020.294](https://doi.org/10.1017/jfm.2020.294).
- [2] J. E. Ffowcs-Williams and L. H. Hall, *Aerodynamic sound generation by turbulent flow in the vicinity of a scattering half plane*, *Journal of Fluid Mechanics* **40**, 657 (1970).
- [3] R. E. A. Arndt, D. F. Long, and M. N. Glauser, *The proper orthogonal decomposition of pressure fluctuations surrounding a turbulent jet*, *Journal of Fluid Mechanics* **340**, 1 (1997).
- [4] D. Papamoschou, *Prediction of Jet Noise Shielding*, in *48th AIAA Aerospace Sciences Meeting Including the New Horizons Forum and Aerospace Exposition* (Orlando, FL, USA, 2010).
- [5] T. Suzuki and T. Colonius, *Instability waves in a subsonic round jet detected using a near-field phased microphone array*, *Journal of Fluid Mechanics* **565**, 197 (2006).
- [6] C. E. Tinney and P. Jordan, *The near pressure field of co-axial subsonic jets*, *Journal of Fluid Mechanics* **611**, 175 (2008).
- [7] A. Towne, O. T. Schmidt, and T. Colonius, *Spectral proper orthogonal decomposition and its relationship to dynamic mode decomposition and resolvent analysis*, *Journal of Fluid Mechanics* **847**, 821 (2018).
- [8] O. T. Schmidt, A. Towne, G. Rigas, T. Colonius, and G. A. Brès, *Spectral analysis of jet turbulence*, *Journal of Fluid Mechanics* **855**, 953 (2018).
- [9] A. V. G. Cavalieri, P. Jordan, T. Colonius, and Y. Gervais, *Axisymmetric superdirectivity in subsonic jets*, *Journal of Fluid Mechanics* **704**, 388 (2012).
- [10] C. Brown, *Jet-Surface Interaction Test: Far-Field Noise Results*, in *Proceedings of the ASME Turbo Expo 2012: Power for Land, Sea and Air* (Copenhagen, Denmark, 2012) pp. 1–13.

- [11] G. G. Podboy, *Jet-Surface Interaction Test: Phased Array Noise Source Localization Results*, [NASA/TM—2013-218085](#) (2013), [10.1115/GT2012-69801](#).
- [12] C. Brown and J. Bridges, *Small Hot Jet Acoustic Rig Validation*, Tech. Rep. (NASA/TM-2001-214234, Cleveland, OH, USA, 2006).
- [13] W. C. P. van der Velden, D. Casalino, P. Gopalakrishnan, A. Jammalamadaka, Y. Li, R. Zhang, and H. Chen, *Jet Noise Prediction : Validation and Physical Insight*, in *24th AIAA/CEAS Aeroacoustics Conference* (Atlanta, GA, USA, 2018) pp. 1–16.
- [14] G. Brès, J. W. Nichols, S. Lele, and F. E. Ham, *Towards Best Practices for Jet Noise Predictions with Unstructured Large Eddy Simulations*, in *42nd AIAA Fluid Dynamics Conference and Exhibit* (New Orleans, LA, USA, 2012).
- [15] T. Colonius, S. K. Lele, and P. Moin, *Sound generation in a mixing layer*, [Journal of Fluid Mechanics](#) **330**, 375 (1997).
- [16] J. Bridges and M. Wernet, *Establishing Consensus Turbulence Statistics for Hot Subsonic Jets*, in *16th AIAA/CEAS Aeroacoustics Conference* (Stockholm, Sweden, 2010) pp. 1–41.
- [17] R. W. Head and M. J. Fisher, *Jet/Surface Interaction Noise: - Analysis of Farfield Low Frequency Augmentations of Jet Noise due to the Presence of a Solid Shield*, in *3rd AIAA Aeroacoustics Conference* (Palo Alto, CA, USA, 1976).
- [18] A. V. G. Cavalieri, P. Jordan, W. R. Wolf, and Y. Gervais, *Scattering of wavepackets by a flat plate in the vicinity of a turbulent jet*, [Journal of Sound and Vibration](#) **333**, 6516 (2014).
- [19] P. Jordan and T. Colonius, *Wave Packets and Turbulent Jet Noise*, [Annual Review of Fluid Mechanics](#) **45**, 173 (2013).
- [20] M. J. Lighthill, *On Sound Generated Aerodynamically I. General Theory*, [Proceedings of the Royal Society of London. Series A. Mathematical and Physical Sciences](#) **211**, 564 (1952).
- [21] J. L. T. Lawrence, M. Azarpeyvand, and R. H. Self, *Interaction between a Flat Plate and a Circular Subsonic Jet*, in *17th AIAA/CEAS Aeroacoustics Conference* (Portland, OR, USA, 2011).
- [22] J. E. Ffowcs-Williams and D. L. Hawkings, *Sound Generation by Turbulence and Surfaces in Arbitrary Motion*, [Philosophical Transactions of the Royal Society A: Mathematical, Physical and Engineering Sciences](#) **264**, 321 (1969).
- [23] D. G. Crighton and P. Huerre, *Shear-layer pressure fluctuations and superdirective acoustic sources*, [Journal of Fluid Mechanics](#) **220**, 355 (1990).
- [24] D. E. S. Breakey, P. Jordan, A. V. G. Cavalieri, O. Léon, M. Zhang, G. Lehnasch, T. Colonius, and D. Rodríguez, *Near-field wavepackets and the far-field sound of a subsonic jet*, in *19th AIAA/CEAS Aeroacoustics Conference* (Berlin, Germany, 2013) p. 81.

- [25] L. Sirovich, *Turbulence and the dynamics of coherent structures, part I: coherent structures*, Quarterly of Applied Mathematics **XLV**, 561 (1987).
- [26] P. Welch, *The Use of Fast Fourier Transform for the Estimation of Power Spectra: A Method Based on Time Averaging Over Short, Modified Periodograms*, IEEE Transactions on Audio and Electroacoustics **15** (1967).
- [27] S. Unnikrishnan, A. V. G. Cavalieri, and D. V. Gaitonde, *Acoustically informed statistics for wave-packet models*, in *AIAA Journal*, Vol. 57 (American Institute of Aeronautics and Astronautics Inc., 2019) pp. 2421–2434.
- [28] S. C. Crow, *Acoustic gain of a turbulent jet*, in *Phys. Soc. Meeting, paper IE, vol. 6* (Boulder, CO, USA, 1972).
- [29] J. Laufer and T. Yen, *Noise generation by a low-Mach-number jet*, *Journal of Fluid Mechanics* **134**, 1 (1983).

# 6

## JET-INSTALLATION NOISE REDUCTION WITH FLOW-PERMEABLE TRAILING EDGES

*The aim of science is not to open the door to infinite wisdom,  
but to set a limit to infinite error.*

Bertolt Brecht

*This chapter reports the application of flow-permeable materials as a solution for reducing jet-installation noise. Experiments are carried out with a flat plate placed near a single-stream subsonic jet, with the trailing edge replaced with different flow-permeable inserts, such as a metal foam and a perforated plate structure. With the former, an overall noise mitigation is achieved in the entire frequency range where jet-installation noise is dominant, with 9 dB reduction at the spectral peak. The perforated plate provides lower noise reduction than the metal foam, particularly at low frequencies; this is linked to a higher resistivity of the former, which translates into a less effective pressure balance between the upper and lower sides of the plate near the trailing edge. Moreover, the plate with the metal-foam trailing edge has a distinct peak in noise at mid frequencies. Based on the analyses of different treated surface lengths, it is conjectured that the solid-permeable junction acts as a new scattering region, and thus its position also affects the far-field noise. Nonetheless, both types of inserts provide significant noise reduction and are potential solutions for mitigating jet-installation noise.*

---

Parts of this chapter have been included in Reference [1].

## 6.1. OBJECTIVES

PERMEABLE materials have been shown to be successful noise reduction solutions for several applications, such as flap side edge [2, 3], turbulence-impingement noise [4, 5] and turbulent boundary-layer trailing-edge (TBL-TE) noise [6–8]. Due to similarities between these noise generation mechanisms and JIN, it is believed that permeable materials are also effective solutions for the latter, particularly considering how they affect the near-field unsteady flow.

Therefore, this chapter aims to investigate the capability of flow-permeable materials to provide JIN reduction, when mounted at the trailing edge of the scattering surface. Firstly, it is conjectured that the pressure imbalance on a surface in the vicinity of a jet, caused by impinging waves on only one side, can be alleviated with permeable materials. Moreover, this effect would be coupled with a less abrupt impedance discontinuity at the trailing-edge region, given that the permeable material has an intermediary impedance between that of the solid surface and that of the flow downstream of the trailing edge. Therefore, these materials are expected to mitigate the trailing-edge source, potentially resulting in sound levels close to those of an isolated jet.

For this purpose, experiments are carried out with a flat plate placed in the vicinity of a jet, with the trailing-edge region replaced with permeable materials, such as a metal foam and a perforated plate structure. These materials have different properties, such as porosity and permeability, and thus it is possible to verify the effect of these parameters on the generated noise.

The jet velocity field is obtained using particle image velocimetry, whereas the acoustic measurements are performed with a microphone arc array. By analyzing the trends for different configurations and flow conditions, the effects of the permeable materials on JIN are determined.

## 6.2. EXPERIMENTAL SET-UP

The experiments are performed in the Free jet AeroacouSTic facility (FAST) at the von Kármán Institute for Fluid Dynamics (VKI). This facility comprises a circular jet rig located in a semi-anechoic room, as shown in Fig. 6.1a, with a cut-off frequency of 350 Hz [9]. The air is supplied by a 7 bar pressure line located beneath the test chamber, which is also bypassed to a seeding generator for PIV measurements. The seeded flow merges with the pressurized air in a buffer tank to ensure correct mixing. The jet blows vertically into an extractor equipped with a muffler [9]. In the anechoic chamber, a laser source and cameras are mounted for PIV measurements, whereas a microphone arc-array is present for the acoustic ones. The picture in Fig. 6.1b shows the jet nozzle installed with the flat plate inside the facility.

A circular convergent nozzle with an exit diameter  $D_j = 50$  mm and contraction ratio of 36:1 is designed based on the geometry of the SMC000 nozzle, which has been used for several investigations of isolated and installed subsonic turbulent jets [10–12], and described in Chapter 5. This nozzle, manufactured in aluminium, is attached to a straight pipe with 300 mm of diameter. A cut view of the nozzle is shown in Fig. 6.2 along with its main dimensions. The origin of the coordinates system used in the analyses is positioned at the center of the nozzle exit plane.

## 6.2. EXPERIMENTAL SET-UP

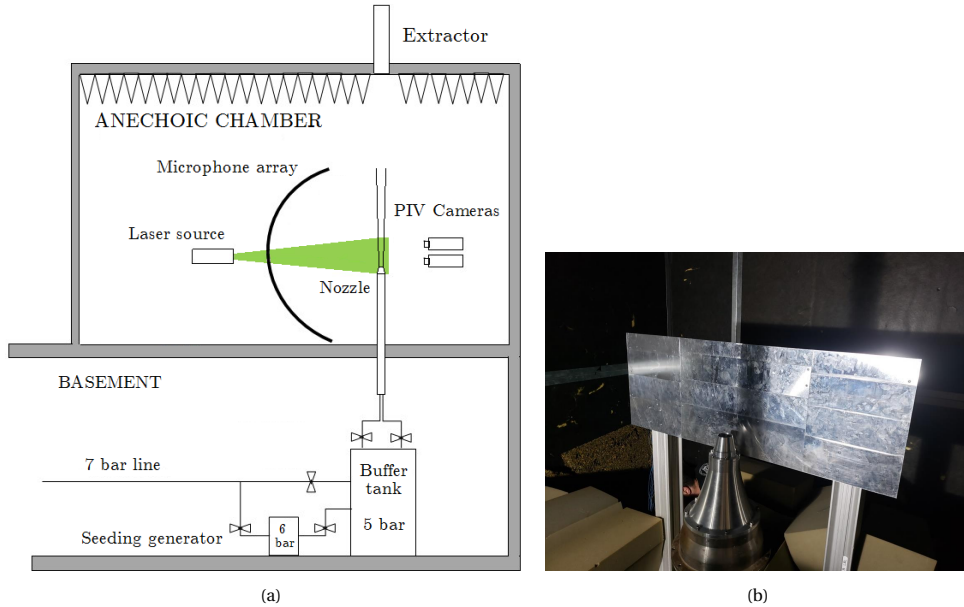


Figure 6.1: (a) Sketch of the FAST facility layout with a nozzle mounted in the anechoic chamber and the air supply system at the basement below. Adapted from [9]. (b) Nozzle mounted with the flat plate inside the facility.

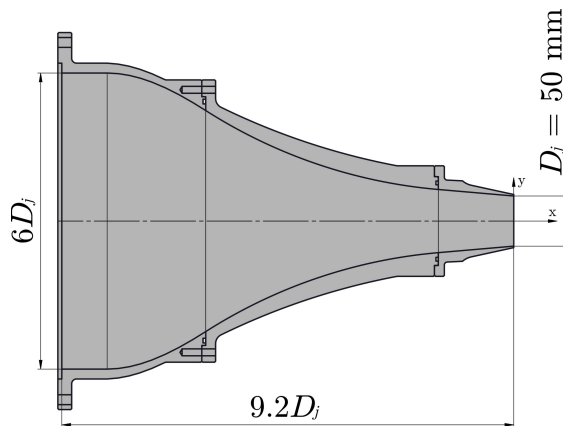


Figure 6.2: Cut view of the nozzle (dimensions as function of the exit diameter  $D_j = 50 \text{ mm}$ ).

For the installed configuration, a stainless steel flat plate is mounted in the vicinity of the nozzle. The plate is realized with a modular structure, which allows for different surface lengths to be easily investigated. The length of each part is shown in Fig. 6.3. The surface has a total dimension of  $500 \text{ mm} \times 1140 \text{ mm} \times 10 \text{ mm}$ . The large width is chosen to avoid side-edge scattering. The aft piece consists of a sharp trailing edge with a chamfer angle of  $40^\circ$ . This modular design also allows for an easy replacement

of the solid structure by the flow-permeable materials. Two pieces at the middle section (shown in blue in Fig. 6.3) can be replaced by the flow-permeable ones, allowing for the investigation of different porosity lengths ( $L_p = 1D_j$  and  $L_p = 3D_j$ ).

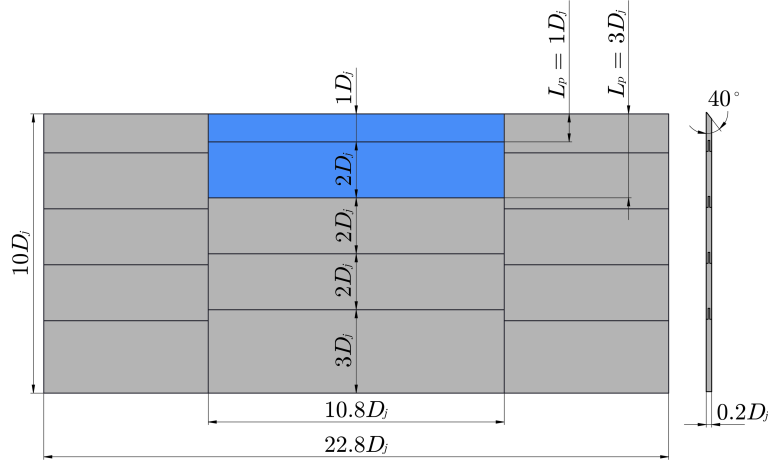


Figure 6.3: Modular flat plate (dimensions as function of the exit diameter  $D_j$ ). Pieces shown in blue can be replaced by the flow-permeable materials.

Different geometric cases are tested by changing the length  $L$  and height  $h$  of the plate. As shown in Fig. 6.4, the length is defined as the distance between the trailing edge and the nozzle exit plane, and the height as the radial position with respect to the jet centerline. A baseline installed case is defined with  $L = 6D_j$  and  $h = 1.5D_j$ . The leading edge of the plate is mounted upstream of the nozzle exit plane to avoid scattering at that region. A different plate length is also investigated ( $L = 8D_j$ ) for a fixed  $h = 1.5D_j$ , as well as a different radial position ( $h = 2D_j$ ) for a fixed  $L = 6D_j$ . Due to set-up constraints, it is not possible to mount the plate at a radial position  $h < 1.5D_j$ . Therefore, the effect of the plate height is addressed by moving it away from the jet. Moreover, with a length shorter than  $L = 6D_j$  at that position, it is possible that the relative noise increase due to installation effects would be much lower, particularly for mid and high jet Mach numbers, which could compromise the parametric analysis of the flow-permeable treatment.

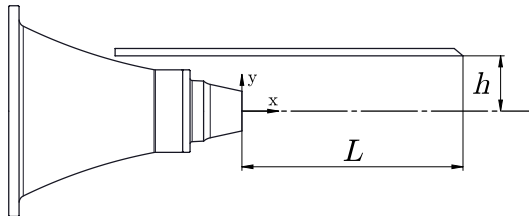


Figure 6.4: Installed jet configuration. Geometric cases are investigated by changing the flat plate length  $L$  and radial position  $h$ .

The tests are performed at three jet flow velocities with different acoustic Mach numbers  $M_a$ , where the jet velocity  $U_j$  is divided by the ambient speed of sound  $c_0$ . The flow characteristics such as the nozzle pressure ratio (NPR) and the static temperature ratio  $T_R$  are reported in Table 6.1, as well as the Reynolds number  $Re$ , based on the nozzle exit diameter. The measurements are conducted at static conditions, i.e. no flow external to jet, at average ambient conditions of  $p_{amb} = 100.6$  kPa and  $T_{amb} = 294$  K.

Table 6.1: Jet flow conditions in terms of acoustic Mach number ( $M_a$ ), nozzle pressure ratio (NPR), temperature ratio ( $T_R$ ) and Reynolds number ( $Re$ ).

Condition	$M_a$ [-]	NPR [-]	$T_R$ [-]	$Re$ [ $10^5$ ]
1	0.3	1.06	0.988	3.58
2	0.5	1.18	0.959	6.16
3	0.8	1.54	0.892	10.6

### 6.2.1. FLOW-PERMEABLE MATERIALS

Two types of noise reduction solutions based on flow-permeable materials are investigated in this chapter. The first one is an open-cell NiCrAl foam manufactured by the company Alantum. The metal foam is manufactured through electrodeposition of pure Ni on a polyurethane foam, which is subsequently coated with high-alloyed powder [13]. This material consists of a homogeneous microstructure with a three-dimensional repetition of a dodecahedron-shaped cell [8]. Rubio Carpio *et al.* [14] have investigated the application of this material with different cell diameters  $d_c$  for airfoil TBL-TE noise reduction. A structure with nominal  $d_c = 800\mu\text{m}$  is chosen for this work since its porosity and permeability characteristics are available, and significant TBL-TE noise reduction has been obtained with this structure [14]. Two inserts are manufactured for the plate, as shown in Fig. 6.5a in order to assess the effect of porosity length on the noise reduction. The second type of flow-permeable material consists of a 3D-printed perforated insert with straight holes connecting the upper and lower side of the plate, as shown in Fig. 6.5b. This insert is manufactured in R5, which is a liquid photopolymer that offers good surface finishing and strength properties [15]. The holes have a diameter  $d_h = 800\mu\text{m}$  and a spacing of  $l_h = 2$  mm.

The flow-permeable materials are characterized by properties such as porosity  $\sigma$ , inertial and viscous resistivity coefficients ( $R_I$  and  $R_V$ , respectively), and the permeability  $K$ , as reported in Chapter 3. For the metal foam, the porosity and permeability parameters were obtained by Rubio-Carpio *et al.* [14]. The former was obtained by measuring the density of small samples, whereas the latter was obtained from characterization experiments performed with a permeability rig [14]. A similar procedure has been carried out for the 3D-printed perforated material [16]. The properties of the materials are reported in Table 6.2.

### 6.2.2. INSTRUMENTATION AND MEASUREMENT TECHNIQUES



(a)



(b)

Figure 6.5: Flow-permeable trailing-edge inserts applied to the flat plate. (a) Metal foam -  $d_c = 800\mu\text{m}$ . Adapted from [8]. (b) Perforated -  $d_h = 800\mu\text{m}$ .

Table 6.2: Properties of the flow-permeable materials in terms of porosity ( $\sigma$ ), inertial ( $R_I$ ) and viscous ( $R_V$ ) resistivity, and permeability ( $K$ ).

Material	$\sigma$ [%]	$R_I$ [ $\text{m}^{-1}$ ]	$R_V$ [ $\text{s}^{-1}$ ]	$K$ [ $\times 10^{-9} \text{m}^2$ ]
Metal foam	91.7	2612	5390	2.71
Perforated	12.6	7283	9245	1.58

### FLOW FIELD MEASUREMENTS

A two-dimensional jet velocity field is obtained through planar PIV measurements at the  $xy$ -plane (normal to the nozzle exit). This method allows for the measurement of time-averaged velocity components  $u$  and  $v$  (in the axial and radial directions, respectively), and the r.m.s.  $u'_{\text{rms}}$  and  $v'_{\text{rms}}$ . The PIV measurements are performed only for the isolated jet configuration, since the investigated configurations (length and height) are chosen such to avoid grazing flow on the surface. It has been shown in a previous investigation that this does not affect the noise generated by turbulence mixing [17].

Seeding particles are produced by a PIVTEC Pivpart45 generator, comprised by 45 Laskin nozzles and using Shell Ondina 919 oil, with average size of  $1\mu\text{m}$ . These particles have a relaxation time of about  $1\mu\text{s}$  [18], which is suitable to follow the flow acceleration in the nozzle. The illumination is provided by laser pulses generated with a double-cavity Quantel CFR200 Nd:YAG system. This equipment provides a laser wavelength of  $532\text{nm}$ , with a maximum energy of  $200\text{mJ/pulse}$ , and a pulse duration of  $7\text{ns}$ . Two LaVision Imager SX4M cameras (resolution:  $2360 \times 1776$  pixel; frame rate:  $15\text{Hz}$ ; pixel size:  $5.5 \times$

## 6.2. EXPERIMENTAL SET-UP

5.5  $\mu\text{m}$ ; minimum time interval: 250 ns; digital output: 12 bit), positioned 0.5 m distant of the jet axis, are used for image recording. The cameras are equipped with two Nikkor lenses of 50 mm focal length. This configuration allows for measurements of two fields-of-view (FOV), in order to capture a larger portion of the jet development, as shown in Fig. 6.6a. The FOVs of each camera are shown in Fig. 6.6b with an overlap of  $1.25D_j$  between them. The final FOV has a dimension of  $12D_j \times 4D_j$  (0.6 m  $\times$  0.2 m), and it is shown by the black lines. The resolution in the final FOV is approximately 6 pixel/mm.

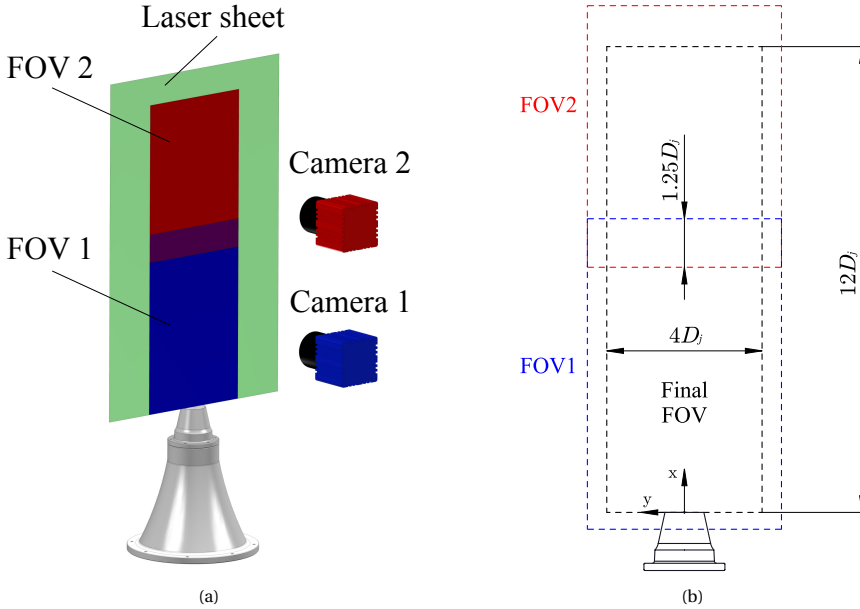


Figure 6.6: (a) Concept of the PIV set-up with 2 cameras and 2 fields-of-view. (b) Fields-of-view from each camera (blue and red planes) and final FOV (black), with dimensions.

With this set-up, 1000 pairs of particle images are acquired with a sampling rate of 15 Hz. The illumination and image acquisition are triggered synchronously by the LaVision DaVis 8.4 software, which is also used for the post-processing of the images. The separation time between image pairs is tuned with respect to the jet velocity in order to obtain a maximum of 25 pixels displacement at the jet core. This value is chosen to ensure a displacement of at least 3 pixels at regions of lower velocity. A multi-pass cross-correlation algorithm [19] with window deformation [20] is applied. The final interrogation window size is  $24 \times 24 \text{ pixel}^2$  with an overlap factor of 75%, which provides a final spatial resolution of 4 mm and a vector spacing of 1 mm. Spurious vectors, in the order of 1% of the total amount, are discarded by applying a universal outlier detector and are replaced by interpolation based on adjacent data [21]. The main parameters of the PIV set-up are reported in Table 6.3.

The estimation of the uncertainty in the PIV measurements is performed following the method proposed by Wieneke [22]. The calculations result in a maximum uncertainty of  $0.03u$  for the mean velocity, and  $0.04u'_{rms}$  inside the potential core region. At

Table 6.3: PIV set-up and acquisition parameters.

Parameter	Value
Cameras	2 x LaVision Imager SX4M
Acquisition frequency [Hz]	15
Max. pixel displacement [px]	25
Field-of-view 1-2 [mm]	400 x 310
Final field-of-view [mm]	600 x 200
Spatial scaling factor [px/mm]	6
Interrogation window [px <sup>2</sup> ]	24 x 24
Overlap factor [%]	75
Vectors per velocity field	600 x 200
Vector spacing [mm <sup>2</sup> ]	1 x 1

the lipline ( $y = 0.5D_j$ ), due to the strong flow unsteadiness, maximum uncertainty values of  $0.06u$  and  $0.08u'_{rms}$  are obtained.

#### ACOUSTIC MEASUREMENTS

The acoustic measurements are carried out with 12 Bruel & Kjaer 4938 1/4" microphones (frequency range: 4 Hz to 70 kHz; pressure-field response:  $\pm 2$  dB; max. output: 172 dB ref.  $2 \times 10^{-5}$  Pa). The microphones are integrated to Bruel & Kjaer 2670 - 1/4" microphone preamplifiers, and a Bruel & Kjaer NEXUS Type 2690-A conditioner is also used to amplify the recorded signals. The microphones are mounted on an arc-array dimensioned for measurements at 1 m radius ( $20D_j$ , centered at the origin of the coordinates system). The polar angle follows the convention of  $\theta = 0^\circ$  in the upstream direction of the jet axis. Therefore, the microphone at  $\theta = 90^\circ$  is aligned with the nozzle exit. The microphones are mounted from  $\theta = 40^\circ$  to  $\theta = 150^\circ$ , spaced of  $10^\circ$ , as shown in Fig. 6.7.

The arc-array is mounted at the reflected side of the plate (jet in between the plate and array), in order to assess the effect of the flow-permeable materials on the reflection of jet acoustic waves as well. The measurements are performed with a sampling frequency of 51.2 kHz for 20 seconds. For post-processing, the acoustic data are split into blocks of 2048 samples for each Fourier transform, and windowed with a Hanning weighting function with 50% overlap. These parameters result in a frequency resolution of 25 Hz. The spectra shown in the following sections have been also scaled to an observer at a distance of  $100D_j$  from the origin, similarly as performed in the JIN benchmark studies at NASA Glenn [10], as well as in Chapter 5.

### 6.3. JET FLOW FIELD

In this section, the flow field of the isolated jet is discussed. The PIV measurements are performed for the 3 investigated acoustic Mach numbers and the results are displayed in terms of time-averaged axial velocity  $u$  and r.m.s. ( $u'_{rms}$ ). The jet development for  $Ma = 0.5$  is shown in the contour plot in Fig. 6.8. The region corresponding to the potential core and the downstream velocity decay can be detected, as well as the spreading of the jet and symmetry with respect to the centerline.

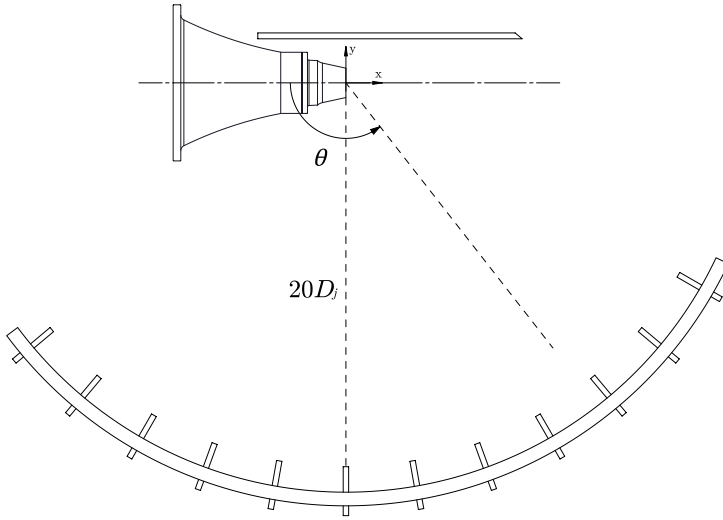


Figure 6.7: Sketch of the microphone arc-array for far-field measurements. 12 microphones are placed from 40° to 150° ( $\theta = 0^\circ$  is upstream of the jet axis), spaced of 10°. The array is mounted at the reflected side of the plate for the installed configuration.

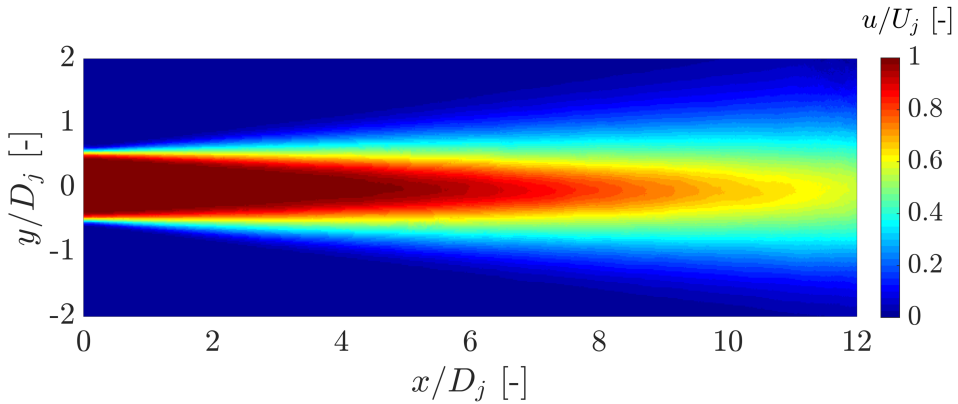


Figure 6.8: Contour plot of the time-averaged jet axial velocity  $u$  for a  $M_a = 0.5$  condition.

The velocity profiles are extracted at the jet centerline and plotted in Fig. 6.9. The quantities are non-dimensionalized by the respective jet nominal velocity  $U_j$ . The potential core length  $X_c$ , defined as the distance between the point where  $u = 0.98U_j$  and the nozzle exit, is reported in Table 6.4 for all jet velocities. These values are compared with results obtained from Witze’s equation for predicting the potential core length  $X_W$  of compressible free jets [12, 23]:

$$\frac{X_W}{D_j} = \frac{4.375(\rho_j/\rho_\infty)^{0.28}}{1 - 0.16M_j}, \quad (6.1)$$

where  $\rho_j$  and  $\rho_\infty$  are the jet and ambient densities, respectively. A good agreement is obtained between the experimental and predicted results. The centerline velocity decay downstream of the potential core is also shown to follow the trend defined by Witze with the equation [23]:

$$\frac{u}{U_j} = 1 - e^{\alpha/(1-x/X_W)}, \quad (6.2)$$

where  $\alpha$  is a constant equal to 1.43 [12].

The increase in potential core length with the jet velocity is related to the change in the size of the structures in the mixing-layer with the jet Reynolds number [23]. For  $Ma = 0.8$ , the structures are likely to be smaller and thus, the merge of the shear layer at the centerline occurs further downstream. This is also confirmed by the r.m.s. of velocity fluctuations, plotted in Fig. 6.9b, which are also lower for higher jet velocities.

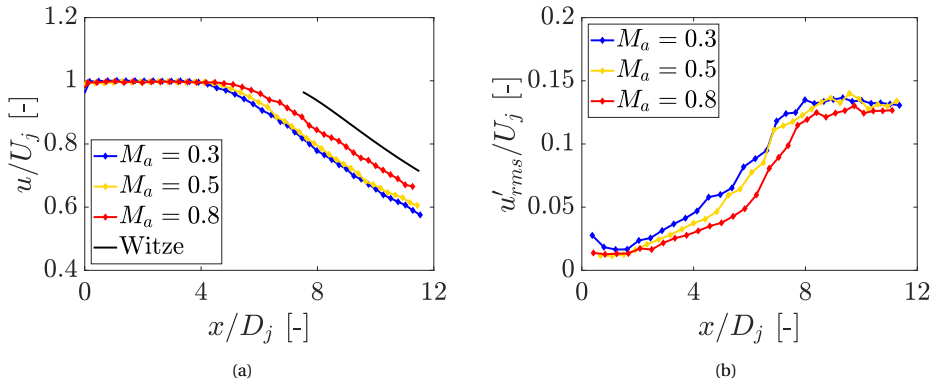


Figure 6.9: Profiles of (a) time-averaged axial velocity and (b) r.m.s. of axial velocity at the jet centerline for three jet velocities. The centerline velocity decay follows the trend defined by Witze [23].

Table 6.4: Potential core lengths obtained from experimental measurements ( $X_c$ ) and Witze's equation ( $X_W$ ) for three jet velocities.

$Ma$ [-]	$X_c/D_j$ [-]	$X_W/D_j$ [-]
0.3	4.4	4.6
0.5	5.0	5.1
0.8	5.4	5.8

Velocity profiles in the radial direction are also obtained at two axial stations, corresponding to the trailing-edge positions of the investigated installed jet configurations ( $x = 6D_j$  and  $x = 8D_j$ ). The profiles are plotted in Fig. 6.10, along with a line at  $y = 1.5D_j$ , which is the radial position where the plate is closest to the jet, for  $Ma = 0.3$ . Similar results have been obtained for the other jet velocities. It is shown that the axial velocity is zero at  $y = 1.5D_j$  for  $x = 6D_j$  and, therefore, a plate with a trailing edge at this position

is located outside of the plume. Conversely, for  $x = 8D_j$ , at  $y = 1.5D_j$ , the local axial velocity is non-zero and equal to  $0.05U_j$ . However, due to the relatively low velocity at this point, it is not likely that the surface significantly changes the characteristics of the turbulent structures in the mixing-layer, i.e. no changes in the noise due to turbulence mixing are expected even for the longest surface. These results also allow for the calculation of the jet spreading angle  $\delta$ . Values of  $\delta = 9^\circ$  ( $M_a = 0.3$ );  $\delta = 8.9^\circ$  ( $M_a = 0.5$ ) and  $\delta = 8.6^\circ$  ( $M_a = 0.8$ ) are obtained. These results are consistent with those from the NASA Glenn tests [12], and they confirm that the jet is fully turbulent.

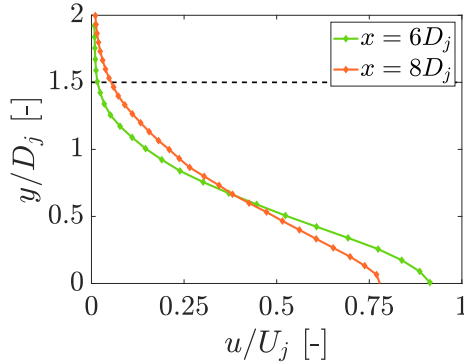
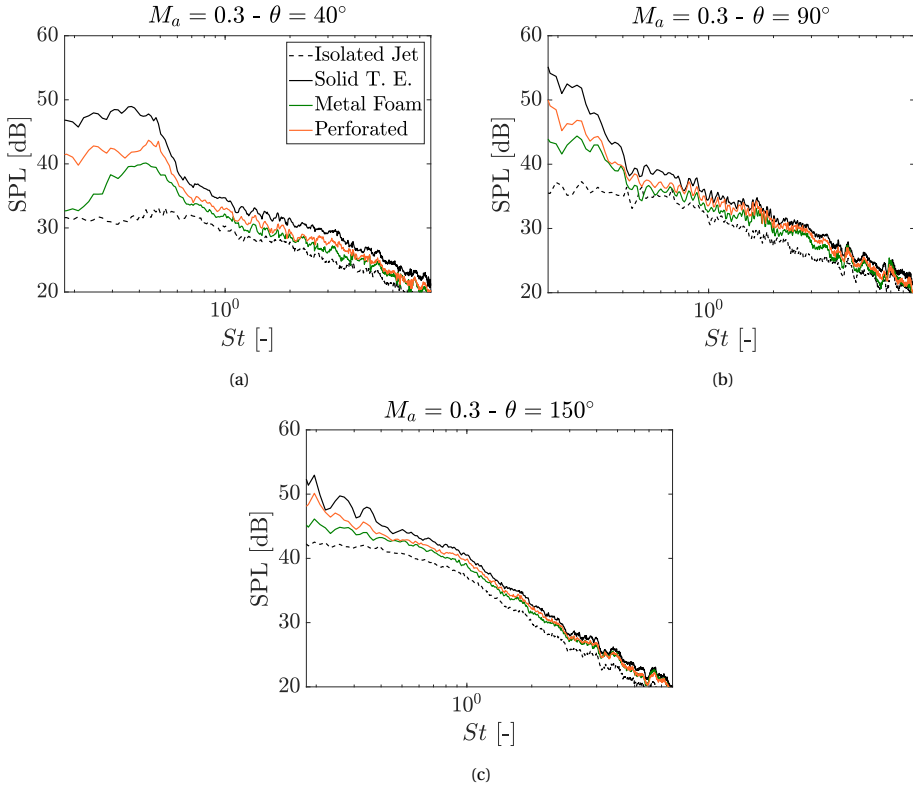


Figure 6.10: Profiles of time-averaged axial velocity in the radial direction at three axial stations. The dashed line corresponds to the closest flat plate position, relative to the jet in the installed configurations.

## 6.4. FAR-FIELD ACOUSTIC RESULTS

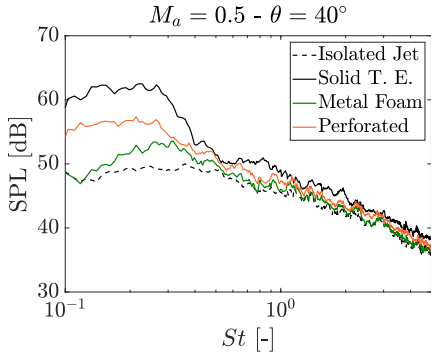
In this section, the results of the acoustic measurements for the installed jet with flow-permeable materials are reported and compared with the isolated and installed (solid trailing edge) jets, initially for the baseline plate configuration ( $L = 6D_j$  and  $h = 1.5D_j$ ). Two types of flow-permeable materials, with different porosity and resistivity, are investigated: a metal foam and a perforated plate with straight holes; both inserts have a length  $L_p = 3D_j$ . The results are displayed in Fig. 6.11 as Sound Pressure Level (SPL - ref.  $2 \times 10^{-5}$  Pa) versus Strouhal number  $St$  ( $St = f \times D_j / U_j$ ), at three polar angles ( $\theta = 40^\circ$ ,  $\theta = 90^\circ$  and  $\theta = 150^\circ$ ) and different jet velocities. The spectra have been plotted starting at a frequency of 350 Hz ( $St = 0.18$  for  $M_a = 0.3$ ), which is the minimum value for which the room has anechoic properties.

Firstly, comparing the spectra for isolated and installed jets (solid plate), it is shown that installation effects are responsible for a strong noise increase at low and mid frequencies; for  $M_a = 0.3$  and  $\theta = 40^\circ$ , there is a 17 dB increase in SPL with respect to the isolated case at the installed spectral peak ( $St = 0.37$ ). This strong noise amplification occurs up to  $St = 0.7$  for this condition, and at higher frequencies there is a constant shift of approximately 3 dB from the isolated curve, which characterizes reflection of acoustic waves on the surface. In the sideline direction ( $\theta = 90^\circ$ ), the SPL increases for  $St < 0.3$ , whereas for  $0.3 < St < 0.6$  there is a reduction with respect to the upstream direction. Therefore, for  $\theta = 90^\circ$ , the spectral peak shifts to a lower frequency, possibly

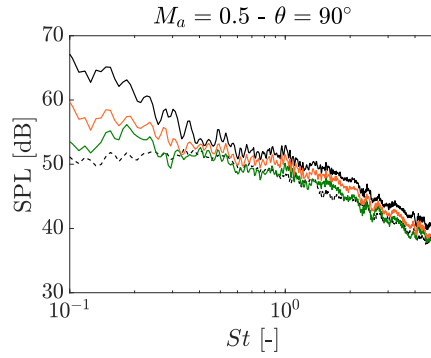


lower than the range where the measured data are reliable. This implies that the effect of the flow-permeable materials at the spectral peak might be not significant for a full-scale application, for which the peak is likely located below the hearing range. Nonetheless, for a frequency of  $St = 0.25$ , there is also a 17 dB increase with respect to the isolated case. In the downstream direction of the jet ( $\theta = 150^\circ$ ), there is a maximum amplification of 7 dB at  $St = 0.25$  due to the dipolar directivity of the noise generated by the plate, as well as increased noise from turbulence mixing by the jet. For higher jet velocities, similar trends are obtained, but the relative amplification with respect to the isolated noise levels is lower due to increased significance of turbulence-mixing noise.

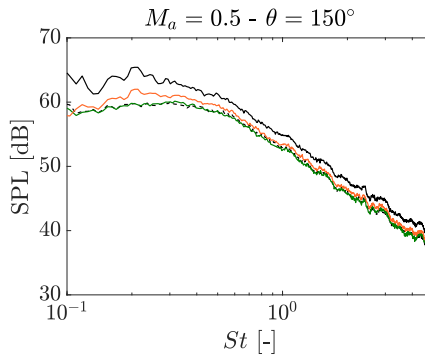
For the plates with flow-permeable treatments, the spectra show considerable noise reduction with respect to the solid installed case, mainly at low and mid frequencies, where installation effects are dominant. For  $Ma = 0.3$  and  $\theta = 40^\circ$ , reductions of 9 dB and 7 dB are seen at the spectral peak ( $St = 0.37$ ) for the metal foam and perforated inserts, respectively. The spectral amplitude is also reduced for  $St > 0.7$ , indicating that the flow-permeable materials, particularly the metal foam, reduce the effects of acoustic wave reflection on the surface. For  $\theta = 90^\circ$ , despite the strong low-frequency noise increase, there is still a significant reduction with the permeable trailing edges; 9 dB and 6 dB for  $St < 0.25$  with the metal foam and perforated, respectively. Finally, for  $\theta = 150^\circ$ , 5 dB and 3 dB reductions occur at  $St = 0.25$ . Moreover, since the installation effects are weak in



(d)



(e)



(f)

this direction, the noise levels with the flow-permeable trailing edges are similar to those of the isolated jet.

Comparing the two different treatments, the metal foam provides more benefits than the perforated inserts for all tested cases. Since the former has a higher permeability, it is likely that the differences in noise levels between the two cases can be attributed to a better pressure balance between the upper and lower sides of the plate for the metal foam case, thus reducing the surface pressure fluctuations near the trailing edge and, consequently, the noise due to scattering. The differences between the two flow-permeable configurations is more noticeable at low frequencies ( $St < 0.4$ ). For  $\theta = 40^\circ$ , the noise reduction with the perforated trailing edge is approximately constant with frequency for  $St < 0.5$ , whereas for the metal foam there is a change in the spectral shape, with a new distinct peak at  $St = 0.45$ . This is an indication that there is an additional noise source other than the trailing edge.

Similar trends are obtained for higher jet velocities. For  $Ma = 0.5$ , there is a similar absolute noise abatement at the spectral peak as the previous case (10 dB reduction with the metal foam and 6 dB with the perforated). For this velocity, the noise increase due to installation effects is relatively lower when compared to the  $Ma = 0.3$  jet. Therefore, with the same absolute noise reduction provided by the flow-permeable materials, the sound levels with the permeable materials are closer to those of the isolated configu-

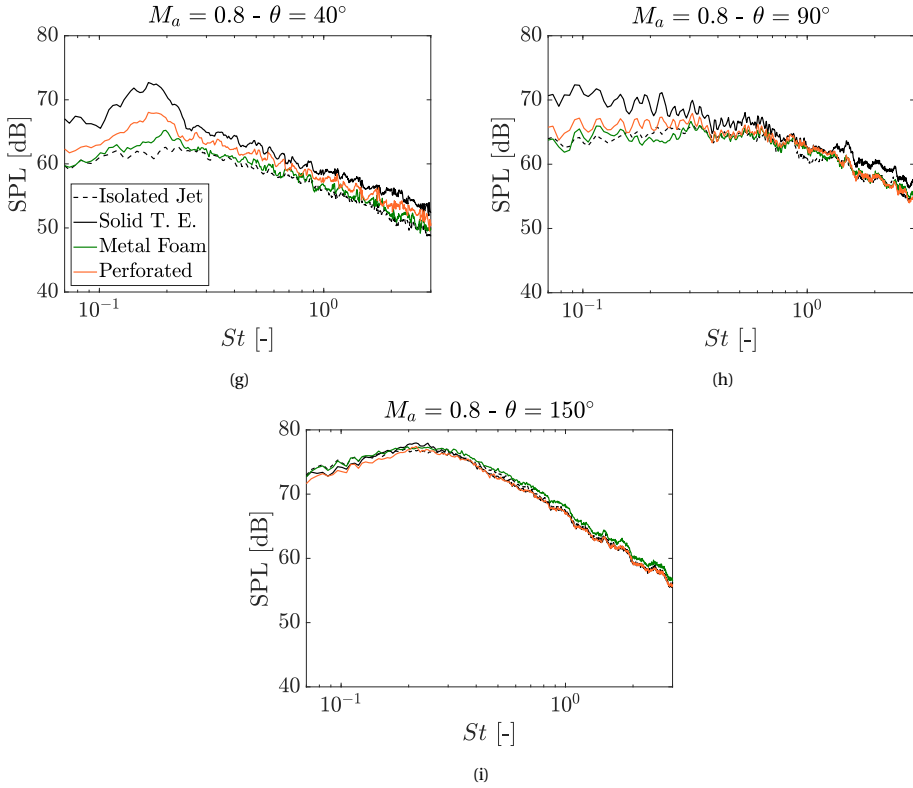


Figure 6.11: Isolated and installed jet spectra, with solid and flow-permeable surfaces ( $L_p = 3D_j$ ), at three polar angles ( $\theta = 40^\circ$ ,  $\theta = 90^\circ$  and  $\theta = 150^\circ$ ) and three velocities. (a), (b) and (c)  $M_a = 0.3$ . (d), (e) and (f)  $M_a = 0.5$ . (g), (h) and (i)  $M_a = 0.8$ .

ration. This effect becomes more visible for the  $M_a = 0.8$  jet, where the curves of both treated surfaces practically collapse with the isolated one for  $\theta > 90^\circ$ , indicating that the trailing-edge source has been completely mitigated in these cases.

The Overall Sound Pressure Level (OASPL) for each case is calculated at all polar angles by integrating the SPL spectra in the range of  $350 \text{ Hz} < f < 20 \text{ kHz}$  and the results are shown in the polar plots in Fig. 6.12, for three jet velocities.

The directivity plots show that the highest differences between isolated and installed (solid plate) cases are found in the upstream direction, which is consistent with noise from scattering at the plate trailing edge [24]. In the downstream direction, this difference is smaller and the installed curves tend to collapse with the ones of the isolated jet, especially for the highest jet velocity. The results also show that the flow-permeable materials are effective in reducing jet-installation noise in all assessed directions, particularly upstream. This indicates that the dipole sources on the plate are mitigated. In the downstream direction, for the metal foam case, the levels reach those of the isolated jet for  $\theta > 120^\circ$  and  $M_a > 0.5$ , indicating that there is no change in the turbulence-mixing noise component due to the presence of the plate.

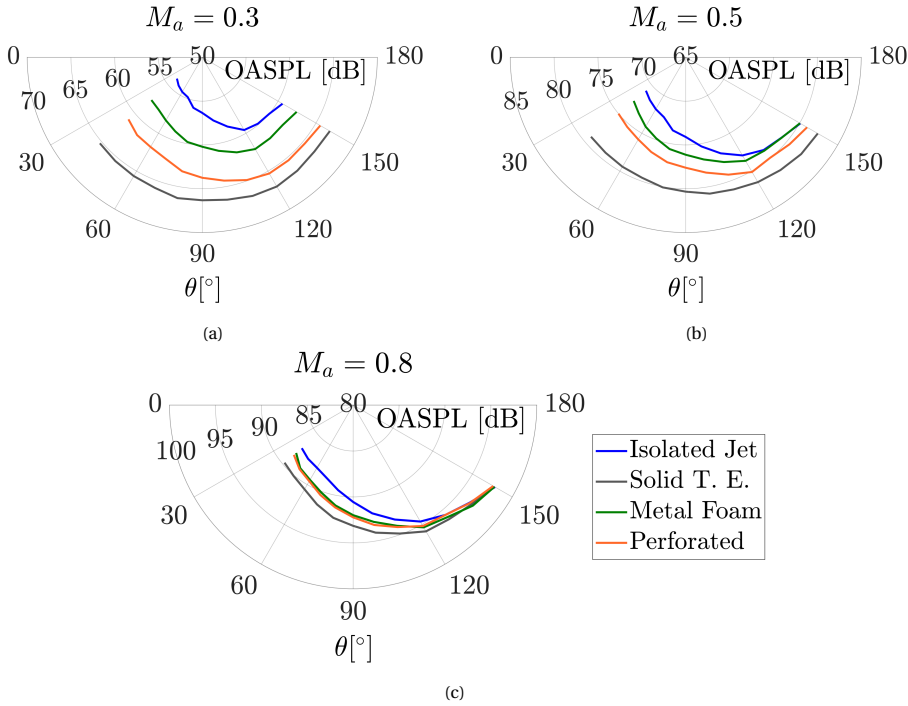


Figure 6.12: Directivity plots of Overall Sound Pressure Level (OASPL) of isolated and installed jets with solid and flow-permeable surfaces ( $L_p = 3D_j$ ), for three jet velocities.

The differences between the OASPL for flow-permeable and solid surfaces are reported in Table 6.5, for a polar angle  $\theta = 40^\circ$ . The overall increase due to installation effects with respect to the isolated jet is also included for reference. It can be seen that the metal foam provides higher noise reduction than the perforated structure, particularly for  $M_a = 0.3$ . From the 11.5 dB overall increase due to installation effects, it is possible to reduce 7.7 dB by applying the metal foam at the plate trailing edge. For higher jet velocities, the installation noise is practically eliminated with this porous material. Despite having a lower permeability, the perforated trailing edge still provides significant noise reduction, of approximately 4 dB for  $M_a = 0.3$  and  $M_a = 0.5$ .

The dependence of the OASPL with the jet velocity for an angle  $\theta = 40^\circ$  is also calculated and plotted in Fig. 6.13 for each case. Reference curves are also added for  $\text{OASPL} \propto U_j^8$ , which is consistent for turbulence-mixing noise [25], and  $\text{OASPL} \propto U_j^5$ , consistent with scattering at the surface trailing edge [26]. By applying the permeable treatment, the exponent of noise levels with the jet velocity increases from  $n = 5.8$  to  $n = 6.4$ , for the perforated plate, and to  $n = 7.2$  for the metal foam. The isolated jet has  $n = 7.9$ . These results are in qualitative agreement with those from Geyer and Sarradj [7] and Jaworski and Peake [27]. This confirms that, when flow-permeable treatments are applied to the surface, the scattering becomes less dominant with respect to other sources such as turbulence-mixing.

Table 6.5: Difference in OASPL between solid and flow-permeable (metal foam and perforated) installed cases for a polar angle  $\theta = 40^\circ$  and three jet velocities. The overall increases due to installation effects with respect to isolated levels are also included as reference.

$M_a$ [-]	$\Delta\text{OASPL}_{\text{SLD-ISO}}$ [dB]	$\Delta\text{OASPL}_{\text{SLD-MF}}$ [dB]	$\Delta\text{OASPL}_{\text{SLD-PERF}}$ [dB]
0.3	11.5	7.7	4.3
0.5	8.2	6.4	4.1
0.8	2.5	1.7	1.4

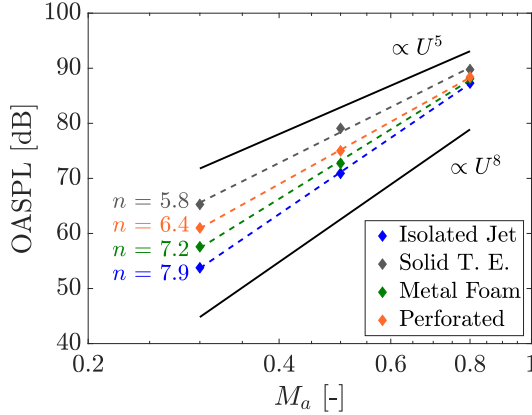


Figure 6.13: Scaling of Overall Sound Pressure Level with the jet acoustic Mach number for isolated and installed configurations, with solid and flow-permeable trailing edges.

The effect of the configuration geometry on the noise reduction that can be achieved using flow-permeable materials is investigated in the following. Firstly, the effect of the plate radial position is addressed by moving the plate in this direction. The spectra shown in Fig. 6.14 are obtained for a plate with  $L = 6D_j$  and  $h = 2.0D_j$  at a polar angle  $\theta = 40^\circ$ . This configuration is shown in Fig. 6.14a with solid lines; the dashed lines correspond to the baseline case ( $L = 6D_j$  and  $h = 1.5D_j$ ). The results show that for  $h = 2.0D_j$  and  $M_a = 0.3$ , for example, noise reductions up to 10 dB and 6 dB with respect to the solid case are achieved for the metal foam and perforated plate, respectively, for  $St = 0.37$ . These values are similar to those obtained for the previous case with the plate closer to the jet ( $h = 1.5D_j$ ). For the metal foam trailing edge, the noise levels collapse with those of the isolated configuration for  $M_a = 0.5$  and higher. The perforated insert also provides significant noise reduction; there is still a trailing-edge noise component at low frequencies for  $M_a = 0.5$  (up to 4 dB with respect to the isolated levels), but at  $M_a = 0.8$  the installation effects are also not visible for this configuration.

Since lower absolute levels are obtained in the spectra for the treated plate farther from the jet, it is interesting to plot the results in terms of noise reductions with respect to each solid case. The curves in Fig. 6.15 are given in terms of  $\Delta\text{SPL}$  for the respective plate height, and for each permeable configuration, for  $M_a = 0.3$ . Higher jet velocities are

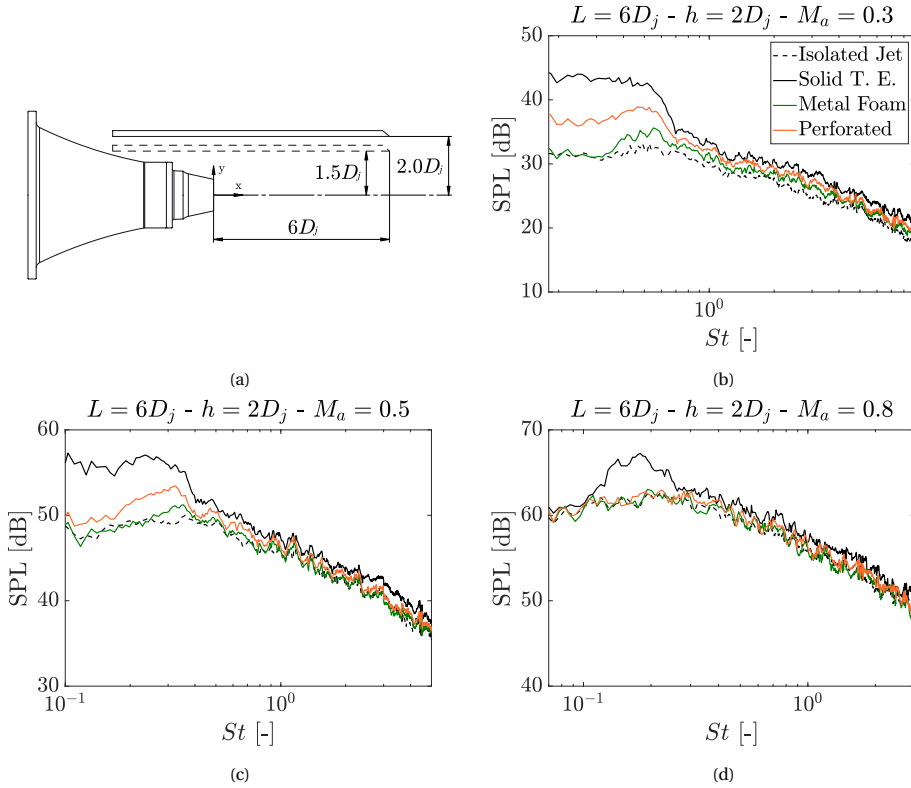


Figure 6.14: Isolated and installed jet spectra, with solid and flow-permeable surfaces ( $L_p = 3D_j$ ), obtained for a plate with  $L = 6D_j$  and  $h = 2.0D_j$  (effect of surface height) at a polar angle  $\theta = 40^\circ$  and three velocities.

not shown since the turbulence-mixing noise becomes significant and it is not possible to properly assess the effect of the permeable materials. It can be seen that the curves are similar, with minor local deviations, indicating that the absolute noise reductions provided by the permeable materials are independent on the plate radial position, i.e. independent on the amplitude of impinging pressure waves. It is likely that this property is also the reason why the SPL for the installed jets with flow-permeable trailing-edges approach more the isolated jet levels for higher jet velocities.

The effect of the plate length is investigated for a surface with  $L = 8D_j$  and  $h = 1.5D_j$ , as shown in Fig. 6.16 for  $\theta = 40^\circ$ . The results show that, for this geometry, there is a significant noise increase at low frequencies ( $St < 0.35$ , for  $Ma = 0.3$ ). Moreover, the benefits provided by the flow-permeable materials are lower than in the previous cases (6 dB decrease at  $St = 0.35$ , for  $Ma = 0.3$  and both types of inserts). At mid frequencies ( $0.35 < St < 0.7$ , for  $Ma = 0.3$ ), the metal foam and perforated inserts provide similar noise reduction for this configuration. The main differences between the two of them occur in the range of noise increase due to the increment in the plate length. This is likely the result of the different permeability of the surfaces at the trailing edge, where large-

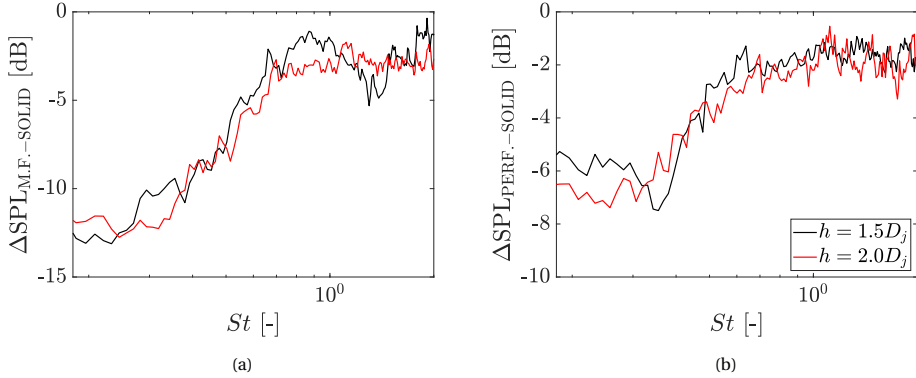


Figure 6.15: Reduction in noise levels with respect to the solid case for each plate height, obtained at  $\theta = 40^\circ$  and for  $Ma = 0.3$ . (a) Metal foam. (b) Perforated.

scale pressure waves impinge on the plate; the metal foam provides a better pressure balance between the upper and lower sides of the plate, thus better reducing the surface pressure fluctuations at low frequencies. On the other hand, it is likely that the noise at  $0.35 < St < 0.7$  is generated by surface fluctuations upstream of the flow-permeable region, which is the same for both cases. Similar trends occur for the other jet velocities.

This effect can be verified by analysing the influence of the flow-permeable insert length on the noise reduction, for a fixed plate length  $L = 6D_j$  and height  $h = 1.5D_j$ . Measurements are taken for inserts with length  $L_p = 1D_j$ , and compared to the ones previously shown ( $L_p = 3D_j$ ). Spectra are plotted in Fig. 6.17, for a polar angle  $\theta = 40^\circ$  and three  $Ma$ . The results show that, for the metal foam, the smaller insert still provides significant noise abatement, particularly for  $Ma = 0.3$  (6 dB reduction at the peak). For  $Ma = 0.5$ , similar absolute noise reductions are obtained and, for  $Ma = 0.8$ , the curves are similar since turbulence-mixing noise is significant. Therefore, longer flow-permeable sections provide higher benefits since there is a shorter solid section of the plate subjected to strong surface pressure fluctuations. For the perforated structure, the small insert ( $L_p = 1D_j$ ) provides less noise reduction, of approximately 4 dB at  $St = 0.37$ , for  $Ma = 0.3$ . The difference in amplitudes between the curves for the two insert lengths is also more significant at low frequencies ( $St < 0.3$  for  $Ma = 0.3$ ), indicating that the additional solid length, for the cases with a shorter insert, generates noise in this frequency range. This is a similar behaviour to that of increasing the overall plate length, as shown in Fig. 6.16. Nonetheless, it can be concluded that replacing a small section of the trailing edge with a permeable material is sufficient for achieving noise reduction. This is important since those types of structures usually lead to performance degradation (loss of lift and drag increase) [8, 28].

It is shown that the solid extension of the plate affects the final spectral shape and amplitude, also shifting the frequency of peak SPL. Therefore, it is also important to analyze the effect of changing the length of the porous insert, but keeping the size of the solid section of the plate constant. For that purpose, spectra of two cases are compared:  $L = 6D_j$  with  $L_p = 1D_j$  and  $L = 8D_j$  with  $L_p = 3D_j$ . Therefore, both cases have

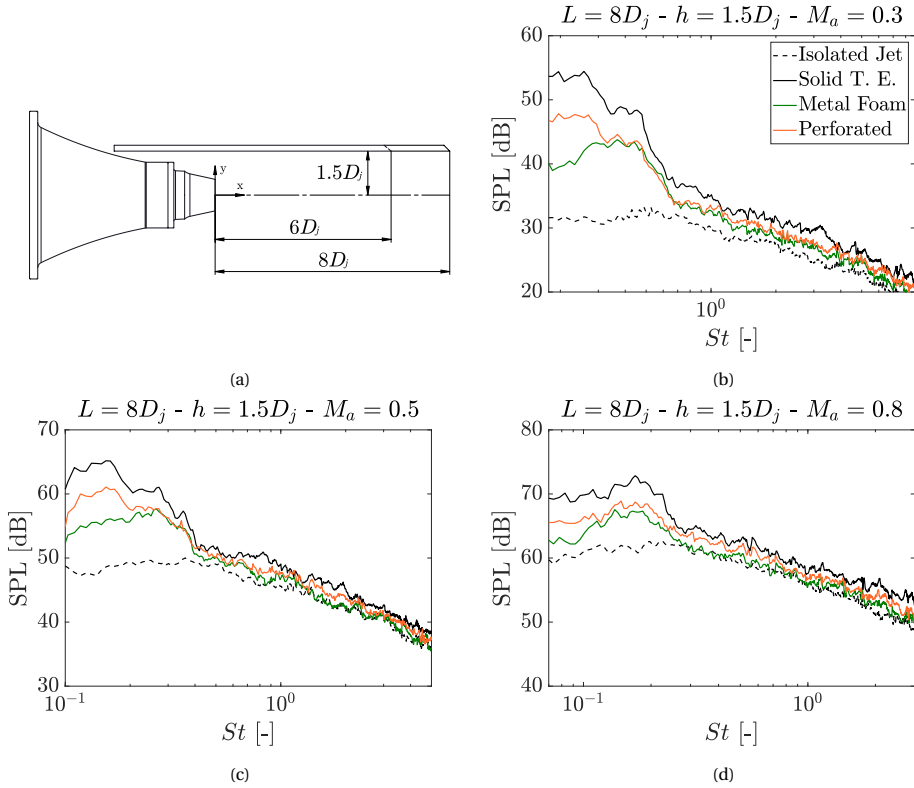


Figure 6.16: Isolated and installed jet spectra, with solid and flow-permeable surfaces ( $L_p = 3D_j$ ), obtained for a plate with  $L = 8D_j$  and  $h = 1.5D_j$  (effect of plate length) at a polar angle  $\theta = 40^\circ$  and three velocities.

a solid section of  $5D_j$  between the nozzle exit and the flow-permeable section. Results are shown in Fig. 6.18, for the two types of permeable materials and three  $Ma$ . The results are similar to those shown in Fig. 6.17. The case with an overall longer plate has more noise generated at lower frequencies ( $St < 0.3$  for  $Ma = 0.3$ ), for both metal foam and perforated inserts; at  $St = 0.27$ , there is a 5 dB difference between the metal foam curves and 4.4 dB for the perforated ones. This is likely attributed to the difference in total plate length so that the additional noise is generated due to the impingement of high-amplitude and low-frequency pressure waves on the flow-permeable region of the plate. On the other hand, the noise at mid frequencies does not show significant change when comparing the two cases. Therefore, it is probable that the dominant source in this range is the same for both of them, and it is likely that the source is now located at the solid-permeable junction in the plate.

It is suggested that the junction between solid and flow-permeable surfaces has become the dominant source location for the metal foam case. The effect of the junction has been described in the literature as an additional geometric singularity, and thus, as a new scattering region, as shown by Kisil and Ayton [29]. Scattering at the junction is

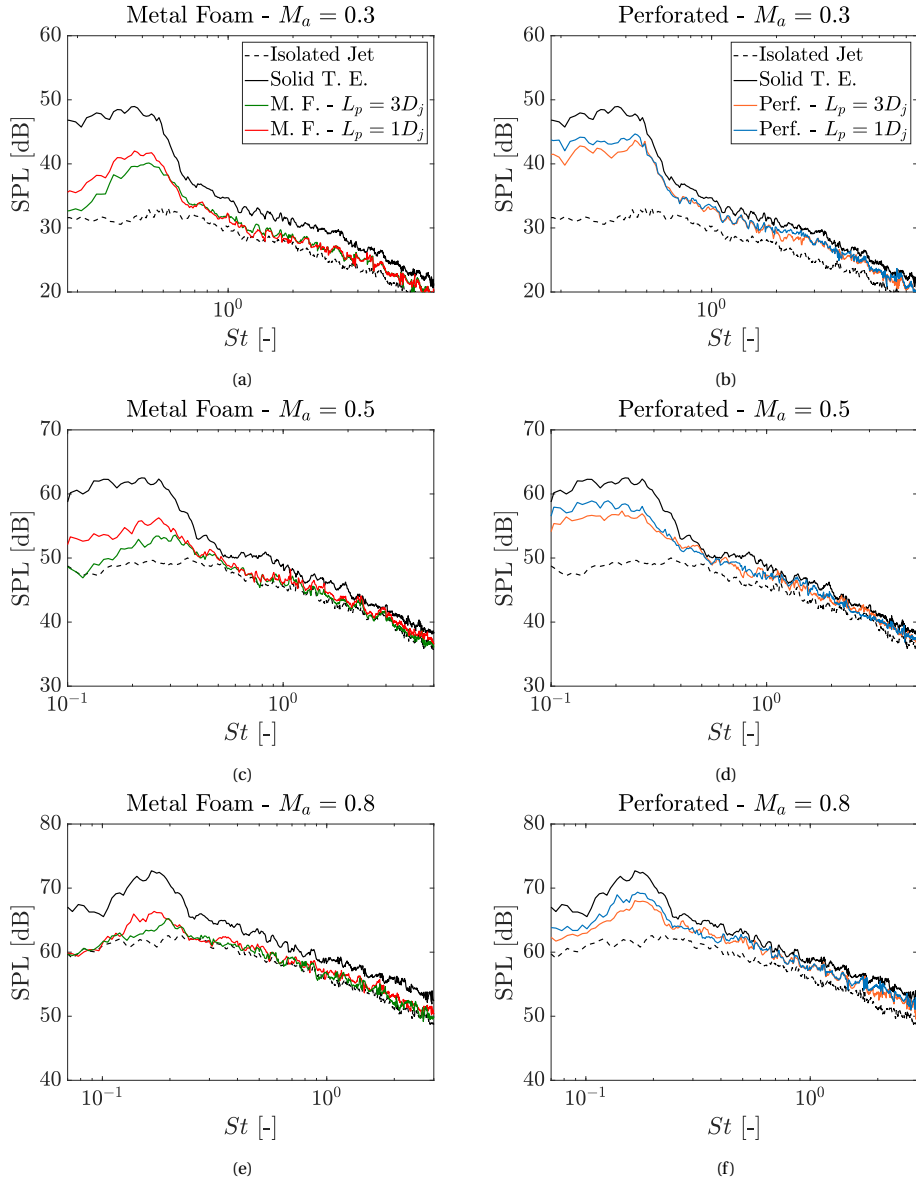


Figure 6.17: Isolated and installed jet spectra, with solid and flow-permeable surfaces ( $L_p = 3D_j$  and  $L_p = 1D_j$  - effect of porosity length), for a plate with  $L = 6D_j$  and  $h = 1.5D_j$ , at a polar angle  $\theta = 40^\circ$  and three velocities.

then responsible for noise increase at mid and high frequencies, also changing the directivity pattern of the overall configuration [29]. Moreover, beamforming results from Rubio-Carpio et al. [8] showed that, for frequencies where TBL-TE noise reduction is

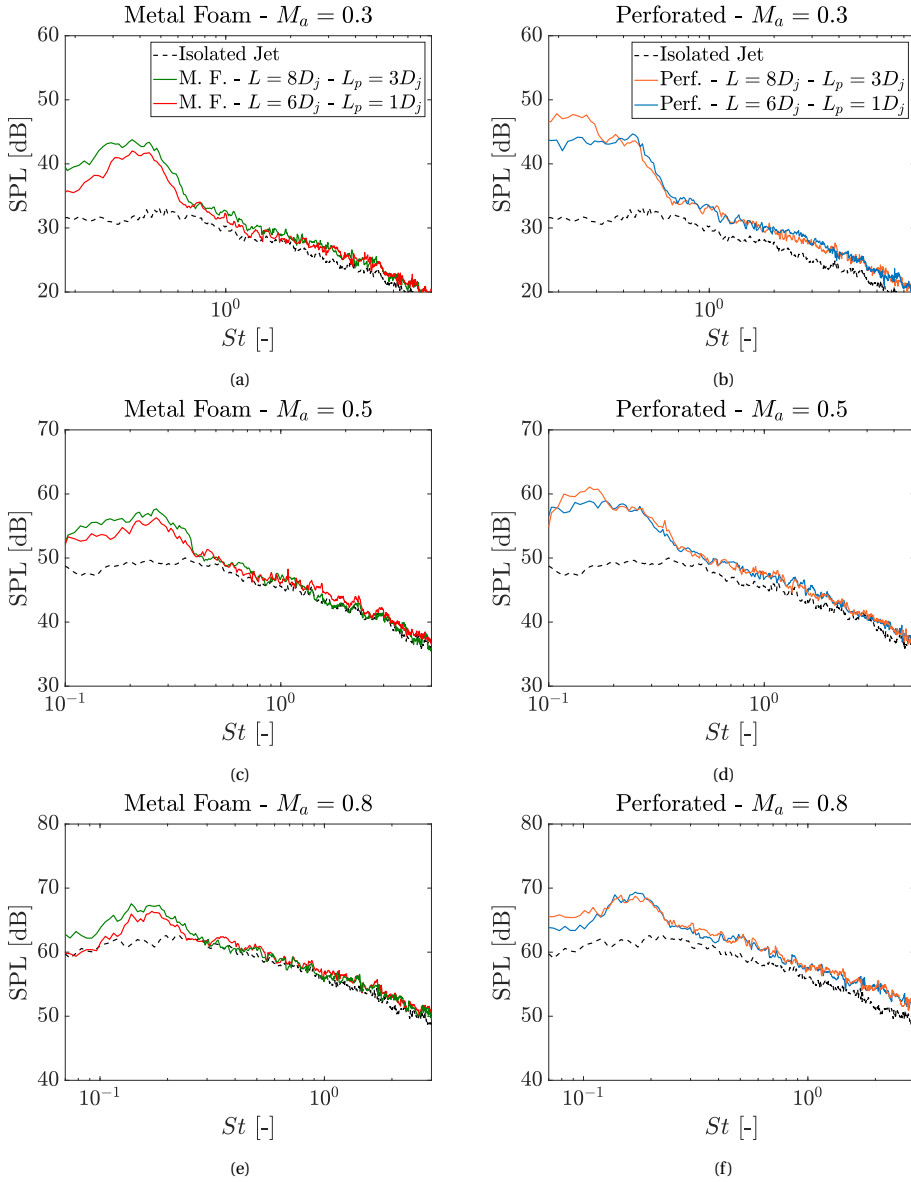


Figure 6.18: Isolated and installed jet spectra, with flow-permeable inserts and same solid length ( $L = 8D_j$  with  $L_p = 3D_j$  and  $L = 6D_j$  with  $L_p = 1D_j$ ), at a polar angle  $\theta = 40^\circ$  and three velocities.

achieved with flow-permeable materials, the dominant source is placed at the solid-flow-permeable junction [8]. Therefore, it is possible that there is an additional contribution from that region, particularly for the cases with the metal foam due to its high permeability, which still results in a geometrical discontinuity. The junction effect would

thus be the cause of the different spectral shape, as well as of the SPL peak at a higher frequency, relative to the fully solid and perforated cases. The results previously shown for the metal foam case are in agreement with this hypothesis; for the reduced insert length, the junction is placed at  $x = 5D_j$  (as opposed to  $x = 3D_j$  in the baseline case), and the spectral peak shifts towards a lower frequency (Fig. 6.17). On the other hand, when the junction is placed at the same position and the porous extent is changed, there is simply an increase in amplitude, but the spectral peak frequency remains unchanged (Fig. 6.18). This effect is likely not obtained with the perforated configuration, since the low permeability does not result in a strong impedance jump at the junction, and, consequently, scattering at that region. Further work is necessary to confirm these hypotheses.

## 6.5. CONCLUDING REMARKS

An experimental study on the effect of flow-permeable materials on the noise produced by an installed jet is performed. The configuration is comprised by a single-stream subsonic jet and a nearby flat plate, placed in the jet near-field. Two types of flow-permeable structures are investigated: a metal foam and a perforated insert with straight holes normal to the axis, with the former having a higher porosity and permeability than the latter.

Planar PIV measurements are carried out to characterize the jet velocity field. Based on the potential core length and spreading angle, it is concluded that the jet has a turbulent behaviour for all tested velocities. Moreover, it is confirmed that there is no direct grazing of the jet on the plate, except for the longest surface tested. However, for this case, the surface is in a region of very low velocities compared to the potential core, and it is likely not affecting the noise generated by turbulence mixing. Acoustic measurements show that the installation effects are responsible for strong low-frequency noise increase with respect to isolated levels. This amplification is more significant at a low jet velocity, where the dipole sources on the surface are more acoustically efficient than the quadrupole sources from turbulent mixing. The spectral shape and amplitude are shown to be dependent on the geometry of the configuration; longer surfaces produce more noise at low frequencies, whereas moving the plate towards the jet in the radial direction results in noise increase, especially at mid frequencies.

Significant noise reduction is achieved when the solid plate trailing edge is replaced by flow-permeable inserts, particularly in the low/mid frequency range, where the scattering is the dominant mechanism. Comparing the two types of structures, the metal foam is more effective in reducing JIN, likely due to a higher permeability, which can mitigate the pressure imbalance between the upper and lower sides of the plate, and thus reduce the noise generated by surface pressure fluctuations. For low jet velocities, a noise decrease of up to 10 dB is obtained at the spectral peak with the metal foam, but the installation noise is still visible. When the jet velocity is increased, the attenuation provided by the flow-permeable treatment brings the noise levels closer to the isolated case, and the trailing-edge source is no longer dominant with respect to the jet quadrupoles. It is worth mentioning that the highest noise levels for the investigated installed configurations occur at low frequencies ( $St < 0.3$  for  $M_a = 0.3$ ), particularly at the sideline direction ( $\theta = 90^\circ$ ). For a full-scale aircraft, these frequencies may not be of particular significance. However, the flow-permeable trailing edges assessed in this work also provide noise reductions at mid and high frequencies, including reflection effects

on the surface, which would be significant in a full-scale configuration.

The effect of surface treatment is also assessed for different configurations. By moving the plate away from the jet, flow-permeable materials provide similar absolute noise reduction as the baseline case. Conversely, by increasing the plate length, lower noise abatement is obtained with the flow-permeable treatments, particularly at low frequencies ( $St < 0.35$  for  $M_a = 0.3$ ), with the metal foam still providing higher benefits. On the other hand, the noise at mid frequencies ( $0.35 < St < 0.7$  for  $M_a = 0.3$ ) is similar for the two types of insert, indicating that it is generated by the impingement of pressure waves in the solid region of the plate, upstream of the flow-permeable treatments.

For a fixed plate length, a shorter flow-permeable insert is shown to provide noise reductions with respect to the solid case, but in a lower degree compared to the larger insert. The main differences occur at low frequencies; this indicates that the increased noise is due to the additional solid length, compared to the case with the longer insert. The frequency of highest SPL also shifts towards low frequencies. On the other hand, when the plate length is changed, but the solid-permeable junction is kept at the same axial position, the flow-permeable materials behave differently. For the metal foam, there is an increase in amplitude, but no significant change to the spectral peak frequency, whereas for the perforated there is a low-frequency noise increase with a change in the spectral peak. It is believed that this difference is caused by the high permeability of the metal foam, which produces a new singularity and thus a new scattering region at the solid-permeable junction.

These results show that a surface treatment with flow-permeable materials is a potentially promising mitigation solution for jet-installation noise. However, the mechanisms that provide such reductions are still unclear. Further work is required to investigate the phenomena happening at the junction region and inside the flow-permeable structure, particularly focusing on the change of impedance, pressure imbalance and the effect of permeability/resistivity of the flow-permeable structures, since it is possible to achieve substantial noise reduction with a perforated structure, even with a low porosity.

## REFERENCES

- [1] L. Rego, D. Ragni, F. Avallone, D. Casalino, R. Zamponi, and C. Schram, *Jet-installation noise reduction with flow-permeable materials*, [Journal of Sound and Vibration](#) **498**, 115959 (2021).
- [2] J. D. Revell, H. L. Kuntz, F. J. Balena, B. L. Storms, and R. P. Dougherty, *Trailing-Edge Flap Noise Reduction by Porous Acoustic Treatment*, in [3rd AIAA/CEAS Aeroacoustics Conference](#) (Atlanta, GA, USA, 1997).
- [3] D. Angland, X. Zhang, and N. Molin, *Measurements of Flow Around a Flap Side Edge with Porous Edge Treatment*, [AIAA Journal](#) (2009), **10.2514/1.39311**.
- [4] M. Roger, C. Schram, and L. de Santana, *Reduction of airfoil turbulence-impingement noise by means of leading-edge serrations and/or porous materials*, in [19th AIAA/CEAS Aeroacoustics Conference](#) (2013) p. 105.
- [5] M. Roger and S. Moreau, *Airfoil Turbulence-Impingement Noise Reduction by Poros-*

- ity or Wavy Leading-Edge Cut: Experimental Investigations*, in *Inter-Noise* (Hamburg, Germany, 2016).
- [6] M. Herr, K. Rossignol, J. Delfs, N. Lippitz, and M. Mößner, *Specification of Porous Materials for Low-Noise Trailing-Edge Applications*, in *20th AIAA/CEAS Aeroacoustics Conference* (Atlanta, GA, USA, 2014).
- [7] T. Geyer and E. Sarradj, *Trailing edge noise of partially porous airfoils*, in *20th AIAA/CEAS Aeroacoustics Conference* (Atlanta, GA, USA, 2014).
- [8] A. Rubio Carpio, R. Merino Martínez, F. Avallone, D. Ragni, M. Snellen, and S. Van Der Zwaag, *Experimental characterization of the turbulent boundary layer over a porous trailing edge for noise abatement*, *Journal of Sound and Vibration* **443**, 537 (2019).
- [9] D. Guariglia, A. Rubio Carpio, and C. Schram, *Design of a Facility for Studying Shock-Cell Noise on Single and Coaxial Jets*, *Aerospace* **5**, 25 (2018).
- [10] C. Brown, *Jet-Surface Interaction Test: Far-Field Noise Results*, in *Proceedings of the ASME Turbo Expo 2012: Power for Land, Sea and Air* (Copenhagen, Denmark, 2012) pp. 1–13.
- [11] C. Brown and J. Bridges, *Small Hot Jet Acoustic Rig Validation*, Tech. Rep. (NASA/TM-2001-214234, Cleveland, OH, USA, 2006).
- [12] J. Bridges and M. Wernet, *Establishing Consensus Turbulence Statistics for Hot Subsonic Jets*, in *16th AIAA/CEAS Aeroacoustics Conference* (Stockholm, Sweden, 2010) pp. 1–41.
- [13] S. Kim and C. Lee, *A Review on Manufacturing and Application of Open-cell Metal Foam*, *Procedia Materials Science* **4**, 305 (2014).
- [14] A. Rubio Carpio, R. Merino Martínez, F. Avallone, D. Ragni, M. Snellen, and S. Van Der Zwaag, *Broadband Trailing Edge Noise Reduction Using Permeable Metal Foams*, in *InterNoise Conference* (Hong Kong, 2017).
- [15] Tenco DDM, *DLP Digital Light Processing Data Sheet*, .
- [16] A. Rubio Carpio, F. Avallone, D. Ragni, M. Snellen, and S. van der Zwaag, *Quantitative criteria to design optimal permeable trailing edges for noise abatement*, *Journal of Sound and Vibration* **485** (2020), 10.1016/j.jsv.2020.115596.
- [17] L. Rego, F. Avallone, D. Ragni, and D. Casalino, *Noise Amplification Effects due to Jet-Surface Interaction*, in *AIAA Scitech 2019 Forum* (San Diego, CA, USA, 2019).
- [18] D. Ragni, F. Schrijer, B. W. Van Oudheusden, and F. Scarano, *Particle tracer response across shocks measured by PIV*, *Experiments in Fluids* **50**, 53 (2011).
- [19] F. Scarano and M. L. Riethmuller, *Advances in iterative multigrid PIV image processing*, *Experiments in Fluids* **29**, S051 (2000).

- [20] F. Scarano, *Iterative image deformation methods in PIV*, *Measurement Science and Technology* **13** (2001).
- [21] J. Westerweel and F. Scarano, *Universal outlier detection for PIV data*, *Experiments in Fluids* **39**, 1096 (2005).
- [22] B. Wieneke, *PIV uncertainty quantification from correlation statistics*, *Measurement Science and Technology* **26** (2015), 10.1088/0957-0233/26/7/074002.
- [23] P. O. Witze, *Centerline velocity decay of compressible free jets*, *AIAA Journal* **12**, 417 (1974).
- [24] R. W. Head and M. J. Fisher, *Jet/Surface Interaction Noise: - Analysis of Farfield Low Frequency Augmentations of Jet Noise due to the Presence of a Solid Shield*, in *3rd AIAA Aeroacoustics Conference* (Palo Alto, CA, USA, 1976).
- [25] M. J. Lighthill, *On Sound Generated Aerodynamically I. General Theory*, *Proceedings of the Royal Society of London. Series A. Mathematical and Physical Sciences* **211**, 564 (1952).
- [26] J. E. Ffowcs-Williams and L. H. Hall, *Aerodynamic sound generation by turbulent flow in the vicinity of a scattering half plane*, *Journal of Fluid Mechanics* **40**, 657 (1970).
- [27] J. W. Jaworski and N. Peake, *Aerodynamic noise from a poroelastic edge with implications for the silent flight of owls*, *Journal of Fluid Mechanics* **723**, 456 (2013).
- [28] E. Sarradj and T. Geyer, *Noise Generation by Porous Airfoils*, in *13th AIAA/CEAS Aeroacoustics Conference* (Rome, Italy, 2007).
- [29] A. Kisil and L. J. Ayton, *Aerodynamic noise from rigid trailing edges with finite porous extensions*, *Journal of Fluid Mechanics* **836**, 117 (2018).



# 7

## MECHANISMS OF JET-INSTALLATION NOISE REDUCTION WITH FLOW-PERMEABLE TRAILING EDGES

*The greatest enemy of knowledge is not ignorance, it is the illusion of knowledge.*

Stephen Hawking

*This chapter reports an investigation on the mechanisms by which flow-permeable materials provide noise reduction in an installed jet configuration. Numerical simulations are carried out with a flat plate placed in the near field of a jet. Different configurations of permeable trailing edges are studied: a metal foam, a perforated plate and a diamond-shaped structure. Beamforming results show that the dominant acoustic source is located at the solid-permeable junction for the metal foam and diamond structures, whereas the perforated one has the source positioned near the trailing edge, similarly to the solid case. The results also point to a significant mitigation of the noise due to scattering, which is no longer the dominant mechanism in any frequency range. This is confirmed by lower values of spanwise surface pressure coherence for the permeable trailing edge, compared to the solid case, as well as a dipolar directivity pattern instead of a cardioid one. Therefore, the clear dominant mechanism in the permeable region of the plate is due to the impingement of pressure waves from the jet.*

---

Parts of this chapter have been included in Reference [1].

## 7.1. OBJECTIVES

It has been demonstrated in Chapter 6 that the application of flow-permeable materials at the trailing edge of a surface located near a jet leads to JIN reduction. In the previously described experiment, two permeable configurations are investigated: a metal foam and a perforated plate. In terms of noise mitigation, the former performs better, particularly in the frequency range where JIN is the dominant source, likely due to a better pressure balance between the upper and lower sides of the plate [2].

However, some questions on this subject remain open, particularly regarding the dominant sources and mechanisms in the installed jet configuration with a permeable trailing edge. It is believed that the junction between solid and porous regions of the plate has become a new scattering location and the dominant source for certain frequencies [2], but this hypothesis has not been confirmed yet. Moreover, those results could not determine with certainty how the unsteady flow field around the plate is affected by the flow-permeable materials, as well as distinguish their effect on the noise due to surface pressure fluctuations and trailing-edge scattering separately. Finally, it should also be investigated which properties of those materials are the most relevant for the noise reduction.

Therefore, this chapter reports a study on the flow field and acoustic characteristics of an installed jet configuration of a surface with a permeable trailing edge via numerical simulations. The simulations allow for detailed information of the near field to be extracted, which are linked to the far-field acoustic results. The pressure field on the plate and the unsteady flow rate through the permeable material are analysed, which allows for an assessment of properties such as resistivity on the final noise signature. These results, combined with an analysis of acoustic directivity and source localization through beamforming, also provide information on how each of the noise mechanisms are affected by the permeable structures, as well as the effect of the solid-porous junction.

## 7.2. COMPUTATIONAL SET-UP

### 7.2.1. INSTALLED JET CONFIGURATION AND FLOW CONDITIONS

The baseline configuration studied in this work replicates the installed jet model reported in Chapter 6, with a flat plate placed in the vicinity of a single-stream jet nozzle. The plate length, which corresponds to the distance between the nozzle exit plane and the trailing edge, is defined as  $L = 6D_j$ , whereas the radial position of the surface with respect to the jet centerline is set as  $h = 1.5D_j$ , as shown in Fig. 7.1. The plate has a thickness  $t = 10$  mm and it has a chamfer angle of  $40^\circ$  at the trailing edge. It also extends  $3D_j$  upstream of the nozzle exit plane to avoid scattering effects at the leading edge and properly account for noise shielding at shallow upstream angles. In the spanwise direction, the plate has a width of  $36D_j$  to avoid side-edge scattering.

Two flow conditions, characterized by subsonic jets with acoustic Mach numbers ( $M_a = U_j/c_\infty$ )  $M_a = 0.3$  and  $M_a = 0.5$ , are simulated. The jet flow characteristics are included in Table 7.1, such as the Nozzle Pressure Ratio (NPR), the temperature ratio  $T_R$  (ratio between the jet and ambient static temperatures), and the Reynolds number  $Re$ , based on the nozzle exit diameter. Due to similarities between trends for the two jet

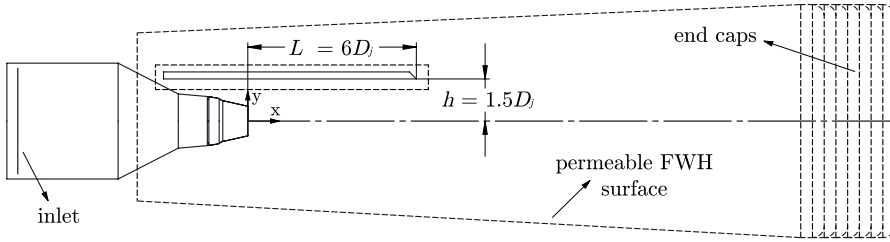


Figure 7.1: Installed jet configuration with a flat plate length  $L = 6D_j$  and radial position  $h = 1.5D_j$ . A permeable FW-H surface encompasses the jet and the flat plate. Caps are placed at the downstream end of the surface, and cut-outs are placed in the regions of the plate and nozzle.

conditions, the results for the remainder of this chapter are plotted for the  $M_a = 0.5$  jet, unless otherwise stated.

Table 7.1: Jet flow conditions in terms of acoustic Mach number ( $M_a$ ), nozzle pressure ratio (NPR), temperature ratio ( $T_R$ ) and Reynolds number ( $Re$ ).

Condition	$M_a$ [-]	NPR [-]	$T_R$ [-]	$Re$ [ $10^5$ ]
1	0.3	1.067	0.98	3.58
2	0.5	1.196	0.95	5.96

### 7.2.2. FLOW-PERMEABLE MATERIALS

Different flow-permeable materials are investigated in this work, with distinct microstructures and properties, in order to assess the effects of geometry, porosity and resistivity in the noise production. The first permeable trailing edge is represented by a porous media model, which simulates the characteristics of an open-cell metal foam, such as the one described in Chapter 6 [3]. This strategy is used due to the high geometrical complexity of the micro-structure, and it has been also adopted by Teruna et al. [4] for airfoil TBL-TE noise studies. This porous media model consists of equivalent fluid regions governed by Darcy's law, which states that the flow pressure gradient through a permeable material is proportional to the local flow velocity, as reported in Chapter 3. This model, however, is not able to include the roughness of the material and its effect on noise production [4].

The interface between this equivalent fluid region and the rest of the domain consists in double-sided surfaces similar to a sliding mesh [5]. Moreover, the mass flux at the interface is conserved by making use of the material porosity  $\sigma$ . To implement the model in the computational set-up, the same strategy adopted by Teruna et al. [4] is applied. The trailing-edge is divided into two regions: the PM (porous medium) and the APM (acoustic porous medium). Both regions are governed by Darcy's law, but the latter also takes into account the acoustic absorption of the material [4]. The trailing edge is then replaced by a PM-APM combination, as shown in Fig. 7.2. The APM, which includes porosity effects, is placed as an outer layer with thickness  $t_{APM} = 1$  mm on both upper

and lower sides, whereas the inner layer is set with PM conditions ( $t_{PM} = 8 \text{ mm}$ ). For both regions, the inertial and viscous resistivities are set based on the respective thickness [4], as shown in Table 7.2. These properties replicate a metal foam structure with cell diameter  $d_c = 800 \mu\text{m}$ , equivalent to that reported in Chapter 6. The resistivities are set the same in all three directions due to the isotropic characteristics of the material.

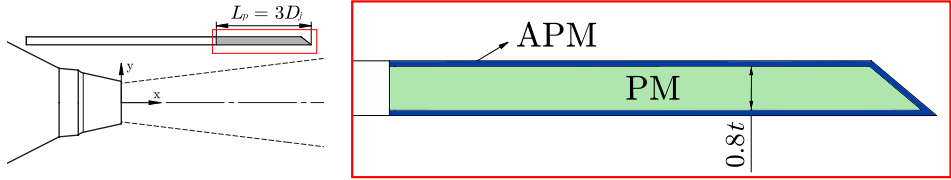


Figure 7.2: Flow-permeable trailing edge with length  $L_p = 3D_j$ . The metal foam trailing edge is modeled with an equivalent Darcy fluid region, comprised by a Porous Medium (PM - inner layer) and an Acoustic Porous Medium (APM - outer layer), which considers the material porosity.

Table 7.2: Porosity ( $\sigma$ ), inertial ( $R_I$ ) and viscous ( $R_V$ ) resistivity parameters applied to the equivalent fluid regions, which replicate the properties of a metal foam with cell diameter  $d_c = 800 \mu\text{m}$ .

Region	$\sigma$ [%]	$R_I$ [ $\text{m}^{-1}$ ]	$R_V$ [ $\text{s}^{-1}$ ]
APM	91.7	2854	6575
PM	-	2520	5489

The second type of flow-permeable structure investigated is a perforated trailing edge, with cylindrical holes normal to the jet axis, connecting the upper and lower sides of the plate, as shown in Fig. 7.3a. A configuration with hole diameter  $d_h = 800 \mu\text{m}$  is assessed, as shown in Fig. 7.3b, which has been also investigated in Chapter 6.

Finally, a trailing edge with a diamond-shaped micro-structure, based on a tessellation of the cubic cell shown in Fig. 7.4a, is also investigated. This cubic cell is built from cylinders with diameter  $d_d = 1 \text{ mm}$ , merged at a  $120^\circ$  angle. The purpose of this geometry is to replicate the benefits provided by a metal foam trailing edge, but with a simpler and modular micro-structure, with a clearly defined and repeatable geometry. The final trailing-edge geometry is shown in Fig 7.4b. This configuration also allows for permeability in the axial direction of the jet, as opposed to the perforated trailing edge, for which there is flow only in the radial direction. For the perforated and diamond cases, the actual trailing-edge geometry is simulated, and no porous media model is applied.

The properties of the flow-permeable materials are reported in Table 7.3, in terms of porosity  $\sigma$ , inertial and viscous resistivity coefficients ( $R_I$  and  $R_V$ , respectively), and the permeability  $K$ . The original metal foam parameters [6] are included for comparison.

For all configurations, the flow-permeable region of the plate has a length  $L_p = 3D_j$  and span  $b_p = 6D_j$ , centered at the jet symmetry plane, represented by the blue region in Fig. 7.5. In the measurements reported in Chapter 6, the span of the flow-permeable materials was originally  $10D_j$ . However, it has been verified that shortening this region to  $6D_j$  does not change the far-field noise, but highly reduces the computational cost.

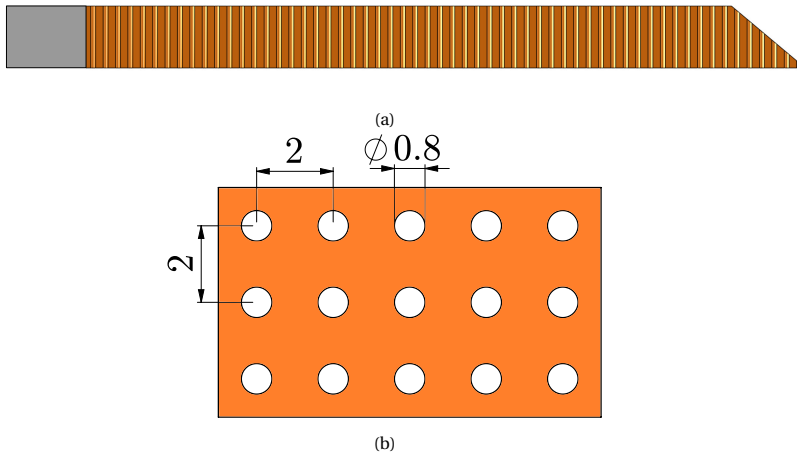


Figure 7.3: (a) Perforated trailing edge with cylindrical holes. (b) Hole dimensions of the perforated structure. Dimensions in mm.

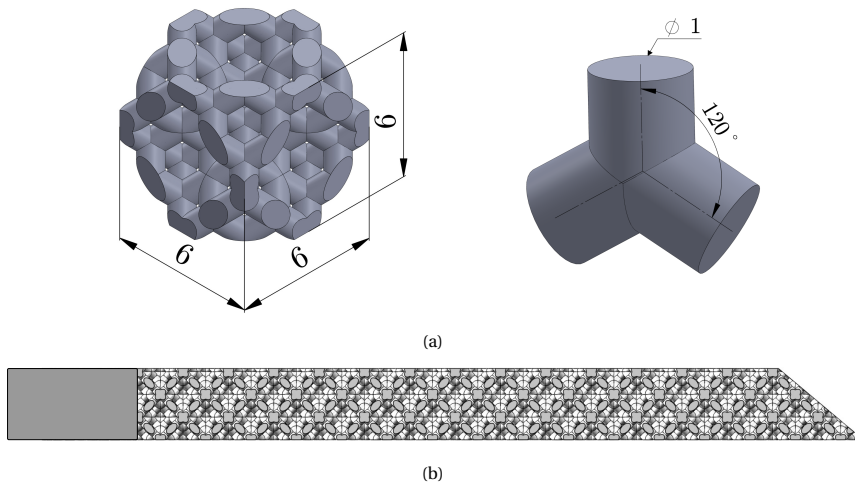


Figure 7.4: (a) Diamond-shaped cubic structure created by the intersection of cylinders with a 1 mm diameter at an angle of  $120^\circ$ . (b) Flow-permeable trailing edge with the diamond structure. Dimensions in mm.

The area shown in green represents the solid region of the plate where data are sampled (sampling on both upper and lower sides of the surface).

### 7.2.3. SET-UP COMPONENTS AND SIMULATION PARAMETERS

The computational set-up consists in a nozzle and flat plate placed in an almost quiescent domain, as described in Chapter 5. The main components of the setup are shown in Fig. 7.1, along with the permeable FW-H surface and 7 end caps. The physical time

Table 7.3: Properties of the flow-permeable materials in terms of porosity ( $\sigma$ ), inertial ( $R_I$ ) and viscous ( $R_V$ ) resistivity, and permeability ( $K$ ).

Material	$\sigma$ [%]	$R_I$ [ $\text{m}^{-1}$ ]	$R_V$ [ $\text{s}^{-1}$ ]	$K$ [ $\times 10^{-9} \text{m}^2$ ]
Metal foam	91.7	2612	5390	2.71
Perforated	12.6	7283	9245	1.58
Diamond	61.6	4060	802	18.2

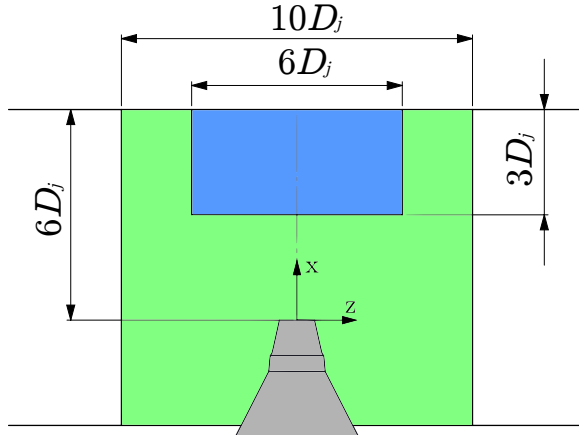


Figure 7.5: Dimensions of the flat plate with flow-permeable trailing edge (blue region). The area shown in green represents the solid region of the plate where data is sampled.

of the simulations is divided into an initial transient, consisting of 5 flow passes through the FW-H surface, and an acquisition time of 27 flow passes (total simulation time of 32 flow passes). The latter is defined based on the minimum output frequency to be analyzed (defined as  $St = 0.02$ ), and the number of spectral averages (defined as 20), for an overlap coefficient of 0.5 in the Fast Fourier Transform (FFT) computation. For the finest grid resolution investigated, the physical time step is  $1.5 \times 10^{-7}$  s. The unsteady pressure on the FW-H surface is sampled with a frequency of 72 kHz and 120 kHz for conditions 1 and 2, respectively. The resultant physical simulation time and acquisition parameters are shown in Table 7.4 for the simulated jet flow conditions. The frequency resolution refers to the minimum frequency band obtained from the FFT of the acoustic signals, based on the acquisition time and the selected number of averages.

Table 7.4: Simulation physical time and acquisition parameters.

Condition	$M_a$ [-]	Physical Simulation Time [s]	FW-H Acquisition Time [s]	Frequency Resolution [Hz]
1	0.3	0.440	0.373	27
2	0.5	0.264	0.224	44

The far-field noise levels are computed with a microphone arc array, centered at the nozzle exit plane, with a radius of  $100D_j$ . Microphones are placed at an interval of  $5^\circ$ , ranging from  $\theta = 50^\circ$  to  $\theta = 165^\circ$  ( $\theta = 180^\circ$  corresponds to the jet axis). The noise levels are evaluated at both shielded and reflected sides of the plate, as shown in Fig. 7.6a. Acoustic signals are also obtained from the solid FW-H formulation [7] using the pressure fluctuations sampled on the plate. The sampled region consists in a span of  $10D_j$  (similarly as the permeable FW-H width), centered at the jet symmetry plane, and the whole plate chord. This region, therefore, also includes a solid section near the trailing edge, as shown in Fig. 7.5. For the cases with permeable trailing edges, the far-field contributions of the solid and porous sections of the plate can be evaluated separately.

Acoustic data are also obtained at a microphone phased array for source localization with the beamforming technique [8]. A frequency-domain form of the FW-H analogy [9] is applied on the permeable surface data, which provides the cross-spectral matrix for the entire array. The array is located on a plane parallel to the plate surface, at a distance of  $20D_j$  from the jet axis on the reflected side, and centered at the nozzle exit plane. The array has 364 microphones arranged in a modified Underbrink multi-arm spiral design [10], with an effective diameter of  $3000D_j$  in the streamwise direction and  $160D_j$  in the spanwise direction, as shown in Fig. 7.6b. The array aperture and location are chosen in order to provide a streamwise spatial resolution of  $0.2D_j$  ( $0.065L_p$ ) at a frequency of 300 Hz, based on the Rayleigh criterion equation [11]. The used steering vector formulation is reported in Chapter 4 for conventional beamforming, assuming monopole sources. The scan plane is chosen as a square with a  $10D_j$  edge on the bottom surface of the plate, and centered at  $(5D_j, 1.5D_j, 0)$ . A grid size of  $0.02D_j$  is used in the  $x$ - and  $z$ -directions.

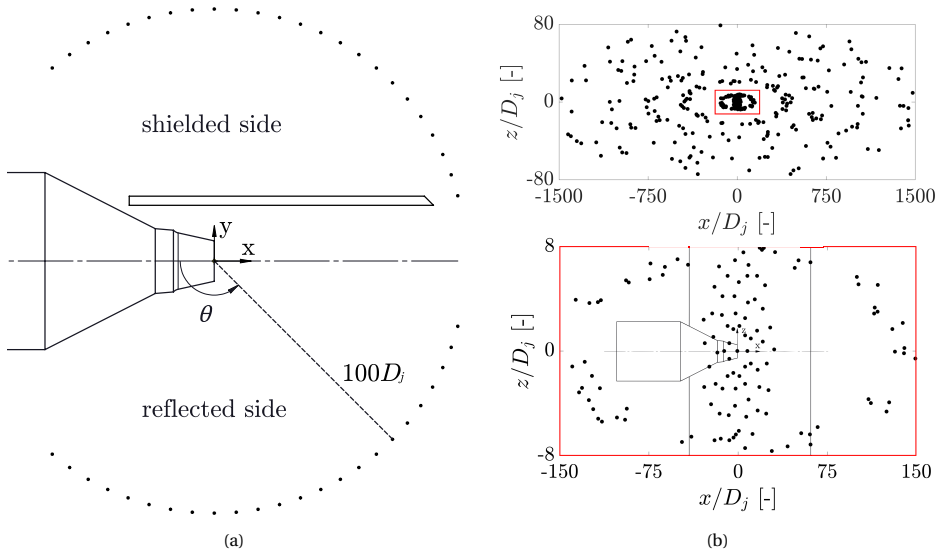


Figure 7.6: Far-field microphone positions. (a) 48 microphones in the polar array, divided for the reflected and shielded sides. Microphone distance not to scale (b) 364 microphones in the phased array, parallel to the surface plane. The bottom figure is a zoomed region at the center of the array. Nozzle and plate dimensions not to scale.

### 7.3. JET FLOW FIELD AND SET-UP VALIDATION

The jet flow field is described in this section. A contour of the time-averaged velocity field for the installed jet at  $M_a = 0.5$  (condition 2) is shown in Fig. 7.7. The region corresponding to the potential core and the downstream velocity decay are visible, as well as the spreading of the jet and symmetry with respect to the centerline. There is also no grazing flow occurring on the surface, and thus the jet development is not affected by the plate.

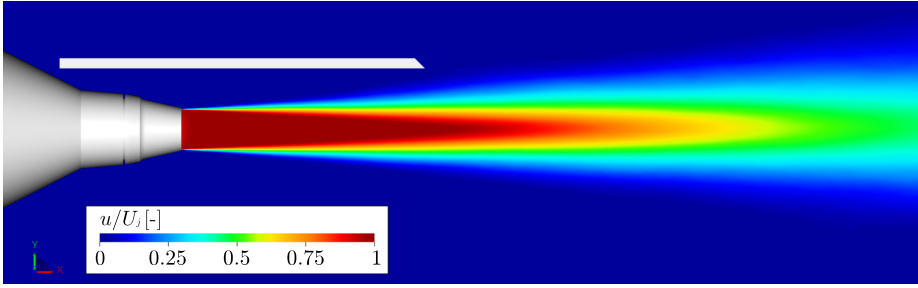


Figure 7.7: Contour of time-averaged axial velocity  $u$  for the installed jet at condition 2 ( $M_a = 0.5$ ), non-dimensionalized by the jet nominal velocity  $U_j$ .

The time-averaged velocity profile is extracted at the jet centerline ( $y = 0$ ) and plotted as the black curve in Fig. 7.8. Additionally, the velocity profile in the radial direction is also plotted in Fig. 7.8 (red curve), for  $x = 6D_j$  (equivalent to the trailing edge position). The axial velocity reaches the free-stream level of  $0.01U_j$  at a position  $y \approx 1.2D_j$ , and thus it is confirmed that there is no steady jet flow grazing on the surface. The spreading angle of the jet is also computed as  $\delta = 8.5^\circ$ , which is consistent for the investigated nozzle geometry [12]. Similar results are obtained for the jet at  $M_a = 0.3$ .

A grid convergence study is performed to assess the sensitivity of the numerical results to the discretization of the computational domain. The mesh resolution is defined as the number of voxels at the nozzle exit diameter, and the resultant element size is used throughout the jet plume. Three grids are investigated: coarse (resolution = 32 voxels/ $D_j$ ), medium (resolution = 45 voxels/ $D_j$ ), and fine (resolution = 64 voxels/ $D_j$ ). The features of each grid are summarized in Table 7.5 for the installed jet with a metal foam trailing edge case (PM-APM formulation).

Table 7.5: Grid characteristics for convergence analysis for the installed jet configuration with the PM-APM trailing edge.

Grid	Resolution	Voxel Size at Nozzle Exit and Jet Plume [mm]	Finest Voxel Size [mm]	Number of Voxels [ $10^6$ ]	kCPUh
Coarse	32	1.59	0.199	331	18.8
Medium	45	1.13	0.141	647	46.4
Fine	64	0.79	0.099	1688	147

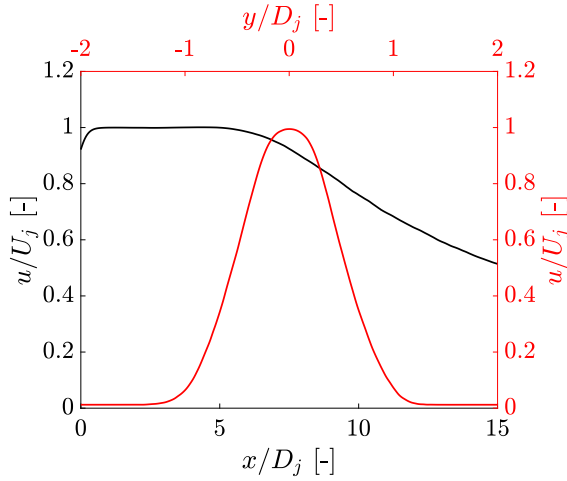


Figure 7.8: Time-averaged axial velocity profiles for the installed jet at condition 2 ( $M_a = 0.5$ ). Black curve - centerline velocity ( $y = 0$ ). Red curve - radial profile at  $x = 6D_j$ .

An image of the medium resolution mesh at the symmetry plane of the geometry ( $z = 0$ ) is shown in Fig. 7.9 for the perforated trailing-edge case, which has the smallest channels. The different levels of grid refinement are defined by virtual volumes known as variable resolution (VR) regions. In total, 13 VRs are applied for the installed jet set-up, with the finest element (VR13) placed at the nozzle lip and in the permeable materials. For this resolution, the finest element size is 0.141 mm, as reported in Table 5.4. For each higher level of VR, the element size doubles. As shown in Fig. 7.9, the lipline region directly downstream of the nozzle exit is refined (VR13 and VR12) in order to properly capture the early stages of the shear layer formation. The remainder of the jet flow up to  $x = 10D_j$  is included in VR11, whereas VR10 is the region comprised by FW-H surface. With the medium grid resolution, a  $y^+ = 70$  is computed at the nozzle exit. At the trailing edge, since there is no steady flow around the flat plate, it is not possible to extract a  $y^+$  value.

The installed jet set-up with a fully solid plate has been previously validated in Chapter 5 both in terms of steady flow field and acoustics. It is also necessary to validate the unsteady properties of the jet flow, which are important for the analyses in this work, against experimental data. For that purpose, the unsteady pressure is computed for the isolated case at  $x = 6D_j - y = 1.5D_j$  (trailing-edge position in the installed case) with  $M_a = 0.5$  and medium grid resolution, and compared with microphone measurements performed in the campaign reported in Chapter 6. The spectra are shown in Fig. 7.10 in terms of Power Spectral Density (PSD) versus Strouhal number ( $St = f \times D_j / U_j$ ). A reference pressure of  $2 \times 10^{-5}$  Pa is used for the conversion to dB.

The spectra show good agreement in the low-frequency range, up to  $St = 0.4$  with maximum deviations of approximately 2 dB/Hz. For  $St > 0.4$ , which is in the inertial subrange/acoustic field for this position as shown by the sharp decay in the spectrum, there are differences in the order of 4 dB/Hz. However, this frequency range is not of par-

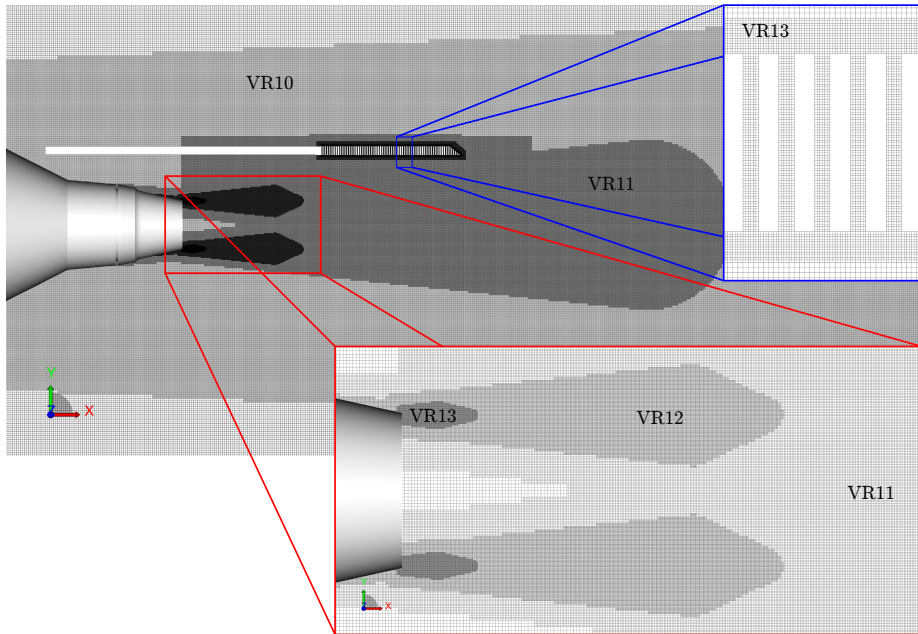


Figure 7.9: Mesh at the symmetry plane of the installed jet set-up with a flat plate with perforated trailing edge. The finest element size for the medium resolution is 0.14 mm (VR13). This level of refinement is placed downstream of the nozzle lip and in the porous material. The following VR levels indicate a doubling in element size.

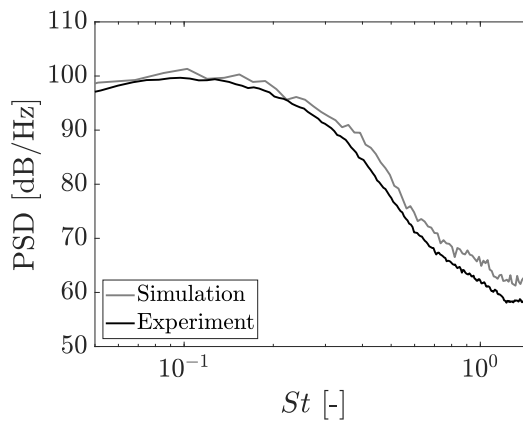


Figure 7.10: Near-field pressure spectra computed at  $x = 6D_j - y = 1.5D_j$  for the isolated jet at  $Ma = 0.5$  and compared with experimental microphone measurements [2].

ticular interest for jet-installation effects nor the noise reduction provided by the permeable materials, based on the results in Chapter 6, which are concentrated in the energy-containing region of the spectrum ( $St < 0.3$ ).

A grid convergence study and set-up validation are also carried out in terms of far-field spectra for the cases with flow-permeable trailing-edges. The effect of grid resolution is assessed for the configuration with a metal foam trailing edge, as shown in Fig. 7.11a, for a  $Ma = 0.5$  jet. The spectra are obtained for a polar angle  $\theta = 90^\circ$  (reflected side) and are plotted in terms of Sound Pressure Level (SPL), for a constant frequency band of 100 Hz. The spectra are also compared with experimental results from Chapter 6 for set-up validation. The frequency band of the experimental data has been changed to 100 Hz, so that it is comparable with the computational results.

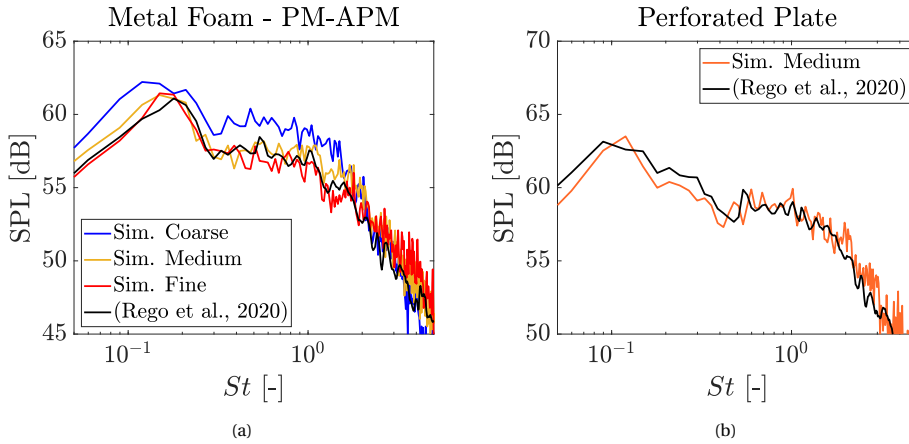


Figure 7.11: Grid convergence analysis and validation. Far-field spectra of the installed jet with a (a) Metal foam trailing edge for different grid resolutions, compared to experimental results [2]. (b) Perforated trailing edge at medium grid resolution, compared to experimental results [2]. Spectra obtained at  $\theta = 90^\circ$  and for  $Ma = 0.5$ .

As shown in Fig. 7.11a, the spectral shape is correctly predicted by the simulations from all grids. The curve for the coarse mesh has a slightly higher amplitude up to  $St = 2$ , indicating that smaller flow structures are not accurately resolved, and consequently their energy content is included in that frequency range. For  $St > 2$ , there is a sharp decay in amplitude due to the grid cut-off size. The spectra for the medium and fine grids, on the other hand, display similar amplitudes, within 1 dB variation, indicating grid convergence. There is also a good agreement with the experimental results, with maximum deviations on the order of 1.5 dB, indicating that the PM-APM approach for the modeling of the metal foam is valid along with the prescribed resistivity inputs. The computational set-up is also validated for when the actual flow-permeable geometry is used in the simulations. The spectrum for the perforated plate case, computed at  $\theta = 90^\circ$  and for the medium resolution, is compared with experimental results, as shown on Fig. 7.11b. Similarly as the metal foam, there is a good agreement between the simulation and experiment, with a correct predicted spectral shape, and a maximum deviation of 2 dB. Therefore, the analyses carried out in the remainder of this paper are obtained for a medium resolution grid, which is shown to predict accurate results in order to understand the physical mechanisms in the configuration with a relatively low computational cost.

## 7.4. FAR-FIELD NOISE

### 7.4.1. FAR-FIELD SPECTRA

In this section, the far-field SPL spectra for the installed jet with flow-permeable trailing-edges are reported and compared to the reference solid configuration and the isolated jet. The spectra are obtained for a constant frequency band of 100 Hz, at a polar angle  $\theta = 90^\circ$  (reflected side), and plotted in Fig. 7.12 for both jet conditions.

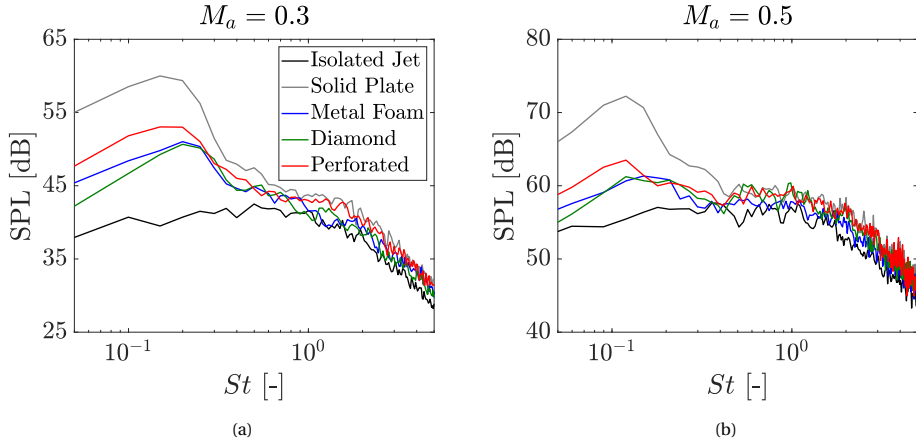


Figure 7.12: Far-field spectra for the flow-permeable trailing edge configurations, compared with isolated jet and the reference solid case, for  $\theta = 90^\circ$  (a)  $Ma = 0.3$ . (b)  $Ma = 0.5$ .

Comparing the results for the isolated jet and the installed case with the solid plate, it is shown that installation effects result in a low-frequency noise amplification; the maximum increase with respect to the isolated case is 21 dB at  $St = 0.15$  ( $Ma = 0.3$ ), and 17 dB at  $St = 0.12$  ( $Ma = 0.5$ ). For the latter, with a higher jet velocity, the quadrupole sources due to turbulent mixing become acoustically more efficient with respect to the dipoles on the plate, and thus the relative low-frequency noise amplification due to installation effects is lower. At mid and high frequencies ( $St > 0.6$  for  $Ma = 0.3$  and  $St > 0.4$  for  $Ma = 0.5$ ), there is a constant offset between the installed and isolated spectra of approximately 3 dB due to reflection of acoustic waves generated by quadrupole sources [13, 14].

The configurations with flow-permeable trailing edges show significant noise reduction with respect to the solid case, particularly for  $St < 0.4$ , where installation effects are dominant. For  $Ma = 0.3$ , reductions of 10 dB are obtained at the spectral peak ( $St = 0.15$ ) for the metal foam and diamond trailing edges, whereas the perforated provides 7 dB reduction. For frequencies higher than the spectral peak, the noise levels of all flow-permeable configurations become similar. Similar trends occur for  $Ma = 0.5$ , with reductions of 12 dB (metal foam and diamond) and 9 dB (perforated) relative to the solid case, at the spectral peak ( $St = 0.12$ ). The metal foam and diamond display similar amplitude, except at very low frequencies ( $St < 0.1$ ), for which the latter performs better. For the higher jet velocity, the noise levels of the flow-permeable configurations are closer to the isolated one, which is in agreement with the results of Chapter 6.

### 7.4.2. FAR-FIELD NOISE BREAKDOWN

Despite the visible reduction in SPL amplitude due to the permeable trailing edges, the dominant sources for those configurations are not yet clear. It has been hypothesized that the noise at the original trailing edge is largely reduced, and the junction becomes a region of strong acoustic scattering and possibly the dominant source for the permeable cases. In order to verify this hypothesis, the beamforming technique is applied to study the location of the dominant acoustic source, as described in Section 7.2.3. The results are evaluated for a scan plane on the lower side of the plate, initially for the fully solid case as a baseline, at  $St = 0.12$  (far-field spectral peak) and  $St = 0.24$ , as shown in Fig. 7.13, for the  $M_a = 0.5$  jet. Similar results are obtained for the other condition.

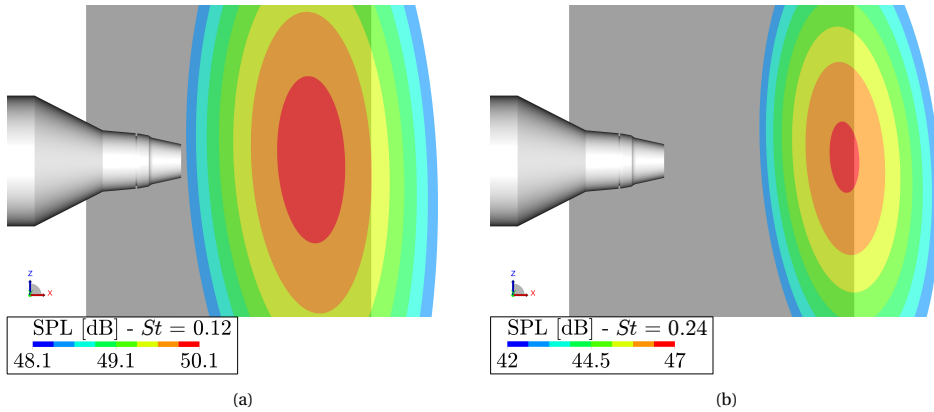


Figure 7.13: Acoustic source location from beamforming applied to the installed jet with a fully solid plate ( $M_a = 0.5$ ). (a)  $St = 0.12$ . (b)  $St = 0.24$ .

The contour plot in Fig. 7.13a shows that, for a frequency  $St = 0.12$ , the dominant acoustic source on the lower side of the plate is placed upstream of the trailing-edge, centered at  $x = 4.1D_j$ . On the other hand, for  $St = 0.24$ , the source is located at the trailing edge. Therefore, the results indicate that for  $St = 0.12$  the impingement of pressure fluctuations is the dominant noise mechanism, whereas for  $St = 0.24$  the scattering at the edge is more significant. Results for intermediate frequencies ( $0.12 < St < 0.24$ ), not displayed for the sake of brevity, show that the source progressively moves towards the trailing edge, as the frequency is increased. The contours also show that the SPL for the source at  $St = 0.12$  is higher than for  $St = 0.24$ , in agreement with the far-field spectra. The discussion on the dominant noise generation mechanisms will be addressed in Section 7.6.

Source localization is also applied to the flow-permeable configurations. The results are shown in the contour plots of Fig. 7.14, for the  $M_a = 0.5$  jet and  $St = 0.12$ . Different color scales are used for each configuration in order to facilitate the visualization. For the metal foam and diamond trailing edges, the dominant acoustic source at a frequency  $St = 0.12$  is located near the junction between the solid and flow-permeable regions of the plate ( $x = 3D_j$ ). For those configurations, this region acts as a geometric discontinuity and, therefore, it is also a scattering region for hydrodynamic waves in the jet mixing

layer. At the junction, it is also expected that the sound field is governed by diffraction effects, for which some of the energy present in near-field hydrodynamic fluctuations in the jet mixing layer is converted into acoustic waves at the edge [15]. For the perforated case, a behavior similar to that of the original solid case is obtained, with the source upstream of the trailing edge ( $x = 4.6D_j$ ), but downstream of the junction.

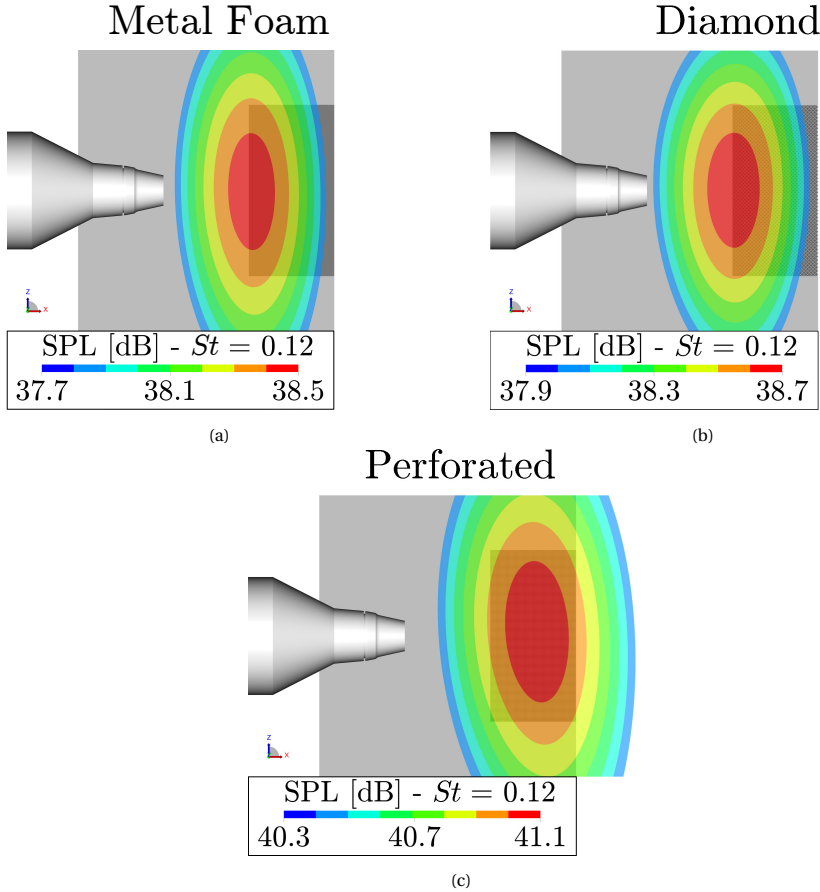


Figure 7.14: Acoustic source location from beamforming applied to the installed jet with flow-permeable trailing edges, for a frequency  $St = 0.12$  and  $Ma = 0.5$ . (a) Metal foam. (b) Diamond. (c) Perforated.

Since the junction has become the dominant source location for the metal foam and diamond configurations, it is useful to compare the noise generated by the solid ( $x < 3D_j$ ) and porous ( $x > 3D_j$ ) regions of the plate separately. For that purpose, the far-field noise produced by pressure fluctuations on the plate is computed through the FW-H analogy [7] applied to those surfaces. However, it is necessary first to verify that this approach provides correct results, as well as confirm that the computed noise due to jet-installation is independent of the chosen FW-H surface. Therefore, the spectra shown in Fig. 7.15 are obtained for the fully solid plate case from fluctuations on the

permeable FW-H surface encompassing the whole geometry, as well as those on the flat plate surfaces (upper and lower sides, leading edge and trailing edge). The spectra are obtained for a polar angle  $\theta = 90^\circ$  and  $M_a = 0.5$ . The black curve is the same as the solid plate spectrum of Fig. 7.12b.

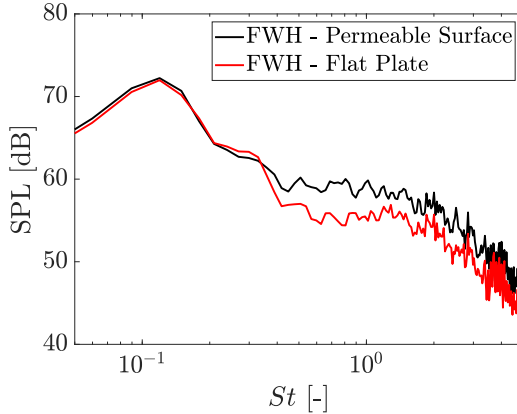


Figure 7.15: Far-field SPL spectra for the installed jet with a fully solid plate, obtained from the FW-H analogy applied to different surfaces: a permeable cylinder encompassing the whole geometry (black curve) and considering just the fluctuations on the flat plate surface (red curve). Spectra obtained for  $\theta = 90^\circ$  and  $M_a = 0.5$ .

There is a good agreement between the curves up to  $St = 0.3$ , which is the frequency range where jet-installation noise is dominant. This shows that the noise levels are accurately predicted and independent of the chosen FW-H surface. At higher frequencies, the curves do not agree since the spectrum obtained from the flat plate pressure fluctuations does not properly capture the quadrupole sources in the jet mixing layer nor reflection effects. However, this frequency range is not relevant for the current analysis.

For the permeable trailing edge cases, the spectra are computed individually for each region of the plate, i.e. solid (orange curve) and porous (blue curve), as plotted in Fig. 7.16, for  $\theta = 90^\circ$  and  $M_a = 0.5$ . The isolated jet spectrum is also included for reference, as well as the noise generated by the entire plate (green curve), which is equivalent to the sum of the solid and porous regions.

For the metal foam, the spectra show that the noise generated by the solid region of the plate is dominant with respect to the porous part, except for low frequencies up to  $St = 0.09$ . For the diamond configuration, the solid region of the plate is dominant in the entire analyzed frequency range. The perforated case, on the other hand, displays the opposite behaviour: the porous region has a higher amplitude than the solid one, even up to high frequencies ( $St = 1.3$ ). These results are in agreement with the dominant acoustic source position obtained from beamforming, as shown in Fig. 7.14. Moreover, considering the noise generated by the entire plate for each configuration (green curves), it is visible that for the metal foam and diamond cases, the amplitude is approximately of the same order as the isolated jet. It is also interesting to notice that, for the metal foam, the frequency range where the porous section generates more noise than the solid

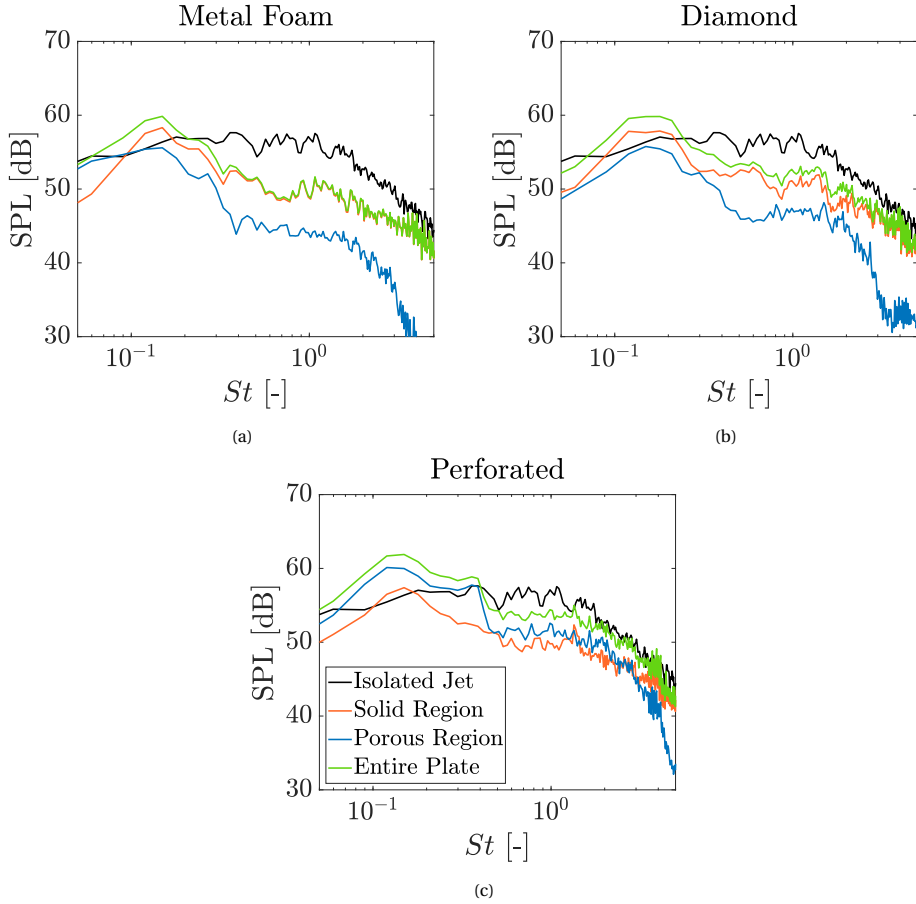


Figure 7.16: Far-field noise spectra generated by solid (orange curve) and porous (blue curve) regions of the plate separately, for each flow-permeable configuration and  $Ma = 0.5$ . The solid section of the plate extends up to  $x = 3D_j$ , whereas the permeable one is located at  $3D_j < x < 6D_j$ . The green curve represents the noise generated by the entire plate (sum of solid and porous regions). (a) Metal foam. (b) Diamond. (c) Perforated.

one ( $St \leq 0.09$ ) is the same as in the spectra of Fig. 7.12 where the noise for the metal foam configuration is higher than that of the diamond. Therefore, this difference occurs because more noise is generated by the porous region of the plate, so it is likely due to the different material properties. This is verified in the next section.

## 7.5. VOLUMETRIC FLOW RATE AND SURFACE PRESSURE FLUCTUATIONS

In this section, the difference between the far-field noise levels of the permeable configurations is linked to the properties of each material, particularly the resistivity, which, according to Darcy's law, affects directly the pressure drop across the surface. In order

to verify this hypothesis, the r.m.s. volumetric flow rate, integrated through the permeable region of the plate, is computed and reported in Table 7.6, for both jet conditions. The values are non-dimensionalized by the nominal jet volumetric flow rate for each condition ( $U_j \times \pi D_j^2/4$ ). The flow rate through an equivalent virtual surface, with the same dimensions as the permeable trailing edges ( $3D_j < x < 6D_j$ ,  $y = 1.5D_j$  and  $-3D_j < z < 3D_j$ ), is also computed for the isolated jet. This surface simply consists of a measurement plane in the isolated jet, parallel to the lower side of the plate surface in the installed case and does not affect the flow development. Regarding the volumetric flow rate, the extreme cases are the isolated jet, for which there is no flow blockage, and the installed case with solid plate, for which there is total blockage and zero flow rate through the surface. The goal of the analysis is then to define where each permeable case is located with respect to those two extremes and link the findings to the properties of the material (porosity and permeability) and the surface pressure fluctuations which are directly correlated to the produced noise.

Table 7.6: Root-mean-square volumetric flow rate through the porous region for each flow-permeable configuration, non-dimensionalized by the nominal jet mass flow of each condition. The flow rate through an equivalent surface is also computed for the isolated jet as a reference value.

$Ma$ [-]	$\dot{m}_{\text{isolated}} [10^{-3}]$	$\dot{m}_{\text{metal foam}} [10^{-3}]$	$\dot{m}_{\text{diamond}} [10^{-3}]$	$\dot{m}_{\text{perforated}} [10^{-3}]$
0.3	7.32	6.09	6.87	4.42
0.5	7.98	7.13	7.54	4.77

The results show that the non-dimensionalized values are similar for both conditions, indicating that the flow velocity through the porous material is likely proportional to the jet velocity. Moreover, comparing the different configurations, the diamond and metal foam have similar volumetric flow rates, both higher than that of the perforated. Therefore, the latter provides higher blockage to the unsteady flow normal to the plate surface. The flow rates through the metal foam and diamond trailing edges are also close to the reference value of the isolated jet, indicating that a further increase in the structure permeability is not likely to result in significant changes to the flow rate, and possibly no change to the noise levels.

The unsteady flow through the permeable trailing edge affects the pressure balance across the surface, which is directly responsible for the noise generation. Therefore, the distribution of pressure fluctuations  $\hat{P}$  on the surface is analyzed in the frequency domain for each flow-permeable configuration and compared with the reference solid case. Firstly, contour plots of the pressure on the lower side of the plate are shown in Fig. 7.17 in logarithmic scale, for a frequency  $St = 0.12$ , and for the solid and metal foam cases respectively. The other flow-permeable cases display similar trends as the metal foam. The values are non-dimensionalized by the nominal jet dynamic pressure ( $0.5\rho U_j^2$ ). It is worth mentioning that these plots also consider pressure fluctuations of hydrodynamic characteristic and, therefore, they are not necessarily equivalent to acoustic source maps.

The maximum amplitude of pressure fluctuations for the metal foam is visibly lower than for the reference solid case because of the flow through the porous material. Since

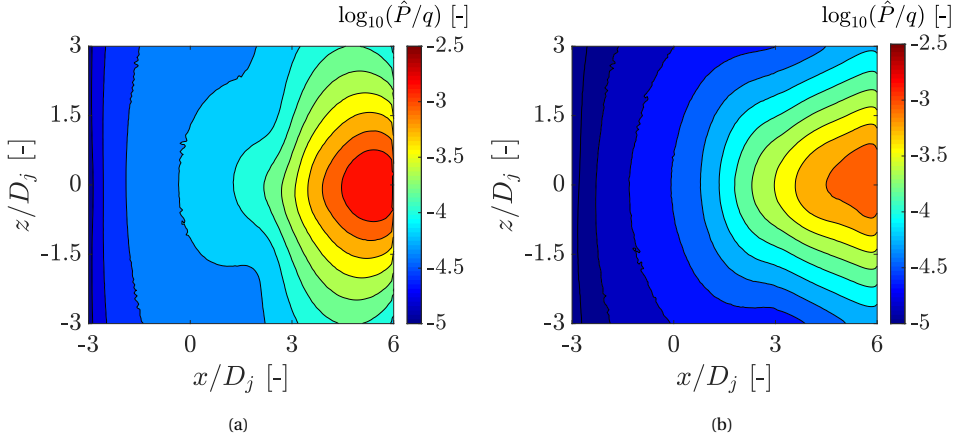


Figure 7.17: Pressure distribution on the lower side of the plate, for a frequency  $St = 0.12$  and  $Ma = 0.5$ . (a) Fully solid plate. (b) Metal foam trailing edge.

there is communication between the upper and lower sides of the plate near the trailing edge, the unsteady flow generated by the jet mixing layer is no longer bounded by the surface at this region, and the consequent vertical velocity component through the permeable material leads to a reduction of the surface static pressure.

In more detail, the pressure distribution in the streamwise direction of the plate, in the symmetry plane ( $z = 0$ ), is plotted in Fig. 7.18a. It is shown that the amplitude of pressure fluctuations for the cases with flow-permeable trailing edges is lower than that of the solid case, except for the region around  $x = 3D_j$ . This point corresponds to the solid-porous junction of the plate, which acts as a scattering region. This behaviour is present for the metal foam and diamond cases, and confirmed by the beamforming results of Fig. 7.14. Moreover, the amplitude near the trailing edge is lower for all flow-permeable cases with respect to the solid one and the trend is consistent with the volumetric flow rate through each configuration. The metal foam only differs from the diamond close to the trailing-edge position. Finally, near the nozzle exit ( $x < 1.5D_j$ ), the jet has not yet developed sufficiently in order to generate strong hydrodynamic pressure fluctuations. This effect, coupled with a nearly constant amplitude up to  $x = 1.5D_j$  for the solid case, suggests that the pressure fluctuations in this region are dominated by acoustic waves scattered at the plate trailing edge. These acoustic waves have a dipole/cardioid directivity pattern and thus travel upstream of the trailing edge. For the permeable cases, there is a consistent increase in amplitude moving downstream, indicating that the scattered acoustic waves are weaker than the linear hydrodynamic field of the jet. Therefore, the difference between the solid and permeable cases in this region is linked to a weaker scattering mechanism for the permeable cases.

A similar analysis is also carried out in the spanwise direction of the plate, at a fixed streamwise position  $x = 5D_j$ , as shown in Fig. 7.18b. At this position, the amplitude of pressure fluctuations for the flow-permeable cases is lower than that of the solid case throughout the entire span of the porous region. The metal foam and diamond curves

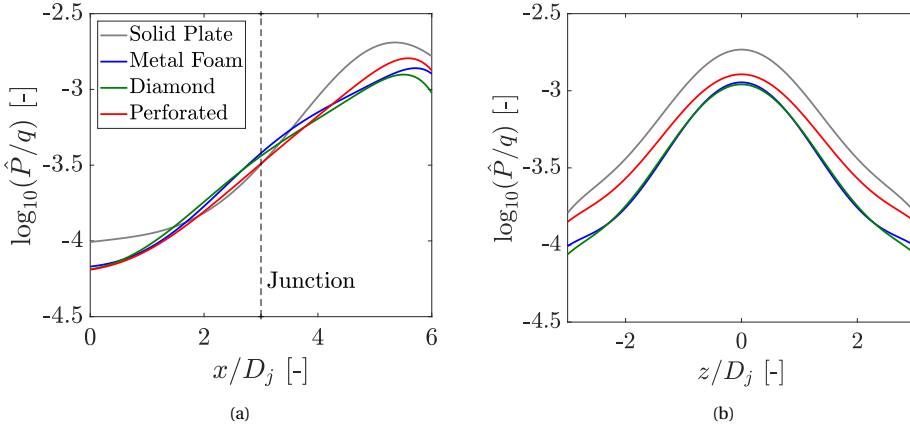


Figure 7.18: Amplitude of pressure fluctuations on the lower side of the plate, for a frequency  $St = 0.12$  and  $Ma = 0.5$  (a) Streamwise direction at  $z = 0$ . (b) Spanwise direction at  $x = 5D_j$ .

practically collapse, whereas the perforated has higher amplitude, particularly at  $z = \pm 3D_j$ . This is likely due to a misalignment between the unsteady flow from the jet (always in the radial direction) and the axis of the holes in the perforation, leading to a reduced volumetric flow rate far from the centerline. However, the amplitude of fluctuations at that region is almost one order of magnitude lower than at the centerline. Since the trailing edge is located in the linear hydrodynamic field of the jet [16], where the pressure decays exponentially with radial distance from the shear layer, the center of the plate ( $z = 0$ ) is subjected to impingement of stronger pressure fluctuations with respect to the spanwise extremities of the permeable materials ( $z = \pm 3D_j$ ). Therefore, it is expected that the difference between the permeable cases near  $z = \pm 3D_j$  does not have a significant contribution to the far-field noise.

## 7.6. NOISE FROM PRESSURE WAVE IMPINGEMENT AND TRAILING EDGE SCATTERING

The results in the previous section have shown how the permeable trailing edges modify the flow around the plate with consequent changes to the surface pressure distribution. However, it is still necessary to assess how the noise generation mechanisms on the solid plate, i.e. the impingement of pressure waves on the surface and the scattering at the edge, are individually affected by the permeable T.E.s. The main distinction between these mechanisms is their directivity pattern (dipole and cardioid shapes, respectively). Therefore, in order to determine the conditions and frequency range where each of them is dominant, far-field spectra are plotted for three polar angles ( $\theta = 30^\circ$ ,  $\theta = 60^\circ$  and  $\theta = 90^\circ$ ), initially for the solid plate case, as shown in Fig. 7.19. These spectra are obtained solely from the pressure fluctuations on the surface in order to disregard noise from turbulence mixing. Moreover, these spectra are computed for a constant frequency band of 50 Hz so that a more accurate analysis in frequency is carried out.

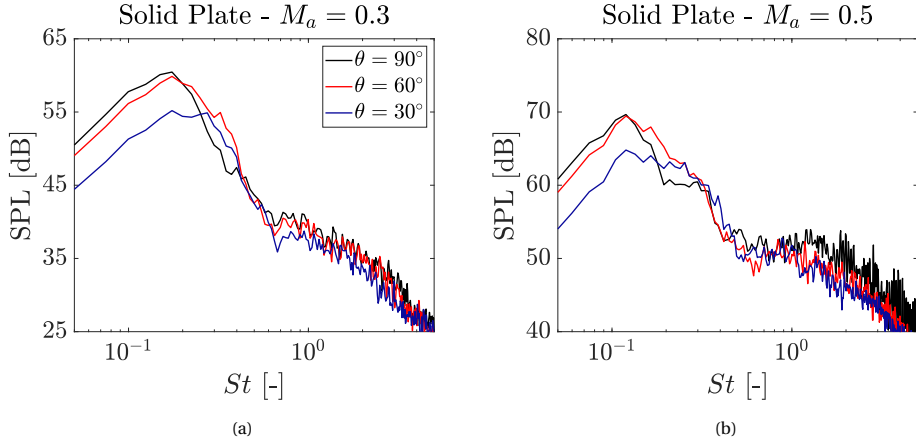


Figure 7.19: Far-field spectra of the surface pressure fluctuations for the installed jet (solid plate) at different polar angles. (a)  $M_a = 0.3$ . (b)  $M_a = 0.5$ .

As shown in Fig. 7.19, the far-field spectra of surface pressure fluctuations for  $\theta = 90^\circ$  have similar shape and amplitude as those shown in Fig. 7.12 for the installed jet with a fully solid plate, particularly at low and mid frequencies. However, for  $\theta = 60^\circ$ , the spectral shape changes: for  $M_a = 0.3$ , the amplitude decreases slightly for  $St < 0.2$ , but increases for  $0.2 < St < 0.4$ , with respect to  $\theta = 90^\circ$ . For  $\theta = 30^\circ$ , the amplitude is mostly lower than that for  $\theta = 90^\circ$ , except in the frequency range  $0.28 < St < 0.4$ . A similar trend occurs for  $M_a = 0.5$ .

The low-frequency noise reduction with a decrease in polar angle can be associated with a dipolar directivity pattern, which has a maximum at the direction normal to the surface ( $\theta = 90^\circ$ ). As a consequence, the dominant noise generation mechanism in that frequency range is the impingement of pressure waves on the plate. On the other hand, for the frequency range where there is an increase in amplitude with respect to  $\theta = 90^\circ$ , the dominant noise mechanism is the scattering of hydrodynamic pressure waves at the trailing edge, which has a cardioid directivity. However, for the latter, it would be expected that the curve for  $\theta = 30^\circ$  had an even higher amplitude than  $\theta = 60^\circ$ , which is not the case. It is believed that this results from a combination of both mechanisms in the latter case, for which the noise produced by them have similar amplitude.

In order to verify that the far-field spectra has different dominant noise mechanisms at different frequencies, the curves for each polar angle can be scaled with a directivity characteristic of a dipole ( $\sin^2(\theta)$ ) and a cardioid ( $\cos^2(\theta/2)$ ), according to the polar angle convention. For each jet condition, the dipole scaling is applied to low frequencies, up to the spectral peak, whereas the cardioid scaling is applied to mid frequencies, starting at the peak up to the frequency where installation effects are dominant with respect to turbulence mixing. The scaled spectra are shown in Fig. 7.20, with the annotated scaling applied to each frequency range. A good agreement is obtained between the curves, particularly in the dipole region and around the spectral peak. The collapsing of the spectra are, therefore, an indication that the different noise generation mechanisms in

an installed jet are dominant at different frequency ranges. Moreover, the small differences for the  $\theta = 60^\circ$  scaled curve at mid frequencies suggest that, for this case, the dipole effects are still considerable in this frequency range.

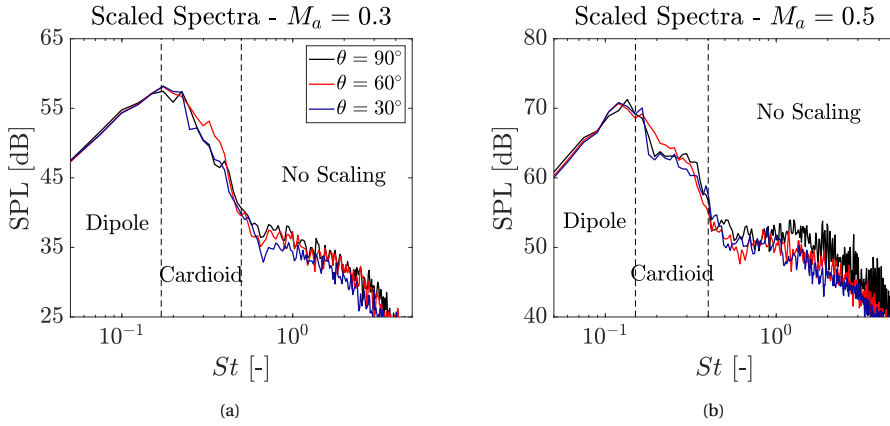


Figure 7.20: Far-field spectra of the surface pressure fluctuations for the installed jet (solid plate) at different polar angles, scaled with a dipole directivity ( $\sin^2(\theta)$ ) at low frequencies, and a cardioid ( $(\cos^2(\theta/2))$ ) at mid frequencies. (a)  $Ma = 0.3$ . (b)  $Ma = 0.5$ .

With the far-field spectrum of an installed jet with a fully solid plate properly characterized in terms of the dominant mechanisms at different frequencies, the effect of a permeable trailing edge on JIN can be properly addressed by linking the final noise signature to each noise generation mechanism. Spectra at different polar angles are obtained for the solid and porous regions of the plate separately. For the former, there are no significant differences between the results of different configurations. Therefore, the far-field spectra from the solid region ( $x < 3D_j$ ) for the configuration with the metal foam trailing edge is shown in Fig. 7.21a.

The spectra shown in Fig. 7.21a have a similar trend as those in Fig. 7.19 for the fully solid plate; at low frequencies the amplitude tends to decrease at shallow polar angles, whereas it increases with  $\theta$  for mid frequencies. Therefore, a scaling based on dipolar/cardioid directivity can be applied to these spectra at different frequency ranges. The best agreement is found, when a dipole scaling is applied up to  $St = 0.21$ , and a cardioid one for  $0.21 < St < 0.4$ . Therefore, for this case, the scaling regions are not related to the spectral peak. The maximum frequency for dipole scaling is higher than that obtained from the original solid plate ( $St = 0.12$ ). This is due to the position of the new geometric singularity (solid-porous junction), at  $x = 3D_j$ ; at this point, the energy content of large-scale structures is lower than at the original trailing-edge position ( $x = 6D_j$ ). Therefore, the contribution due to scattering at low frequencies is reduced, and thus a wider frequency range is dominated by dipole sources. It is also possible that the scattering efficiency at the junction is lower since the change of surface impedance from solid-porous is less abrupt than that from solid-air, as in the original solid case. Further research into this hypothesis is necessary.

For the permeable region of the plate ( $3D_j < x < 6D_j$ ), the spectra for all configu-

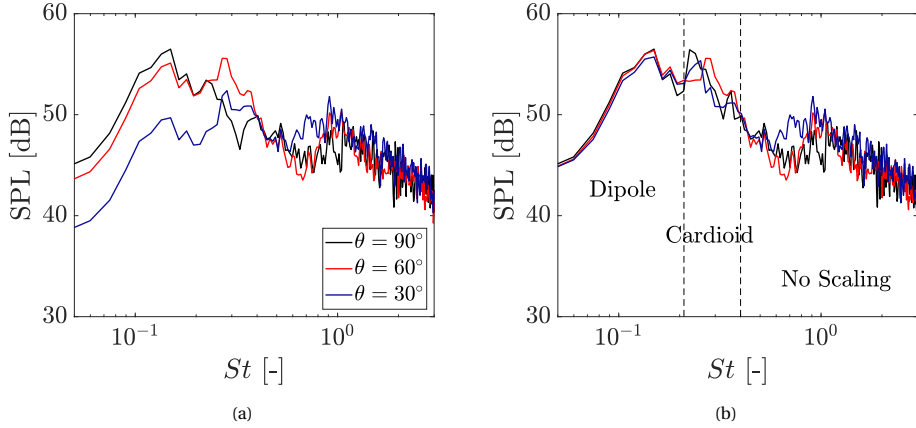


Figure 7.21: Far-field noise generated by the solid region of the surface ( $x < 3D_j$ ) with a metal foam trailing edge for  $M_a = 0.5$ . (a) SPL spectra for different polar angles. (b) Scaled SPL spectra based on dipole/cardioid directivity.

rations are shown in Fig. 7.22. The spectra display a similar trend: the SPL decreases with decreasing  $\theta$  for the entire assessed frequency range. These results indicate that the dominant noise generation mechanism in the porous region is the pressure wave impingement. In order to confirm this assumption, a dipole directivity scaling is applied to the curves up to  $St = 0.4$ . The results in Fig. 7.23 show that a good agreement is obtained with the scaled spectra, confirming the mechanism responsible for noise generation for those cases. The absence of a frequency range with cardioid directivity indicates that the scattering mechanism is largely reduced at the original trailing-edge position. These results are in qualitative agreement with those from Jaworski and Peake [17], who demonstrated that the far-field noise at low frequencies, caused by edge scattering, changes from a fifth-power scaling with the flow velocity to a sixth-power one when the trailing edge is replaced by a permeable structure. This means that the far-field noise is no longer dominated by edge scattering ( $U^5$ ), but instead it has a dipole characteristic ( $U^6$ ), which is also visible in the spectra of Fig. 7.23. It is necessary, however, to assess how the permeable trailing edges affect noise scattering in the near field.

According to Amiet [18], one of the parameters that affect the scattered noise produced by turbulence convecting past a trailing edge is the spanwise correlation at that region. Therefore, it is interesting to assess how the flow-permeable trailing edges affect this parameter, with respect to the original solid case. The coherence  $\gamma$  between pressure signals in the spanwise direction at the trailing-edge region ( $x = 6D_j$ ) is computed, using the signal at the symmetry plane ( $z = 0$ ) as reference. The results are plotted in Fig. 7.24 for a frequency  $St = 0.12$ . It is shown that the spanwise coherence is highest for the solid trailing-edge case. The flow-permeable cases, however, display similar values throughout the span, indicating that the permeability of the insert or the shape of the channels do not play a significant role for this parameter. Therefore, it is concluded that the noise due to scattering at the plate trailing edge is decreased not only due to a lower

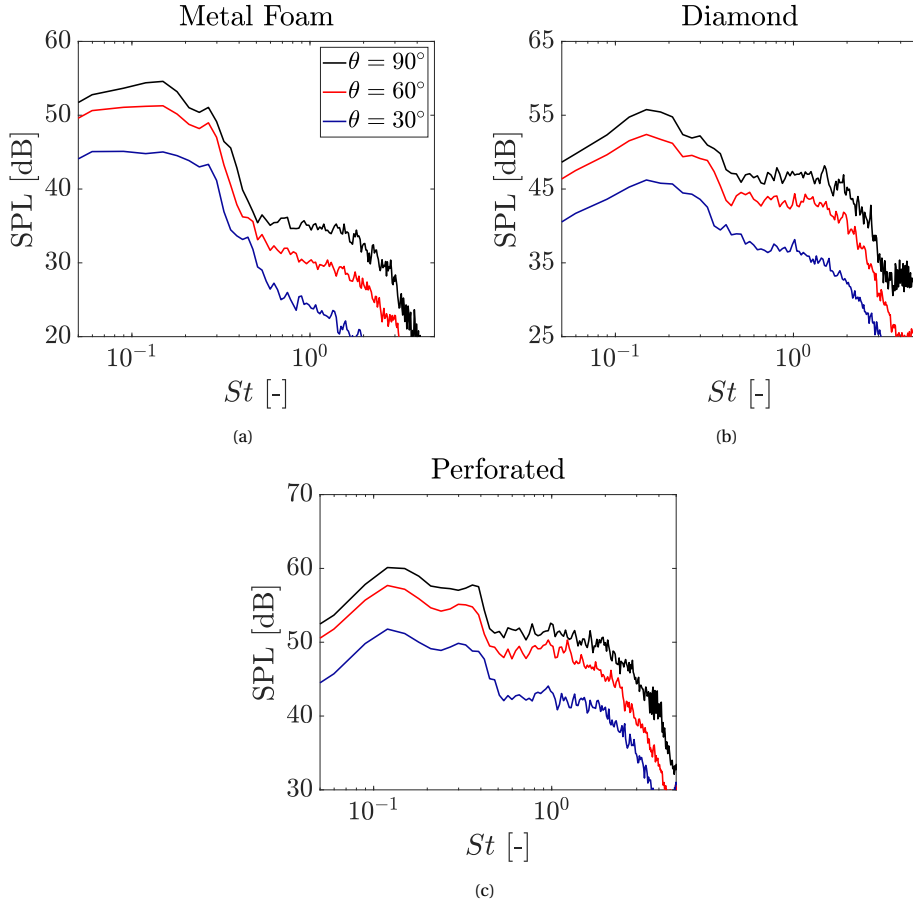


Figure 7.22: Far-field noise generated by the porous region of the surface ( $3D_j < x < 6D_j$ ), for different polar angles and  $M_a = 0.5$ . (a) Metal foam. (b) Diamond. (c) Perforated.

amplitude of surface pressure fluctuations, but also due to a lower spanwise coherence, which is similar for all permeable configurations.

As a confirmation that the noise due to scattering at the original trailing edge position is no longer dominant, the phase angle  $\phi$  between the pressure fluctuations on the upper and lower sides of the plate is computed, at a position  $x = 5D_j$ , as plotted in Fig. 7.25a. The results show a higher phase angle for the solid plate than those with permeable trailing edges. For the former, this phase difference is due to scattered acoustic waves traveling upstream, whereas for the latter, the lower phase shift is consistent with hydrodynamic fluctuations on both sides of the plate; acoustic waves scattered at the trailing edge are, therefore, considerably weaker in those cases. Moreover, the phase angle is also similar for all permeable cases, including the perforated plate, indicating that the insert resistivity is not affecting the phase of the pressure fluctuations traveling from the lower to the upper side of the plate. Combining these results with the spanwise

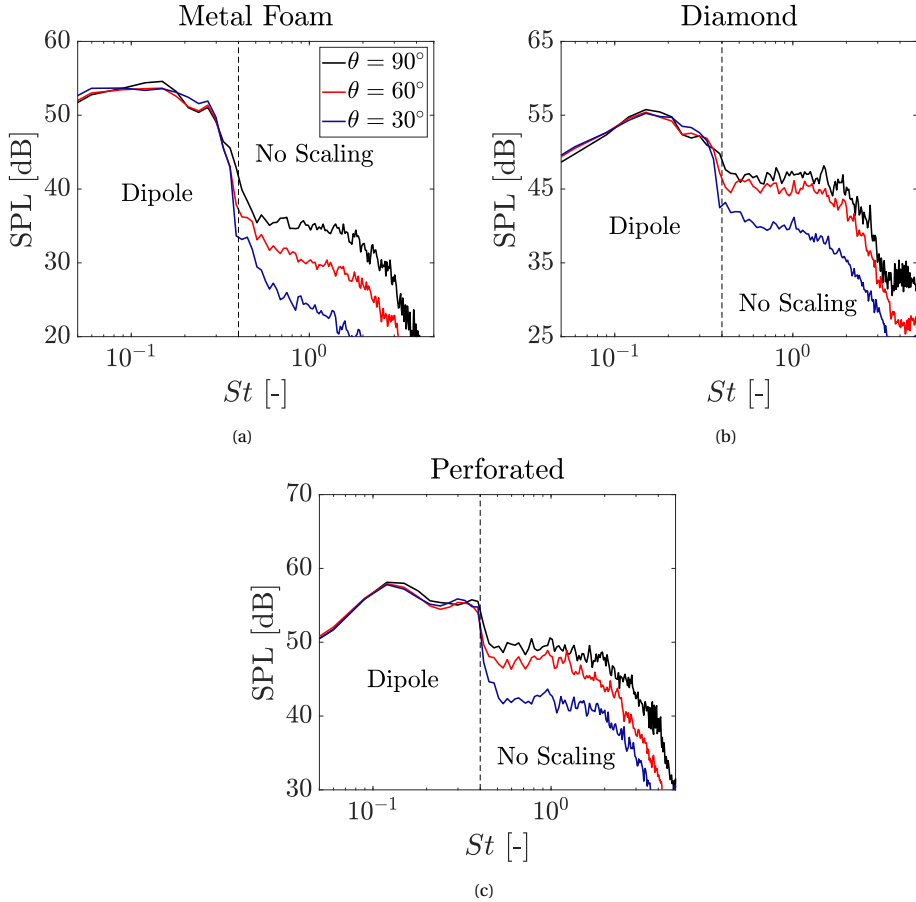


Figure 7.23: Far-field noise generated by the porous region of the surface ( $3D_j < x < 6D_j$ ), for different polar angles and  $M_a = 0.5$ . (a) Metal foam. (b) Diamond. (c) Perforated.

coherence analysis, it is concluded that the reduction of noise due to edge scattering is independent of the trailing edge resistivity, for the investigated cases. Additionally, the lower amplitude of pressure fluctuations for the permeable cases with respect to the solid one near the nozzle exit, as shown in Fig. 7.18a, is a direct consequence of lower noise due to scattering. Finally, the phase angle is also computed upstream of the junction, as shown Fig. 7.25b. At this position, the phase shift is similar for the solid and permeable cases, indicating the effects of scattering at the solid-permeable junction.

Based on the obtained results, it is concluded that the scattering mechanism at the original trailing-edge position is no longer significant for the permeable configurations. This is valid for all types of inserts, thus showing how a structure with low permeability, such as the perforated, is still capable of providing considerable JIN reduction. The dominant noise generating mechanism in the permeable region is shown to be related to surface pressure fluctuations, which are intimately linked to the permeability/resistivity

## 7.7. CONCLUDING REMARKS

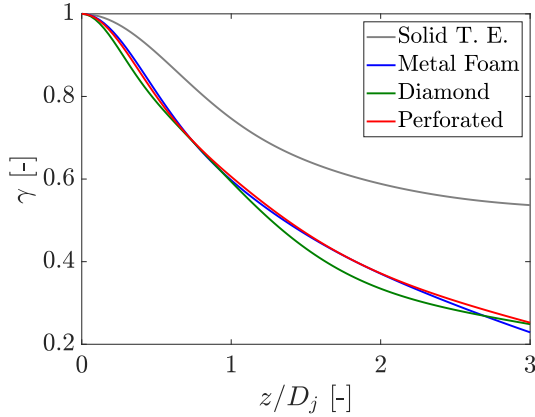


Figure 7.24: Coherence values from surface pressure in the spanwise direction at the plate trailing edge ( $x = 6D_j$ ), computed with the signal at the symmetry plane ( $z = 0$ ) as reference for the solid and flow-permeable cases. Data plotted for  $St = 0.12$  and  $M_a = 0.5$ .

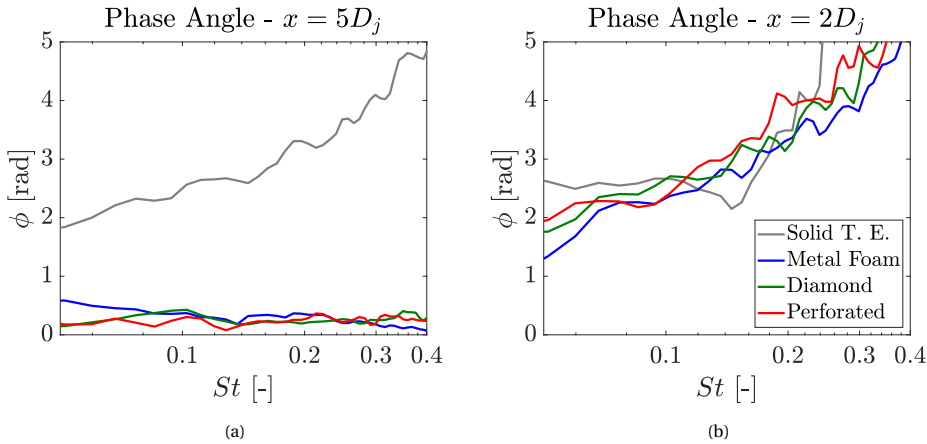


Figure 7.25: Phase angle between pressure fluctuations on the lower and upper sides of the plate, computed for  $M_a = 0.5$  at (a)  $x = 5D_j$  and (b)  $x = 2D_j$ .

of the material, since these parameters define the flow rate through the permeable structure and, consequently, the amplitude of fluctuations. Considering the overall surface, this effect is summed to the noise produced by the solid region of the plate, generated both due to impingement of pressure waves as well as scattering at the solid-permeable junction, which is a new discontinuity introduced in the geometry.

## 7.7. CONCLUDING REMARKS

A numerical investigation on jet-installation noise reduction with the application of permeable trailing edges is performed. The focus of this work consists in studying how

those permeable structures provide noise reduction, by analyzing their effect on the main noise generation mechanisms of a plate in the vicinity of a jet, i.e. noise produced either by surface pressure fluctuations or trailing-edge scattering.

The model for the analyses is comprised by a nozzle, generating a single-stream subsonic jet, and a flat plate placed in the linear hydrodynamic field with no grazing flow. The investigated permeable structures consist in a metal foam, which is modeled as an equivalent porous medium following Darcy's equation, due to its complex geometry. A perforated trailing edge, with straight holes normal to the jet axis, and a diamond-shaped structure are also investigated, but for these cases the actual geometry is simulated. The metal foam and diamond structures have a lower resistivity compared to perforated one. The permeable region of the plate has a length of  $3D_j$  upstream of the trailing edge in the streamwise direction, and a  $6D_j$  span.

Far-field results of the installed jet with a solid plate show a significant low-frequency noise increase with respect to the isolated configuration (17 dB at  $St = 0.12$ , for  $M_a = 0.5$ ). By replacing the trailing-edge with a permeable structure, noise reduction of 12 dB are achieved at the spectral peak ( $St = 0.12$  and  $M_a = 0.5$ ) for the metal foam and diamond, whereas 9 dB reduction is obtained with the perforated structure. Beamforming results show that the dominant acoustic source is located at the solid-permeable junction for the metal foam and diamond cases, confirming the hypotheses from Chapter 6, whereas for the perforated it is located on the insert, upstream of the original trailing edge, similarly as the solid case. It is shown that the pressure fluctuations on the perforated trailing edge are considerably higher than the other structures, for which most of the noise is generated by the solid section of the plate.

The r.m.s. volumetric flow rate through the permeable structures is in line with the properties of the materials and the far-field results. A lower flow rate is obtained for the perforated one, whereas they are similar for the metal foam and diamond, and they are close to the value without surface. Therefore, it is concluded that the difference in noise levels between the permeable configurations is caused by the resistivity of each material. A higher flow rate translates into lower amplitude of pressure fluctuations on the surface, and consequently lower noise emission.

By analyzing far-field results for different polar angles, different behaviours are observed for the solid and permeable sections of the plate. The former exhibits the same characteristics as the original solid plate, with noise at low frequencies displaying a dipolar directivity and, at relatively higher frequencies, with a cardioid shape. This dual behaviour is also verified through beamforming results. For the permeable region, on the other hand, the spectra display a consistent dipolar directivity throughout the entire frequency range where the installation effects are dominant. This occurs for all investigated permeable configurations, thus showing that the scattering mechanism at the original trailing-edge position is strongly reduced, even for the perforated case, which has a high resistivity. These results are confirmed by analyzing the spanwise coherence and the phase shift between the upper and lower sides of the plate. Therefore, noise due to scattering at the trailing edge is largely reduced for all permeable configurations, and the dominant mechanism in that region of the plate is the pressure wave impingement.

Further work on this topic will focus on mitigating the effect of the solid-porous junction, which becomes a new singularity in the geometry and a region of significant noise

generation. For this purpose, a gradual increase in permeability towards the trailing edge is likely to mitigate the generated noise. Moreover, the permeable structures should also be investigated in a realistic wing geometry, as well as with free stream in order to quantify their effect on the aerodynamic properties such as lift and drag.

## REFERENCES

- [1] L. Rego, F. Avallone, D. Ragni, and D. Casalino, *On the mechanisms of jet-installation noise reduction with flow-permeable trailing edges*, [Journal of Sound and Vibration](#) **520** (2022), [10.1016/j.jsv.2021.116582](#).
- [2] L. Rego, D. Ragni, F. Avallone, D. Casalino, R. Zamponi, and C. Schram, *Jet-installation noise reduction with flow-permeable materials*, [Journal of Sound and Vibration](#) **498**, 115959 (2021).
- [3] A. Rubio Carpio, R. Merino Martínez, F. Avallone, D. Ragni, M. Snellen, and S. Van Der Zwaag, *Experimental characterization of the turbulent boundary layer over a porous trailing edge for noise abatement*, [Journal of Sound and Vibration](#) **443**, 537 (2019).
- [4] C. Teruna, F. Manegar, F. Avallone, D. Ragni, D. Casalino, and T. Carolus, *Noise reduction mechanisms of an open-cell metal-foam trailing edge*, [Journal of Fluid Mechanics](#) **898** (2020), [10.1017/jfm.2020.363](#).
- [5] C. Sun, F. Pérot, R. Zhang, P. T. Lew, A. Mann, V. Gupta, D. M. Freed, I. Staroselsky, and H. Chen, *Lattice Boltzmann formulation for flows with acoustic porous media*, [Comptes Rendus Mécanique](#) **343**, 533 (2015).
- [6] A. Rubio Carpio, R. Merino Martínez, F. Avallone, D. Ragni, M. Snellen, and S. Van Der Zwaag, *Broadband Trailing Edge Noise Reduction Using Permeable Metal Foams*, in *InterNoise Conference* (Hong Kong, 2017).
- [7] J. E. Ffowcs-Williams and D. L. Hawkings, *Sound Generation by Turbulence and Surfaces in Arbitrary Motion*, [Philosophical Transactions of the Royal Society A: Mathematical, Physical and Engineering Sciences](#) **264**, 321 (1969).
- [8] T. J. Mueller, *Aeroacoustic Measurements*, 1st ed. (Springer-Verlag, Berlin, Germany, 2002).
- [9] D. P. Lockard, *An efficient, two-dimensional implementation of the Ffowcs Williams and Hawkings equation*, [Journal of Sound and Vibration](#) **229**, 897 (2000).
- [10] J. R. Underbrink, *Circularly symmetric, zero redundancy, planar array having broad frequency range applications*, (2001).
- [11] P. Sijtsma, R. Merino-Martinez, A. M. N. Malgoezar, and M. Snellen, *High-resolution CLEAN-SC: Theory and experimental validation*, [International Journal of Aeroacoustics](#) **16**, 274 (2017).

- 
- [12] C. Brown and J. Bridges, *Small Hot Jet Acoustic Rig Validation*, Tech. Rep. (NASA/TM-2001-214234, Cleveland, OH, USA, 2006).
- [13] R. W. Head and M. J. Fisher, *Jet/Surface Interaction Noise: - Analysis of Farfield Low Frequency Augmentations of Jet Noise due to the Presence of a Solid Shield*, in *3rd AIAA Aeroacoustics Conference* (Palo Alto, CA, USA, 1976).
- [14] A. V. G. Cavalieri, P. Jordan, W. R. Wolf, and Y. Gervais, *Scattering of wavepackets by a flat plate in the vicinity of a turbulent jet*, *Journal of Sound and Vibration* **333**, 6516 (2014).
- [15] J. E. Ffowcs-Williams and L. H. Hall, *Aerodynamic sound generation by turbulent flow in the vicinity of a scattering half plane*, *Journal of Fluid Mechanics* **40**, 657 (1970).
- [16] L. Rego, F. Avallone, D. Ragni, and D. Casalino, *Jet-installation noise and near-field characteristics of jet-surface interaction*, *Journal of Fluid Mechanics* **895** (2020), [10.1017/jfm.2020.294](https://doi.org/10.1017/jfm.2020.294).
- [17] J. W. Jaworski and N. Peake, *Aerodynamic noise from a poroelastic edge with implications for the silent flight of owls*, *Journal of Fluid Mechanics* **723**, 456 (2013).
- [18] R. K. Amiet, *Noise due to turbulent flow past a trailing edge*, *Journal of Sound and Vibration* **47**, 387 (1976).

# 8

## ACOUSTIC LINERS FOR JET-INSTALLATION NOISE REDUCTION

*Life is a continuous exercise in creative problem solving.*

Michael J. Gelb

*A Helmholtz resonator with a curved cavity is studied for reducing jet-installation noise in a configuration comprised by a subsonic jet and a nearby flat plate. The face-sheet and cavity are designed with the Guess method and the impedance is verified through an experiment and a simulation of an impedance tube. Numerical simulations of the installed jet are performed with an array of resonators placed inside the plate with the face-sheet on the lower side, targeting noise reduction at a ground observer. Far-field spectra show that noise reduction in the order of 7 dB is obtained with respect to the baseline solid plate, at the resonance frequency. The results also show that a slight noise reduction (2 - 3 dB) occurs for an observer on the shielded side of the plate, but in a significantly narrower band around the resonance frequency. This is attributed to the absorption of acoustic waves from the jet itself prior to their scattering at the trailing edge, coupled with a less abrupt impedance discontinuity at the trailing edge. Consequently, the resonators also act by reducing the strength of the acoustic source at the designed resonance frequency.*

---

Parts of this chapter have been included in Reference [1].

## 8.1. OBJECTIVES

IN this chapter, acoustic liners are studied as JIN reduction solutions in a configuration with a jet and a nearby flat plate. Single- and Double-Degree of Freedom (SDOF and DDOF) resonator concepts are developed with the aim to mitigate sound in the frequency range where installation effects are dominant. For low-frequency applications, which is the case of JIN, the cavity of the resonator needs to be significantly long. However, it is desired that the liners occupy the minimum amount of space, either when mounted in the engine or in the airframe surfaces. To tackle this issue, curved-cavity resonators are investigated for low-frequency noise attenuation, wherein the cavity has an L-shape such that the facesheet and backplate planes are orthogonal [2–4].

The absorption characteristics of this concept are investigated by means of both experimental and numerical impedance tube set-ups. After the validation of the concept, numerical simulations of the installed jet with the resonators mounted in the plate are carried out. The results are analysed in terms of far-field spectra, which quantify the noise reduction given by the resonators, as well as provide information on their effect on the acoustic source at the trailing edge. Finally, a combination of permeable materials and acoustic liners is investigated, wherein the latter are applied to mitigate the noise produced by the solid-permeable junction in the plate.

## 8.2. INSTALLED JET CASE

### 8.2.1. COMPUTATIONAL SET-UP

The selected test case for this work is the installed jet configuration reported in the previous chapters, which consists of a solid flat plate placed in the vicinity of a single-stream jet nozzle, as shown in Fig. 8.1. Two geometrical flat plate configurations are studied: length  $L = 4D_j$  with height  $h = 1D_j$ , and  $L = 6D_j$  with  $h = 1.5D_j$ . The length corresponds to the distance between the nozzle exit plane and the trailing edge, whereas the height is the position of the lower side of the plate with respect to the jet centerline.

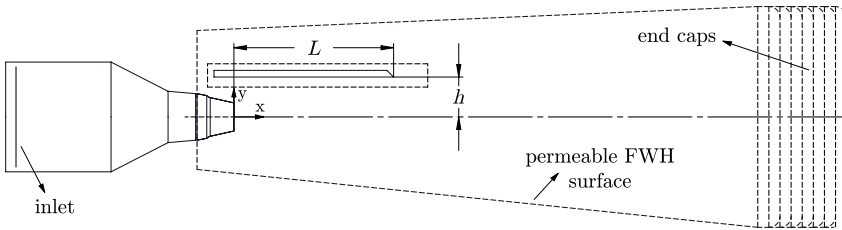


Figure 8.1: Installed jet configuration with a flat plate with length  $L$  and height  $h$ , placed outside of the steady jet flow [5].

Based on the configuration in Fig. 8.1, an array of resonators is mounted inside the plate with the porous face-sheet on the lower side (reflected side). Therefore, the plate thickness for each case is dependent on the cavity dimensions. Different resonator sizes are applied for each geometric case since the target acoustic wave amplitude and frequency range are also case-dependent.

An additional hybrid configuration comprised by a flat plate with a perforated trailing edge (circular channels) and resonators distributed in the remaining section is studied. The goal of this configuration is to achieve further noise reduction than that obtained from each individual solution. The perforations are applied near the trailing edge, at the region with maximum surface pressure fluctuations, in order to reduce the noise due to scattering. The resonators, on the other hand, are applied to mitigate the remaining noise produced by the plate, especially at the solid-permeable junction. This is carried out for the  $L = 4D_j$  -  $h = 1D_j$  geometry and the  $Ma = 0.5$  jet. The perforated region of the plate extends  $1D_j$  upstream of the trailing edge in the streamwise direction and it has a total span of  $6D_j$ . The perforation pattern is shown in Fig. 8.2 and the porosity/resistivity properties of the structure are included in Table 8.1. This analysis is reported in Section 8.6.

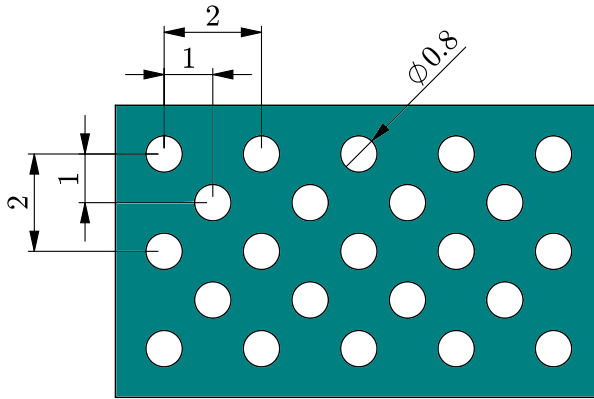


Figure 8.2: Channel dimensions for the perforated trailing edge. Dimensions in mm.

Table 8.1: Porosity ( $\sigma$ ), inertial ( $R_I$ ) and viscous ( $R_V$ ) resistivity of the perforated trailing edge.

$\sigma$ [%]	$R_I$ [ $\text{m}^{-1}$ ]	$R_V$ [ $\text{s}^{-1}$ ]
25.2	3660	4754

Two flow conditions are investigated, characterized by subsonic jets with acoustic Mach number ( $Ma = U_j/c_\infty$ )  $Ma = 0.35$  and  $Ma = 0.5$ . The latter is the main one assessed in this work, and the one used for deriving the inputs for the resonator design. The former is studied in order to determine off-design results for the resonator and verify a possible degradation of the sound absorption. Jet flow properties are reported in Table 8.2, such as the Nozzle Pressure Ratio (NPR), the temperature ratio  $T_R$  (ratio between the jet and ambient static temperature), and the Reynolds number  $Re$ , based on the nozzle exit diameter. Static flow parameters of ambient pressure and temperature are taken from reference [5].

The far-field noise levels are computed on a microphone arc array, centered at the

Table 8.2: Jet flow conditions based on Nozzle Pressure Ratio (NPR), acoustic Mach number  $M_a$  and Reynolds number  $Re$ .

Condition	NPR [-]	$T_R$ [-]	$M_a$ [-]	$Re$ [ $10^5$ ]
1	1.090	0.98	0.35	4.14
2	1.196	0.95	0.50	5.92

nozzle exit plane, with a radius of  $100D_j$ , using data sampled on the permeable FW-H surface. The physical time of the simulations is divided into an initial transient, consisting of 5 flow passes through the FW-H surface, considering the nominal jet velocity as reference, and an acquisition time of 27 flow passes (total simulation time of 32 flow passes). The unsteady pressure on the FW-H surface is sampled with a frequency of 84 kHz and 120 kHz for conditions 1 and 2, respectively. The resultant physical simulation time and acquisition parameters are shown in Table 8.3 for the simulated jet flow conditions. The frequency resolution refers to the minimum frequency band obtained from the FFT of the acoustic signals, based on the acquisition time and the block length and overlap applied in the signal processing.

Acoustic data are also obtained at a microphone phased array for source localization with the beamforming technique [6]. The array is located on a plane parallel to the plate surface, at a distance of  $20D_j$  from the jet axis on the reflected side, and centered at the nozzle exit plane. The array has 364 microphones arranged in a modified Underbrink multi-arm spiral design [7], with an effective diameter of  $3000D_j$  in the streamwise direction and  $160D_j$  in the spanwise direction (refer to Fig. 7.6b in Chapter 7).

Table 8.3: Simulation physical time and acquisition parameters.

Condition	$M_a$ [-]	Physical Simulation Time [s]	FW-H Acquisition Time [s]	Frequency Resolution [Hz]
1	0.35	0.344	0.320	31
2	0.50	0.264	0.224	44

The features of each grid are summarized in Table 8.4 for the installed jet set-up. The resolution is defined as the number of voxels (volumetric cell element in the domain) at the nozzle exit diameter, and the resultant element size is used throughout the jet plume. The finest voxel size is placed at the lip line near the nozzle to accurately capture the shear layer formation, and in the face-sheet/septum orifices for the lined plate cases. For the medium grid resolution, the physical time step is  $2.1 \times 10^{-7}$  s.

### 8.2.2. ACOUSTIC INPUT PARAMETERS

In order to design a resonator for the proposed test cases, it is necessary for the acoustic characteristics of the system to be known beforehand, i.e. the peak frequency and amplitude of pressure fluctuations generated by the plate. For this work, they are extracted from the results of Chapter 5. The SPL spectra shown in Fig. 8.3 are computed from the

Table 8.4: Grid characteristics for convergence analysis of the installed jet configuration.

Grid	Resolution	Voxel Size at Nozzle Exit [mm]	Finest Voxel Size [mm]	Number of Voxels [ $10^6$ ]	kCPUh
Coarse	32	1.59	0.199	331	18.8
Medium	45	1.13	0.141	647	46.4
Fine	64	0.79	0.099	1688	147

maximum level of pressure fluctuations on the reflected side of the plate, for both geometric configurations with a  $M_a = 0.5$  jet. The values are obtained for a 100 Hz frequency band and a reference pressure of  $2 \times 10^{-5}$  Pa is used for the conversion to dB. The peak frequency for each case is highlighted with a vertical dashed line.

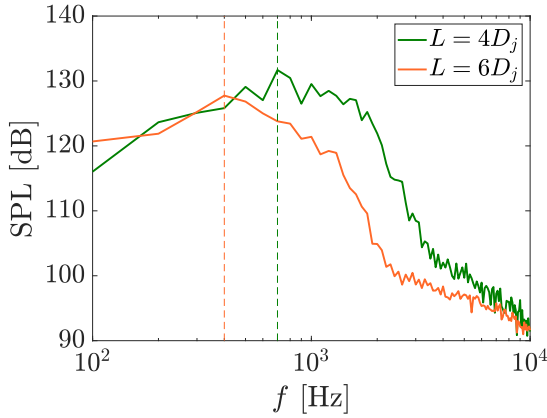


Figure 8.3: Spectra of maximum SPL on the reflected side of the surface for the two plate geometries, at a  $M_a = 0.5$  condition.

Both spectra display a high amplitude, in the order of 130 dB, particularly at low frequencies (up to 1 kHz). For the  $L = 4D_j$  configuration, the peak frequency is found as  $f_{\text{peak}} = 700$  Hz, whereas for  $L = 6D_j$  a  $f_{\text{peak}} = 400$  Hz is obtained. With the longer plate, strong fluctuations are obtained at low frequencies due to increasing energy content of large scale structures when moving downstream of the nozzle exit. Moreover, the difference in amplitude between the two curves, particularly at mid and high frequencies, is linked to the radial position of the plate, the  $L = 4D_j$  plate is closer to the shear layer ( $h = 1D_j$ ) in comparison to the  $L = 6D_j$  one ( $h = 1.5D_j$ ). The resonators for each configuration are designed targeting those peak frequencies for maximum absorption.

The correct input to calculate the acoustic particle velocity in the design equations is the standard deviation of the pressure time signal, equivalent to the Overall Sound Pressure Level (OASPL). This distinction is particularly important for a JIN application, which has a clear broadband characteristic, rather than tonal. The OASPL is, therefore,

computed and plotted on the reflected side of the plate for the  $L = 4D_j$  configuration and  $M_a = 0.5$  jet, as shown in Fig. 8.4 in dB scale.

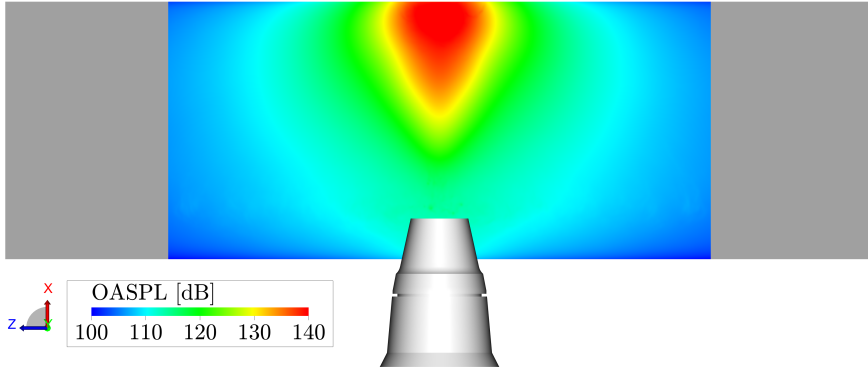


Figure 8.4: OASPL on the reflected side of the plate for the installed jet configuration with  $L = 4D_j$  and  $h = 1D_j$ , at a  $M_a = 0.5$  condition.

The amplitude of surface pressure fluctuations increases in the downstream direction, with the highest levels located near the trailing edge, at the symmetry plane of the plate (OASPL<sub>max</sub> = 140 dB for this configuration). This behaviour is due to a combination of increased energy content of the turbulent structures in the jet downstream of the nozzle exit, and the spreading of the flow in the radial direction, resulting in a closer proximity between the plate and the turbulent structures in the jet mixing layer. A similar trend is obtained for the  $L = 6D_j$  configuration, but with an OASPL<sub>max</sub> = 135 dB. For the design of the resonator, these OASPL<sub>max</sub> values are used to calculate the acoustic particle velocity and, consequently, the non-linear term in the impedance formulation.

### 8.3. RESONATOR DESIGN AND VALIDATION

With the acoustic inputs in hand, it is necessary to define further constraints for the design of the resonators. The most significant one is the limited space in the  $y$ -direction due to the thickness of the plate, which is expected to be kept small. Therefore, a curved-cavity concept is selected for this application, wherein the cavity curves towards the spanwise direction of the plate. This concept is based on a folded cavity design [4]. The drawings in Fig. 8.5 display the SDOF concept adopted for this work, along with the main parameters of the resonator geometry.

A tridimensional and a cut view of the liner are shown in Fig. 8.5a, where the face-sheet, cavity and solid backplate are identified. Unlike the concept of an L-shaped cavity proposed by Sugimoto, Murray and Astley [4], this design eliminates the vertical portion of the cavity, thus resulting in a smaller size in the direction normal to the face-sheet (direction of the plate thickness for the JIN application). There is also a curved section below the face-sheet to provide a smooth change in direction of the sound waves. The main geometric variables are shown in the drawings in Fig. 8.5b. The number of orifices and dimensions  $t$  and  $d$  are selected as input, and the method outputs the face-sheet dimensions and cavity length. For this concept, a square cavity cross-section has been

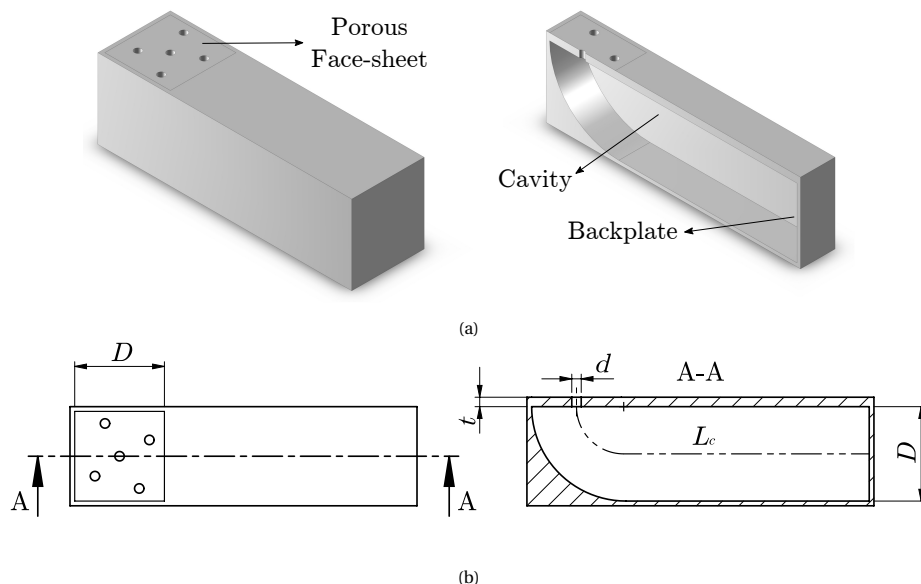


Figure 8.5: (a) Tridimensional view of the curved resonator concept for JIN application. The porous face-sheet the cavity and the backplate are highlighted. (b) Top and cut views of the resonator with the main geometric parameters.

selected with edge  $D$ . The cavity length is defined as the overall distance between the central orifice and the backplate, considering the one-quarter circle path and the straight section. Therefore, while the circular path is a result of the cavity height, the straight part is dimensioned to match the length provided by the design method.

It has been selected that all configurations in this work have five orifices distributed over the face-sheet with edge  $D$ , with one at the center and the remaining placed in an X shape and at variable distances from the central one. Preliminary simulations of the installed jet with the resonator orifices placed equidistantly have shown a strong tone in the noise spectrum. This tone occurs at a frequency corresponding to a wavelength of one-quarter of the distance between the orifices. Moreover, tones have been also shown to occur when three or more orifices are placed in a single line. Therefore, to avoid tonal noise generation by the resonators, the outer orifices are placed at different distances with respect to the central one, and their centers are not collinear.

Before calculating the dimensions of the resonators for each installed jet configuration, it is necessary to verify that the curved cavity concept has the same impedance and absorption coefficient values as those that are output from the design methodology. For this purpose, the impedance of the curved cavity resonator is measured experimentally with the impedance tube at KU Leuven. The set-up for the experiment is shown in Fig. 8.6.

The set-up consists in a steel duct of 40 mm internal diameter and 1.5 m length [8]. At one end of the duct, there is a 60 W horn driver to generate acoustic waves with a given

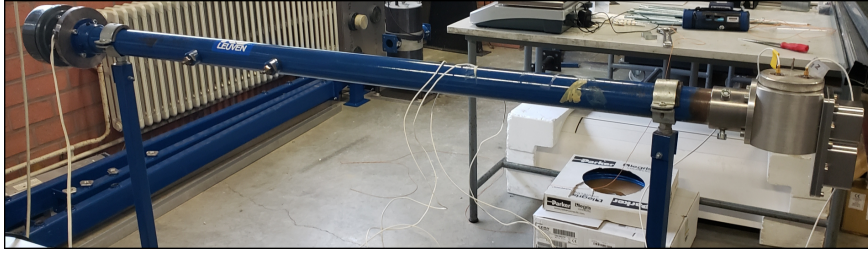


Figure 8.6: Impedance tube set-up. On the left hand side of the duct there is the sound source, whereas on the right hand side there are the pressure sensors and the resonator model.

amplitude and frequency. For this work, white noise has been generated at a given Sound Pressure Level (SPL). At the other end of the duct, the resonator model is attached. Two PCB-106B sensors are placed inside the duct to record pressure fluctuations. A Siemens Scadas Mobile acquisition system in combination with the Siemens Testlab software is used to generate the excitation signal and to measure the transfer function between the two microphones, which is used to compute the impedance of the resonator. Further information on the set-up can be found in reference [8].

The resonator impedance is determined using the two-microphone transfer-function method [9]. This technique is based on identifying the incident and reflected acoustic waves at a sample, using the transfer function measured between the two pressure sensors in the duct to determine the reflection coefficient and, consequently, the impedance of the model [9]. From this value, the resistance and reactance components, as well as the absorption coefficient can be calculated.

Moreover, the results from this experiment are also used to validate a numerical impedance tube set-up, which is used to compute the properties of resonators with different dimensions, since the experimental set-up is constrained to a single duct diameter. The numerical set-up is shown in Fig. 8.7, with the duct, the resonator sample (shown in green) and probes to record the necessary data for impedance computation (red points). Aside from reduced costs, the advantage of a numerical set-up is that the diameter of the duct can be adapted for different face-sheet sizes, and a wider frequency range can be covered.

The length of the duct, as well as the physical simulation time are a function of the prescribed minimum frequency to be analyzed, defined as 50 Hz for all configurations. The maximum frequency of the analysis is a consequence of the duct diameter, and thus, of the face-sheet dimensions. However, for all tested cases, the threshold is significantly higher than the JIN frequency range of interest. The mesh resolution for this set-up is defined as the number of grid elements in the diameter or thickness of the orifices of the face-sheet or septum (for the DDOF case), whichever one is the smallest. The simulation time-step is defined as the minimum grid size divided by the speed of sound. For a medium grid resolution, with 15 elements in the face-sheet diameter, the obtained time-step is  $2.02 \times 10^{-7}$  s.

The input acoustic waves are generated with a broadband wave-packet model of constant amplitude in the frequency range of the analysis, simulating a white noise in-

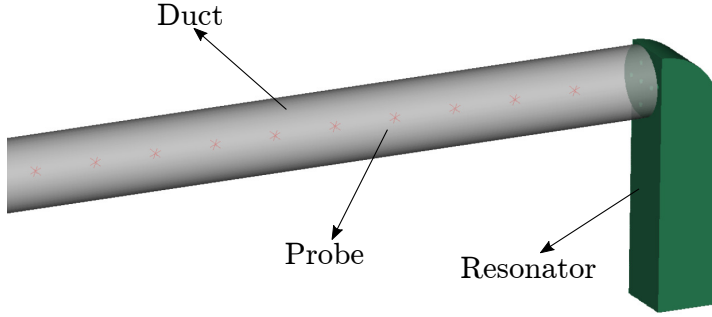


Figure 8.7: Numerical set-up of an impedance tube. The duct is shown in grey, the resonator in green and the red dots are the probes where data is sampled.

put. Ten probes are equidistantly placed inside the tube, upstream of the resonator, which record velocity and pressure signals used to compute the impedance. The simulations are carried out with LBM-VLES. The same solver is used for the simulations of the installed jet set-up with both solid and lined plates.

Despite the proposed concept having a square face-sheet and internal cross-section, geometries with circular face-sheets with equivalent area and a diameter  $D_{\text{face-sheet}}$  are used in order to have the sample properly connected to the impedance tube. With the same face-sheet area, the porosity does not change with respect to design conditions. Due to the dimensions of the tube for the experiment, a concept was especially designed for validation purposes. Moreover, the acoustic input parameters have been chosen in order to approximate those of the installed jet cases, but also following the limitations of the experimental set-up. For example, the maximum achievable OASPL for white noise input in the tube is 120 dB. The geometric parameters of the resonator used in the validation experiments are reported in Table 8.5. The resistance, reactance and absorption coefficient are compared to the results obtained from the design method, as well as the numerical simulations of the impedance tube, as shown in Fig. 8.8.

Table 8.5: Design parameters for the resonator used in the impedance tube experiment and validation.

Orifices	$d$ [mm]	$t$ [mm]	$D$ [mm]	$D_{\text{face-sheet}}$ [mm]	$L_c$ [mm]	$f_{\text{res}}$ [Hz]	$p_i$ [dB]
5	2	1	35	40	67	400	120

The graphs in Fig. 8.8 show a good agreement between the design methodology and both the experiment and numerical simulation of the impedance tube. The agreement is best near the point of maximum absorption and small deviations are seen at higher frequencies, mostly due to a mismatch in the resistance values. Therefore, it is concluded that the proposed concept has sound absorption characteristics proper of a standard Helmholtz resonator. Moreover, the Guess method is shown to provide a good estimation for the resonator dimensions at the required conditions.

Aside from experimental validation, it is necessary to assess the grid convergence of the impedance tube numerical results. The results plotted in Fig. 8.8 are obtained with

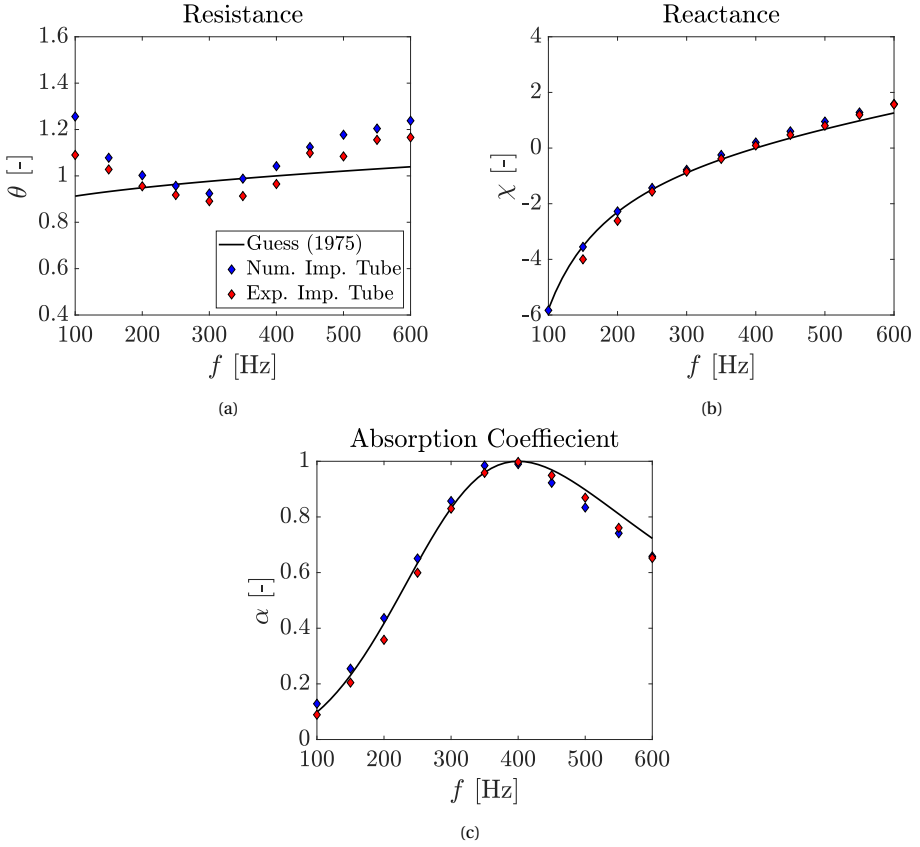


Figure 8.8: Comparison of resonator impedance characteristics and absorption coefficient, obtained from the Guess method [10], and the impedance tube experiment and numerical simulations.

20 grid elements (fine resolution) along the smallest dimension in the face-sheet channels, i.e. the thickness  $t$ , for this configuration. Therefore, to assess convergence, simulations have been carried out with 10 (coarse resolution) and 15 (medium resolution) grid elements in the channel thickness, and the impedance parameters are compared in Fig. 8.9. The resistance results for the coarse and medium resolutions show some oscillation at very low frequencies, although less noticeable for the latter. The reactance and absorption coefficient curves show small differences at very low frequencies as well. However, the results for the medium resolution agree well with those of the fine grid, particularly near the absorption peak, which is the region of highest interest. These results are also in qualitative agreement with an impedance characterization in a grazing flow tube, performed by Avallone et al. [11]. Therefore, to avoid high computational costs, further simulations shown in this work are performed with 15 elements in the orifice diameter.

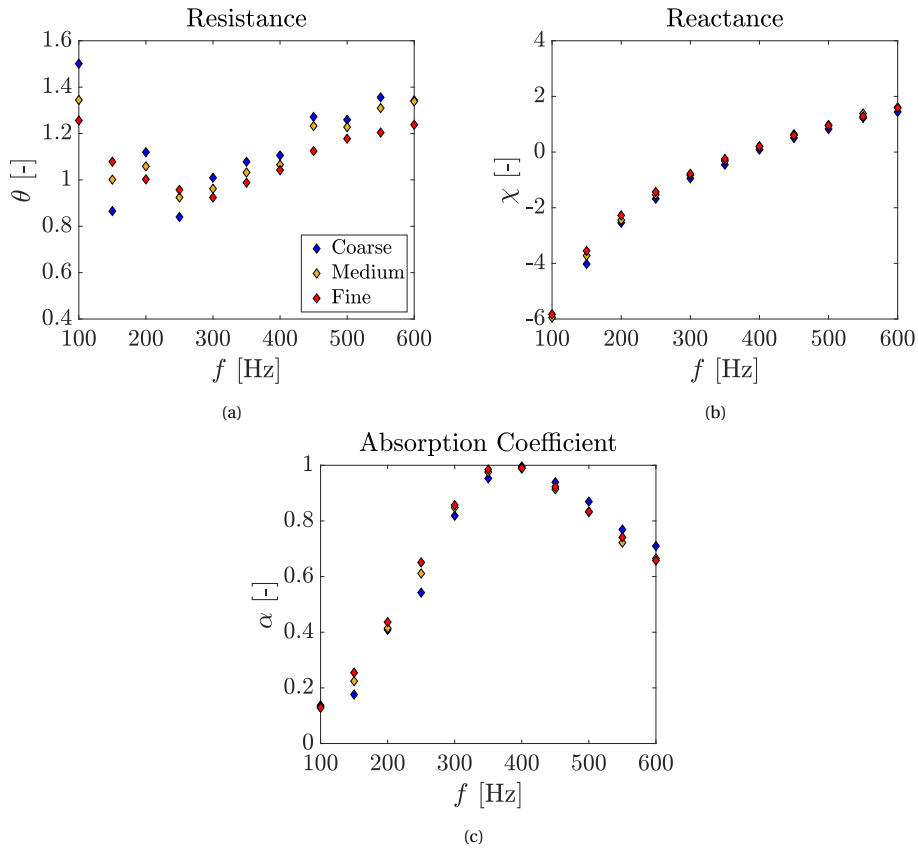


Figure 8.9: Comparison of resonator impedance characteristics and absorption coefficient, obtained from numerical impedance tube simulations, for different grid sizes.

## 8.4. RESONATOR IMPEDANCE CHARACTERISTICS

The SDOF resonators for the installed jet test cases are designed and the absorption curves are compared to results from the numerical impedance tube. The parameters are reported in Table 8.6 and the absorption coefficient curve is plotted for each case in Fig. 8.10. The orifice thickness has been increased with respect to the validation case in order to reduce the necessary cavity length, particularly for the resonator designed for the  $L = 6D_j$  configuration. This allows for more cavities to be placed inside the plate, thus potentially increasing the sound absorption. The absorption coefficient curves show a good agreement between the design methodology and the numerical impedance tube results. The peaks match the desired frequencies and only small deviations in amplitude are visible far from the peak, particularly at very high frequencies. Therefore, it is expected that the designed resonator geometries provide noise reduction when mounted in the flat plate in the vicinity of the jet.

These resonators are also used as a starting point for a DDOF design with the goal of

Table 8.6: Design parameters for the SDOF resonators applied in the JIN test cases.

Configuration	Orifices	$d$ [mm]	$t$ [mm]	$D$ [mm]	$L_c$ [mm]	$f_{\text{res}}$ [Hz]	$p_i$ [dB]
$L = 4D_j$	5	2	2	20	61	700	140
$L = 6D_j$	5	2	4	22	90	400	135

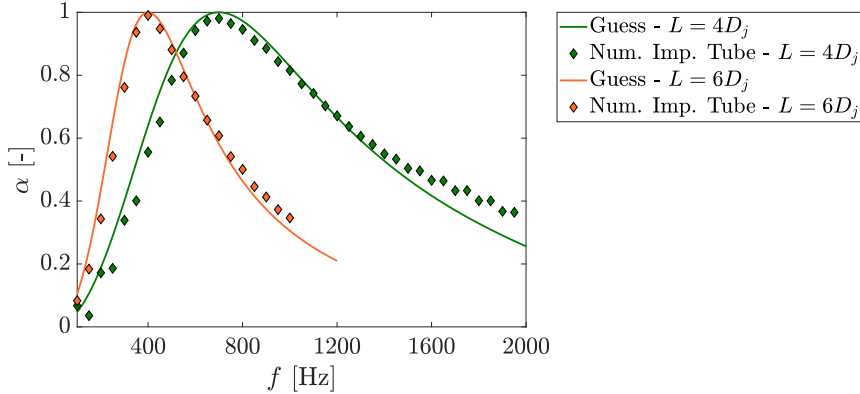


Figure 8.10: Absorption coefficient for the resonators designed for the two JIN test case geometries. The lines correspond to the results obtained from the Guess method [10] and symbols are the results from the numerical impedance tube simulation.

extending the frequency range of high absorption. Since the target is to reduce a broad-band region of the spectra in the installed jet configuration, the second absorption peak of the resonator needs to occur at a slightly higher frequency than the first one. This has been chosen since frequencies relatively lower to the JIN spectral peak may not be of significance in a full-scale application. Moreover, the DDOF geometrical parameters have been also constrained to provide similar absorption coefficient as the SDOF at low frequencies up to the peak. Due to the addition of the septum, and the consequent change in the overall impedance, the resonator geometry for each case has been adapted, as reported in Table 8.7.

The absorption coefficient curves for each case are shown in Fig. 8.11, and compared with the respective SDOF resonator. Results are obtained from both the analytical expressions and the numerical impedance tube. The results show a good agreement between the design method and the simulations up to the first peak in the absorption coefficient curve. There is a small amplitude mismatch at the valley between peaks and a deviation in the frequency of the second peak. The amplitude at the second peak, however, is reasonably predicted. More importantly, the results show that the DDOF concept increases the absorption characteristics of the liners at relatively higher frequencies, but still in the range of interest for the JIN test cases. Moreover, there is no significant reduction of the absorption coefficient near the first peak, with respect to the SDOF concept. There is a slight decrease in amplitude at very low frequencies, but those are not of significant interest, particularly when considering a full-scale application.

Table 8.7: Design parameters for the DDOF resonators to be applied in the JIN test cases.

	$L = 4D_j$	$L = 6D_j$
Face-Sheet Orifices	5	5
$d_{\text{face-sheet}}$ [mm]	2	2
$t_{\text{face-sheet}}$ [mm]	2	2
$D$ [mm]	17	20
$L_c$ [mm]	65	100
Septum Orifices	3	3
$d_{\text{septum}}$ [mm]	2	2
$t_{\text{septum}}$ [mm]	4	4
$h_c$ [-]	0.75	0.65
$p_{\text{face-sheet}}$ [dB]	140	135
$p_{\text{septum}}$ [dB]	136	135

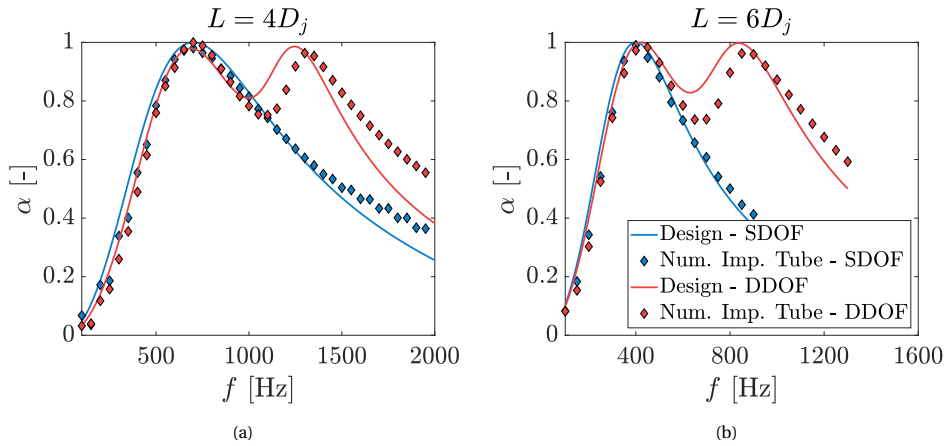


Figure 8.11: Absorption coefficient for the SDOF and DDOF resonators designed for the two JIN test case geometries. (a) Concept for the  $L = 4D_j$  case. (b) Concept for the  $L = 6D_j$  case. The lines correspond to the results obtained from the design equations and symbols are the results from the numerical impedance tube simulation.

Finally, the resonators for the  $L = 4D_j$  configuration are also assessed for a different jet velocity ( $M_a = 0.35$ ), and thus at off-design conditions. A similar analysis of the installed jet with a solid plate has provided a maximum OASPL of 135 dB on the lower side for this flow condition, thus lower than the design value. Using this as input, the resultant absorption coefficient has been computed for the SDOF and the DDOF concepts for the  $L = 4D_j$  test case, as shown in Fig. 8.12. For the SDOF concept, there is a reduction of the peak amplitude of approximately 6% with respect to design conditions, and thus it is expected that the liner will still perform efficiently at this condition. For the DDOF, there is a similar trend as for the previous cases regarding the agreement between the analytical expressions and the simulations. Nonetheless, similar absorption values to the SDOF

are obtained near the first peak, whereas the second peak has a even higher amplitude at this condition, which is predicted by both methodologies with only a mismatch in frequency. Therefore, this concept is also expected to provide noise reduction for the JIN test cases.

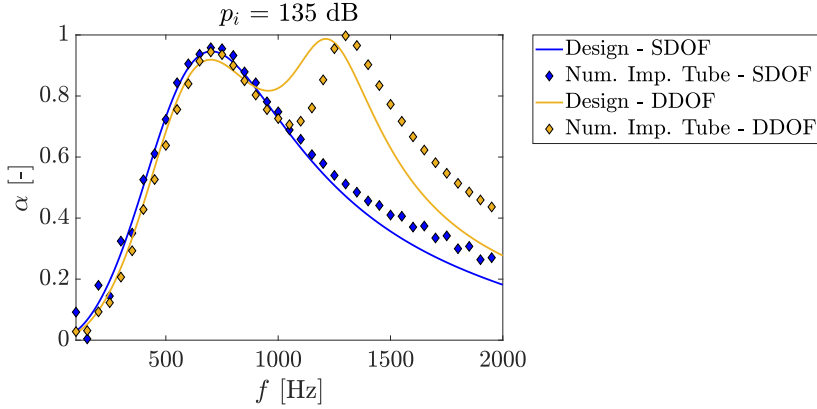


Figure 8.12: Absorption coefficient for the resonators designed for the  $L = 4D_j$  JIN test case with a  $M_a = 0.35$  jet. The input pressure amplitude for this case is 135 dB. The lines correspond to the results obtained from the design equations and symbols are the results from the numerical impedance tube simulation.

## 8.5. JET-INSTALLATION NOISE WITH LINED PLATE

Since the liners have been characterized for all cases and conditions, the next step is to locate the resonators in the plate. The arrangement consists of several rows of resonators throughout the plate length, as shown in Fig. 8.13. Since the test cases simulate a jet-flap interaction in an aircraft geometry, the goal is to reduce noise for an observer on the ground, i.e. at the reflected side of the plate. Therefore, the face-sheets of the resonators are located on the lower side of the surface, whereas on the upper side a solid surface is kept. The face-sheets are initially placed in the  $z = 0$  position, which also corresponds to the region of maximum noise production. Thereafter, the direction of the cavities alternate for each row in order to have a better distribution of the porous face-sheets throughout the surface. The number of rows is limited by the plate length of each case and the maximum span to place a face-sheet has been limited to  $10D_j$ , which also corresponds to the data sampling region on the plate.

### 8.5.1. FAR-FIELD SPECTRA

In this section, the results from the simulations of the installed jet with the lined plates are compared to the baseline solid case. SPL spectra are plotted in Fig. 8.14 for the two geometric cases. The spectra are obtained for a constant frequency band of 100 Hz, at polar angles  $\theta = \pm 90^\circ$  (reflected and shielded sides).

The lined plate provides significant noise reduction with respect to the baseline solid configuration, particularly for the observer at the reflected side ( $\theta = 90^\circ$ ). For the  $L = 4D_j$  -  $h = 1D_j$  case, shown in Fig. 8.14a, a reduction of 7.5 dB is obtained at 700 Hz, which

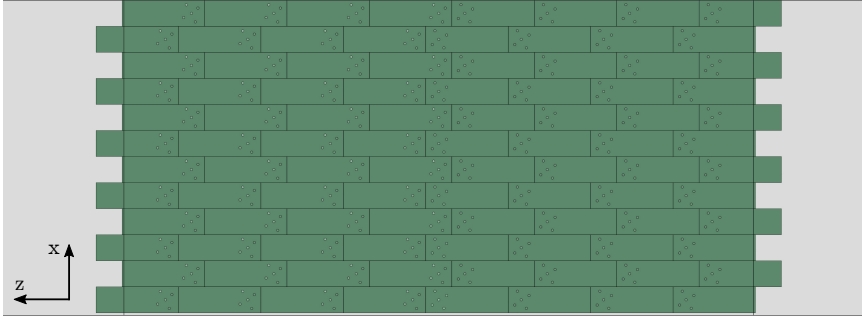


Figure 8.13: Bottom view of the flat plate with rows of resonators mounted inside. Porous face-sheets are distributed throughout the surface by alternating the cavity direction for each row.

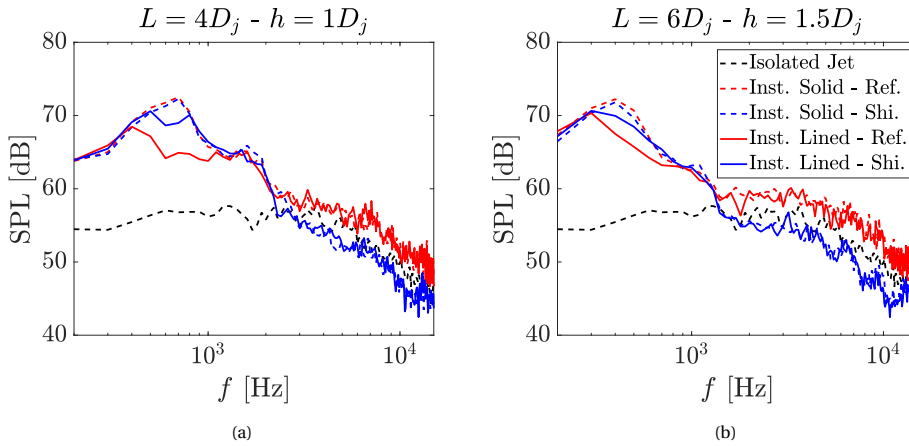


Figure 8.14: Far-field spectra of the installed jet configurations, comparing the lined and solid plate results. Isolated jet noise levels are included as reference. Spectra obtained for  $\theta = \pm 90^\circ$  (reflected and shielded sides) and  $M_a = 0.5$ . (a)  $L = 4D_j - h = 1D_j$ . (b)  $L = 6D_j - h = 1.5D_j$ .

is the design resonance frequency of the cavity. Moreover, the SPL is visibly lower in the range  $400 \text{ Hz} < f < 1100 \text{ Hz}$ , for which  $\alpha > 0.7$ , according to the plot in Fig. 8.10. No noise reduction is visible at higher frequencies, for which turbulence mixing noise reflected on the plate is the dominant mechanism. A similar behaviour occurs for the  $L = 6D_j - h = 1.5D_j$ , with a reduction of 5 dB at the resonance frequency ( $f_{\text{res}} = 400 \text{ Hz}$ ) for the reflected side observer. Noise abatement for this case occurs for  $300 \text{ Hz} < f < 700 \text{ Hz}$ , which shows that the liner performs better at frequencies higher than the absorption peak, in agreement with the absorption coefficient curve.

An interesting result is obtained for the observer at the shielded side ( $\theta = -90^\circ$ ). Although the face-sheets are present only on the lower side of the plate, a small noise reduction occurs near the resonance frequency of the resonator, in the order of 3 dB and 1.8 dB for the  $L = 4D_j$  and  $L = 6D_j$  configurations, respectively. Since there can be no acoustic absorption on the upper side of the plate, as there are no perforations there, it

is concluded that the presence of the resonators also changes the source characteristics, prior to the scattering phenomenon. However, given the differences in SPL for observers at different sides of the lined plate, the noise reduction obtained at the reflected side is still predominantly due to the acoustic absorption by the resonators. This is also visible in the directivity curves in Fig. 8.15, for the  $L = 4D_j$  case.

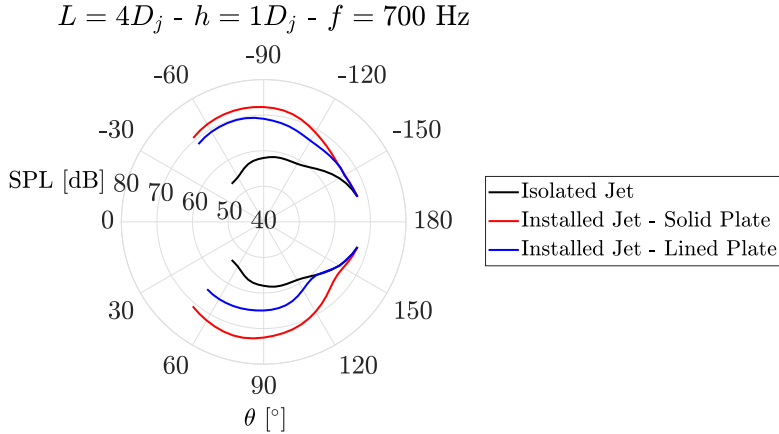


Figure 8.15: SPL directivity curves of the isolated and installed jets with solid and lined plates, for a frequency  $f = 700 \text{ Hz}$ . The installed configuration corresponds to the  $L = 4D_j - h = 1D_j$  case, at  $M_a = 0.5$ .

The results show that the lined plate provides significant noise reduction (around 7 dB) for polar angles at the reflected side up to  $\theta = 150^\circ$ . At shallow downstream angles, where turbulence-mixing noise becomes dominant, the curve collapses with that of the isolated jet at  $\theta \geq 130^\circ$  for the lined case, whereas for the solid one this happens only at  $\theta \geq 160^\circ$ . At the shielded side, the lined plate generates noise approximately 2-3 dB lower than the baseline solid case, up to  $\theta = -140^\circ$ . Therefore, it is shown that the liner provides noise reduction at all angles where the plate is the main noise source. Moreover, the noise reduction for most angles on the shielded side indeed points to a change in the source properties, whose underlying mechanisms are addressed in Section 8.5.2.

Having obtained successful results with the SDOF liner, the next step is to assess the noise reduction capabilities of the DDOF concept. The spectra of the installed jet with a DDOF lined plate are also computed and compared with the SDOF configuration, as shown in Fig. 8.16 for the two installed jet geometries. The results are plotted only for the reflected side since no visible differences between the SDOF and DDOF configurations have been found for the shielded one.

The spectra for both installed jet geometries display the same trend: at low frequencies the SDOF and DDOF lined plate cases provide the same noise levels, but at mid frequencies the latter outperforms the former. For the  $L = 4D_j$  case, for example, the DDOF provides an additional noise reduction of 3 dB at  $f = 1400 \text{ Hz}$ . The frequency range where the DDOF liner provides additional noise reduction with respect to the SDOF one has been marked with dotted lines. For both cases, this region is approximately centered around the second peak in the resonator absorption curve, as shown in Fig. 8.11. For  $L = 4D_j$ , this corresponds to  $1000 \text{ Hz} < f < 2000 \text{ Hz}$ , whereas for  $L = 6D_j$ , it is  $700 \text{ Hz}$

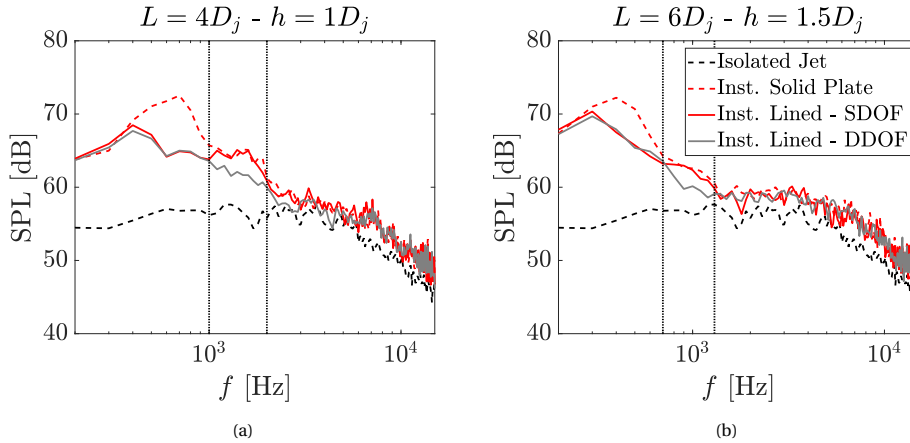


Figure 8.16: Far-field spectra of the installed jet configurations, comparing the SDOF and DDOF lined configurations. Noise levels of the isolated and installed jets with solid plate are included as reference. Spectra obtained for  $\theta = 90^\circ$  (reflected side) and  $M_a = 0.5$ . (a)  $L = 4D_j - h = 1D_j$ . (b)  $L = 6D_j - h = 1.5D_j$ .

$< f < 1300$  Hz. Therefore, the DDOF resonator concept is capable of even further JIN reduction.

Finally, the noise levels of the lined plate configuration are assessed for the  $M_a = 0.35$  jet condition. The SPL spectra for both SDOF and DDOF cases are plotted and compared to the reference solid case, as shown in Fig. 8.17, for  $\theta = 90^\circ$  (reflected side). The results show that the liners still provide significant noise abatement at this condition, with a 6 dB reduction at  $f = 700$  Hz with the SDOF concept relative to the solid case, and visible difference up to  $f = 1000$  Hz. Moreover, the DDOF concept shows the same trend as for  $M_a = 0.5$  with an additional 3 dB reduction for  $1000 \text{ Hz} < f < 2000$  Hz with respect to the SDOF. This shows that the lined plate can still provide significant JIN reduction even at an off-design condition.

The dependence of the OASPL with the jet velocity is plotted in Fig. 8.18 for the solid and lined (SDOF) installed jet cases, as well as the isolated jet, considering an observer at  $\theta = 90^\circ$ . The results for the DDOF case are similar to the SDOF one and thus have been omitted. The exponent  $n$  for the jet velocity is retrieved for each case and also shown in the figure. The isolated jet noise is shown to vary with  $U_j^{7.76}$ , which characterizes turbulence-mixing noise [12]. The installed jet with the solid plate has a dependence of  $U_j^{5.66}$ , which is characteristic of edge scattering [13]. Finally, with the lined plate, the noise is proportional to  $U_j^{6.11}$ , thus showing a decrease in the dominance of the scattering mechanism in the overall noise production.

### 8.5.2. SURFACE PRESSURE FLUCTUATIONS

The far-field spectra have shown that the designed liner concepts in this work are effective in reducing JIN. However, results for an observer at the shielded side of the plate indicate that the resonators are not only dampening the acoustic waves scattered at the trailing edge, which is their expected working mechanism, but also effectively changing

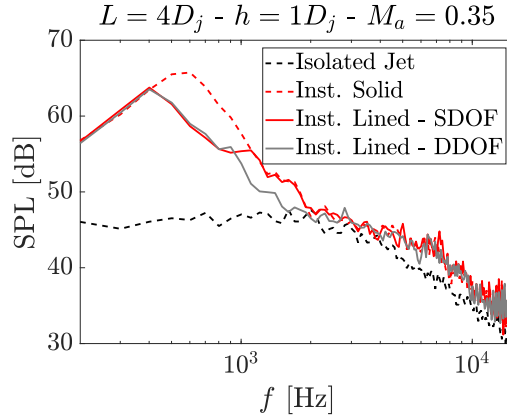


Figure 8.17: Spectra of the installed jet configuration for lined (SDOF and DDOF) and solid plates at  $M_a = 0.35$ , obtained for a configuration  $L = 4D_j - h = 1D_j$ . Noise levels of the respective isolated jet are plotted as reference. Spectra obtained for  $\theta = 90^\circ$  (reflected side).

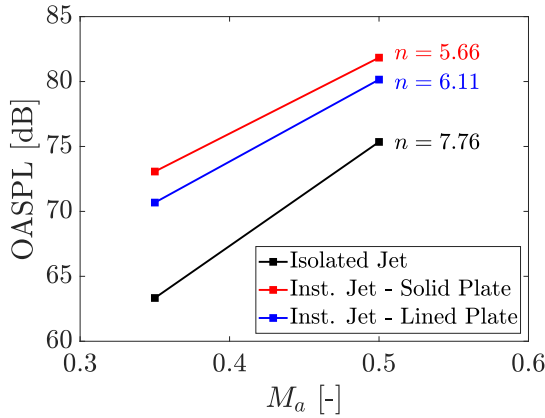


Figure 8.18: Overall Sound Pressure Level (OASPL) dependence on the jet acoustic Mach number for isolated and installed cases with solid and lined plates.

the source properties. In order to verify this, the near-field pressure fluctuations on the upper and lower sides of the plate are analysed. The pressure autospectrum ( $\hat{P}(f)$ ) on both sides of the plate is plotted in logarithmic scale for different streamwise positions at the  $z = 0$  plane, for the  $L = 4D_j - h = 1D_j$  configuration, and for two different frequencies ( $f = 700$  Hz and  $f = 800$  Hz), as shown in Fig. 8.19. These frequencies have been chosen since, for the former, the liners provide noise reduction on both sides of the plate according to the far-field spectra, whereas for the latter, this occurs only on the reflected side.

On the lower side of the plate, for  $f = 700$  Hz, three streamwise regions on the plate can be distinguished based on the trend between the lined and solid plates. In the up-

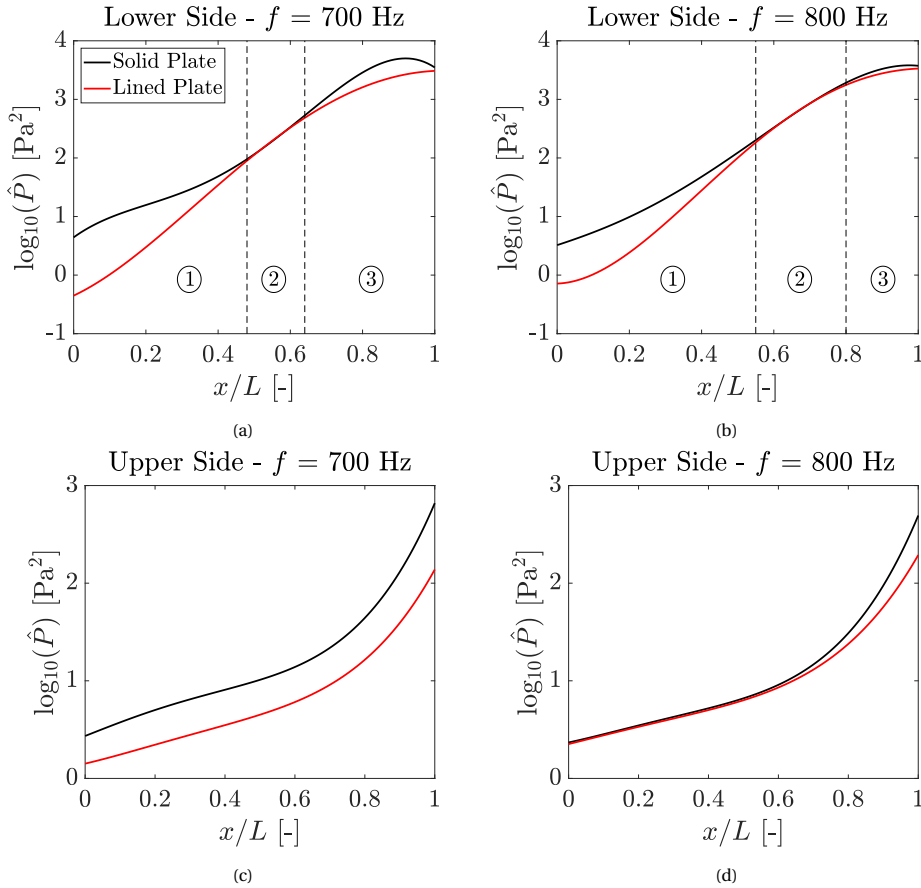


Figure 8.19: Amplitude of pressure fluctuations ( $\hat{P}$ ) in the streamwise direction on the lower and upper sides of the plate, at the  $z = 0$  plane, at frequencies  $f = 700$  Hz and  $f = 800$  Hz. Results obtained for the installed jet with solid and SDOF lined plates and configuration  $L = 4D_j - h = 1D_j$ .

stream part of the plate (region 1), there is a significant difference between the pressure amplitudes of the lined and solid plates. This is attributed to the dampening of scattered acoustic waves, traveling upstream from the plate trailing edge, by the resonators throughout the surface. Thereafter, the curves collapse in what is defined as region 2, where it is believed that pressure waves from the jet impinging on the plate are stronger and thus mask the acoustic waves scattered at the trailing edge. Finally at region 3, near the trailing edge, the lined plate has a smaller amplitude of fluctuations with respect to the solid one, indicating that part of the impinging waves from the jet are being dampened prior to scattering. For  $f = 800$  Hz, regions 1 and 2 can be clearly distinguished, but there is no significant difference between the amplitude of curves near the trailing edge. Although the curve of the lined plate is slightly lower, this difference is possibly not significant in order to affect the far-field noise.

Therefore, it is believed that near the plate trailing edge, the resonators are dampening the acoustic waves generated by the jet itself, before they are scattered, thus reducing the overall source intensity. Moreover, the liners act to reduce the surface impedance, particularly at the resonance frequency, which in turn leads to a less abrupt discontinuity at the trailing edge. As a result, the scattering mechanism also becomes weaker. The pressure fluctuations on the upper side of the plate also contribute to this conclusion since for  $f = 700$  Hz there is a constant offset between the curves, likely due to a weakening of the acoustic source, whereas for  $f = 800$  Hz, only small differences occur locally near the trailing edge, which do not seem to affect the remainder of the upper surface, thus also not affecting the far-field noise. It is also believed that this effect on the lower side is more pronounced near the trailing edge because the amplitude of pressure fluctuations at that region match more closely the design conditions of the resonator, in this case the  $p_i$  parameter. It is not yet clear, however, why this effect is restricted to such a narrow frequency range around the absorption peak. It is believed that this is due to the characteristics of the incident waves from the jet, which only closely match the design conditions of the resonators at this frequency range. Further research into this hypothesis is necessary.

### 8.6. LINED PLATE WITH PERFORATED TRAILING EDGE

In this section, the flat plate configuration with a perforated trailing edge and, ultimately, the hybrid one with perforations and resonators are assessed. Results for the former are initially plotted, which are also used for the design of the resonators. The spectra shown in Fig. 8.20 are obtained for a constant frequency band of 100 Hz, at polar angles  $\theta = 90^\circ$  (reflected side).

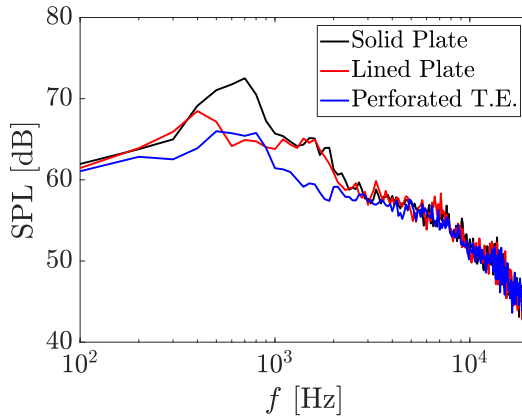


Figure 8.20: Far-field spectrum of the installed jet with a perforated trailing edge. Noise levels for the solid and lined plate configurations are included as reference. Spectra obtained for  $\theta = 90^\circ$  and  $M_a = 0.5$ .

The spectrum of the perforated trailing-edge case (blue curve) shows that noise is reduced in the range  $200 \text{ Hz} < f < 2000 \text{ Hz}$ , with a 7 dB decrease at the spectral peak of the solid configuration ( $f = 700$  Hz). Therefore, the perforations and the resonators

provide similar noise reduction at the spectral peak; the advantage of the former is the wider frequency range of mitigation. It is also visible that there is still a peak around 700 Hz, which is kept as desired resonance frequency for the resonators applied in the hybrid configuration. However, for this case, instead of mitigating the noise generated by the trailing edge, the target is to reduce noise produced by the solid-permeable junction, which is the dominant source for the perforated case, as shown by the beamforming map in Fig. 8.21.

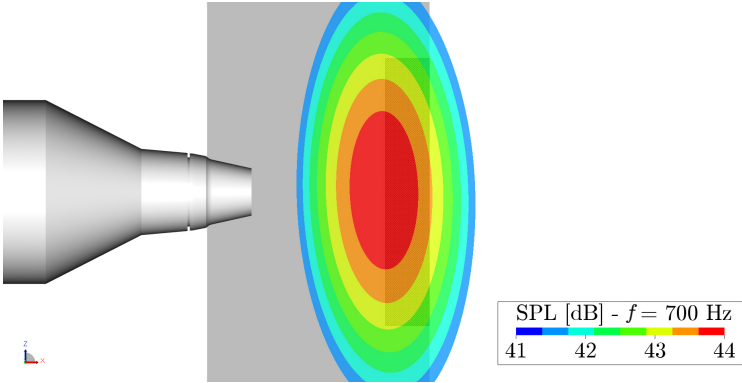


Figure 8.21: Acoustic source location from beamforming applied to the installed jet with the perforated trailing edge, for a frequency  $f = 700$  Hz.

The resonator design follows the procedure reported in Section 1.3, adapted to the properties of the perforated case. The configuration of the lined flat plate with a perforated trailing edge is shown in Fig. 8.22. The spectrum for the hybrid lined-perforated trailing-edge configuration is then plotted in Fig. 8.23, with the simple perforated and fully solid plate results as reference.

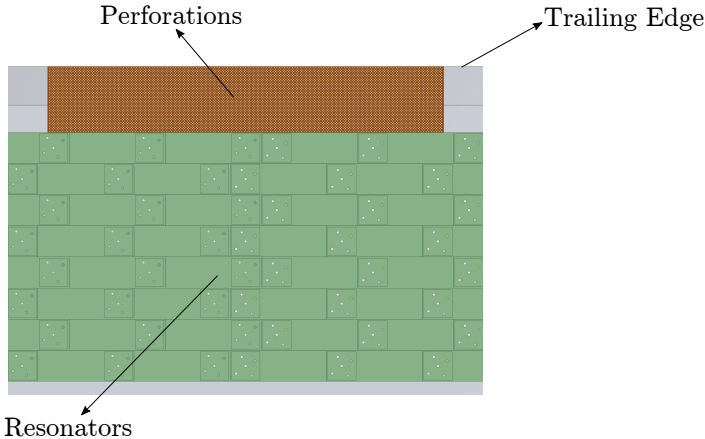


Figure 8.22: Bottom view of the flat plate with a perforated trailing edge and resonators mounted inside.

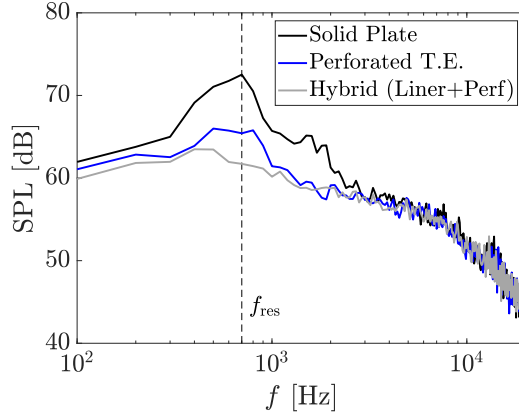


Figure 8.23: Far-field spectrum of the installed jet with a hybrid flat plate configuration (perforated trailing edge and resonators). Noise levels for the solid and perforated trailing edge configurations are included as reference. Spectra obtained for  $\theta = 90^\circ$  and  $M_a = 0.5$ .

For the hybrid configuration, the resonators provide additional noise reduction of 3.5 dB at resonance, with respect to the simple perforated case. Moreover, noise mitigation occurs in the range of  $400 \text{ Hz} < f < 1000 \text{ Hz}$ . Therefore, the broadband hump for the perforated case, visible in the blue curve, vanishes and minimum noise levels are achieved for all the studied configurations in this chapter. Therefore, it is shown that the noise scattered at the solid-permeable junction can be mitigated by the resonators. With respect to the baseline solid case, a reduction of 11 dB is obtained at the spectral peak.

## 8.7. CONCLUDING REMARKS

A curved Helmholtz resonator concept is studied for reducing jet-installation noise in a configuration comprised by a single-stream subsonic jet and a nearby flat plate. The main goal of this work is to assess the noise reduction provided by the resonators, targeting the acoustic waves produced by scattering at the plate trailing edge.

The Guess method [10] is applied to obtain the dimensions of the face-sheet and the cavity length, whereas the orifice parameters are defined as input. The amplitude of the incident pressure wave and the desired resonance frequency, which are part of the impedance formulation, are obtained from simulations of the installed jet with a fully solid plate (baseline case). The former is taken from the surface pressure fluctuations on the lower side, whereas the latter corresponds to the peak frequency in the spectrum of the installed jet configuration. Both single and double degree-of-freedom liners are studied, for which the latter contains a porous septum inside the cavity in order to expand the frequency range of high sound attenuation.

The cavity curvature is necessary in order to keep the plate thickness small. Therefore, in order to validate the design and verify that the curvature does not affect the properties of the resonator, an experiment with an impedance tube has been performed to measure the liner impedance. A good agreement has been obtained, particularly at fre-

quencies close to the absorption peak. Numerical simulations of an impedance tube have been also performed in order to characterize resonators with different dimensions, particularly for the application in the different JIN test cases and flow conditions. The simulation results are also validated against the experiment. For the DDOF resonators, the first peak in the absorption coefficient curve is well predicted by the design methodology, but the small differences occur near the second peak. This is not a significant issue, however, since the desired trends are still visible in the impedance tube simulation results.

In the installed jet set-up, an array of resonators is placed inside the plate with the face-sheet on the lower side (reflected side). Far-field spectra show that noise reduction in the order of 7 dB is obtained at the resonance frequency for the SDOF lined plate configuration with respect to the solid plate configuration. Moreover, the lined plate has lower sound pressure levels in a broad frequency range around the resonance, thus significantly reducing the installation noise. Directivity plots show that this noise mitigation occurs for all polar angles where the flat plate is the dominant noise source. For the configuration with the DDOF resonator, further noise reduction (approximately 3 dB) is obtained at mid frequencies, which correspond to the second peak in the absorption coefficient curve. Therefore, the DDOF liner outperforms the SDOF one by expanding the frequency range of noise reduction. Simulations at an off-design condition (lower jet Mach number and consequently, lower amplitude of incident wave) show that the liners are still effective in reducing noise. By computing the dependence of the overall sound pressure level with the jet velocity, it is shown that the trailing-edge source becomes less dominant with respect to turbulence-mixing noise for the liner plate.

Finally, the results also show that a slight noise reduction also occurs on the shielded side of the plate, but at a significantly narrower band around the resonance frequency. The SPL amplitude is also higher than that on the reflected side. Computations of the surface pressure fluctuations show three distinct regions by comparing the solid and lined plates. At the resonance frequency, near the leading edge the amplitude of fluctuations on the lined plate is significantly lower than the baseline, which is due to the attenuation of the scattered waves traveling upstream from the trailing edge. A second region is visible where the curves collapse, where fluctuations of hydrodynamic characteristic are likely dominant. Finally, near the trailing edge, again the lined plate has a lower amplitude of fluctuations than the baseline. This is believed to be the result of the absorption of acoustic waves from the jet itself prior to their scattering at the trailing edge, and a less abrupt impedance discontinuity at the trailing edge. Consequently, this reduces the overall trailing-edge source strength, which also affects the noise propagated at the reflected side. This effect is, however, not visible outside of the resonance frequency, which explains the reason for the narrow frequency range where noise reduction is obtained at the shielded side.

A hybrid configuration comprised of open-cell permeable materials and Helmholtz resonators is also effective in mitigating jet-installation noise, for which the former provides noise reduction due to flow communication between the two sides of the surface and the resonators are used to reduce the sound produced at the solid-permeable junction.

Therefore, it is concluded that acoustic liners with curved cavities are suitable noise

reduction solutions for jet-installation noise, which is an inherently broadband and high amplitude source. Further research on this topic includes an analysis with the resonators mounted in an actual flap geometry, where its effects on the lift and drag forces can be estimated.

## REFERENCES

- [1] L. Rego, F. Avallone, D. Ragni, D. Casalino, and H. Denayer, *Acoustic liners for jet-installation noise reduction*, Submitted to the Journal of Sound and Vibration (2022).
- [2] D. T. Sawdy and R. J. Beckemeyer, *Bandwidth attenuation with a folded cavity liner in a circular flow duct*, *AIAA Journal* **18**, 766 (1980).
- [3] J. Yu and E. Chien, *Folding Cavity Acoustic Liner for Combustion Noise Reduction*, in *12th AIAA/CEAS Aeroacoustics Conference* (Cambridge, MA, USA, 2006).
- [4] R. Sugimoto, P. Murray, and R. J. Astley, *Folded cavity liners for turbofan engine intakes*, in *18th AIAA/CEAS Aeroacoustics Conference (33rd AIAA Aeroacoustics Conference)* (American Institute of Aeronautics and Astronautics Inc., 2012).
- [5] L. Rego, F. Avallone, D. Ragni, and D. Casalino, *Jet-installation noise and near-field characteristics of jet-surface interaction*, *Journal of Fluid Mechanics* **895** (2020), 10.1017/jfm.2020.294.
- [6] T. J. Mueller, *Aeroacoustic Measurements*, 1st ed. (Springer-Verlag, Berlin, Germany, 2002).
- [7] J. R. Underbrink, *Circularly symmetric, zero redundancy, planar array having broad frequency range applications*, (2001).
- [8] R. Boonen, P. Sas, W. Desmet, W. Lauriks, and G. Vermeir, *Calibration of the two microphone transfer function method with hard wall impedance measurements at different reference sections*, *Mechanical Systems and Signal Processing* **23**, 1662 (2009).
- [9] ISO-10534-2, *Determination of sound absorption coefficient and impedance in impedance tubes*, Tech. Rep. (International Organisation for Standardization, Genève, Switzerland, 1998).
- [10] A. W. Guess, *Calculation of perforated plate liner parameters from specified acoustic resistance and reactance*, *Journal of Sound and Vibration* **40**, 119 (1975).
- [11] F. Avallone, P. Manjunath, D. Ragni, and D. Casalino, *Lattice-Boltzmann Very Large Eddy Simulation of a Multi-Orifice Acoustic Liner with Turbulent Grazing Flow*, in *25th AIAA/CEAS Aeroacoustics Conference* (American Institute of Aeronautics and Astronautics, Reston, Virginia, 2019).
- [12] M. J. Lighthill, *On Sound Generated Aerodynamically I. General Theory*, *Proceedings of the Royal Society of London. Series A. Mathematical and Physical Sciences* **211**, 564 (1952).

## REFERENCES

---

- [13] J. E. Ffowcs-Williams and L. H. Hall, *Aerodynamic sound generation by turbulent flow in the vicinity of a scattering half plane*, [Journal of Fluid Mechanics](#) **40**, 657 (1970).



# 9

## PERMEABLE FLAPS FOR JET-INSTALLATION NOISE REDUCTION AT IN-FLIGHT CONDITIONS

*Scientists study the world as it is, engineers create the world that never has been.*

Theodore von Kármán

*An experimental investigation on jet-installation noise reduction with permeable flaps on an aircraft half-model is performed, focusing on the effects of those structures on the noise levels as well as on the aerodynamic properties of the model (lift and drag forces). Two perforated flaps with different hole patterns are investigated: the first one has a uniform distribution with equal spacing in both streamwise and spanwise directions, whereas the second one has a permeability increase towards the trailing edge. Aerodynamic force measurements carried out with a balance show that the permeable flaps are responsible for a lift reduction in the order of 7%, and a slight drag increase, in the order of 0.5%, with the gradient permeability flap providing better results. Acoustic results, obtained from phased array measurements at in-flight conditions, show jet-installation noise reduction of approximately 3 dB with both permeable flaps.*

## 9.1. OBJECTIVES

**I**N the previous chapters, the studies on jet-installation noise and the proposed mitigation solutions have been performed for a simplified configuration comprised by a flat plate located next to a jet flow. For that reason, only the acoustic effect of permeable materials has been verified as their impact on aerodynamic performance could not be assessed due to the absence of a free stream. Therefore, it is necessary to investigate if permeable materials are still a feasible solution in a realistic aircraft configuration and that they are not responsible for significant aerodynamic performance degradation, i.e. lift decrease and/or drag increase. Moreover, obtaining IJN reduction with a realistic geometry and at in-flight conditions is a challenging task, as reported by Mengle *et al.* [1]. The presence of the external flow is likely to reduce the acoustic benefits provided by the permeable materials, with respect to a static measurement condition.

To address this knowledge gap, wind tunnel measurements are performed with a half-model representative of a commercial aircraft, equipped with permeable deployed flaps, and the results reported in this chapter. Permeability is achieved through perforations on the flap surface connecting the lower and upper sides in a direction normal to the chord line. In order to minimize potential effects on performance, the perforations are restricted to a spanwise section in the vicinity of the jet flow. Acoustic measurements with a microphone phased array are performed in order to verify the achieved noise reduction. Moreover, aerodynamic measurements with a force balance and a multi-hole pressure probe are carried out to study the effect of the permeable materials on the model lift and drag forces as well as the flow downstream of the flaps.

## 9.2. EXPERIMENTAL SET-UP

### 9.2.1. WIND TUNNEL FACILITY AND MODELS

The experiments are performed in the Low-Speed Wind Tunnel (LST) at the German-Dutch Wind Tunnels (DNW) facility in Marknesse, The Netherlands. The LST is an atmospheric, closed-circuit wind tunnel with a working section of 5.75 m x 3.0 m x 2.25 m in length, width and height, respectively. It has a contraction ratio of 9, a maximum operating speed of 80 m/s and maximum non-uniformity of 0.2% of the flow speed.

A half model representative of a commercial aircraft is used for the measurements [2]. It comprises a half-fuselage and a wing with deployed flaps, as shown in Fig. 9.1a. A peniche of 30 mm thickness is also included below the half fuselage. No tail planes or slats have been considered in the study since they are not relevant for jet-installation noise and would add complexity to the study. The model dimensions are shown in Fig. 9.1b. The flaps are deflected of 35°, which is representative of a landing condition, wherein the trailing edge is positioned the closest to the jet flow and the IJN source is the strongest. A zig-zag trip is applied on the wing at a position of 3% of the local chord, whereas on the fuselage the trip was applied near the nose [2].

A separate nacelle piece is used to generate a single-stream jet flow from compressed air continuously supplied (maximum mass flow rate of 5 kg/s at 80 bar). The nacelle has a length of 1.1 m and an exit diameter  $D_j = 113$  mm. The centerline is approximately aligned with the junction between inboard and outboard flaps at a height of 0.73 m from the tunnel floor. Moreover, the flap trailing edge at the nacelle centerline is positioned

## 9.2. EXPERIMENTAL SET-UP

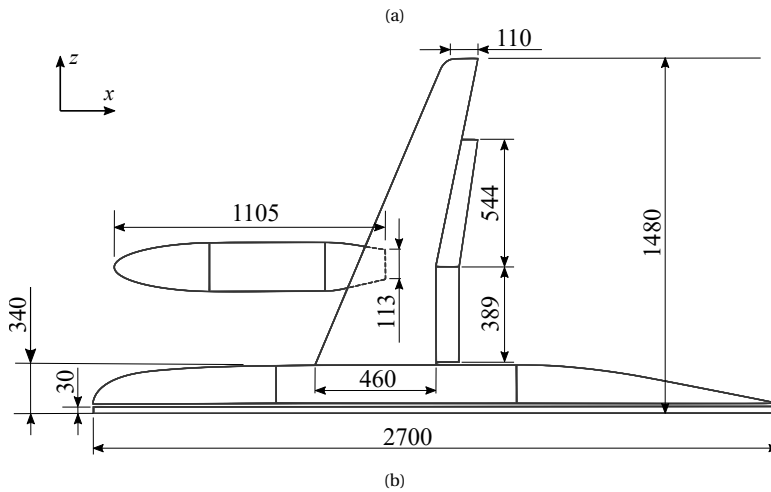


Figure 9.1: (a) Model set-up in the wind tunnel, comprised by the fuselage, wing, deployed flaps and the nacelle. On the side wall, microphones are placed for acoustic measurements, whereas a wake rake is used for flow field mapping. (b) Main dimensions of the model.

at an axial distance of  $3.4D_j$  ( $x$ -axis) with respect to the nozzle exit plane, and a radial distance of  $0.72D_j$  ( $y$ -axis) with respect to the nozzle centerline. The nacelle is mounted on an angled strut, attached to the tunnel floor, and there is no pylon connecting it to the airframe.

### 9.2.2. PERMEABLE FLAPS

The IJN reduction solutions studied in this work are partially permeable flaps, comprised by a perforated structure with straight channels normal to the flap chord line. In the chordwise direction, the perforations start at 25% of the flap chord in order to avoid flow communication between the upper and lower sides near the suction peak. In the spanwise direction, the perforations are placed near the junction between the inboard and outboard flaps, which approximately coincides with the jet centerline, and with a span of  $1.5D_j$  (167 mm) at each flap. Near the flap tip (both inboard and outboard), there is a small region without perforations due to a manufacturing requirement. The perforations also avoid the bracket areas. The channels have a diameter of 0.8 mm and two different configurations in terms of hole spacing are investigated. The first one has a uniform spacing of 4 mm between channels at the same chordwise and spanwise rows, as shown in Fig. 9.2, and it is referred in this manuscript as UPF (uniform permeability flap).

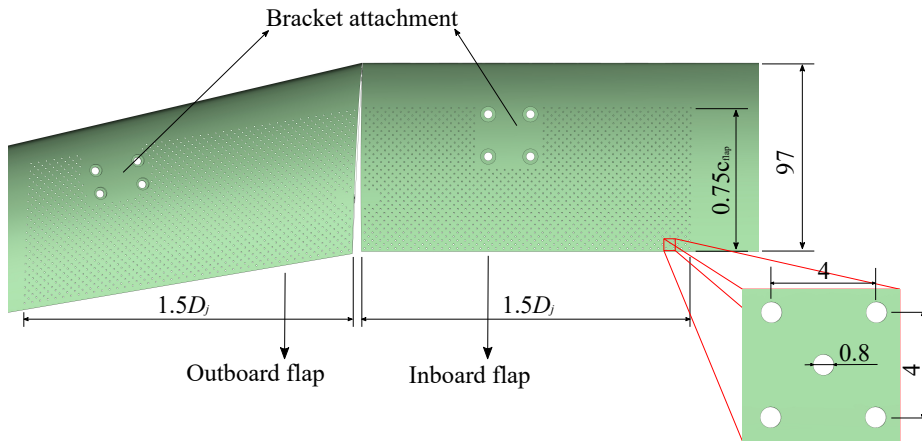


Figure 9.2: Perforated flap with uniform permeability. The perforated region is restricted to the inboard-outboard flap junction, which is approximately coincident to the jet centerline. Dimensions in mm.

A second configuration comprises a gradient permeability increase towards the flap trailing edge, obtained by progressively reducing the hole spacing (GPF - gradient permeability flap). This concept is investigated since it is hypothesized that it can provide additional aerodynamic and aeroacoustic benefits [3]. By increasing the hole spacing near the leading edge, it is likely that the effect of the permeable flap on lift and drag will be lower with respect to the uniform pattern. Moreover, a higher permeability at the trailing edge can lead to lower noise emission since this is the region where the source is strongest. Finally, with a smooth change in surface impedance from the solid to the permeable regions, it is believed that junction scattering effects can be mitigated [4].

In order for the two cases to be comparable, the integral permeability of the structure must be the same for both. Therefore, the hole spacing of the GPF has been designed to match the integral permeability of the UPF, as described next.

Instead of having alternating rows with the channels in an X-pattern, the GPF has a logarithmic increase in hole spacing in the streamwise direction, from 1.6 mm at the

trailing edge to 3.2 mm at the leading edge. In the spanwise direction, the spacing is constant within each row; for the first one, near the leading edge, the hole spacing is 6.4 mm, whereas for the last one (at the trailing edge) it is 3.2 mm. This increase in spacing also follows a logarithmic pattern. The higher hole spacing in the spanwise direction with respect to the streamwise one has been chosen since pressure fluctuations caused by the jet on the flap surface are the strongest near the centerline (inboard-outboard flap junction). Thus, it is not necessary to have a high permeability away from this region. The GPF concept is shown in Fig. 9.3.

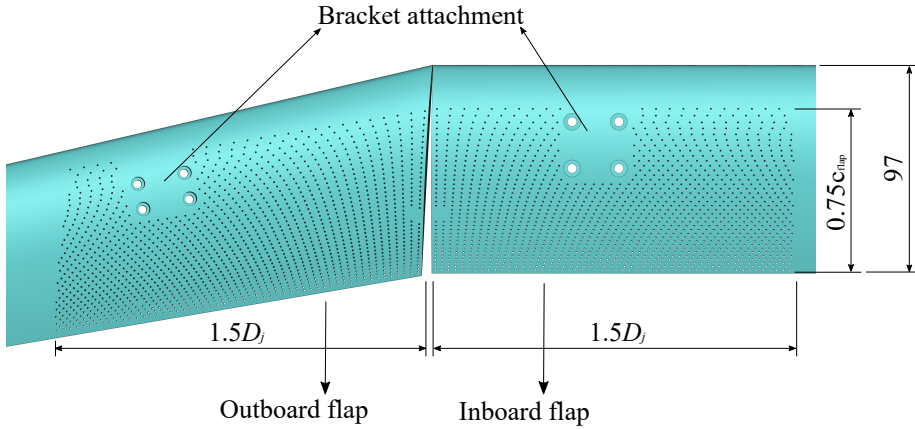


Figure 9.3: Perforated flap with gradient permeability. Dimensions in mm.

The porosity ( $\sigma$ ) of each configuration, defined as the ratio between the volume of the permeable flaps ( $V_p$ ) with respect to the baseline solid one ( $V_s$ ), as shown in Eq. (9.1), is reported in Table 9.1. It is shown that the porosity values between the UPF and GPF configurations are similar, which is a necessary condition to obtain the same permeability.

$$\sigma = 1 - \frac{V_p}{V_s}. \quad (9.1)$$

Table 9.1: Porosity values for each permeable flap configuration.

	$\sigma$ [%]
UPF - Inboard	1.89
UPF - Outboard	2.00
GPF - Inboard	1.73
GPF - Outboard	1.87

In order to verify that both concepts have similar integral permeability, the approach proposed by Rubio Carpio *et al.* [5] is applied. The local permeability of the GPF in the streamwise direction is computed based on the hole spacing at each row and plotted in

Fig. 9.4. The integral of the curves yields an overall permeability  $K_{UPF} = 6.82 \times 10^{-10}$  and  $K_{GPF} = 7.23 \times 10^{-10}$ . A similar trend is obtained by computing the spanwise permeability for each row. Therefore, it is verified that the two permeable flap concepts have similar overall properties and the main difference between them is the hole pattern.

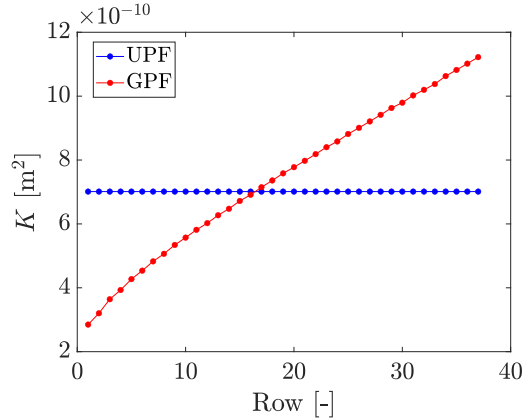


Figure 9.4: Local permeability of the uniform and gradient flap concepts.

### 9.2.3. INSTRUMENTATION AND MEASUREMENT TECHNIQUES

#### AERODYNAMIC MEASUREMENTS

The model is mounted on a turntable on the floor and attached to a balance for aerodynamic force measurements. The three force components and moments are measured, although only the lift and drag are considered for the comparison between solid and permeable flaps. The maximum loads that can be withstood by the balance are 20 kN in the normal direction, 2 kN in the axial direction and 1.5 kNm of pitching moment, with uncertainties of 4 N, 2.5 N and 2 Nm, respectively. Since the nacelle is not attached to the model, it has been removed during the force balance measurements, which are carried out for a jet-off condition.

Flow-field measurements are also carried out in order to investigate the effect of the permeable flaps on the wake of the model and possibly even on the jet flow itself. Therefore, the measurements are performed downstream of the model with a rake of 18 5-hole pressure probes (see Fig. 9.1a) in order to obtain the 3 flow velocity components. The probes are spaced of 15 mm and thus the total length of the rake is 255 mm. They are connected to a 64-port ESP ZOC Scanivalve module with a differential pressure range of 5 psi and an uncertainty of 0.1% of this range. Regarding the measured quantities, the following uncertainty values are obtained: local incidence angle  $\leq 0.2^\circ$ , sideslip angle  $\leq 0.2^\circ$ , Mach number  $\leq 0.02$ , and total pressure  $\leq 2\%$ .

A  $yz$ -plane, located  $6D_j$  downstream of the nozzle exit, is chosen for the measurements. It is centered at the nozzle centerline with dimensions of 500 mm x 500 mm. The measurements are carried out in 2 sweeps in the  $y$ -direction with a 7 mm spacing between points; in the  $z$ -direction the point spacing is the same as the probe spacing of 15

mm. This plane includes the wake of the wing/flap and an axial section of the jet flow. By comparing the velocity components for each configuration, it can be assessed how the permeable flaps affect the flow around the wing, and the results can be linked to the aerodynamic forces measured with the balance.

The jet velocity is measured and controlled via pressure and temperature probes placed inside the nozzle. The former are connected to the ESP ZOC Scanivalve module, similarly as the multi-hole probes, whereas the latter are connected to a TempPoint measurement system with a maximum uncertainty of 1 K. The aerodynamic measurements are performed for a free-stream velocity of 60 m/s ( $M_f = 0.18$ ) and a nominal jet velocity of 170 m/s ( $M_j = 0.5$ ) for the three geometric configurations. The Reynolds number based on the free-stream velocity and the mean aerodynamic chord of the model is  $Re_f = 1.4 \times 10^6$ , whereas the one based on the nozzle exit diameter and the jet speed is  $Re_j = 1.29 \times 10^6$ .

### ACOUSTIC MEASUREMENTS

The acoustic measurements are carried out with a microphone phased array mounted on a side wall of the working section. Due to the presence of the nozzle strut, which can reflect and diffract acoustic waves propagating from the source of interest to the microphones, the array has been mounted facing the upper side of the model (shielded side of the jet). This configuration still allows for jet-installation noise measurements since the source of interest is located at the flap trailing edge and it is not subjected to shielding effects.

The phased array comprises 64 G.R.A.S. 40PH free-field microphones (frequency response:  $\pm 1$  dB; frequency range: 10 Hz to 20 kHz; maximum output: 135 dB, ref.  $2 \times 10^{-5}$  Pa) with integrated CCP pre-amplifiers. The microphones are arranged in an optimized multi-arm spiral configuration [6, 7], as shown in Fig. 9.5. The effective diameters in the  $x$ - and  $z$ -directions are 2 m and 1.5 m, respectively. In order to mitigate spurious noise due to the tunnel boundary layer, the microphones are recessed 5 mm in the wall and the cavities are covered with Kevlar patches, as shown in Fig. 9.1a.

The acquisition is performed with a sampling frequency of 51.2 kHz for 60 seconds and the recorded signals are used for acoustic source localization using Conventional Frequency-Domain Beamforming [8]. In order to compute the Cross-Spectral Matrix (CSM), the signals are divided into blocks of 1024 samples and windowed with a Hanning weighing function, with a 50% overlap; the CSMs obtained from each block are then averaged. The source maps are constructed on a scan plane parallel to the array, at the trailing-edge position of the junction between the inboard and outboard flaps ( $y = 1.59$  m). The scan plane dimensions are 3.2 m  $\times$  2.25 m, which corresponds to the extension of the model in the  $x$ - direction and the full height of the tunnel, subdivided into grid elements of 16 mm  $\times$  12 mm (200 grid elements in each direction). Afterwards, the narrow-band noise spectra are obtained via the Source Power Integration method [9, 10] applied to a region of interest (ROI) at the flap trailing-edge, and plotted with a frequency band of 50 Hz. This ROI has dimensions of 1 m  $\times$  1 m, centered at the source on the flap trailing edge. The acoustic measurements are carried out for a jet velocity of  $M_j = 0.50$  and different free-stream conditions, both static ( $M_f = 0$ ) and flight ( $M_f = 0.09$  and  $M_f = 0.18$ ) for an angle of attack  $\alpha = 0^\circ$ . The parameters for each measurement type are summarized in Table 9.2.

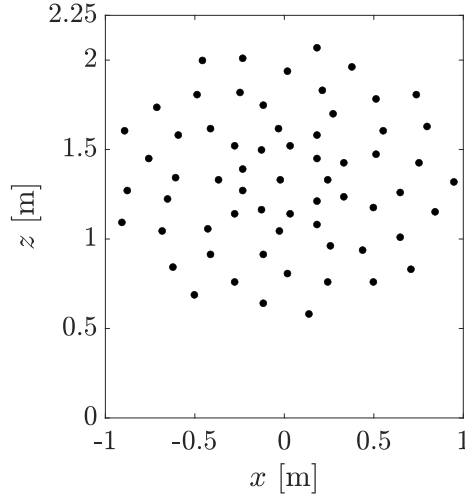


Figure 9.5: Microphone positions in the phased array.

Table 9.2: Flow parameters for each measurement type.

Measurement Type	$M_j$ [-]	$M_f$ [-]	$\alpha$ [°]
Force Balance	0.5	0.18	0 - 12
Flow-field Mapping	0.5	0.18	0
Acoustic	0.5	0 / 0.09 / 0.18	0

## 9.3. RESULTS AND DISCUSSIONS

### 9.3.1. AERODYNAMIC FORCES

The aerodynamic forces are analyzed in this section for the different flap configurations, as shown in Fig. 9.6 in terms of non-dimensional coefficients.

The results in Fig. 9.6a show that permeable flaps cause lift reduction throughout the whole range of measured angles of attack. Lift coefficient values for specific angles are reported in Table 9.3. For  $\alpha = 0^\circ$ , the UPF is responsible for a  $C_L$  reduction in the order of 11%, with respect to the baseline solid case, whereas for the GPF, the reduction at this angle is in the order of 7% likely due to a lower permeability near the flap suction peak, where most of the lift is generated. Since these measurements are performed without the jet flow, this behaviour is thus linked to steady flow around the flap and permeability effects. As the angle of attack is increased, the difference relative to the baseline is slightly reduced. For the solid flap,  $C_{L_{\max}}$  is reached for  $\alpha = 8^\circ$ ; at this angle, the UPF results in a 6% lift reduction, whereas the GPF result in 4% decrease. There is also a shift in the angle of maximum lift for the UPE, possibly caused by delayed boundary-layer separation at that angle. Further research into this behavior is necessary.

In terms of drag force, the permeable flaps have a lower impact; the  $C_D$  values for

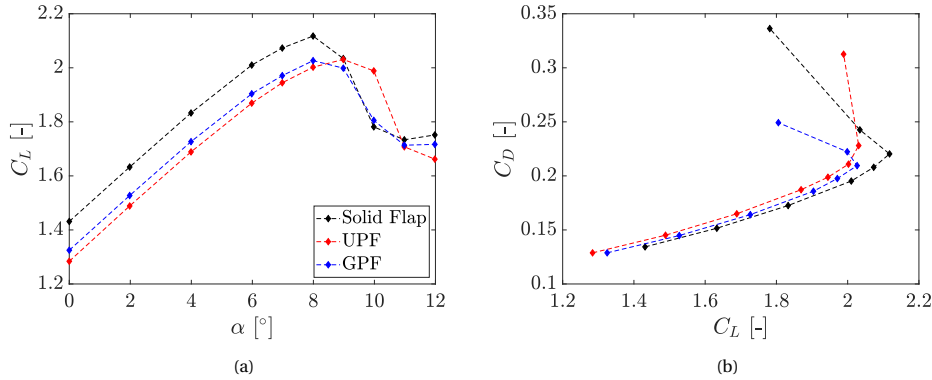


Figure 9.6: (a) Lift coefficient curve for the baseline solid flap and permeable configurations (b) Drag polar curve for the baseline solid flap and permeable configurations.

the UPF and GPF are lower than that of the baseline case, as reported in Table 9.3, which can be related to the lift decrease caused by the flow communication between upper and lower sides (reduction of induced drag). Therefore, the drag polar, shown in Fig. 9.6b, is plotted as a function of the measured lift coefficient for each case. Both permeable flaps result in higher drag values with respect to the baseline solid configuration, with the GPF providing a lower penalty than the UPF. By fitting the pre-stall region of the curves (considering  $C_L < 2$ ) with a second order polynomial, and targeting the lift coefficient of the baseline case for  $\alpha = 0^\circ$  ( $C_L = 1.43$ ), it is found that the UPF results in 3% drag augmentation, whereas for the GPF the increase is only of 0.5%.

Table 9.3: Lift and drag coefficients for the three investigated flap configurations, at two different angles of attack.

Flap Configuration	$C_L$ [-]		$C_D$ [-]	
	$\alpha = 0^\circ$	$\alpha = 8^\circ$	$\alpha = 0^\circ$	$\alpha = 8^\circ$
Solid	1.431	2.117	0.1343	0.2203
UPF	1.284	2.002	0.1287	0.2108
GPF	1.325	2.026	0.1288	0.2095

### 9.3.2. FLOW FIELD

Flow-field maps are obtained from the 5-hole probe measurements downstream of the model, which allow for an assessment of the effect of the permeable flaps on the model wake and jet development, and can be used for a deeper understanding of the results in the previous section. The contour plots in Fig. 9.7 show the time-averaged velocity component  $u$  (in the  $x$ -direction), non-dimensionalized by the free-stream speed, at a plane located  $6D_j$  downstream of the nozzle exit, for the three flap configurations.

The central region, corresponding to the jet flow, is slightly saturated in order to allow sufficient visibility of the model wake. The horizontal dotted lines correspond to regions where the velocity profiles are plotted for the three configurations.

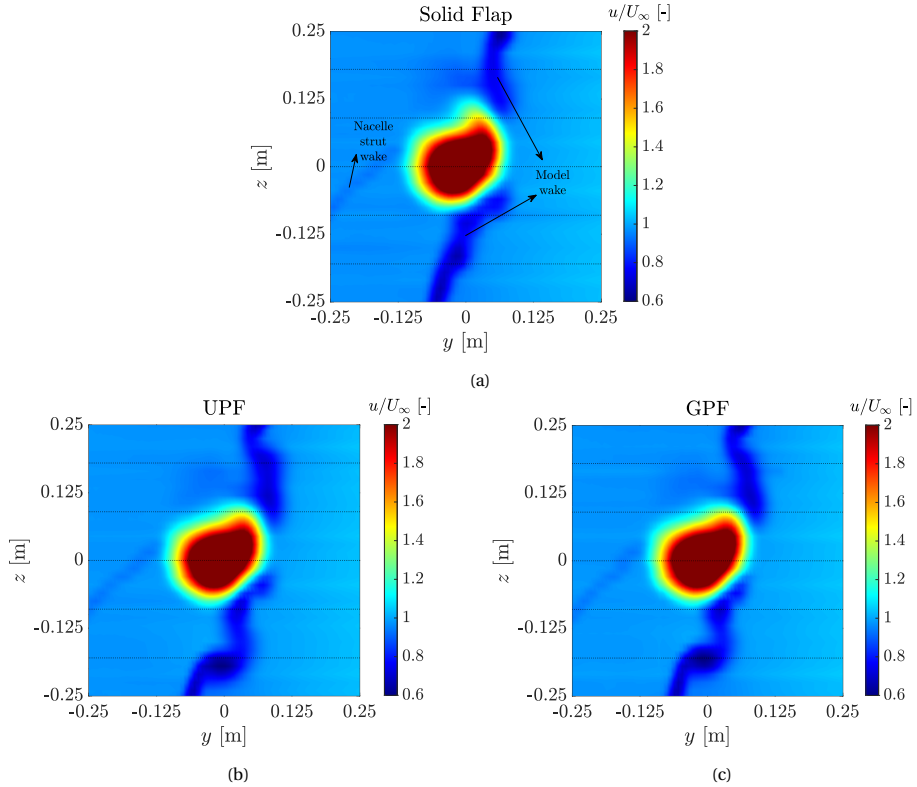


Figure 9.7: Flow-field maps of the velocity component  $u$  at a  $yz$ -plane located  $6D_j$  downstream of the nozzle exit. The central region corresponds to the jet flow and the lower velocity regions are caused by the model and nacelle strut wakes, as annotated. (a) Baseline solid flap. (b) Uniform permeability flap. (c) Gradient permeability flap. The dotted lines correspond to stations where the velocity profiles are extracted.

In Fig. 9.7a, for the solid flap case, the high velocity region of the jet flow is clearly distinguished in the center. On the left-hand side of the plot, the nacelle strut wake is slightly visible, although it does not seem to affect the jet or the model wake. The jet, however, does not display a round shape likely due to impingement on the wing/flap as well as due to the velocity induced by the wing in the negative  $y$ -direction.

For the permeable flaps, the velocity in the model wake is visibly lower than that of the solid one, particularly in the region  $0.1 \text{ m} < z < 0.2 \text{ m}$ . Moreover, a very low-velocity region occurs at  $z = -0.18 \text{ m}$  resembling a strong vortex. For a quantitative comparison between the three configurations, the velocity profiles in the regions corresponding to the black dotted lines are plotted in Fig. 9.8.

Starting from the upper side, the profiles at  $z = 0.18 \text{ m}$  are shown in Fig. 9.8a. For the permeable flaps, the wake velocity deficit is higher than that of the solid one. Moreover,

### 9.3. RESULTS AND DISCUSSIONS

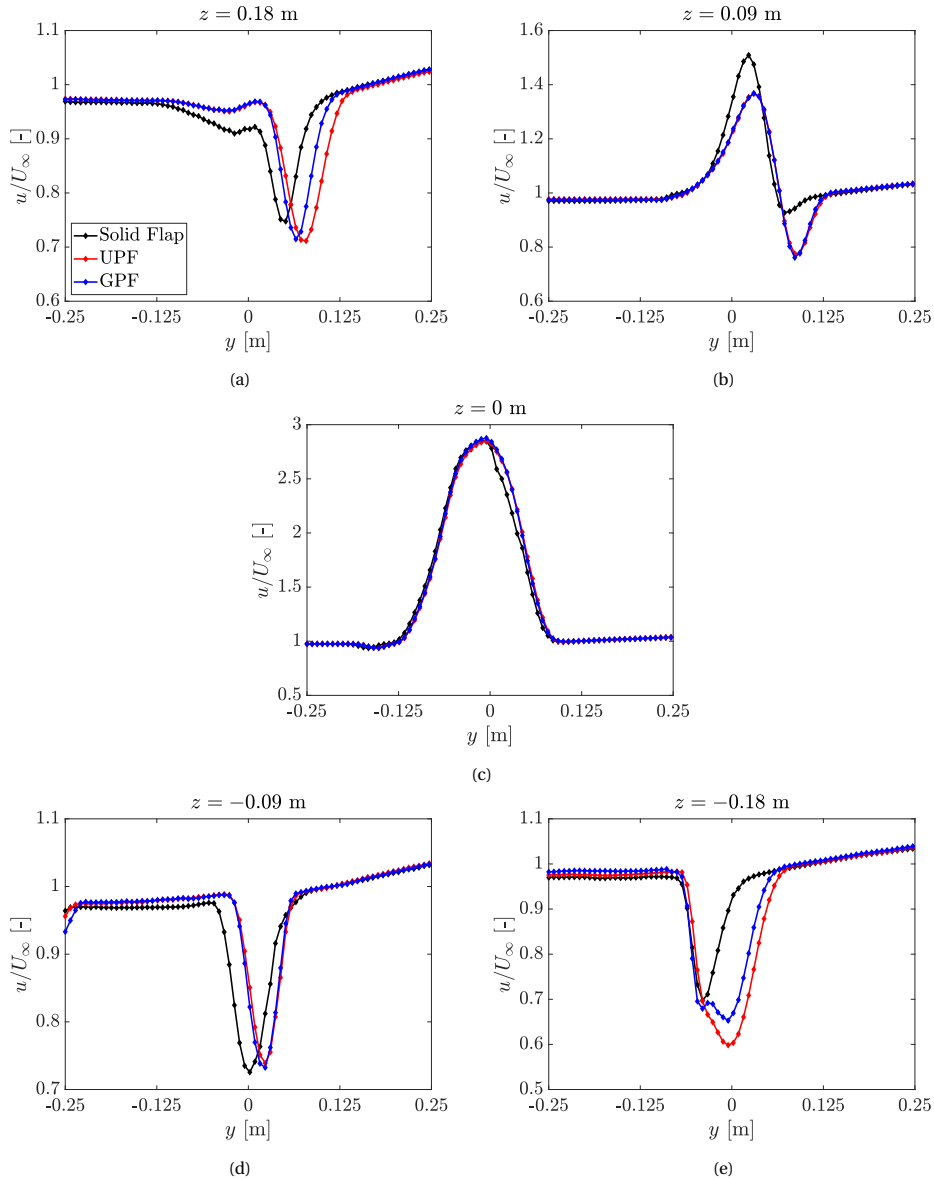


Figure 9.8: Profiles of  $u$ -velocity at five spanwise stations, displaying the model wake and the jet flow for the three flap configurations. (a)  $z = 0.18$  m. (b)  $z = 0.09$  m. (c)  $z = 0$  m (d)  $z = -0.09$  m (e)  $z = -0.18$  m

the region of lowest velocity is located to the right-hand side with respect to the solid case, showing that the wake of the former does not have a strong downward velocity component. This is likely due to either flow separation caused by the communication between the upper and lower sides of the flap or an effective reduction of the local angle

of attack. This behaviour is more noticeable for the UPF, which has a higher permeability near the leading edge.

A similar behaviour is shown for  $z = 0.09$  m in Fig. 9.8b, with a velocity deficit at  $y \approx 0.1$  m for the permeable cases, which does not occur for the solid one. Moreover, the higher velocity near  $y = 0$  indicates the presence of the steady jet flow, although the amplitude for the permeable cases is lower, likely due to interaction with a stronger model wake. For  $z = 0$ , shown in Fig. 9.8c, no visible wake region is detected since this position corresponds approximately to the jet centerline and the velocity amplitude is still approximately the nominal jet one ( $M_j = 0.5$  or  $2.83U_\infty$ ). A slight asymmetry is shown for the solid case, with slightly lower values in the positive  $y$ -direction. This is believed to be due to a region of jet impingement on the flaps, which block a small part of the flow in that direction.

The profiles at  $z = -0.09$  m, shown in Fig. 9.8d display the same characteristics of those from Fig. 9.8a. However, the profiles at Fig. 9.8e show a much wider wake for the permeable flaps, with a clearly higher integral velocity deficit. Moreover, the wakes do not appear to be symmetric in  $y$ , indicating the occurrence of an additional phenomenon. From the maps in Fig. 9.7, the flow in this region appears to be similar to a vortex. Therefore, it is useful to compute the flow vorticity  $\omega$  in the  $x$ -direction, as plotted in Fig. 9.9.

The high vorticity in the central region of the plots corresponds to the mixing layer of the jet and it displays similar values for all three configurations. However, for  $z = -0.18$  m, a strong vortex is visible in the plots for the permeable flaps. Nevertheless, the origin of this vortex are unclear. It is hypothesized that a flow structure similar to a side-edge vortex is formed in the spanwise region where permeability starts. This hypothesis is reinforced by the position of the vortex approximately coinciding with that of the spanwise solid-permeable junction. A strong vorticity region also occurs at the outboard side ( $z = 0.18$  m) of the permeable flaps, once again near the end of the porous section in the spanwise direction, further increasing the likelihood of the side-edge vortex hypothesis. The higher vorticity at the inboard side can be linked to a higher flow circulation near the root of the wing with respect to a section closer to the tip. These vortices also likely have a significant contribution to the lift reduction measured for these configurations, as reported in the previous section. Further research into the possible generation of these vortices and their impact is necessary.

### 9.3.3. BEAMFORMING MAPS AND NOISE SPECTRA

In this section, the acoustic results from the phased array measurements coupled with the beamforming technique are discussed. The source maps for the three flap configurations are plotted in Fig. 9.10 for a frequency  $f = 700$  Hz, corresponding to  $St = 0.47$  ( $St_j = f \times D_j / U_j$ ). The maps are obtained for  $M_j = 0.5$  and  $M_f = 0.18$ .

The beamforming maps show that the dominant acoustic source at this frequency is located near the flap trailing edge and approximately centered at the nozzle centerline, indicating that it occurs due to the interaction between the flap and the jet flow. For a jet-off condition, this source is not present in the beamforming maps, which in turn are dominated by the tunnel background noise and thus not shown. For all three flap configurations, the source is located at the same position but with a lower amplitude for

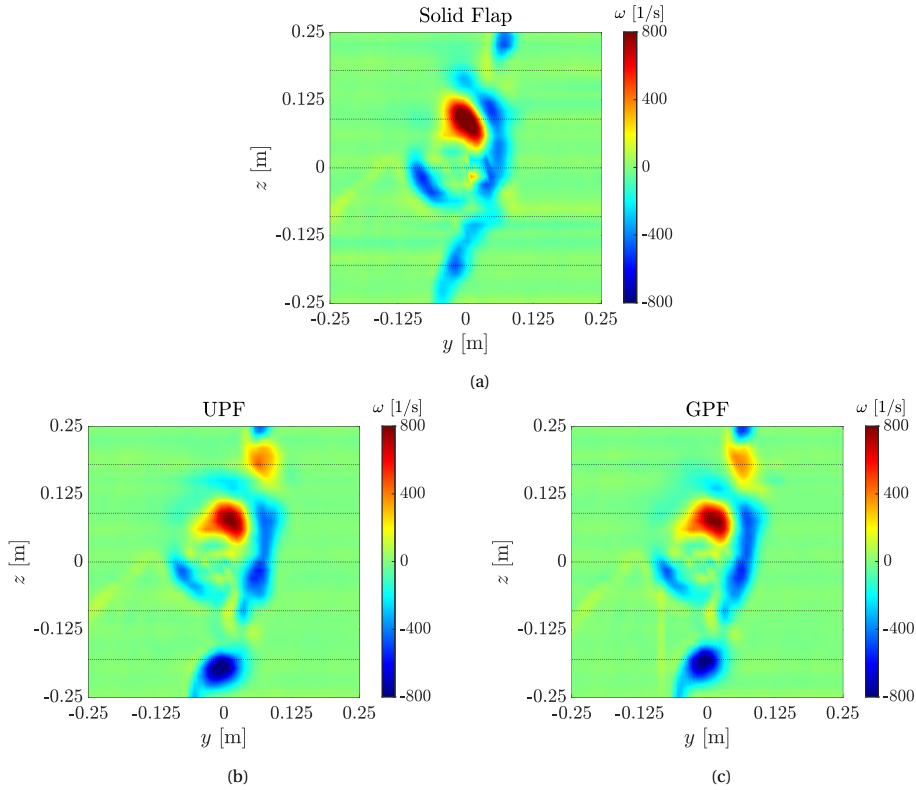


Figure 9.9: Flow-field maps of the vorticity  $\omega$  in the  $x$ -direction. (a) Baseline solid flap. (b) Uniform permeability flap. (c) Gradient permeability flap.

the permeable cases. For the baseline solid case, the peak source amplitude, in terms of Sound Pressure Level (SPL), is approximately 88.5 dB, whereas both the UPF and GPF have maximum amplitudes of 85.5 dB. No significant differences are visible between the permeable cases. Therefore, it is shown that the permeable flaps are effective in reducing JIN under flight conditions.

In order to verify the effect of the permeable flaps at different frequencies, SPL spectra are computed using the source power integration technique [9, 10] applied to the region delimited by the dashed lines in Fig. 9.10. Thus, the results focus on the flap trailing-edge source and the effect of spurious sources is mitigated. The spectra are plotted for a minimum frequency of 300 Hz, below which the tunnel background noise is dominant, and a maximum of 4 kHz, wherein the presence of sidelobes and spurious sources from the tunnel and nozzle in the beamforming maps reduce the accuracy of the analysis.

The spectra show that the permeable flaps provide noise reduction in a wide range of frequencies. For  $400 \text{ Hz} < f < 1000 \text{ Hz}$ , both the UPF and the GPF have lower SPL than the baseline solid case, with an approximately constant reduction of 3 dB in this range.

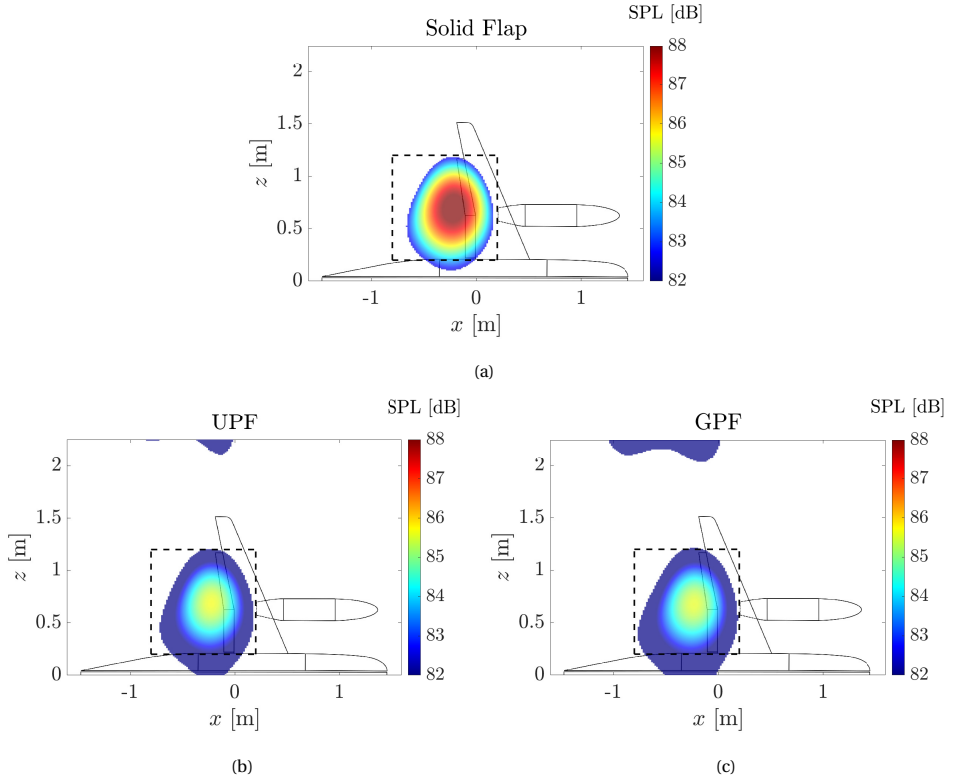


Figure 9.10: Acoustic source maps obtained from beamforming for a frequency  $f = 700$  Hz ( $St_j = 0.47$ ). (a) Baseline solid flap. (b) Uniform permeability flap. (c) Gradient permeability flap. The dashed section corresponds to the region-of-interest, wherein source power integration is applied.

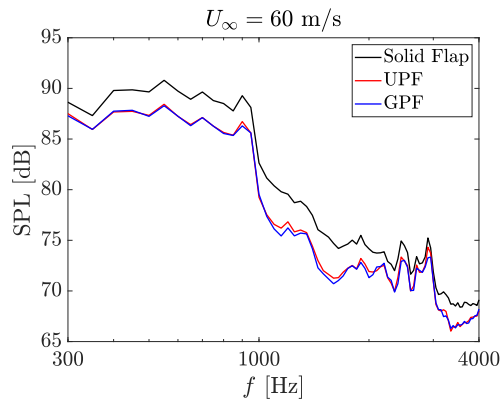


Figure 9.11: SPL spectra obtained from source power integration applied to the flap trailing-edge region for all three configurations.

## 9.4. CONCLUDING REMARKS

The sharp drop occurring at approximately 1000 Hz is typical when only the trailing-edge source is considered, while disregarding the contribution by turbulence mixing [11], as done by beamforming. Moreover, both permeable flap configurations have similar noise amplitudes throughout the entire frequency range analyzed. Therefore, it is likely that the hole placement does not play a large role in the amplitude of the trailing-edge source, or it is not as significant as the integral permeability of the structure.

The effect of free-stream on the JIN levels and the relative reduction provided by the permeable flaps is assessed by plotting the SPL spectra for different free-stream speeds, as shown in Fig. 9.12.

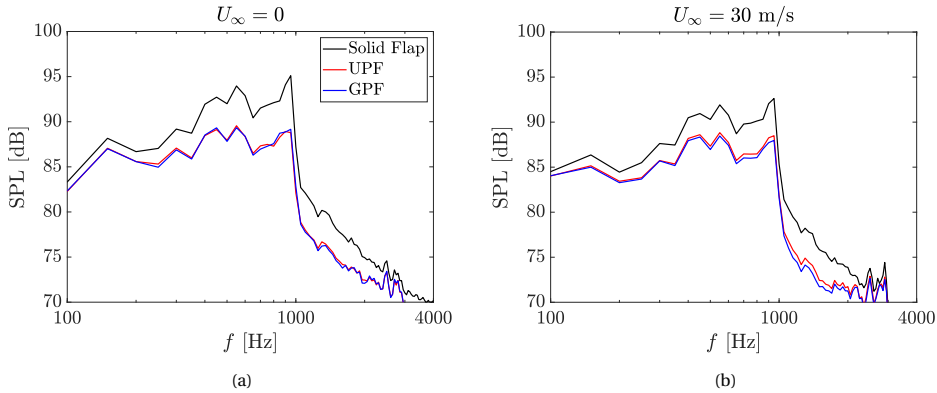


Figure 9.12: SPL spectra obtained from source power integration applied to the flap trailing-edge region for all three configurations at different free-stream speeds. (a)  $U_\infty = 0$ . (b)  $U_\infty = 30$  m/s.

The results for the static condition ( $U_\infty = 0$ ) are plotted in 9.12a. Initially, it is shown that the noise levels for the solid flap case are higher than those reported in Fig. 9.11 for the same case. For a frequency of 900 Hz, for example, the SPL for the static case is approximately 94 dB, whereas with a free-stream speed of 60 m/s, the noise levels are 89.3 dB. This occurs because in the presence of free-stream the shear stresses in the jet mixing-layer are lower with respect to the static condition, thus reducing the amplitude of the velocity and pressure fluctuations prior to their scattering at the flap trailing edge. This is further verified by intermediary SPL values obtained with a free-stream speed of 30 m/s, as shown in Fig. 9.12b and reported in Table 9.4. For the permeable flaps, on the other hand, the noise levels are less sensitive to the free-stream speed, as reported in Table 9.4 as well. This is likely due to a reduced sensitivity of the dominant source to the amplitude of impinging pressure fluctuations. Due to the flow communication between the upper and lower sides of the flap, there is a weaker pressure imbalance at the flap trailing edge, which in turn plays a relatively lower role in the produced noise levels with respect to the solid case.

## 9.4. CONCLUDING REMARKS

An experimental investigation on jet-installation noise reduction with the application of permeable flaps is performed. A half-model representative of a commercial aircraft with

Table 9.4: SPL obtained from the noise spectra for the three flap configurations at different free-stream speeds for a frequency  $f = 900$  Hz.

	$U_\infty = 0$	$U_\infty = 30$ m/s	$U_\infty = 60$ m/s
Solid Flap	94.0	92.0	89.3
UPF	88.9	88.2	86.7
GPF	88.8	87.7	86.3

flaps deployed in a landing configuration is selected for the tests. A separate nozzle is included for generating the jet flow in the vicinity of the airframe.

Acoustic results obtained from phased array microphone measurements show a clear source at the flap trailing edge, approximately centered at the nozzle centerline, caused by interaction with the jet flow. With the permeable flaps, the source position remains unchanged, but a clear reduction in amplitude, in the order of 3 dB is verified. The noise reduction provided by the permeable flaps is consistent in the entire frequency range where IJN is the dominant source, and thus it is concluded that they are effective noise reduction solutions. For a static condition, without free-stream, the noise reduction provided by the permeable flaps reaches 5 dB due to the higher amplitude of pressure fluctuations in the jet mixing layer for this condition.

Aerodynamic force measurements carried out with a balance show that the permeable flaps are responsible for a lift reduction in the order of 7% at zero degree angle of attack. This is due to the flow communication between the upper and lower sides of the flap, which are likely to alter the boundary layer properties on the surface due to the pressure gradient between the two sides. In terms of drag, the permeable flaps result in only a minor increase for a similar lift coefficient, with respect to the baseline configuration. Comparing the two permeable cases, the gradient permeability flap outperforms the uniform one, likely due to a lower permeability near the flap suction peak, where most of the lift is generated. In the studied configuration with a high flap deflection, it is expected that this effect is the strongest. For a take-off condition, wherein a lift decrease would be more harmful, the permeable flaps would have a lower impact on the aerodynamic performance due to a lower deflection angle and thus lower pressure differential between the upper and lower surfaces.

Flow velocity maps show that the permeable flaps generate a stronger wake than their solid counterpart. This is possibly due to boundary-layer separation occurring due to the communication between the upper and lower sides of the flap, which introduces a flow component normal to the chord. Therefore, the wake velocity deficit is higher and the downward induced velocity by the wing is not as significant with respect to the solid case, thus likely the cause for the lower lift force. Additionally, vorticity maps reveal the presence of two large vortices near the spanwise regions where the perforations start at both inboard and outboard sides. It is believed that the perforations produce a flow structure similar to a side-edge vortex, which can be also responsible for a portion of the aerodynamic penalties reported since these vortices reduce the local angle of attack and, consequently, the generated lift.

It is shown that the permeable flaps are able to significantly reduce jet-installation noise for an aircraft configuration under flight conditions. It has been also shown that the aerodynamic penalties (lift decrease and drag increase) caused by the permeable flaps can be mitigated by defining a proper hole placement on the structure; by introducing a gradient permeability, for example, an equal noise reduction as provided by an uniform permeability can be obtained with lower performance degradation. Therefore, with an optimization of this parameter both in the streamwise and spanwise directions, considering the pressure fluctuations on the flap surface, for example, a permeable flap is a feasible JIN reduction solution both in terms of acoustics and performance.

## REFERENCES

- [1] V. G. Mingle, L. Brusniak, R. Elkoby, and R. H. Thomas, *Reducing Propulsion Airframe Aeroacoustic Interactions with Uniquely Tailored Chevrons: 3. Jet-Flap Interaction*, in *12th AIAA/CEAS Aeroacoustics Conference* (Cambridge, MA, USA, 2006).
- [2] J. W. Slooff, W. B. de Wolf, H. M. M. van der Wal, and J. E. J. Maseland, *Aerodynamic and aero-acoustic effects of flap tip fences*, Tech. Rep. (Dutch National Aerospace Laboratory - NLR, NLR-TP-2002-004, 2002).
- [3] L. Rego, F. Avallone, D. Ragni, and D. Casalino, *On the mechanisms of jet-installation noise reduction with flow-permeable trailing edges*, *Journal of Sound and Vibration* **520** (2022), [10.1016/j.jsv.2021.116582](https://doi.org/10.1016/j.jsv.2021.116582).
- [4] L. Rego, D. Ragni, F. Avallone, D. Casalino, R. Zamponi, and C. Schram, *Jet-installation noise reduction with flow-permeable materials*, *Journal of Sound and Vibration* **498**, 115959 (2021).
- [5] A. Rubio Carpio, F. Avallone, D. Ragni, M. Snellen, and S. van der Zwaag, *Quantitative criteria to design optimal permeable trailing edges for noise abatement*, *Journal of Sound and Vibration* **485** (2020), [10.1016/j.jsv.2020.115596](https://doi.org/10.1016/j.jsv.2020.115596).
- [6] S. Luesutthiviboon, A. Malgoezar, M. Snellen, P. Sijtsma, and D. Simons, *Improving source discrimination performance by using an optimized acoustic array and adaptive high-resolution CLEAN-SC beamforming*, in *7th Berlin Beamforming Conference* (Berlin, Germany, 2018).
- [7] S. Luesutthiviboon, A. M. Malgoezar, R. Merino-Martinez, M. Snellen, P. Sijtsma, and D. G. Simons, *Enhanced HR-CLEAN-SC for resolving multiple closely spaced sound sources*, *International Journal of Aeroacoustics* **18**, 392 (2019).
- [8] T. J. Mueller, *Aeroacoustic Measurements*, 1st ed. (Springer-Verlag, Berlin, Germany, 2002).
- [9] T. F. Brooks and W. M. Humphreys, *Effect of directional array size on the measurement of airframe noise components*, in *5th AIAA/CEAS Aeroacoustics Conference and Exhibit* (American Institute of Aeronautics and Astronautics Inc, AIAA, Bellevue, WA, USA, 1999).

- [10] P. Sijtsma, *Phased array beamforming applied to wind tunnel and fly-over tests*, Tech. Rep. (National Aerospace Laboratory (NLR), Amsterdam, The Netherlands, 2010).
- [11] L. Rego, F. Avallone, D. Ragni, and D. Casalino, *Jet-installation noise and near-field characteristics of jet-surface interaction*, *Journal of Fluid Mechanics* **895** (2020), [10.1017/jfm.2020.294](https://doi.org/10.1017/jfm.2020.294).

# 10

## CONCLUSIONS AND RECOMMENDATIONS

*What we have done for ourselves alone dies with us.  
What we have done for others and the world remains, and is immortal.*

Albert Pike

## 10.1. SUMMARY AND CONCLUSIONS

THIS thesis reports a comprehensive study on jet-installation noise and its mitigation through passive solutions applied on the scattering surface. In this final chapter, the research goals defined in Chapter 1 are assessed in terms of the work reported in the previous sections.

1. **Perform an analysis on jet-installation noise in order to explain how the far-field noise is affected by the near-field characteristics of the isolated jet, such as the amplitude of pressure fluctuations and their frequency content.**

The study is carried out by means of high-fidelity, scale-resolving numerical simulations using LBM-VLES with a configuration comprised by a single-stream nozzle and a nearby flat plate, as reported in Chapter 5.

It is shown that the characteristics of the jet pressure field have a strong influence on the noise produced by the scattering at the plate trailing edge. The frequency range where installation effects are significant is dependent on the dominant wavenumbers present in the jet mixing layer, for a given trailing-edge position. In more detail, an equivalent source localization method is proposed and coupled with compactness inequalities defined by Ffowcs-Williams and Hall to determine wavenumber-based envelopes that predict features in the installed far-field spectra, such as the spectral peak frequency and the maximum frequency for which installation effects are the dominant acoustic source. Through this analysis, these two frequencies of interest for the installed case can be estimated with only isolated jet information.

On the other hand, the far-field spectral amplitude of an installed jet has been linked to the characteristics of coherent structures present in the mixing layer through scaling laws for different plate geometries. In the radial direction, the noise levels scale with the exponential of the plate height, which is a characteristic of the linear hydrodynamic region of the jet. However, it is shown that this scaling needs to be coupled with a frequency shift due to the different dominant scattered wavenumbers for each case, which in turn can be obtained using the compactness analysis with an equivalent source. Along the axial direction, Spectral POD is applied; the first eigenvector displays characteristics of instability waves, and it is modelled with a Gaussian envelope, related to the hydrodynamic wavelength. The amplitude of the Gaussian at different axial positions, for each frequency, is found to be an appropriate scaling parameter for the installed far-field noise for configurations with different plate lengths.

2. **Evaluate the noise reduction capabilities of permeable materials and acoustic liners mounted at the trailing edge of a surface in the vicinity of a jet.**

In order to study jet-installation noise reduction with permeable materials applied on the scattering surface, an experimental study is carried out with a single-stream subsonic jet and a nearby flat plate, placed in the jet near-field (Chapter 6).

Significant noise reduction is achieved with the flow-permeable inserts, particularly in the low/mid frequency range, where the scattering is the dominant mechanism. A low resistivity material such as a metal foam is more effective in reducing

JIN than a more resistive perforated plate. The higher permeability can better mitigate the pressure imbalance between the upper and lower sides of the plate, and thus reduce the noise generated by surface pressure fluctuations.

The absolute noise reduction provided by the permeable materials is also found to be independent on the amplitude of impingement pressure waves. By moving the plate away from the jet, the permeable materials provide similar reduction as the baseline case, bringing the noise levels closer to the isolated case. Conversely, by increasing the plate length, lower noise abatement is obtained with the permeable trailing edges, particularly at low frequencies, showing that the wavelength plays an important role in the noise reduction provided by the permeable materials.

On the other hand, the far-field spectral shape of the configuration with the metal foam trailing edge is different to that of the perforated one, which in turn is similar to that of the solid case. This is believed to be related to the high permeability of the metal foam, which produces a new geometric discontinuity and thus a new scattering region at the solid-permeable junction.

These results show that a surface treatment with flow-permeable materials is a promising mitigation solution for jet-installation noise, and its properties must be optimized for a given wing/engine installation.

Additionally, the effectiveness of acoustic liners as jet-installation noise reduction solutions has been similarly assessed, with a nozzle and a nearby flat plate, but through LBM-VLES numerical simulations (Chapter 8).

Due to the low frequency target resonance, a curved Helmholtz resonator concept is necessary in order to keep the plate thickness small. The resonator characteristics and dimensions are obtained through the Guess method and validated through impedance tube experiments and simulations.

For an array of resonators placed inside the plate with the face-sheet on the jet side, far-field spectra show that noise reduction is achieved with respect to the solid case, in a broad frequency range. The DDOF liner further expands this range towards higher frequencies outperforming the SDOF one. It is thereby shown that acoustic liners can be effective jet-installation noise mitigation solutions. The benefits obtained with the liners are, however, less than those gained with the permeable materials since they have different working mechanisms.

### **3. Study the main mechanisms behind the achieved noise reduction, linking the results to the properties of the permeable materials and the near-field properties of the isolated jet.**

Complementary to the experiment previously described, a numerical investigation is performed on the same configuration in order to assess the effect of the permeable materials on the main noise generation mechanisms of an installed jet (Chapter 7).

It is found that a lower resistivity leads to a higher unsteady volumetric flow rate through the permeable material, which results into lower amplitude of pressure fluctuations on the surface, and consequently lower noise emission. Moreover, for

structures with low resistivity, the dominant acoustic source is located at the solid-permeable junction, confirming the previous hypothesis that this region becomes an impedance discontinuity and thus a scattering region.

A dual behaviour in the directivity plots (dipolar/cardioid directivity), observed for the solid plate case is no longer present for the permeable ones. For the latter, the spectra display a consistent dipolar directivity throughout the entire frequency range where the installation effects are dominant. This occurs for all investigated permeable configurations, thus showing that the scattering mechanism at the original trailing-edge position is strongly reduced, independently of the material resistivity. It is thus concluded that the dominant mechanism in that region of the plate is the pressure wave impingement and the dominant acoustic source is located at the solid-permeable junction.

On the other hand, the noise reduction mechanism of the acoustic liners is more straightforward; the Helmholtz resonators mounted in the plate are able to significantly dampen the acoustic waves produced by the interaction between the jet and plate. However, the results also show that a slight noise reduction occurs at the shielded side of the plate, without an open face-sheet. Therefore, it is concluded that the resonators also alter the scattering properties of the plate due to a less abrupt impedance discontinuity at that region (Chapter 8).

Finally, a hybrid configuration comprised of open-cell permeable materials and Helmholtz resonators has proven to be the most effective solution in mitigating jet-installation noise of those studied in this work. It combines the noise reduction due to flow communication between the two sides of the surface near the trailing edge, while the resonators are used to further reduce noise produced by the solid section of the plate.

**4. Develop a permeable flap concept to be applied on a realistic aircraft geometry and investigate the effect of a porous material under flight conditions, and its effect on the aircraft performance.**

An experimental investigation on jet-installation noise reduction with the application of permeable flaps is performed with a wind-tunnel scale half-model representative of a commercial aircraft (Chapter 9).

Acoustic results show that the permeable flaps are responsible for jet-installation noise reduction in the order of 3 dB, in the entire frequency range where this source is dominant. Therefore, they are effective noise mitigation solutions in an actual aircraft geometry at in-flight conditions (in the presence of external flow).

However, the investigated permeable configurations lead to lift reduction and a minor drag increase for a similar lift coefficient, with respect to the baseline configuration. This is linked to tridimensional flow effects resulting from the formation of vortical structures in the spanwise regions where the perforations start at both inboard and outboard sides, similar to a side-edge vortices.

Therefore, the perforation pattern plays an important role in the aerodynamic performance, particularly at low angles of attack for which the relative contribution of the flap to lift generation is higher. On the other hand, the contribution of the

permeable flap to the overall drag force is not as significant. The permeable flaps have thus the potential to be a feasible solution from both aeroacoustic and aerodynamic sides if the lift can be corrected by a slight increase in angle of attack, or an optimization study of the perforation pattern is performed.

Based on the studies reported in this work, the research objectives defined in Chapter 1 have been properly assessed and accomplished. Further insights into jet-installation noise generation, and its relationship to near-field characteristics, have been obtained as well as its reduction through the application of permeable materials. Different solutions have been proposed and studied in this work, each with their advantages and shortcomings, along with a comprehensive investigation into their physical mechanisms. However, there are several fronts on which this work can be expanded, as listed in the next section.

### 10.2. RECOMMENDATIONS FOR FUTURE WORK

The study reported in Chapter 5 has shown that the characteristics of coherent structures in the mixing layer of a turbulent jet define the amplitude and frequency content of the far-field spectrum of installation noise, for a surface placed in the linear hydrodynamic field. It is possible that the trend of reducing the clearance between the jet flow and the flap results in grazing flow on the latter and thus the mechanisms reported in this work are no longer applicable. Therefore, it is recommended that an investigation is carried out for such a configuration, focusing on the particular effect of scrubbing on the unsteady flow around the surface and possible noise scaling laws that can be obtained based on the near-field features, possibly on the turbulent boundary-layer that is formed on the scrubbed side.

Regarding the applications of permeable materials, they have been shown to be successful in reducing jet-installation noise, but they can be certainly optimized for a given application. The maximum threshold in noise reduction that can be achieved with reducing resistivity should be investigated more in depth, particularly targeting certain frequencies of interest, in order to minimize the effects on the aerodynamic performance.

Additionally, the resistivity distribution on the surface is also an important parameter, which does not strongly affect the noise levels, but rather the lift force. Therefore, a trade-off study by restricting the permeable material to a short section near the edge, where the surface pressure fluctuations are the highest, or imposing a gradient permeability is an important step in increasing the feasibility of this technology. Care must be taken in the design of the permeable structure, however, in order to avoid possible flow separation or vortex formation. Moreover, the effect of permeability should be quantified in other flight conditions such as take-off and cruise, although it is likely that its impact on the aerodynamics is lower than in approach. Finally, a full-scale demonstrator should be carried out, taking into account the impact of flap permeability on structural properties, airworthiness and flight stability.

Regarding acoustic liners for JIN reduction, their impact on the flap aerodynamics needs to be assessed. However, considering that there is no flow communication and the perforations are restricted to the lower side, the aerodynamic impact is expected to be minor. Given the benefits obtained with the double degree-of-freedom liner with

respect to the single one, as shown in this work, a multi DOF configuration should also be studied, which could further broaden the frequency range of noise reduction.

A full-scale study of a lined flap for this application is also necessary in order to ensure that the low frequencies involved can be properly targeted. Moreover, the curved resonator concept should be studied with a realistic flap structure to ensure it can be properly mounted inside of it, while still providing noise reduction. A study with a hybrid permeable-lined flap at in-flight conditions would also provide important results in order to achieve an optimum configuration, limiting the former to the trailing edge and the latter covering the remaining surface. This concept should also have minimal effect on lift and drag, while highly effective for noise reduction.

Finally, this thesis has focused on reducing JIN only through changes on the scattering surface. However, these can be additionally coupled with changes to the jet flow itself, for example, with the addition of chevron or lobed nozzles, or other structures that modify the properties of the mixing layer. These can result in minimum JIN levels or a shift of the spectral peak towards frequencies that are not relevant for full-scale application.

# A

## SIGNAL PROCESSING TECHNIQUES AND ACOUSTIC PARAMETERS

This appendix contains the signal processing techniques applied in this thesis, along with the aerodynamic and acoustic parameters of interest that are obtained through them.

### A.1. TIME-DOMAIN STATISTICS

In a time-resolved experimental measurement or numerical simulation, the time history of the variables of interest is recorded as a discrete signal, with a predefined sampling period (or frequency) and a total sampling time.

It should be mentioned that only stationary and ergodic processes are considered in this work. The former states that the mean value and auto-correlation function of an ensemble of realizations at a given time (ensemble average) are constant and independent of the instant in which they are computed. The latter states that the ensemble average is equal to the mean of the samples of a single realization at different instances of time (time average), and similarly for the auto-correlation. The definitions of mean and auto-correlation are reported as follows [1].

#### A.1.1. MEAN VALUE

The mean value of a discrete variable ( $\bar{x}$ ) represents the central tendency of a random process and it is computed by summing all recorded values and dividing by the total number of samples  $N$ , either in an ensemble or at different instances for a single realization [1]:

$$\bar{x} = \frac{1}{N} \sum_{n=1}^N x_n. \quad (\text{A.1})$$

The time-averaged value is computed for all aerodynamic variables in this work, such as the jet velocity components, and lift and drag forces.

### A.1.2. VARIANCE AND STANDARD DEVIATION

The variance represents the dispersion of the samples and its square root, also known as standard deviation  $x'$ , is calculated by [1]:

$$x' = \sqrt{\frac{1}{N} \sum_{n=1}^N (x_n - \bar{x})^2}. \quad (\text{A.2})$$

The standard deviation is applied to determine the fluctuations of a parameter. This is particularly useful for a turbulent jet in order to determine the velocity fluctuations in the shear layer, for example, which are a measure of the turbulence magnitude in the flow. For acoustics, the standard deviation of pressure measured by a microphone can be used to compute the overall sound pressure level as posteriorly described.

### A.1.3. ROOT-MEAN-SQUARE

The mean square value represents a measure of both the central tendency and dispersion of a parameter, and its square root, also known as Root-Mean-Square (RMS), is computed by [1]:

$$x_{\text{RMS}} = \sqrt{\frac{1}{N} \sum_{n=1}^N (x_n)^2}. \quad (\text{A.3})$$

The RMS of a variable is useful when both the mean value and the fluctuations are important. For example, in this work, the RMS of the volumetric flow rate through the permeable materials is calculated to relate the material resistivity with the pressure balance around the trailing edge and the produced noise.

### A.1.4. AUTO-CORRELATION AND CROSS-CORRELATION

The auto-correlation function  $R_{xx}(\tau)$  is a measure of time-related properties in the data that are separated by fixed time delay  $\tau$  [1]. In other words, the auto-correlation is a measure of the signal similarity at a given time  $t$  with itself at an instance  $t + \tau$  [2].

The auto-correlation is estimated by multiplying the original signal with its delayed counterpart, and finally averaging the resulting product over the number of samples, given by [1]:

$$R_{xx}(\tau) = \frac{1}{N} \sum_{t_1}^{t_n} x(t)x(t + \tau). \quad (\text{A.4})$$

Prior to the multiplication, the signal mean can be also subtracted, resulting in the auto-covariance. In this case, for  $\tau = 0$ , it can thus be shown that the auto-correlation is equal to the signal variance.

The similarity between two different signals can then be estimated through the cross-correlation, given by:

$$R_{xy}(\tau) = \frac{1}{N} \sum_{t_1}^{t_n} x(t)y(t + \tau). \quad (\text{A.5})$$

Similarly, subtracting the mean of each signal before the multiplication leads to the cross-covariance. The peak in the cross-correlation curve indicates the instance in time (time delay) for which the signals are best correlated [2].

The auto- and cross-correlation of a signal (or pair of signals) are indispensable for processing of acoustic data, particularly for comparison with near-field pressure measurements, as well as for phased array measurements and source localization with beam-forming. However, the frequency-domain form of those functions is more commonly applied, as described in the following section.

## A.2. FREQUENCY-DOMAIN STATISTICS

For aeroacoustic problems, it is interesting to deal with the relevant parameters in the frequency domain mainly because the human ear has different sensitivities at different frequency ranges. Therefore, it is necessary to convert the data sampled in the time domain by means of a Fourier transform.

### A.2.1. FOURIER TRANSFORM

The Fourier transform converts a time history into a sum of individual harmonic components, described by sine and cosine functions, which can be represented by a complex exponential [2]:

$$X(f) = \int_{-\infty}^{\infty} x(t) \exp(-2\pi i f t) dt. \quad (\text{A.6})$$

For a discrete signal, the Discrete Fourier Transform (DFT) is given by:

$$X(f) = \sum_{t_1}^{t_N} x(t) \exp(-2\pi i f t). \quad (\text{A.7})$$

The frequency band  $\Delta f$  of the DFT spectrum is dependent on the total signal time  $T$ :

$$\Delta f = \frac{1}{T} = \frac{f_s}{N}, \quad (\text{A.8})$$

where  $f_s$  is the sampling frequency. The frequency band, which is also the minimum resolved frequency (frequency resolution), can thus be increased with a higher sampling time. On the other hand, the maximum resolved frequency is given by  $f_s/2$  (Nyquist frequency) in order to avoid aliasing [2].

Conversely, the Inverse Discrete Fourier Transform converts a spectrum  $X(f)$  to a time signal [2]:

$$x(t) = \frac{1}{N} \sum_{f_1}^{f_N} X(f) \exp(2\pi i f t). \quad (\text{A.9})$$

### A.2.2. POWER SPECTRAL DENSITY

In the frequency domain, the corresponding function to the auto-correlation is the auto-spectrum or Power Spectral Density (PSD)  $S_{xx}(f)$ , which represents the rate of change

of mean square value with frequency [1]. For a signal, the PSD can be estimated by computing the Fourier transform of the auto-correlation function [1]:

$$S_{xx}(f) = \frac{1}{f_s} \sum_{\tau_1}^{\tau_N} R_{xx}(\tau) \exp(-2\pi i f \tau). \quad (\text{A.10})$$

The total area under the PSD function over all frequencies is equivalent to the total mean square value of the time history [1]. The parameter  $S_{xx}(f)$  is also known as the two-sided PSD, which includes the values for negative frequencies as part of the Fourier transform computation. Considering only the positive frequency values, the one-sided PSD  $G_{xx}(f)$  is given by:

$$G_{xx}(f) = 2S_{xx}(f). \quad (\text{A.11})$$

In aeroacoustics, the auto-spectrum of pressure measured by a microphone is an essential indicator of noise levels. In this case, the PSD output has a unit of  $\text{Pa}^2/\text{Hz}$  since it is non-dimensionalized by the sampling frequency. Similarly, the auto-spectrum of velocity fluctuations at a point in the flow provide the turbulent kinetic energy as a function of frequency and it is thus useful for linking near- and far-field behaviour.

### A.2.3. CROSS-POWER SPECTRAL DENSITY

The Cross-Power Spectral Density (CPSD) is the frequency domain form of the cross-correlation and can be computed in the same manner as the PSD:

$$S_{xy}(f) = \frac{1}{f_s} \sum_{\tau_1}^{\tau_N} R_{xy}(\tau) \exp(-2\pi i f \tau), \quad (\text{A.12})$$

$$G_{xy}(f) = 2S_{xy}(f). \quad (\text{A.13})$$

The CPSD allows for computing the similarities between two signals at specific frequencies, as well as provides the phase shift (similar to the time delay in the cross-correlation) between them. The CPSD is widely used in phased array measurements since it retains only the contribution of sources correlated between microphones and mitigates those that are not. For example, for acoustic measurements in hard-walled, closed section wind tunnels the CPSD between the microphone signals allows for reducing the effect of the wall boundary layer on the measured acoustic pressure, thus increasing the signal-to-noise ratio. Moreover, the Cross-Spectral-Matrix used in source localization with beamforming is constructed by computing the CPSD between all the microphones of the array.

### A.2.4. COHERENCE

The CPSD can be used to estimate the coherence between two signals, which is also a measure of similarity between them for specific frequency bands, given by:

$$\gamma_{xy}(f) = \frac{|G_{xy}(f)|^2}{G_{xx}(f)G_{yy}(f)}. \quad (\text{A.14})$$

While the other parameters are given as complex numbers, the coherence is a real value between 0 and 1. If  $\gamma_{xy} = 1$ , the two input signals are identical.

Coherence is useful for comparing near- and far-field properties, as well as computing important parameters in trailing-edge noise such as the spanwise coherence length [3].

#### A.2.5. WELCH'S METHOD

The Welch's method is a convenient way of computing the PSD of a signal. Through this approach, the signal is divided into an integer number of overlapping (or not) blocks [4]. The DFT is then applied to each block, the magnitude squared is calculated and the result divided by the block length; the individual block PSDs are then averaged. This procedure reduces the variance in the auto-spectrum in exchange for a loss in frequency resolution [4].

In Welch's method, the blocks can be windowed by predefined functions in order to increase the weight of the samples at the center of the block with respect to those at the edges, near the regions where the original signal is cut. This allows for reducing noise in the block PSD, thus increasing the accuracy of the method [4]. In order to offset this weighting, block overlap is usually applied (commonly 50% overlap between block samples), wherein samples located at the edges of one block are placed at the center of the next one.

This method can be also applied for computation of CPSD by computing the cross-correlation between each block, followed by the DFT and averaging of cross-spectra. Due to its simplicity and accurate results, the Welch's method has been applied for PSD and CPSD computations in this thesis.

### A.3. SOUND PRESSURE LEVEL AND OVERALL SOUND PRESSURE LEVEL

The main acoustic parameters evaluated in this work are the Sound Pressure Level (SPL) and the Overall Sound Pressure Level (OASPL). The former is obtained from the pressure auto-spectrum at a given location, whereas the latter is given by the standard deviation in pressure, thus it can be obtained directly from the time history or by integrating the auto-spectrum in the entire frequency range [5]. These parameters are reported in decibel scale (dB), for which a reference pressure  $p_{\text{ref}} = 2 \times 10^{-5}$  Pa is used to non-dimensionalize the measured values. Moreover, since the PSD is usually output as  $\text{Pa}^2/\text{Hz}$ , the frequency band is included in the SPL formulation, given by:

$$\text{SPL}(f) = 10 \log_{10} \left( \frac{\text{PSD}(f) \times \Delta f}{p_{\text{ref}}^2} \right), \quad (\text{A.15})$$

$$\text{OASPL} = 20 \log_{10} \left( \frac{p'}{p_{\text{ref}}} \right). \quad (\text{A.16})$$

## REFERENCES

- [1] J. S. Bendat and A. G. Piersol, *Random Data: Analysis and Measurement Procedures* (John Wiley & Sons, Inc., Hoboken, NJ, USA, 2010).
- [2] A. Brandt, *Noise and Vibration Analysis: Signal Analysis and Experimental Procedures* (Wiley, 2011).
- [3] R. K. Amiet, *Noise due to turbulent flow past a trailing edge*, *Journal of Sound and Vibration* **47**, 387 (1976).
- [4] P. Welch, *The Use of Fast Fourier Transform for the Estimation of Power Spectra: A Method Based on Time Averaging Over Short, Modified Periodograms*, *IEEE Transactions on Audio and Electroacoustics* **15** (1967).
- [5] M. J. T. Smith, *Aircraft Noise* (Cambridge University Press, 1989).

# B

## DESIGN AND CHARACTERIZATION OF THE A-TUNNEL JET TEST SECTION

This appendix reports the design and characterization of the jet test section for the Anechoic Tunnel (A-Tunnel) at the Delft University of Technology. It includes the nozzle geometry, flow properties and constraints as well as far-field noise spectra for both isolated and installed configurations.

### B.1. WIND TUNNEL FACILITY

The jet nozzle is designed to be connected to the tunnel circuit, with air supplied by the fans. Therefore, the tunnel characteristics are required as design inputs.

The A-tunnel is an open-jet, closed-circuit, vertical wind tunnel, part of the Low Speed Laboratory (LSL) of the Delft University of Technology. The test section is located inside an anechoic chamber; the walls are lined with wedges made of acoustic absorbing foam, which mitigate sound wave reflection for frequencies higher than 173.5 Hz [1], thus ensuring the quality of acoustic measurements. The anechoic chamber is shown in Fig. B.1 [1]. The nozzle located in the floor has an exit diameter of 0.6 m. Two fans provide a maximum volumetric flow rate of approximately 13500 m<sup>3</sup>/h with a maximum static pressure discharge of approximately 9000 Pa [1]. Further information on the tunnel facility can be found in reference [1].

### B.2. NOZZLE DESIGN

The circular jet nozzle is designed following the methodology reported by Morel [2], wherein the contraction is defined by two cubic polynomials intersecting at a chosen position with respect to the nozzle length. The design requirements are the inlet diameter, which must be equal to 0.6 m, and the exit diameter which is defined as 50 mm.

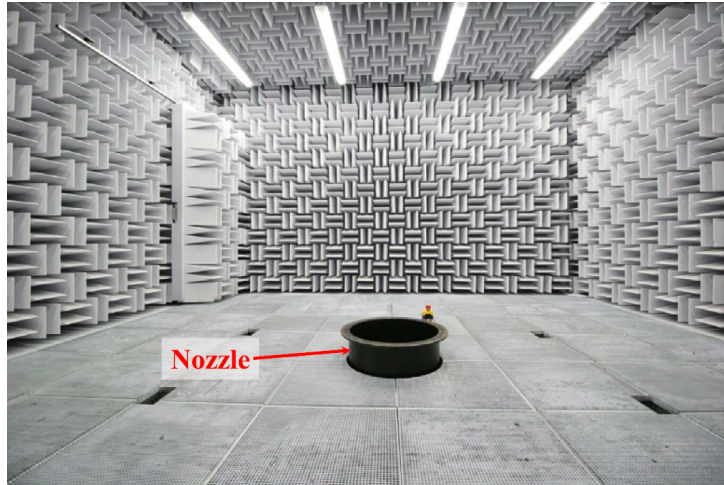


Figure B.1: Anechoic chamber of the A-Tunnel at the Delft University of Technology [1].

These values, however, lead to a contraction ratio of 144, which is beyond the values proposed by Morel [2]. Therefore, it has been decided to apply the cubic profile up to a diameter of 100 mm (leading to a contraction ratio of 36), followed by a straight tapering to a 50 mm exit diameter ( $D_j$ ). The internal shape of the nozzle is shown in Fig. B.2.

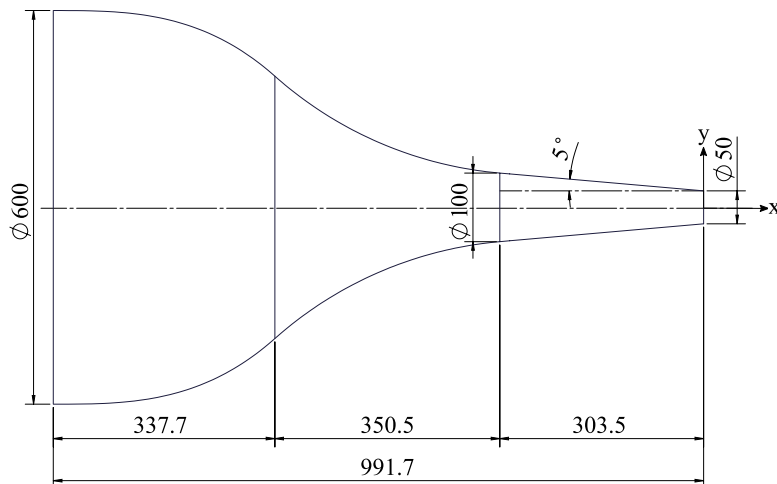


Figure B.2: Internal profile of the jet nozzle with an inlet diameter of 0.6 m and exit diameter of 50 mm. Dimensions in mm.

The design method originally leads to contractions with a straight inlet and outlet [2]. However, for this case, the geometry was cut in order to be tangential to the linear tapering region, with a  $5^\circ$  angle, as shown in Fig. B.2. The total length of the contraction is approximately 1 m, leading to a ratio of 1.33 with respect to the inlet diameter. The

internal shape with cubic profiles has been manufactured through 3D-printing with external aluminium frames as reinforcements, as shown in Fig. B.3. The straight section is fully manufactured in aluminium for a higher stiffness in the high-velocity flow region. This modular construction also allows for quicker investigations on different nozzle outlet configurations, for example.



Figure B.3: Full constructive design of the nozzle with attachment to the tunnel circuit and internal frames in the contraction section.

### B.3. INSTRUMENTATION

In order to characterize the jet flow from both aerodynamic and aeroacoustic perspectives, the following measurements have been carried out. The nominal jet velocity is measured with a Pitot-static tube placed approximately at the jet centerline at  $1D_j$  downstream of the nozzle exit plane. The static and total pressure taps are connected to a Mensor DPG 2400 pressure gauge, with a measurement range of -1 kPa to 6 kPa. A total of 200 samples are obtained with a sampling frequency of 15 Hz [1]. The accuracy of the instrument used is of 0.03% of the read value. These measurements also allow for calibration of the jet nominal velocity with respect to the fans rotational speed.

The jet flow development is characterized through hot-wire measurements using a Dantec 55P11 probe connected to a TSI IFA-300 constant-temperature anemometry (CTA) system [1]. This probe comprises a single wire, which allows for the measurement of the axial jet velocity component. Radial profiles are obtained at several axial positions throughout the flow, from  $1D_j$  up to  $10D_j$ . The data is recorded with a sampling frequency of 51.2 kHz for 15 seconds.

Finally, for the acoustic measurements, an arc-array with 8 G.R.A.S. 46BE microphones (frequency range: 4 Hz to 80 kHz; pressure-field response:  $\pm 2$  dB; max. output: 160 dB ref.  $2 \times 10^{-5}$  Pa) is mounted at a distance of  $24D_j$  from the nozzle exit, as shown

in Fig. B.4. The polar angle follows the convention of  $\theta = 0^\circ$  in the upstream direction of the jet axis. Therefore, the microphone at  $\theta = 90^\circ$  is aligned with the nozzle exit. The microphones are mounted from  $\theta = 60^\circ$  to  $\theta = 130^\circ$ , spaced of  $10^\circ$ , as shown in Fig. B.4. The measurements are performed with a sampling frequency of 51.2 kHz for 60 seconds. For post-processing, the acoustic data are split into blocks of 2048 samples for each Fourier transform, and windowed with a Hanning weighting function with 50% overlap. These parameters result in a frequency resolution of 25 Hz.



Figure B.4: Jet nozzle mounted in the anechoic chamber with microphone arc-array.

For the acoustic measurements of the installed jet configuration, the same flat plate model reported in Chapter 6 has been used. The plate is mounted with a length  $L = 3D_j$ , with respect to the nozzle exit plane, and a height  $h = 1D_j$  with respect to the jet centerline. The plate is located between the arc and the nozzle, and thus the acoustic measurements are carried out at the shielded side of the installed jet.

#### B.4. JET FLOW CHARACTERISTICS

The jet nominal velocity for a given fan rotational speed is shown in Fig. B.5. Results are also included for an exit diameter of 100 mm, obtained by removing the straight tapering section. The curves show that a maximum velocity of 115 m/s ( $M_a = 0.34$ ) is attained with the highest fan rotational speed of 3250 RPM. It is also shown that the curves for both exit diameters collapse, indicating that the limiting factor in the jet speed is the pressure

differential, while the mass flow can be increased with a larger nozzle. Therefore, further contraction of the flow would not lead to a higher jet velocity.

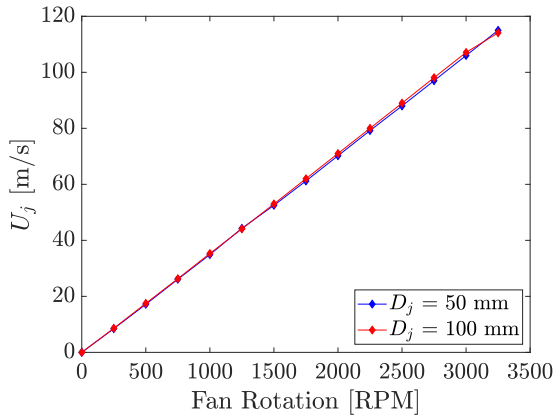


Figure B.5: Jet nominal velocity for different fan rotational speeds and two nozzle exit diameters.

In sequence, the jet flow characteristics are verified for a nominal speed of 60 m/s ( $Re_D = 2 \times 10^5$ , based on the nozzle exit diameter of 50 mm). Firstly, the radial profile of the time-averaged axial velocity is shown in Fig. B.6a. A top-hat curve shows that the velocity is uniform for  $-0.5 < y/D_j < 0.5$ . Moreover, as shown in Fig. B.6b, the standard deviation of velocity  $u'$  is maximum at the lipline, which is the center of the turbulent mixing layer.

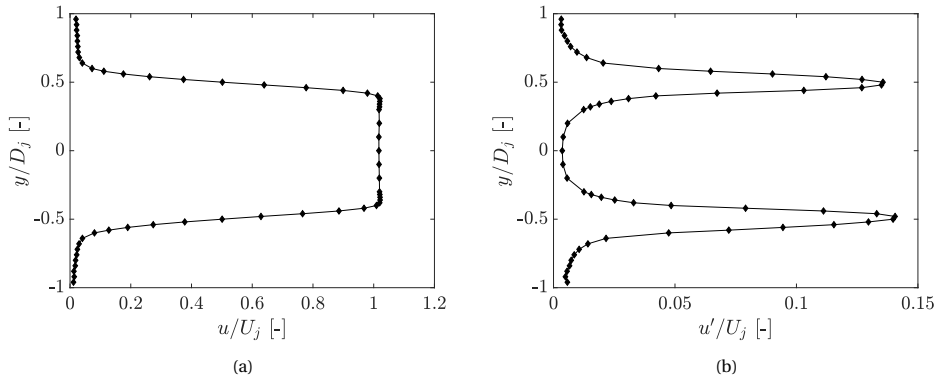


Figure B.6: Profiles of (a) time-averaged axial velocity and (b) r.m.s. of axial velocity at  $x = 1D_j$ .

The jet development in the axial direction is shown in Fig. B.7 from  $1D_j$  up to  $10D_j$  in  $1D_j$  steps. The profiles show a progressive reduction in velocity and spreading of the flow. Finally, the velocity signal measured at the lipline for an axial position  $x = 5D_j$  is used to compute the spectrum of turbulent kinetic energy, non-dimensionalized by the square of the jet nominal velocity, as shown in B.8. The levels are approximately

constant up to  $f = 300$  Hz, after which they decay following Kolmogorov's  $f^{-5/3}$  law [3], up to  $f = 7$  kHz, approximately. These results show the turbulent characteristic of the jet mixing layer and that the nozzle design is satisfactory.

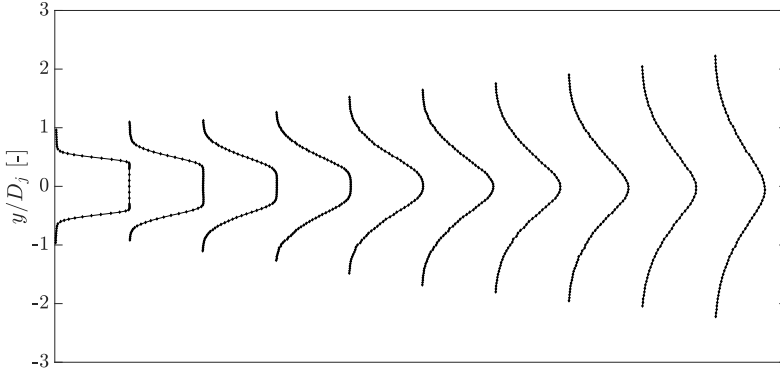


Figure B.7: Jet velocity profiles from  $1D_j$  up to  $10D_j$  in  $1D_j$  steps.

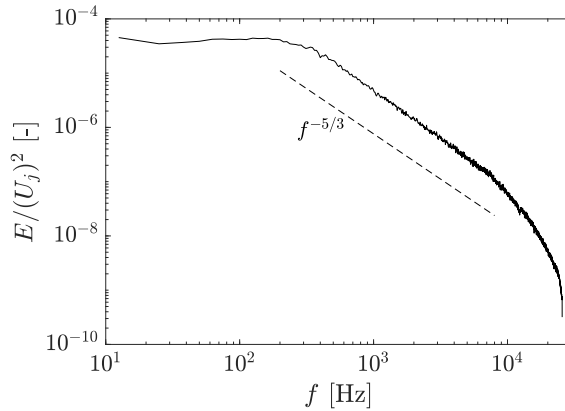


Figure B.8: Spectrum of turbulent kinetic energy, obtained from velocity fluctuations sampled at the jet lip line, for  $x = 5D_j$ .

## B.5. ACOUSTIC CHARACTERISTICS

The acoustic characteristics of the jet are obtained through microphone measurements and the spectra obtained for a polar angle  $\theta = 90^\circ$  are shown in Fig. B.9 for both isolated and installed configurations.

The results show that the isolated jet spectrum has a clear broadband characteristic with noise levels decaying for increasing frequency. The installed jet spectrum has

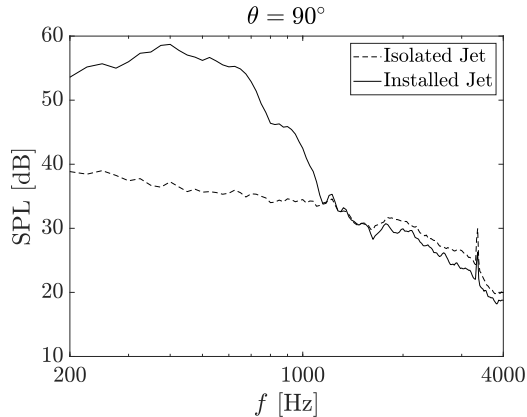


Figure B.9: Far-field noise spectra obtained for a jet with  $U_j = 60$  m/s. The installed configuration comprises a flat plate mounted with  $L = 3D_j$  and  $h = 1D_j$ . Spectra obtained at  $\theta = 90^\circ$  for the shielded side of the jet.

higher noise levels with respect to the isolated one in the frequency range  $200 \text{ Hz} < f < 1000 \text{ Hz}$ . Lower frequencies are not included due to the loss of the anechoic capability of the working section. At frequencies higher than  $f = 4 \text{ kHz}$ , spurious effects have been verified and it is believed that, due to the low flow speed, the jet is no longer the dominant acoustic source in that range. The difference in noise levels between the installed and isolated cases is approximately 20 dB at  $f = 400 \text{ Hz}$  (peak frequency of the installed case). This high increase is also due to the low jet speed, which is in qualitative agreement with the results reported in Chapter 6 [4]. For  $f > 1.5 \text{ kHz}$ , the installed noise levels are lower than the isolated ones due to shielding effect. Finally, a tone is verified at  $f = 3350 \text{ Hz}$  for both cases; it is believed that this is due to a gap between parts of the tunnel circuit. However, it occurs at a frequency much higher than the range wherein installation effects are dominant.

## REFERENCES

- [1] R. Merino-Martínez, A. Rubio Carpio, L. T. Lima Pereira, S. van Herk, F. Avallone, D. Ragni, and M. Kotsonis, *Aeroacoustic design and characterization of the 3D-printed, open-jet, anechoic wind tunnel of Delft University of Technology*, *Applied Acoustics* **170**, 107504 (2020).
- [2] T. Morel, *Comprehensive Design of Axisymmetric Wind Tunnel Contractions*, *Journal of Fluids Engineering* **97**, 225 (1975).
- [3] S. B. Pope, *Turbulent Flows* (Cambridge University Press, 2000).
- [4] L. Rego, D. Ragni, F. Avallone, D. Casalino, R. Zamponi, and C. Schram, *Jet-installation noise reduction with flow-permeable materials*, *Journal of Sound and Vibration* **498**, 115959 (2021).



# LIST OF PUBLICATIONS

## JOURNAL PAPERS

7. **L. Rego**, R. Zamponi, D. Ragni, F. Avallone, D. Casalino, & M. Cruellas Bordes, *Jet-installation noise reduction with permeable flaps at in-flight conditions*, to be submitted to the AIAA Journal, (2022).
6. **L. Rego**, F. Avallone, D. Ragni, D. Casalino, & H. Denayer, *Acoustic liners for jet-installation noise reduction*, Accepted for publication in the Journal of Sound and Vibration, (2022).
5. **L. Rego**, F. Avallone, D. Ragni, & D. Casalino, *On the mechanisms of jet-installation noise reduction with flow-permeable trailing edges*, [Journal of Sound and Vibration](#) **520**, 116582 (2022).
4. C. Teruna, **L. Rego**, D. Casalino, D. Ragni, & F. Avallone, *A numerical study on aircraft noise mitigation using porous stator concepts*, [MDPI Aerospace](#) **9**(2), 70 (2022).
3. C. Teruna, **L. Rego**, F. Avallone, D. Ragni, & D. Casalino, *Applications of the multi-layer porous medium modelling approach for noise mitigation*, [Journal of Aerospace Engineering](#) **34**(6), 04021074 (2021).
2. **L. Rego**, D. Ragni, F. Avallone, D. Casalino, R. Zamponi, & C. Schram, *Jet-installation noise reduction with flow-permeable materials*, [Journal of Sound and Vibration](#) **498**, 115959 (2021).
1. **L. Rego**, F. Avallone, D. Ragni, & D. Casalino, *Jet-installation noise and near-field characteristics of jet-surface interaction*, [Journal of Fluid Mechanics](#) **895**, A2 (2020).

## CONFERENCE PROCEEDINGS

3. **L. Rego**, R. Zamponi, D. Ragni, F. Avallone, D. Casalino, & M. Cruellas Bordes, *Jet-installation noise reduction with permeable flaps at in-flight conditions*, submitted to the 28th AIAA / CEAS Aeroacoustics Conference, (2022).
2. **L. Rego**, F. Avallone, D. Ragni, D. Casalino & W. van der Velden, *Free-Stream Effects on Jet-Installation Noise of a Dual-Stream Engine*, [25th AIAA / CEAS Aeroacoustics Conference](#), (2019).
1. **L. Rego**, F. Avallone, D. Ragni, & D. Casalino, *Noise Amplification Effects due to Jet-Surface Interaction*, [AIAA SciTech Forum](#), (2019).